



Dipl.-Ing. Benedikt Schrode, BSc

Mapping Large Reciprocal-Space Volumes by Rotating Grazing Incidence X-ray Diffraction

DOCTORAL THESIS

to achieve the university degree of
Doktor der technischen Wissenschaften
submitted to

Graz University of Technology

Supervisor

Ao.Univ.-Prof. Dipl.-Ing. Dr.techn. Roland Resel
Institute of Solid State Physics
Graz University of Technology

Affidavit

I declare that I have authored this thesis independently, that I have not used other than the declared sources/resources, and that I have explicitly indicated all material which has been quoted either literally or by content from the sources used. The text document uploaded to TUGRAZonline is identical to the present doctoral thesis.

Date

Signature

Abstract

Thin-film growth with a specific preferred orientation of the crystallites relative to the substrate surface is frequently observed. Additionally, a specific in-plane alignment of the crystallites might be present, *i.e.* a certain crystallographic direction is only found along distinct azimuthal angles of the substrate, *e.g.* due to statistical problems or epitaxial growth. The specific order poses additional requirements in terms of experimental investigations. This thesis presents the method of rotating grazing incidence X-ray diffraction (GIXD), which is especially suited for thin films with in-plane alignment of the crystallites. The rotation of the sample around its surface normal allows access to large volumes of reciprocal space and collection of a wide range of diffraction information. In this thesis, experimental challenges of rotating GIXD are discussed in detail. Furthermore, GIDVis, a software package suitable for data evaluation of rotating GIXD measurements, is presented. GIDVis can be used in several steps of the data evaluation process, for example for the analysis of a calibration measurement, phase and texture evaluation, calculation of pole figures, data stitching, intensity corrections, *etc.* As an example, GIDVis is applied to extract the epitaxial relationships of a thin film of the organic semiconductor 6,13-pentacenequinone (P2O) grown on Au(111) from rotating GIXD data. Moreover, phase and texture analyses of films of the pharmaceutical molecule carbamazepine with statistical problems are presented. Unknown crystal structures require determination of the unit cell parameters. However, standard data evaluation routines cannot be applied due to the low number of observed peaks, the orientation of the crystallites and the possibility of several different crystal phases coexisting on the sample. Therefore, an algorithm is presented which is suited to obtain the lattice parameters from three-dimensional peak positions extracted from rotating GIXD data. As an example, lattice parameters, texture and in-plane alignment of P2O crystallites epitaxially grown on Ag(111) are determined.

Zusammenfassung

Dünnschichtwachstum mit einer Vorzugsorientierung der Kristallite in Bezug auf die Substratoberfläche ist ein häufig beobachtetes Phänomen. Zusätzlich kann eine Ausrichtung der Kristallite in der Substratebene vorliegen. Das bedeutet, dass eine bestimmte kristallographische Richtung auf bestimmte azimutale Winkel des Substrats beschränkt ist, z. B. aufgrund statistischer Probleme oder epitaktischen Wachstums. Diese spezifische Ordnung stellt zusätzliche Anforderungen an die experimentellen Untersuchungen. Die vorliegende Arbeit beschäftigt sich mit der Anwendung von Röntgendiffraktometrie unter streifendem Einfall mit einer zusätzlichen Probenrotation um deren Oberflächennormale („Rotating GIXD“). Diese Methode ist besonders für dünne Filme mit Ausrichtung der Kristallite in der Substrat-Ebene geeignet. Die Probenrotation ermöglicht den Zugang zu großen Bereichen des reziproken Raums und ein Großteil der Beugungsinformationen kann aufgenommen werden. In dieser Arbeit werden die experimentellen Herausforderungen von Rotating GIXD im Detail diskutiert. Darüber hinaus wird das Softwarepaket GIDVis vorgestellt, welches besonders für die Auswertung von Rotating GIXD-Daten geeignet ist. GIDVis kann in mehreren Schritten des Datenauswertungsprozesses angewendet werden, z. B. zur Analyse einer Kalibrationsmessung, zur Phasen- und Texturauswertung, zur Berechnung von Polfiguren, zur Verbindung mehrerer Datensätze, für Intensitätskorrekturen, etc. Als Beispiel wird GIDVis zur Bestimmung der epitaktischen Beziehungen eines Dünnschichtfilms des organischen Halbleiters 6,13-Pentacenchinon (P2O) auf Au(111) aus Rotating GIXD-Daten verwendet. Weiters werden Phasen- und Texturanalysen von Filmen des pharmazeutischen Moleküls Carbamazepin mit statistischen Problemen gezeigt. Unbekannte Kristallstrukturen erfordern die Bestimmung der Einheitszellenparameter. Allerdings sind gewöhnliche Datenauswertungsroutinen aufgrund der geringen Anzahl an Peaks, der Ausrichtung der Kristallite und der möglichen Koexistenz mehrerer unterschiedlicher Kristallphasen auf derselben Probe nicht anwendbar. Deshalb

wird ein Algorithmus vorgestellt, welcher die Berechnung der Einheitszellenparameter aus dreidimensionalen Peakpositionen aus Rotating GIXD-Daten ermöglicht. Als Beispiel werden Einheitszellenparameter, Textur und die Ausrichtung von epitaktisch gewachsenen P2O-Kristalliten auf Ag(111) bestimmt.

Acknowledgements

First, I thank my supervisor Roland Resel for making this work possible and the excellent support throughout the time spent in his group. I also thank you for initiating the contact with Oliver Werzer. Oliver gave me the opportunity to work with him and his group at the University of Graz. I thank Oliver for introducing me to the world of X-ray diffraction in Graz and Trieste, the great collaborations and always having time for questions – scientific or others. Special thanks to Christian Röthel and Stefan Pachmajer. Their expertise in grazing incidence X-ray diffraction, data evaluation, pole figure measurements and their knowledge transfer was a basis for the GIDVis software package. Thank you for the hours spend discussing various topics, from diffraction to sports.

Many thanks to all former and current colleagues at the Institute of Solid State Physics, especially the k-Raum, for help, discussion of problems and the great working atmosphere. Special thanks to the collaboration partners: Josef Simbrunner for his valuable contributions in indexation and his patience when answering all my questions. Torsten Fritz and the members of his group, especially Jari Domke, Marco Grünewald, Falko Sojka and Roman Forker, for giving me the opportunity to gain insight into the sample preparation and their measurement techniques during my stay in Jena as well as their continuous supply of high-quality samples for our measurements. Thanks to the members of the group of Paolo Falcaro, especially Francesco Carraro, and of the group of Rob Ameloot, especially Sabina Rodríguez-Hemida and Timothée Stassin, for the great collaboration in the field of metal-organic frameworks. Thanks to collaboration partners for whom I made measurements. You gave me the opportunity to broaden my scientific horizon and to gain an impression of your working fields.

To all my colleagues from different groups in Graz, Brussels, Leuven, Milano and Bologna who joined one of the various beamtimes during the last years: thank you for the good times during day and night shifts and the free time in between. Spending so much time and going through the ups and downs of the beam, mood and results together makes these beamtimes an unforgettable and invaluable experience.

Thanks to my parents and brothers for their support and the freedom they gave me to follow my interests. Last but not least I thank my girlfriend Ingrid. Thank you for your never-ending support, the fruitful discussions and for proofreading this thesis.

Contents

1	Introduction	13
2	Fundamentals	17
2.1	Three-Dimensional Crystal Structures	17
2.1.1	Points, Directions and Planes	19
2.1.2	Reciprocal Space	22
2.2	Crystal Lattices Described in Two Dimensions	23
2.2.1	Determination of Surface Unit Cells from Three-Dimensional Crystal Structures	25
2.2.2	Example: Silver in (111) Orientation	29
2.2.3	Example: Pentacenequinone (P2O) in (102) Orientation . .	31
2.3	Crystallite Alignment	32
2.4	Epitaxy	34
2.4.1	Notations for Epitaxial Growth	36
2.4.2	Classification of Epitaxy	39
2.5	X-Ray Diffraction	45
2.6	Grazing Incidence X-Ray Diffraction	48
2.6.1	Static Sample	50
2.6.2	Rotating Sample	51
2.7	Indexing X-Ray Diffraction Data	53
2.7.1	Indexing of Grazing Incidence X-Ray Diffraction Data . . .	53

3	Methods	57
3.1	Rotating Grazing Incidence X-ray Diffraction	57
3.1.1	Beamline XRD1 (Elettra)	57
3.2	The Software Package GIDVis	69
3.3	Pole Figure Evaluation and Epitaxy Matrices	72
4	Results	77
4.1	Impact of Sample Misalignment on Grazing Incidence X-Ray Diffraction Patterns and the Resulting Unit Cell Determination	77
4.2	<i>GIDVis</i> : A Comprehensive Software Tool for Geometry-Independent Grazing-Incidence X-ray Diffraction Data Analysis and Pole-Figure Calculations	99
4.3	Solvent Vapor Annealing of Amorphous Carbamazepine Films for Fast Polymorph Screening and Dissolution Alteration	109
4.4	An Efficient Method for Indexing Grazing-Incidence X-ray Diffraction Data of Epitaxially Grown Thin Films	120
4.5	Other Publications Employing Rotating Grazing Incidence X-ray Diffraction	135
4.6	Other Publications Employing Static Grazing Incidence X-ray Diffraction	136
5	Conclusion	139

1 Introduction

Formation of thin films on solid substrates in thermodynamic equilibrium can be described in terms of the surface tension γ of the involved surfaces and interfaces:^[1,2]

$$\gamma_S = \gamma_{SF} + \gamma_F \cos \phi, \quad (1.1)$$

where γ_S , γ_F and γ_{SF} are the surface energy of the substrate, film and substrate-film interface respectively and ϕ is the contact angle. Depending on the individual contributions, three different growth modes can be distinguished. In Frank-van der Merwe growth, wetting of the substrate is favored (*i.e.* $\phi = 0^\circ$, $\gamma_S > \gamma_{SF} + \gamma_F$) and the film grows layer-by-layer. In case the contact angle is larger than 0° , $\gamma_S < \gamma_{SF} + \gamma_F$, strong island formation is observed (Volmer-Weber growth). In Stranski-Krastanov growth, first complete layers are formed on which islands grow afterwards, *i.e.* the contributions to Equation 1.1 change as a function of film thickness. Stranski-Krastanov growth can be seen as a result of lattice mismatch between substrate and adsorbate layer.^[3] The first layers are fully covering the substrate but strained to match the substrate lattice. However, at a certain critical film thickness, the strain would exceed the maximum possible value determined by the adsorbate-adsorbate interaction and individual islands are energetically favored.^[3] Please note that depending on the film preparation technique, growth might be close to the thermodynamic equilibrium (*e.g.* hot-wall epitaxy, drop coating) or far from it (*e.g.* physical vapour deposition, spin coating)^[4,5]. Also the investigated material plays an important role, *e.g.* liquid crystalline phases are often considered to be in thermodynamic equilibrium.^[6,7] If the growth is far from equilibrium, a description using the individual atomic processes occurring during

1 Introduction

film growth (condensation, re-evaporation, diffusion, adsorption, *etc.*) might be favored^[2,8,9] over the simple model of surface energy contributions.

In applications, the thin-film morphology governed by the different growth modes, intermolecular interactions and molecule-substrate interactions plays an important role.^[10–13] For example, molecules with large intermolecular interactions show pronounced island growth^[14] while in most cases of thin films of organic molecules, Stranski-Krastanov growth is observed^[15,16] but also layer-by-layer type growth can be found^[17]. Furthermore, the crystal structure of the material influences its properties and thus needs to be investigated and determined.^[18–21] In thin films as typically used in devices, often so-called substrate-induced phases (SIPs) are found, *i.e.* a crystallographic phase different from the bulk phase is formed as a result of the interaction between adsorbate and substrate.^[5,22–25] Not only the crystal structure itself influences the properties, also the orientation of crystallites on the substrate plays an important role, due to the anisotropy of properties in crystals.^[26–28] In thin films of organic molecules on solid substrates, texture is frequently observed.^[14,29–31] This means that a certain crystallographic plane of the adsorbate is parallel to the substrate surface (out-of-plane orientation). Additionally, a specific in-plane order might be present, *i.e.* a certain crystallographic direction parallel to the substrate surface is restricted to certain azimuthal angles. Here, two different cases can be differentiated: either a very well defined in-plane alignment (*e.g.* in epitaxial growth) or a more random distribution still showing only distinct azimuths of the crystallographic directions (samples with statistical problems, *e.g.* due to a low number of large crystallites).

The in-plane order poses additional requirements in terms of experimental investigations of thin-film samples. First, a suitable measurement technique is required. The low incident angle resulting in limited penetration depth and surface sensitivity makes GIXD an especially suited method.^[32,33] Furthermore, GIXD is already applied to fiber-textured films (*i.e.* films without azimuthal order). To make this technique applicable to ordered films, the sample has to be azimuthally rotated around its surface normal in a well-defined way to access large volumes of reciprocal space and collect a wide range of diffraction information (rotating GIXD).

Another advantage of rotating GIXD over conventional GIXD is that not only samples with very defined order can be investigated, but also films with statistical problems. Challenges of rotating GIXD in terms of the experimental setup and sample alignment as well as possible solutions are described in section 3.1 and section 4.1 of this thesis.

After performing the rotating GIXD experiment, suitable software packages are required to handle the large amounts of data collected. Several data processing steps have to be carried out, starting with the analysis of a calibration measurement and subsequent data conversion to reciprocal space. The obtained diffraction patterns can then be compared to known crystal structures to find possible matches and the texture of the sample. Furthermore, due to the reliable azimuthal rotation, epitaxial relationships of well-ordered films, *i.e.* the azimuthal orientation of the adsorbate crystallites with respect to the substrate crystal, can be determined. During this thesis, the software package GIDVis was developed. It allows complete evaluation of (rotating) GIXD data, including setup calibration using a standard measurement, crystal phase and texture analysis, intensity corrections and pole figure (PF) calculation for subsequent determination of epitaxial relationships. Section 3.2 provides general information on GIDVis. More details can be found in section 4.2, where GIDVis is used to extract epitaxial relationships from rotating GIXD data of a thin film of the organic semiconductor P2O on the Au(111) surface.^[34] For the evaluation of epitaxial relationships and determination of surface unit cells from PFs, a short MATLAB script is presented in section 3.3. An example of phase and texture analysis of films of the pharmaceutical molecule carbamazepine (CBZ) with statistical problems can be found in section 4.3.^[35]

As mentioned above, GIDVis provides the possibility to compare known crystal structures to the observed diffraction pattern. However, in case no matches can be found, for example because the investigated material forms a SIP, special algorithms to determine the lattice parameters are required. Standard data evaluation routines successfully employed in single crystal X-ray diffraction (XRD) cannot be used due to the low number of peaks resulting from the low scattering volume, the out-of-plane and in-plane orientation of the crystallites and the possibility of several

1 Introduction

different crystal phases coexisting on the same sample. Thus, an algorithm to obtain the lattice parameters from three-dimensional peak positions extracted from rotating GIXD measurements was developed.^[36] Its functionality is demonstrated by application to a thin film of P2O epitaxially grown on the Ag(111) surface (section 4.4).

2 Fundamentals

This chapter provides a selection of background information to understand this work since a detailed description of the individual topics would be very lengthy. First, the well-established description of crystallography in three dimensions, *i.e.* choice of the unit cell, planes, directions, *etc.* in real and reciprocal space is discussed. Then, these concepts are transferred to two dimensions. Further, crystallite alignment and epitaxy is described. In the second part, the applied experimental techniques are described.

2.1 Three-Dimensional Crystal Structures

The following section is based on Bennett^[37], Weissmantel et al.^[38] and Hahn^[39], unless noted.

A crystal is the periodic arrangement of atoms in three-dimensional space, which means that translational symmetries are present. To describe this mathematically, the concept of the unit cell is applied. In general, the unit cell is a parallelepiped described by the lattice parameters a , b , c (the lengths of the edges) and the enclosed angles α , β and γ (*cf.* Figure 2.1). Depending on their symmetry, crystal structures can be divided into different crystal systems, *e.g.* the most symmetric one, cubic, if $a = b = c$, $\alpha = \beta = \gamma = 90^\circ$, down to the least symmetric triclinic system ($a \neq b \neq c$, $\alpha \neq \beta \neq \gamma \neq 90^\circ$). Applying translations to the unit cell along the unit cell edges by integer multiples of their lengths creates the crystalline

2 Fundamentals

lattice in three-dimensional space. Atoms are introduced with the so-called basis, which is associated with every lattice point to build up the three-dimensional atom arrangement representing the crystal. Thus, the unit cell contains a certain number of atoms, ranging from single atoms (*e.g.* metals), to molecules with few tens of atoms (*e.g.* P2O) up to several hundred or even thousands of atoms in case of *e.g.* proteins.

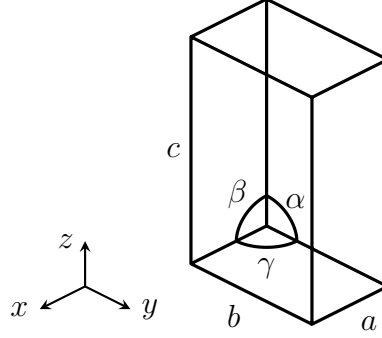


Figure 2.1 Sketch of a three-dimensional unit cell described by the lattice parameters a , b , and c and the enclosed angles α , β and γ .

From the lattice parameters, the lattice vectors \mathbf{a} , \mathbf{b} and \mathbf{c} can be calculated:

$$\mathbf{a} = \begin{pmatrix} a \\ 0 \\ 0 \end{pmatrix}, \quad \mathbf{b} = \begin{pmatrix} b \cos(\gamma) \\ b \sin(\gamma) \\ 0 \end{pmatrix}, \quad \mathbf{c} = \begin{pmatrix} c \cos(\beta) \\ c [\cos(\alpha) - \cos(\beta) \cos(\gamma)] / \sin(\gamma) \\ V / [ab \sin(\gamma)] \end{pmatrix}, \quad (2.1)$$

where V is the unit cell volume and can be calculated by

$$V = abc \left[1 - \cos^2(\alpha) - \cos^2(\beta) - \cos^2(\gamma) + 2 \cos(\alpha) \cos(\beta) \cos(\gamma) \right]^{1/2}. \quad (2.2)$$

The formulas given in Equation 2.1 represent one possible choice of lattice vectors where \mathbf{a} is pointing in the x -direction, \mathbf{b} is chosen to lie in the x - y -plane and \mathbf{c} is determined by a combination of all other lattice parameters so that the vectors describe a right-handed coordinate system. In general, \mathbf{a} , \mathbf{b} and \mathbf{c} should be chosen as short as possible. By applying standard rotation matrices onto \mathbf{a} , \mathbf{b} and \mathbf{c} different lattice vector representations of the same unit cell can be obtained. Furthermore, the choice of the lattice vectors is not unique, but different conditions

exist for their selection depending on the type T of the unit cell (Table 2.1). T is defined as

$$T = (\mathbf{a} \cdot \mathbf{b}) (\mathbf{b} \cdot \mathbf{c}) (\mathbf{c} \cdot \mathbf{a}), \quad (2.3)$$

and it describes whether all unit cell angles are acute (α, β and $\gamma < 90^\circ$, $T > 0$) or non-acute (α, β and $\gamma \geq 90^\circ$, $T \leq 0$). If the requirements are fulfilled, the lattice vectors describe the reduced basis of the unit cell.

2.1.1 Points, Directions and Planes

Due to the translational symmetry, any point \mathbf{P} of the crystalline lattice can be expressed by a linear combination of the lattice vectors:

$$\mathbf{P} = \mathbf{R}_0 + u\mathbf{a} + v\mathbf{b} + w\mathbf{c}, \quad (2.4)$$

where u, v and w are integers and \mathbf{R}_0 becomes zero if the origin coincides with a lattice point. A direction in the crystal is described by the indices $[uvw]$, *e.g.* the direction $[100]$ is equivalent to the lattice vector \mathbf{a} , and $[001]$ is equivalent to \mathbf{c} (which is not necessarily parallel to the Cartesian z -axis, even when constructing \mathbf{c} according to Equation 2.1).

A crystal can also be seen as a set of equidistant crystallographic planes, *i.e.* planes passing through three lattice points each and having the same interplanar spacing. Already in 1817, Weiss suggested to describe a crystallographic plane by its intersection points with the axes system created by the lattice vectors \mathbf{a} , \mathbf{b} and \mathbf{c} .^[40] For example, this would result in the Weiss notation $2\mathbf{a}:4\mathbf{b}:3\mathbf{c}$ for the plane denoted in Figure 2.2, since the plane intersects the axes at $2\mathbf{a}$, $4\mathbf{b}$ and $3\mathbf{c}$. However, this system becomes less useful when planes parallel to one or two lattice vectors are considered. These planes do not intersect one or two axis/axes (except at infinity) and the corresponding index/indices would be infinity. Thus, Miller indices^[41] are used instead. They are based on the reciprocal values of the axes intersections, which are then multiplied with the least common multiple to

Table 2.1 Rules for the construction of the three-dimensional reduced base (\mathbf{a} , \mathbf{b} , \mathbf{c}) for Type-I ($T > 0$) and Type-II ($T \leq 0$) unit cells.

General Rules (Type-I and Type-II)			
$\mathbf{a} \cdot \mathbf{a} \leq \mathbf{b} \cdot \mathbf{b} \leq \mathbf{c} \cdot \mathbf{c}$ $ \mathbf{b} \cdot \mathbf{c} \leq \frac{\mathbf{b} \cdot \mathbf{b}}{2}$ $ \mathbf{a} \cdot \mathbf{c} \leq \frac{\mathbf{a} \cdot \mathbf{a}}{2}$ $ \mathbf{a} \cdot \mathbf{b} \leq \frac{\mathbf{a} \cdot \mathbf{a}}{2}$			
Additional Rules for Type-I		Special Rules for Type-I	
$\mathbf{b} \cdot \mathbf{c} > 0$	if $\mathbf{a} \cdot \mathbf{a} = \mathbf{b} \cdot \mathbf{b}$	then	$\mathbf{b} \cdot \mathbf{c} \leq \mathbf{a} \cdot \mathbf{c}$
$\mathbf{a} \cdot \mathbf{c} > 0$	if $\mathbf{b} \cdot \mathbf{c} = \mathbf{c} \cdot \mathbf{c}$	then	$\mathbf{a} \cdot \mathbf{c} \leq \mathbf{a} \cdot \mathbf{b}$
$\mathbf{a} \cdot \mathbf{b} > 0$	if $\mathbf{b} \cdot \mathbf{c} = \frac{1}{2}\mathbf{b} \cdot \mathbf{b}$	then	$\mathbf{a} \cdot \mathbf{b} \leq 2\mathbf{a} \cdot \mathbf{c}$
	if $\mathbf{a} \cdot \mathbf{c} = \frac{1}{2}\mathbf{a} \cdot \mathbf{a}$	then	$\mathbf{a} \cdot \mathbf{c} \leq 2\mathbf{b} \cdot \mathbf{c}$
Additional Rules for Type-II			
$(\mathbf{b} \cdot \mathbf{c} + \mathbf{a} \cdot \mathbf{c} + \mathbf{a} \cdot \mathbf{b}) \leq \frac{1}{2}(\mathbf{a} \cdot \mathbf{a} + \mathbf{b} \cdot \mathbf{b})$ $\mathbf{b} \cdot \mathbf{c} \leq 0$ $\mathbf{a} \cdot \mathbf{c} \leq 0$ $\mathbf{a} \cdot \mathbf{b} \leq 0$			
Special Rules for Type-II			
if	$\mathbf{a} \cdot \mathbf{a} = \mathbf{b} \cdot \mathbf{b}$	then	$ \mathbf{b} \cdot \mathbf{c} \leq \mathbf{a} \cdot \mathbf{c} $
if	$\mathbf{b} \cdot \mathbf{b} = \mathbf{c} \cdot \mathbf{c}$	then	$ \mathbf{a} \cdot \mathbf{c} \leq \mathbf{a} \cdot \mathbf{b} $
if	$ \mathbf{b} \cdot \mathbf{c} = \frac{1}{2}\mathbf{b} \cdot \mathbf{b}$	then	$\mathbf{a} \cdot \mathbf{b} = 0$
if	$ \mathbf{a} \cdot \mathbf{c} = \frac{1}{2}\mathbf{a} \cdot \mathbf{a}$	then	$\mathbf{a} \cdot \mathbf{b} = 0$
if	$ \mathbf{a} \cdot \mathbf{b} = \frac{1}{2}\mathbf{a} \cdot \mathbf{a}$	then	$\mathbf{a} \cdot \mathbf{c} = 0$
if	$(\mathbf{b} \cdot \mathbf{c} + \mathbf{a} \cdot \mathbf{c} + \mathbf{a} \cdot \mathbf{b}) = \frac{1}{2}(\mathbf{a} \cdot \mathbf{a} + \mathbf{b} \cdot \mathbf{b})$	then	$\mathbf{a} \cdot \mathbf{a} \leq 2 \mathbf{a} \cdot \mathbf{c} + \mathbf{a} \cdot \mathbf{b} $

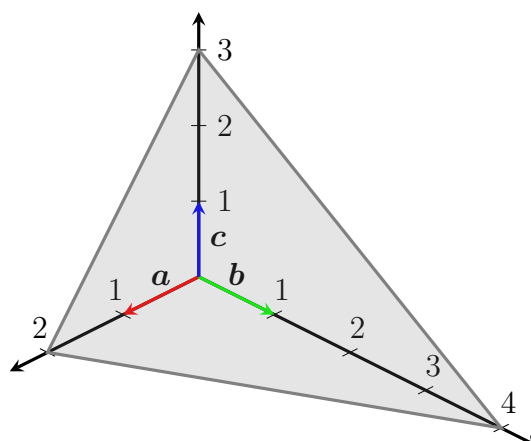


Figure 2.2 The lattice vectors \mathbf{a} , \mathbf{b} and \mathbf{c} (red, green and blue) and the (634) crystal plane (gray).

obtain integer values. For the plane shown in Figure 2.2, the according reciprocal intersection values are $1/2$, $1/4$ and $1/3$. The least common multiple of the intersection points is 12, resulting in the (634) plane. Please note that the plane is actually infinitely extended, not limited to the triangular shape given in Figure 2.2. Using the Miller indices, the problem of a plane without an intersection with a specific axis leads to the corresponding Miller index being zero.^[42]

As already indicated in the previous paragraphs, single crystallographic directions are indicated by square brackets and single crystallographic planes by parentheses. Table 2.2 gives an overview of the complete nomenclature used in crystallography.

Table 2.2 Crystallographic nomenclature in three-dimensional space.

Notation	Meaning
$[uvw]$	a direction in the lattice
$\langle uvw \rangle$	all symmetry equivalent directions
(hkl)	a crystallographic plane
$\{hkl\}$	all symmetry equivalent planes
hkl	a diffraction peak (<i>cf.</i> section 2.5)

2.1.2 Reciprocal Space

In general, reciprocal space is the Fourier transform of real space, and the reciprocal lattice is the Fourier transform of the direct (*i.e.* real-space) lattice. The concept of reciprocal space is often applied in physics since a periodic quantity, *e.g.* electron density inside a crystal, can easily be represented as Fourier series in reciprocal space. Additionally, the diffraction process can be expressed very compact in reciprocal space (*cf.* section 2.5).

Points, vectors, directions and planes of reciprocal space are named equivalently to real space, but with a superscript asterisk (*). From the real-space volume V and the lattice vectors \mathbf{a} , \mathbf{b} and \mathbf{c} , the reciprocal lattice vectors \mathbf{a}^* , \mathbf{b}^* , \mathbf{c}^* can be calculated by

$$\mathbf{a}^* = 2\pi \frac{\mathbf{b} \times \mathbf{c}}{V}, \quad \mathbf{b}^* = 2\pi \frac{\mathbf{c} \times \mathbf{a}}{V}, \quad \mathbf{c}^* = 2\pi \frac{\mathbf{a} \times \mathbf{b}}{V}. \quad (2.5)$$

As it can be seen from Equation 2.5, the unit of the reciprocal space vector is inverse length, typically \AA^{-1} or nm^{-1} . When transforming from real space to reciprocal space, the crystal system is preserved. For example, a cubic real-space lattice is cubic in reciprocal space but with different lattice constants according to Equation 2.5. In analogy to real space, the reciprocal space vector \mathbf{G}_{hkl} is given by

$$\mathbf{G}_{hkl} = h\mathbf{a}^* + k\mathbf{b}^* + l\mathbf{c}^*. \quad (2.6)$$

Please note that the length of the reciprocal space vector $|\mathbf{G}_{hkl}|$ is related to the netplane distance of real space d_{hkl} via

$$|\mathbf{G}_{hkl}| = \frac{2\pi}{d_{hkl}}, \quad (2.7)$$

and the direction $[hkl]^*$ in reciprocal space is perpendicular to the plane (hkl) of real space.

2.2 Crystal Lattices Described in Two Dimensions

Unless noted, the following section is based on Wood^[43], Jona et al.^[44] and Hahn^[39].

Thin-film samples together with surface sensitive measurement techniques do not always require or even do not allow a description using three-dimensional space. For example, low-energy electron diffraction (LEED) only probes top layers of the film^[45] and the complexity can be lowered by reduction to a two-dimensional description. Instead of using the three-dimensional unit cell, the two-dimensional surface unit cell which is lying parallel to the probed plane is constructed. It is defined by the lattice vectors $\mathbf{a} = (a_x, a_y)$ and $\mathbf{b} = (b_x, b_y)$, enclosing the angle γ (*cf.* Figure 2.3), where

$$a = \sqrt{a_x^2 + a_y^2}, \quad (2.8)$$

$$b = \sqrt{b_x^2 + b_y^2}, \quad (2.9)$$

$$\cos(\gamma) = \frac{\mathbf{a} \cdot \mathbf{b}}{ab} = \frac{a_x b_x + a_y b_y}{ab}. \quad (2.10)$$

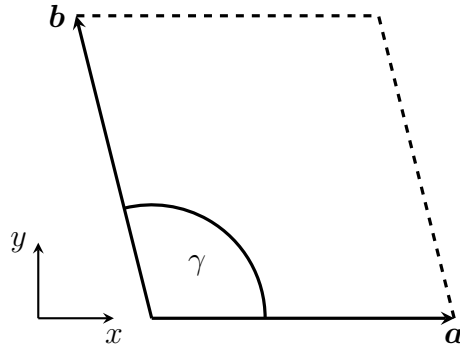


Figure 2.3 Surface unit cell defined by the lattice vectors \mathbf{a} and \mathbf{b} which are enclosing the angle γ .

Translation of the surface unit cell along \mathbf{a} and \mathbf{b} by integer multiples of a and b builds up the regular pattern of lattice points. The area A of the surface unit cell

2 Fundamentals

can be calculated by

$$A = |\mathbf{a} \times \mathbf{b}| = ab \sin(\gamma), \quad (2.11)$$

where a z -component of zero has to be assumed for \mathbf{a} and \mathbf{b} to allow calculation of the cross product.

Similar to three-dimensional crystal structures, surface unit cells can be classified into different systems according to their lattice parameters and the symmetries: The most general case, *i.e.* the least symmetric one, is the oblique system, where no restrictions apply. In the rectangular system, a differs from b and γ equals 90° . In the square and hexagonal system, $a = b$ and $\gamma = 90^\circ$ and $\gamma = 120^\circ$ respectively. Independent of the system, the lattice vectors should be chosen as short as possible and for the oblique and the rectangular system such that $a < b$.

As in three-dimensional space, any lattice point \mathbf{P} can be written as a linear combination of the lattice vectors \mathbf{a} and \mathbf{b} :

$$\mathbf{P} = \mathbf{R}_0 + u\mathbf{a} + v\mathbf{b}. \quad (2.12)$$

A line passing through two lattice points can be described by two Miller indices (hk) , similar to the description of a plane in three dimensions. For example, consider the lattice vectors \mathbf{a} and \mathbf{b} and the gray solid line in Figure 2.4. The line intersects the axes at $3\mathbf{a}$ and $2\mathbf{b}$. Calculating the reciprocal values yields $1/3$ and $1/2$ respectively. The least common multiple is 6, thus the line is the (23) line. A line parallel to one of the lattice vectors does not intersect the corresponding axis and will result in the corresponding Miller index being zero. For example, parallel to \mathbf{a} the (01) line and parallel to \mathbf{b} the (10) line is found (*cf.* Figure 2.4, gray dashed lines). A direction can be described by a linear combination of the lattice vectors and is denoted by $[uv]$; *e.g.* the orange line in Figure 2.4 is the $[31]$ direction, passing through the lattice point $\mathbf{P} = 3\mathbf{a} + \mathbf{b}$ (orange point).

Table 2.3 gives an overview of the nomenclature applied in the description of two-dimensional crystal lattices.

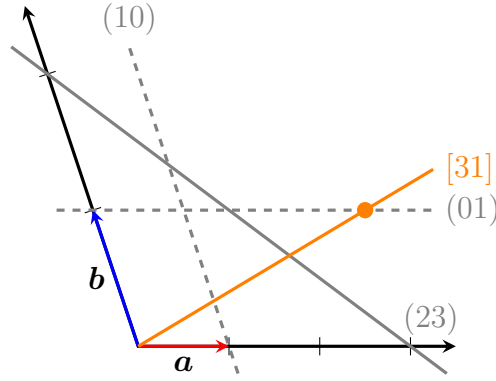


Figure 2.4 Lattice vectors \mathbf{a} and \mathbf{b} defining the real-space lattice, the non-primitive (23) line (gray, solid), the primitive (01) and (10) lines (gray, dashed) and the [31] direction (orange).

Table 2.3 Crystallographic nomenclature in two-dimensional space.

Notation	Meaning
$[uv]$	a direction in the lattice
$\langle uv \rangle$	all symmetry equivalent directions
(hk)	a line/row in the lattice
$\{hk\}$	all symmetry equivalent lines/rows

2.2.1 Determination of Surface Unit Cells from Three-Dimensional Crystal Structures

To determine the corresponding surface unit cell from a three-dimensional crystal structure, the crystallographic plane (hkl) parallel to the substrate needs to be known. Then, two linearly independent crystallographic directions $[uvw]$ parallel to this plane have to be determined, which define the surface unit cell. A crystallographic direction $[uvw]$ is parallel to the plane (hkl) if^[46]

$$(hkl)[uvw] = hu + kv + lw = 0. \quad (2.13)$$

As there is an infinite number of parallel directions, rules for the selection of the “correct” ones can be derived from the corresponding rules for three-dimensional

2 Fundamentals

crystal structures (Table 2.1). By setting the z -component of the two-dimensional lattice vectors \mathbf{a} and \mathbf{b} to zero, a third general lattice vector \mathbf{c} can be calculated by

$$\mathbf{c} = \frac{\mathbf{a} \times \mathbf{b}}{|\mathbf{a} \times \mathbf{b}|} \max([a, b]), \quad (2.14)$$

where the multiplication with the maximum value of a and b is required to fulfil the first general rule $\mathbf{a} \cdot \mathbf{a} \leq \mathbf{b} \cdot \mathbf{b} \leq \mathbf{c} \cdot \mathbf{c}$. Due to this construction of \mathbf{c} ,

$$\mathbf{a} \cdot \mathbf{c} = \mathbf{b} \cdot \mathbf{c} = 0, \quad (2.15)$$

and the type T of the cell is always II, since T will become equally zero (*cf.* Equation 2.3). Using general values for \mathbf{a} and \mathbf{b} together with the definition of \mathbf{c} , the rules of the three-dimensional case (Table 2.1) can be converted to be applied to two-dimensional space (Table 2.4). Several conditions are always fulfilled or considerably simplified due to the construction of \mathbf{c} according to Equation 2.14 and due to Equation 2.15. The conditions R_1 to R_5 in Table 2.4 are further discussed below.

The general rule R_1 implies to select \mathbf{a} shorter than \mathbf{b} . As in the three-dimensional case, the lattice vectors should also be chosen as short as possible.

R_2 can be rewritten using the definition of the dot product to read

$$|\cos(\gamma)| \leq \frac{a}{2b}. \quad (2.16)$$

The right-hand side of this equation can have a maximum value of $1/2$ if $a = b$ and is smaller than $1/2$ if $a < b$ (*cf.* R_1). This means that for $a = b$, γ has to be from the interval $[60^\circ, 120^\circ]$ or from the interval $[240^\circ, 300^\circ]$. Please note that the interval $[240^\circ, 300^\circ]$ is not considered further, because it cannot be differentiated from the interval $[60^\circ, 120^\circ]$ due to the symmetric form of the cosine function ($\cos(\gamma) = \cos(2\pi - \gamma)$). In the general case $a \neq b$, R_2 restricts γ to a narrower, but still symmetric, interval around 90° .

R_3 is always fulfilled if R_2 is valid, since the right-hand side of R_3 will always be

2.2 Crystal Lattices Described in Two Dimensions

larger (due to the sum) than the right-hand side of R_2 .

R_4 basically restricts the angle γ enclosed by \mathbf{a} and \mathbf{b} to $90^\circ \leq \gamma \leq 270^\circ$. If γ is found to be outside this range, one can typically substitute \mathbf{a} by $-\mathbf{a}$ or \mathbf{b} by $-\mathbf{b}$. Please note that in combination with R_2 , the allowed γ range is further reduced to $90^\circ \leq \gamma \leq 120^\circ$. The minimum and maximum values are reached if $a = b$, *i.e.* in the square and hexagonal systems respectively.

Using the definition of the dot product, R_5 becomes $a/b \leq |\cos(\gamma)|$ and thus is always fulfilled if R_1 is valid: the left-hand side of R_5 can have a maximum value of 1 which is always less than or equal to the absolute value of the cosine function, which is restricted to the interval $[0, 1]$.

Please note that there could still be several equivalent unit cells fulfilling all derived rules. For example, in the case of a symmetric substrate surface, typically several crystallographic directions define equivalent surface unit cells. If this is the case, one might select the solution which has more positive hkl indices.

The rules outlined above are implemented in `GIDVis_Crystal`, a part of the software package `GIDVis`^[34]. `GIDVis_Crystal` can be used independently of `GIDVis` and (among others) allows an easy calculation of surface unit cells from three-dimensional crystal structures using the function `SurfaceUC`. For this, the lattice parameters a , b , c , α , β and γ and the (hkl) indices of the orientation plane are required as input and the surface unit cell is determined. The calculation of the surface unit cell is also implemented in `CrystalOverlay` (*cf.* section 3.3).

Table 2.4 Type-II rules for the selection of the three-dimensional lattice vectors \mathbf{a} , \mathbf{b} and \mathbf{c} transformed to the two-dimensional case described by lattice vectors \mathbf{a} and \mathbf{b} .

Three-Dimensional	Two-Dimensional
General Rules	
$\mathbf{a} \cdot \mathbf{a} \leq \mathbf{b} \cdot \mathbf{b}$	R ₁ : $\mathbf{a} \cdot \mathbf{a} \leq \mathbf{b} \cdot \mathbf{b}$
$\mathbf{b} \cdot \mathbf{b} \leq \mathbf{c} \cdot \mathbf{c}$	always fulfilled
$ \mathbf{b} \cdot \mathbf{c} \leq \frac{\mathbf{b} \cdot \mathbf{b}}{2}$	always fulfilled
$ \mathbf{a} \cdot \mathbf{c} \leq \frac{\mathbf{a} \cdot \mathbf{a}}{2}$	always fulfilled
$ \mathbf{a} \cdot \mathbf{b} \leq \frac{\mathbf{a} \cdot \mathbf{a}}{2}$	R ₂ : $ \mathbf{a} \cdot \mathbf{b} \leq \frac{\mathbf{a} \cdot \mathbf{a}}{2}$
Additional Rules for Type-II ($T \leq 0$)	
$(\mathbf{b} \cdot \mathbf{c} + \mathbf{a} \cdot \mathbf{c} + \mathbf{a} \cdot \mathbf{b}) \leq \frac{1}{2}(\mathbf{a} \cdot \mathbf{a} + \mathbf{b} \cdot \mathbf{b})$	R ₃ : $ \mathbf{a} \cdot \mathbf{b} \leq \frac{1}{2}(\mathbf{a} \cdot \mathbf{a} + \mathbf{b} \cdot \mathbf{b})$
$\mathbf{b} \cdot \mathbf{c} \leq 0$	always fulfilled
$\mathbf{a} \cdot \mathbf{c} \leq 0$	always fulfilled
$\mathbf{a} \cdot \mathbf{b} \leq 0$	R ₄ : $\mathbf{a} \cdot \mathbf{b} \leq 0$
Special Rules for Type-II ($T \leq 0$)	
if $\mathbf{a} \cdot \mathbf{a} = \mathbf{b} \cdot \mathbf{b}$ then $ \mathbf{b} \cdot \mathbf{c} \leq \mathbf{a} \cdot \mathbf{c} $	always fulfilled
if $\mathbf{b} \cdot \mathbf{b} = \mathbf{c} \cdot \mathbf{c}$ then $ \mathbf{a} \cdot \mathbf{c} \leq \mathbf{a} \cdot \mathbf{b} $	always fulfilled
if $ \mathbf{b} \cdot \mathbf{c} = \frac{1}{2}\mathbf{b} \cdot \mathbf{b}$ then $\mathbf{a} \cdot \mathbf{b} = 0$	condition cannot become fulfilled
if $ \mathbf{a} \cdot \mathbf{c} = \frac{1}{2}\mathbf{a} \cdot \mathbf{a}$ then $\mathbf{a} \cdot \mathbf{b} = 0$	condition cannot become fulfilled
if $ \mathbf{a} \cdot \mathbf{b} = \frac{1}{2}\mathbf{a} \cdot \mathbf{a}$ then $\mathbf{a} \cdot \mathbf{c} = 0$	always fulfilled
if $(\mathbf{b} \cdot \mathbf{c} + \mathbf{a} \cdot \mathbf{c} + \mathbf{a} \cdot \mathbf{b}) = \frac{1}{2}(\mathbf{a} \cdot \mathbf{a} + \mathbf{b} \cdot \mathbf{b})$ then $\mathbf{a} \cdot \mathbf{a} \leq 2 \mathbf{a} \cdot \mathbf{c} + \mathbf{a} \cdot \mathbf{b} $	R ₅ : if $ \mathbf{a} \cdot \mathbf{b} = \frac{1}{2}(\mathbf{a} \cdot \mathbf{a} + \mathbf{b} \cdot \mathbf{b})$

2.2.2 Example: Silver in (111) Orientation

Silver is described by a face-centered cubic unit cell with a lattice constant a of $4.0862 \text{ \AA}^{[47]}$. In surface science, film growth on the Ag(111) plane is often studied. To determine the corresponding surface unit cell, two linearly independent crystallographic directions parallel to the (111) plane have to be found (*cf.* Equation 2.13). After construction of the three-dimensional unit cell according to Equation 2.1, the surface unit cell lattice vectors \mathbf{a} and \mathbf{b} according to these directions can be calculated. Table 2.5 gives an overview of different combinations of directions parallel to the Ag(111) surface and whether they fulfil the rules derived above.

Table 2.5 Application of rules R_1 to R_4 to different directions parallel to the Ag(111) surface: ✓ ... rule fulfilled, ✗ ... rule not fulfilled, *n.a.* ... not applicable.

\mathbf{a}	\mathbf{b}	R_1	R_2	R_3	R_4	R_5
$[10\bar{1}]$	$[01\bar{1}]$	✓	✓	✓	✗	<i>n.a.</i>
$[10\bar{1}]$	$[\bar{1}2\bar{1}]$	✓	✓	✓	✓	<i>n.a.</i>
$[10\bar{1}]$	$[0\bar{1}1]$	✓	✓	✓	✓	<i>n.a.</i>
$[2\bar{1}\bar{1}]$	$[\bar{1}2\bar{1}]$	✓	✓	✓	✓	<i>n.a.</i>
$[10\bar{1}]$	$[\bar{1}10]$	✓	✓	✓	✓	<i>n.a.</i>

Please note that there are several solutions fulfilling all rules. For example, combining $[10\bar{1}]$ with $[0\bar{1}1]$ and $[10\bar{1}]$ with $[\bar{1}10]$ results in two equivalent surface unit cells due to the 60° symmetry of the Ag(111) surface. Also the $[2\bar{1}\bar{1}]$ and $[\bar{1}2\bar{1}]$ directions, either combined with one of the $\langle 10\bar{1} \rangle$ directions or combined with each other, could be used to define the surface unit cell. However, this results in longer lattice vectors compared to the other solutions and should therefore be avoided. Figure 2.5 shows the two equivalent unit cells of Table 2.5 and the longer directions $[2\bar{1}\bar{1}]$ and $[\bar{1}2\bar{1}]$.

Please note that the obtained surface unit cell solely depends on the combination of crystallographic directions; atom positions inside the unit cell are not taken into account. This leads to the fact that the calculated Ag(111) surface unit cell is not primitive. It would be obtained for *e.g.* the directions $[1/2\ 0\ \bar{1}/2]$ and $[\bar{1}/2\ 1/2\ 0]$ or any

equivalent combination. One of the possible primitive unit cells is also drawn in Figure 2.5.

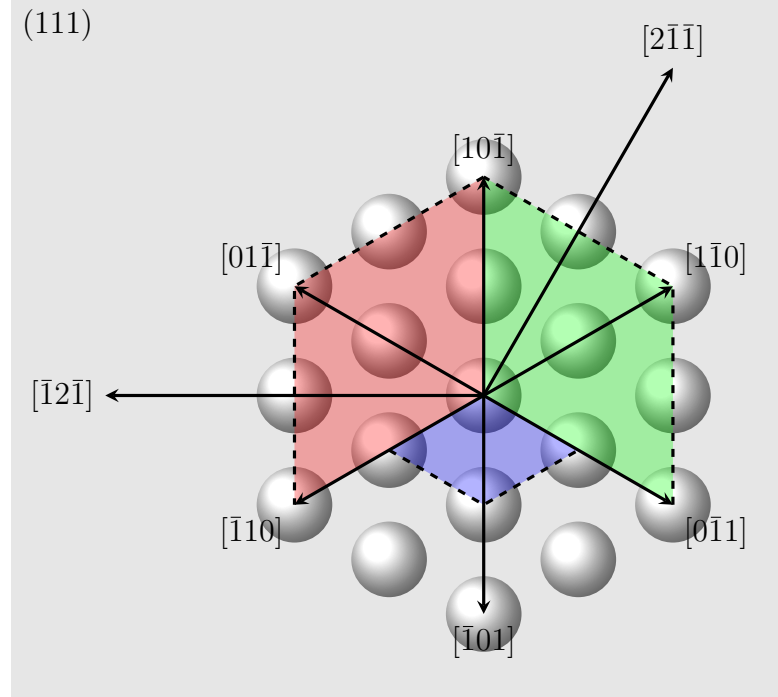


Figure 2.5 The six shortest directions $\langle 10\bar{1} \rangle$ and the $[2\bar{1}\bar{1}]$ and $[\bar{1}2\bar{1}]$ directions in the Ag(111) plane viewed perpendicular to this plane. Two possible, completely equivalent, surface unit cells (red, green) and the primitive surface unit cell (blue), taking the silver atom arrangement on the surface (light gray, atoms not to scale) into account.

The (non-primitive) surface unit cell can be determined by `GIDVis_Crystal`:

```
Cr = GIDVis_Crystal(4.0862, 4.0862, 4.0862, 90, 90, 90, ' ');
[a, b, gamma, uvw1, uvw2, av, bv] = SurfaceUC(Cr, [1 1 1]);
```

which returns the lengths ($a = b = 5.7788 \text{ \AA}$), the enclosed angle ($\gamma = 120^\circ$), the $[uvw]$ indices of the directions defining the surface unit cell ($[10\bar{1}]$ and $[\bar{1}10]$), and the lattice vectors $\mathbf{a} = (4.0862, 0, -4.0862)$ and $\mathbf{b} = (-4.0862, 4.0862, 0)$. To make it clear that the chosen vectors are really parallel to the (111) plane, the created crystal `Cr` can be oriented with the (111) plane parallel to the x - y -plane using the command `Cr.Orient([1 1 1])`. Then, the vectors will become $\mathbf{a} = (5.5819, 1.4957, 0)$ and $\mathbf{b} = (-4.0862, 4.0862, 0)$, *i.e.* the z -component being

zero, showing that \mathbf{a} and \mathbf{b} are lying in the x - y -plane and thus are parallel to the reoriented (111) plane.

2.2.3 Example: Pentacenequinone (P2O) in (102) Orientation

The molecule P2O on highly oriented pyrolytic graphite (HOPG) can be described by the unit cell $a = 5.067 \text{ \AA}$, $b = 8.064 \text{ \AA}$, $c = 8.884 \text{ \AA}$, $\alpha = 91.64^\circ$, $\beta = 93.3^\circ$ and $\gamma = 94.01^\circ$ and is observed to grow with the (102) plane parallel to the substrate surface.^[48] One crystallographic direction fulfilling Equation 2.13 is $[010]$, *i.e.* the b -axis, with a length of 8.064 \AA . Two other possible directions are $[\bar{2}01]$ and $[20\bar{1}]$, both with a length of 13.856 \AA . Both their combinations with the $[010]$ direction fulfil rules R_1 to R_3 . However, only the solution $[010]$ with $[20\bar{1}]$ also fulfils R_4 . This is because the angle enclosed by these two directions is larger than 90° , while for the combination of $[010]$ and $[\bar{2}01]$ it is less than 90° . Figure 2.6 shows both these unit cells (green, red).

Please note that in the case of the $[\bar{2}01]$ direction, one can invert the second direction to $[0\bar{1}0]$, which results in an equivalent unit cell fulfilling R_1 to R_4 (*cf.* Figure 2.6, blue). However, since the number of Miller indices smaller than zero is two in this case as compared to only one in case of $[010]$ and $[20\bar{1}]$, the latter is preferred.

As before, the surface unit cell can be calculated using `GIDVis_Crystal`:

```
Cr = GIDVis_Crystal(5.067, 8.064, 8.884, 91.64, 93.3, 94.01, ' ');
[a, b, gamma, uvw1, uvw2, av, bv] = SurfaceUC(Cr, [1 0 2]);
```

which returns the lengths ($a = 8.064 \text{ \AA}$, $b = 13.856 \text{ \AA}$), the enclosed angle ($\gamma = 91.9^\circ$), the $[uvw]$ indices of the directions defining the surface unit cell ($[010]$ and $[20\bar{1}]$), and the vectors $\mathbf{a} = (-0.564, 8.044, 0)$, $\mathbf{b} = (10.645, 0.291, -8.865)$. Again, the created crystal `Cr` can be oriented with the (102) plane parallel to the x - y -plane using the command `Cr.Orient([1 0 2])` and the vectors will become

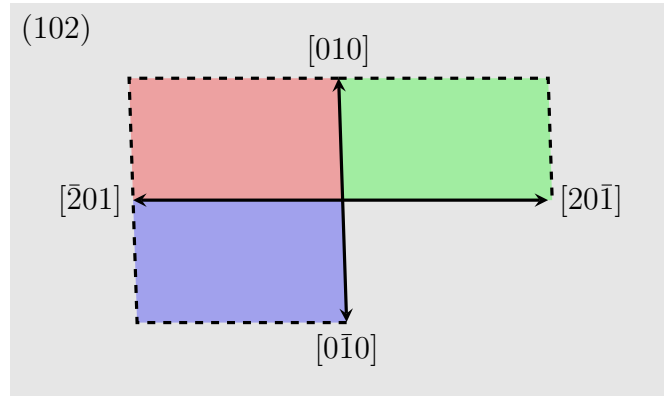


Figure 2.6 Three possible choices of surface unit cells for the P2O (102) plane, where the green and the blue are preferred over the red one (since the red one does not fulfil R_4). The green is preferred over the blue since it is defined by directions which have more positive uvw indices.

$\mathbf{a} = (-0.564, 8.044, 0)$ and $\mathbf{b} = (13.846, 0.515, 0)$, *i.e.* the z -component being zero, showing that \mathbf{a} and \mathbf{b} are lying in the x - y - and thus parallel to the reoriented (102) plane.

2.3 Crystallite Alignment

Thin films can be produced in a variety of ways: solvent-free techniques such as physical or chemical vapor deposition (PVD, CVD)^[49,50], hot-wall epitaxy (HWE)^[4] or (organic) molecular-beam epitaxy (OMBE, MBE)^[51–53]; in contrast to preparation methods employing the dissolved molecule^[54], *e.g.* spin coating, drop casting, dip coating, *etc.* The resulting films can either be amorphous or (partially) crystalline. For organic molecules on flat surfaces, crystallinity is frequently observed and the crystallites often align with one crystallographic plane parallel to the substrate surface, the so-called contact plane, often independent of the preparation technique. The contact plane describes the out-of-plane alignment, *i.e.* the spacing of the crystallographic planes perpendicular to the substrate surface.

In the in-plane direction of the crystallites, *i.e.* parallel to the substrate surface,

two main cases can be differentiated. On the one hand, the crystallites can show random azimuthal orientation, *i.e.* no preferred in-plane alignment is observed, which is called fiber texture or uniplanar alignment^[55]. Figure 2.7a schematically shows a sample with fiber texture in top-view. Crystallites are plotted in gray and a defined crystallographic direction $[uvw]$ of every crystallite is denoted by black arrows. This direction is uniformly distributed over the full angular range. Fiber texture often occurs when an isotropic substrate, *e.g.* silicon oxide, is used for sample preparation^[14,56]. On the other hand, crystallites can have, additional to the out-of-plane alignment, preferred in-plane alignment (uniplanar-axial according to Heffelfinger et al.^[55]), *i.e.* a certain crystallographic direction $[uvw]$ is restricted to distinct azimuthal angles, *e.g.* every 60° in case of Figure 2.7. In-plane alignment often occurs when the adsorbate shows strong interaction with the substrate, *e.g.* in case of organic molecules on single crystal metal surfaces^[57,58]. It can also be introduced by patterned substrates, either naturally occurring (*e.g.* grooves due to the atomic arrangement on the surface^[59] or due to surface reconstruction^[60,61]) or man-made by substrate-surface treatment (*e.g.* sputtering or rubbing)^[62,63]. Also the preparation technique can induce in-plane alignment, *e.g.* when performing dip coating^[5] or applying the bar-assisted meniscus shearing (BAMS) technique^[64].

Please note that an edge case between fiber texture and preferred in-plane alignment can occur as well. Materials showing the tendency to grow with large crystallites will not exhibit a perfectly random azimuthal orientation. This is due to the low number of crystallites, leading to an inhomogeneous distribution of the specific $[uvw]$ directions. Typically, this effect is unwanted and is referred to as samples with statistical problems.

In XRD, fiber-textured samples are typically described by stating the crystal structure and which crystallographic plane is parallel to the substrate. For samples with additional in-plane alignment, epitaxial relationships are further given.^[2] This means that crystallographic directions of the adsorbate parallel to the surface are determined. Then, the angle between these and *e.g.* the rubbing direction or specific crystallographic directions of the substrate is given. A very useful tool for this evaluation are PFs^[65]. For example, P2O on a Au(111) surface grows with

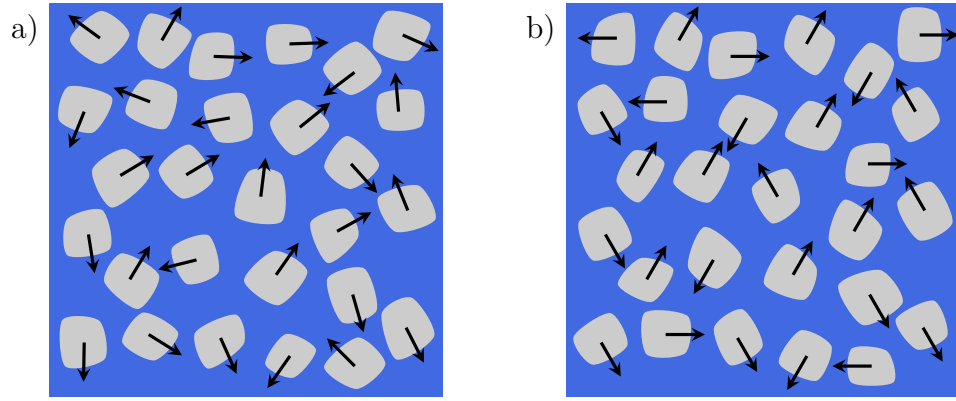


Figure 2.7 Crystallites (gray) with a certain crystallographic direction (black arrow) on a substrate surface (blue): a) fiber texture, b) preferred in-plane alignment.

the (140) planes (or the crystallographically equivalent $(\bar{1}\bar{4}0)$ planes) parallel to the substrate surface, and the [001] direction of P2O, *i.e.* the c -axis, is parallel to the substrate surface (*cf.* Equation 2.13). Evaluation of diffraction data using PFs further shows that the c -axis is also parallel to one of the high symmetry directions $\langle\bar{1}10\rangle$ of the Au(111) surface. This can be compressed to $(111)_{\text{Au}} \parallel \pm (140)_{\text{P2O}}$ and $\langle\bar{1}10\rangle_{\text{Au}} \parallel \langle 001\rangle_{\text{P2O}}$ (*cf.* section 4.2).

2.4 Epitaxy

Closely related to alignment of crystallites is epitaxy. The term “epitaxy” was suggested by Royer and is derived from the greek words ἐπί (epi) and τάξις (taxis) meaning “on” and “arrangement”^[66]. According to Gebhardt et al., “any structure-dependent intergrowth (overgrowth) of two chemically and/or structurally different crystalline or subcrystalline phases is called epitaxy”^[67]. This means that the substrate and the adsorbate share common lattice points.

The common lattice points of substrate and adsorbate are the basis of a simple and intuitive model for growth of an ordered crystalline film on a crystalline substrate.^[68,69] Adsorbate and substrate are described by their surface unit cells

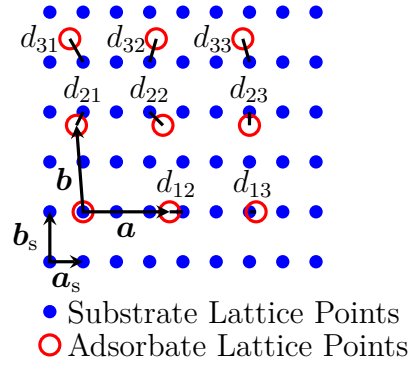


Figure 2.8 Calculation of the lattice misfit D with $X = Y = 3$ using the individual contributions of the distances d_{ij} .

and the respective lattice points. Then, the so-called lattice misfit sum D can be calculated and the model suggests that the surface unit cells arrange themselves such that D is minimum. The lattice misfit sum D is a numerical value obtained by summing the squared distances between lattice points of the adsorbate and the closest lattice point of the substrate d_{ij} and limiting the calculation to a certain order (X, Y) of lattice points:

$$D = \sum_{i=1}^X \sum_{j=1}^Y d_{ij}^2. \quad (2.17)$$

For example, consider Figure 2.8. Blue points are lattice points of the substrate, which are defined by the lattice vectors \mathbf{a}_s and \mathbf{b}_s . The adsorbate lattice is given by the vectors \mathbf{a} and \mathbf{b} and lattice points up to $X = Y = 3$ are plotted with red open circles. For each of the adsorbate lattice points, the distance to the closest substrate lattice point d_{ij} is calculated (black lines). d_{11} is zero since the lattice points are located on top of each other. All other plotted points give contributions and the lattice misfit can be evaluated according to Equation 2.17. Larger X and Y values (*i.e.* more repeat units of the adsorbate lattice) will result in more accurate misfit parameter calculations.

This model can be applied to calculate the preferred azimuthal angle between known substrate and adsorbate surface unit cells: By rotation of the adsorbate lattice points with respect to the underlying substrate, different lattice misfit values

are found, depending on the rotation angle. The minimum possible value of zero is found for the configuration where all adsorbate lattice points match with ones from the substrate (commensurism, see below). Despite its simplicity, this model can be used to explain some types of ordered growth.^[70–72] The lattice misfit sums purely rely on the surface unit cells, not on their atomic content and thus can often give only limited insight. However, the availability of more computational power and improved methods led to more sophisticated approaches towards the prediction of the ordered growth on crystalline substrates. Calculation of the potential energy of different configurations^[69,73–75], molecular dynamics^[76], Monte Carlo simulations^[77] or machine learning approaches^[78,79], all with certain advantages and disadvantages, are already used. Nevertheless, especially large organic systems with high flexibility and larger surface unit cells still require experimental techniques to resolve the order and confirm the theoretically obtained results.

2.4.1 Notations for Epitaxial Growth

Starting from three-dimensional crystal structures, epitaxy is often described with epitaxial relationships as already described above. This means the crystallographic plane (hkl) of the adsorbate which is parallel to the substrate surface $(hkl)_s$ is stated. Additionally, parallel directions of substrate and adsorbate ($[hkl]_s \parallel [hkl]$) or angles between low-index directions are given.

The complexity can be reduced by switching to a description using two-dimensional surface unit cells. This means that the lattice vectors \mathbf{a} and \mathbf{b} of the adsorbate as well as the lattice vectors \mathbf{a}_s and \mathbf{b}_s of the substrate (enclosing the angle γ_s), where the subscript denotes the substrate, have to be known. Then, the adsorbate lattice points can be described using the substrate lattice points as a reference in various ways. For example, one can simply state the lattice parameters $a, b, \gamma, a_s, b_s, \gamma_s$ and the azimuthal rotation angle between the lattice vectors φ (*cf.* Figure 2.9).

Wood’s notation^[43] is similar to this, but makes matching of lattice points clearer.

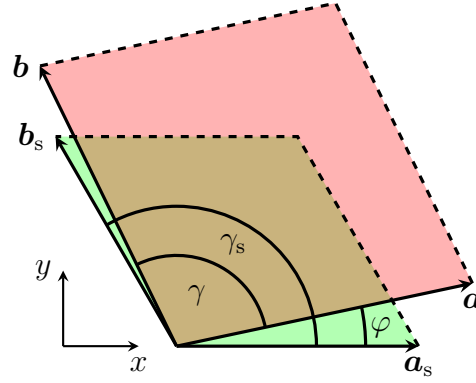


Figure 2.9 Surface unit cell of the adsorbate (red, \mathbf{a} , \mathbf{b} and γ) and of the substrate (green, \mathbf{a}_s , \mathbf{b}_s and γ_s) and the rotation angle φ between substrate and adsorbate surface unit cell.

For example, the term Ni(011)3×1-O describes oxygen (O) on a Ni(011) surface, which arranges in a lattice where $a = 3a_s$ and $b = b_s$ and the adsorbate lattice vectors are parallel to the ones of the substrate. In case the ratio between \mathbf{a} and \mathbf{a}_s and between \mathbf{b} and \mathbf{b}_s is the same, the second term can be omitted, *e.g.* Si(100)12-P, where the adsorbate lattice vectors are twelve times as long as the substrate vectors. A centered lattice is indicated by the letter *c* prior to the $n \times m$ term. If an azimuthal rotation is found between adsorbate and substrate lattice, the rotation angle is given prior to the adsorbate, *e.g.* NaCl(100)5×1-45°-A, where the letter A stands for the adsorbate anthraquinone. As can be seen from the last example, the nomenclature can become quite complex. Thus, Wood's notation is nowadays typically used in simple and/or already widely accepted cases only^[2], *e.g.* the oxygen-reconstructed Cu(110) surface, Cu(110)2×1-O^[80,81] or the Si(111)7×7 surface reconstruction^[82,83].

An alternative notation applies the so-called epitaxy matrix, typically denoted as C or M :^[3,84]

$$\begin{pmatrix} \mathbf{a} \\ \mathbf{b} \end{pmatrix} = \begin{pmatrix} C_{11} & C_{12} \\ C_{21} & C_{22} \end{pmatrix} \begin{pmatrix} \mathbf{a}_s \\ \mathbf{b}_s \end{pmatrix}. \quad (2.18)$$

This means that the lattice vectors \mathbf{a} and \mathbf{b} of the adsorbate are expressed as a

2 Fundamentals

linear combination of the substrate lattice vectors \mathbf{a}_s and \mathbf{b}_s :

$$\mathbf{a} = C_{11}\mathbf{a}_s + C_{12}\mathbf{b}_s, \quad (2.19)$$

$$\mathbf{b} = C_{21}\mathbf{a}_s + C_{22}\mathbf{b}_s, \quad (2.20)$$

which results in the following system of linear equations:

$$\begin{pmatrix} a_x \\ a_y \\ b_x \\ b_y \end{pmatrix} = \begin{pmatrix} a_{s,x} & b_{s,x} & 0 & 0 \\ a_{s,y} & b_{s,y} & 0 & 0 \\ 0 & 0 & a_{s,x} & b_{s,x} \\ 0 & 0 & a_{s,y} & b_{s,y} \end{pmatrix} \begin{pmatrix} C_{11} \\ C_{12} \\ C_{21} \\ C_{22} \end{pmatrix}. \quad (2.21)$$

In case only the lattice parameters ($a, b, \gamma, a_s, b_s, \gamma_s$) and the relative azimuthal rotation angle between substrate and adsorbate φ are known, but not the lattice vectors ($\mathbf{a}, \mathbf{b}, \mathbf{a}_s, \mathbf{b}_s$), the elements C_{ij} of the epitaxy matrix can be calculated using the following relationships^[69]:

$$C_{11} = \frac{a}{a_s} \sin(\gamma_s - \varphi) \sin(\gamma_s), \quad (2.22)$$

$$C_{12} = \frac{a}{b_s} \sin(\varphi) \sin(\gamma_s), \quad (2.23)$$

$$C_{21} = \frac{b}{a_s} \sin(\gamma_s - \varphi - \gamma) \sin(\gamma_s), \quad (2.24)$$

$$C_{22} = \frac{b}{b_s} \sin(\varphi + \gamma) \sin(\gamma_s). \quad (2.25)$$

The determinant of the epitaxy matrix $\det(C)$ is the ratio of the area of the adsorbate A and the substrate surface unit cell A_s :

$$\det(C) = \begin{vmatrix} C_{11} & C_{12} \\ C_{21} & C_{22} \end{vmatrix} = C_{11}C_{22} - C_{21}C_{12} = \frac{A}{A_s}. \quad (2.26)$$

2.4.2 Classification of Epitaxy

Depending on the elements C_{ij} of the matrix, epitaxy can be classified into three different categories.^[85]

Commensurism

In case all elements C_{ij} of the epitaxy matrix are integers, all lattice points of the adsorbate coincide with lattice points of the underlying substrate, which is called commensurism.

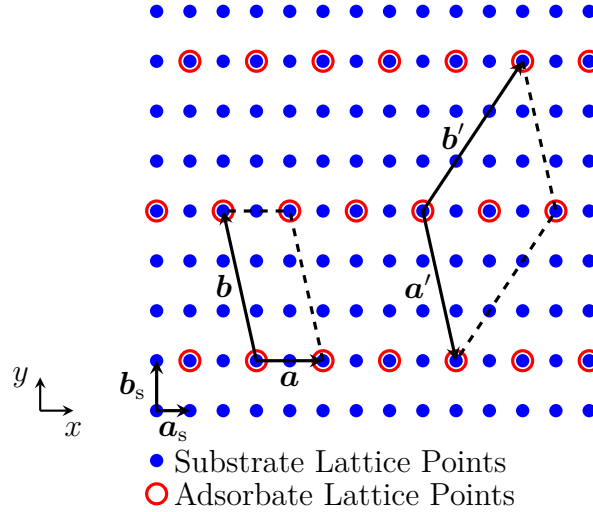


Figure 2.10 Scheme of a commensurate overlayer with two surface unit cells resulting in the same pattern of adsorbate lattice points.

A schematic representation is plotted in Figure 2.10, where lattice points of the substrate and adsorbate are plotted with blue filled circles and open red circles respectively. The substrate is described by the lattice vectors $\mathbf{a}_s = (1, 0)$, $\mathbf{b}_s = (0, 1.5)$, enclosing the angle $\gamma_s = 90^\circ$. For the adsorbate, it is found that the lattice vector \mathbf{a} is parallel to \mathbf{a}_s but twice as long, resulting in $C_{11} = 2$ and $C_{12} = 0$. The lattice vector \mathbf{b} can be expressed as a linear combination of \mathbf{a}_s and \mathbf{b}_s by $C_{21} = -1$ and $C_{22} = 3$. C_{21} is chosen to be -1 to make γ larger than 90° and thus fulfil R_4 .

2 Fundamentals

The overall epitaxy matrix C then becomes

$$C = \begin{pmatrix} 2 & 0 \\ -1 & 3 \end{pmatrix}. \quad (2.27)$$

The same result is obtained when evaluating Equation 2.22 to Equation 2.25 using $a = 2$, $b = \sqrt{21.25}$, $\gamma \approx 102.53^\circ$ and $\varphi = 0^\circ$.

Please note that $C_{12} = 0$ is not required for commensurism. To demonstrate this, Figure 2.10 contains a second surface unit cell which describes the same overlayer (but does not fulfil rule R_2 due to a too large angle $\gamma \approx 134^\circ$). However, the epitaxy matrix becomes

$$C' = \begin{pmatrix} 1 & -3 \\ 3 & 3 \end{pmatrix}. \quad (2.28)$$

Again, the same result is obtained when evaluating Equation 2.22 to Equation 2.25 with $a' \approx 4.61$, $b' \approx 5.41$, $\gamma' \approx 133.78^\circ$ and $\varphi' = -77.47^\circ$.

Please note that although both surface unit cells/epitaxy matrices describe the same lattice points, the description with \mathbf{a} and \mathbf{b} is preferred over \mathbf{a}' and \mathbf{b}' following the conventions (*cf.* section 2.2).

Higher-Order Commensurism

In higher-order commensurism (HOC) (also called Coincidence-II^[69]), not all lines of adsorbate lattice points coincide with lines of substrate lattice points, only every n th line does. This is schematically shown in Figure 2.11. Substrate and adsorbate lattice points are depicted in blue and red, respectively. As can be seen, every 3rd line of the adsorbate coincides with a substrate line, in this case the (01) line. Selecting lattice vectors \mathbf{a} and \mathbf{b} following the rules outlined above, especially selecting \mathbf{a} such that the enclosed angle γ becomes larger than 90° (R_4), the epitaxy

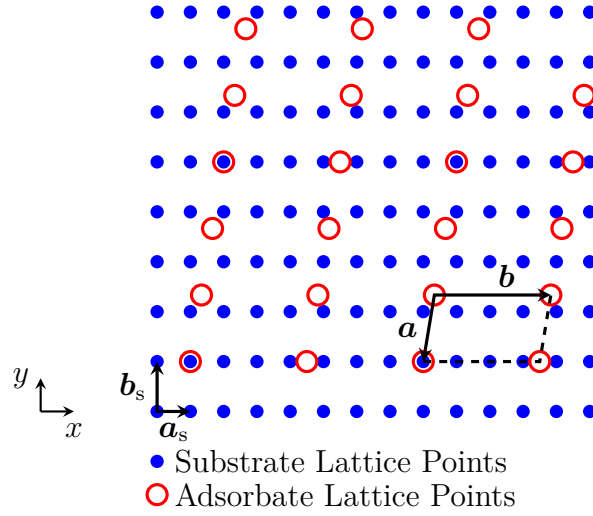


Figure 2.11 Scheme of a higher-order commensurate overlayer and the adsorbate surface unit cell.

matrix becomes

$$C = \begin{pmatrix} -1/3 & -4/3 \\ 3.5 & 0 \end{pmatrix}, \quad (2.29)$$

For the lattice parameters of the adsorbate the values $a \approx 2.03$, $b = 3.5$, $\gamma = 99.46^\circ$, $\varphi = -99.46^\circ$ can be determined.

In general, HOC is found if all epitaxy matrix elements C_{ij} are rational.

On-Line Coincidence

In literature, a differentiation is made between point-on-line (POL)^[69] and line-on-line (LOL)^[86] coincidence due to historic reasons, although they describe a very similar form of epitaxy: For POL, all adsorbate lattice points have to be located on a primitive substrate line, *i.e.* (01) or (10), while for LOL the substrate line is anything else apart from (01) and (10), *i.e.* a non-primitive lattice line. However, the indices of these lines depend on the choice of substrate lattice vectors \mathbf{s}_1 and \mathbf{s}_2 and therefore are not very reliable since the selection of the substrate lattice

2 Fundamentals

vectors is often not following the standard rules (Table 2.4). Thus it was suggested to merge POL and LOL into on-line coincidence (OLC) and to always state the choice of lattice vectors \mathbf{a}_s and \mathbf{b}_s and the order of observed coincidences.^[85] The order of coincidences is given by the integer values h and k (of the adsorbate) and h_s and k_s (of the substrate) fulfilling the equation

$$\begin{pmatrix} h \\ k \end{pmatrix} = \begin{pmatrix} C_{11} & C_{12} \\ C_{21} & C_{22} \end{pmatrix} \begin{pmatrix} h_s \\ k_s \end{pmatrix}. \quad (2.30)$$

There are several possible options for the elements C_{ij} of the epitaxy matrix resulting in OLC, which are all described in literature^[85]. The easiest one is if three matrix elements C_{ij} are rational, one is irrational. Please note that this includes the now special cases of the two types of POL epitaxy, Coincidence-IA and Coincidence-IB, where it is required that one column of the epitaxy matrix contains only integers. The other two matrix elements give rise to the differentiation between IA (all non-integer elements are rational) and IB (one of the non-integer elements is irrational).^[69]

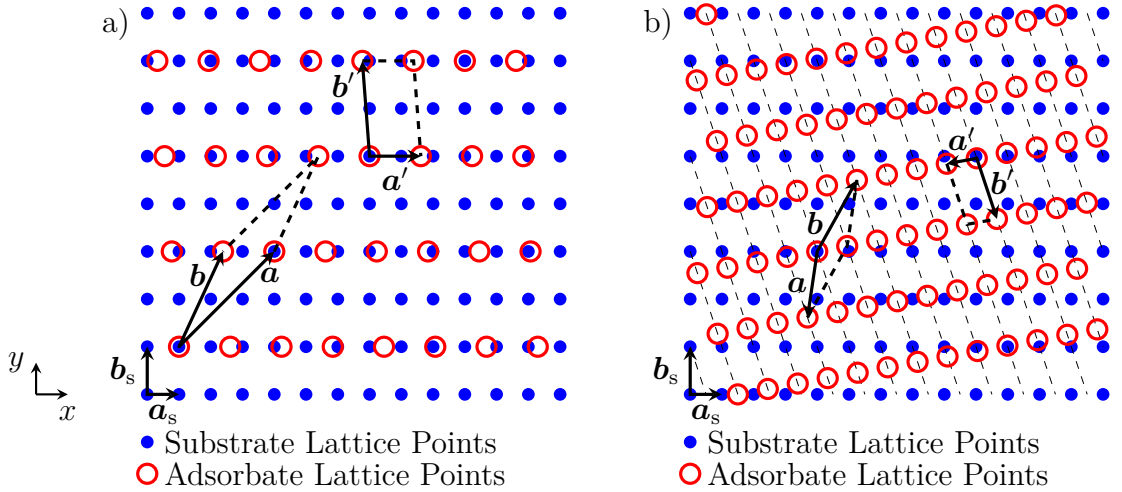


Figure 2.12 Two types of on-line coincidence, where all adsorbate lattice points coincide with the a) primitive (01) and b) (21) lines (dashed) of the substrate respectively.

For example, Figure 2.12a shows the lattice points of the on-line-coincident adsor-

bate with the epitaxy matrix

$$C_a = \begin{pmatrix} 3 & 2 \\ 2 \ln(2) & 2 \end{pmatrix}, \quad (2.31)$$

where one matrix element is irrational ($2 \ln(2)$), all others are rational (and even integers in this case). As can be easily seen, all adsorbate lattice points lie on the lattice line (01) of the substrate (making this structure POL coincident). According to Equation 2.30, the order of coincidence is $(h, k) = (2, 2)$ and $(h_s, k_s) = (0, 1)$. Using the given epitaxy matrix nicely shows the irrationality of a single matrix element, but leads to a rather unusual surface unit cell (*cf.* Figure 2.12a, **a**, **b**), not fulfilling the derived rules (Table 2.4). Selecting a unit cell following the conventions results in the epitaxy matrix

$$C'_a = \begin{pmatrix} 3 - 2 \ln(2) & 0 \\ -3 + 4 \ln(2) & 2 \end{pmatrix}, \quad (2.32)$$

and the lattice parameters $a \approx 1.61$, $b \approx 3.01$, $\gamma \approx 94.33^\circ$ and $\varphi = 0^\circ$. Please note that the determinant of C_a equals the one of C'_a , showing that both epitaxy matrices are equivalent.

Figure 2.12b shows the adsorbate lattice corresponding to the following epitaxy matrix:

$$C_b = \begin{pmatrix} \ln(2) - 1 & -2 \ln(2) \\ 1.25 & 1.5 \end{pmatrix}, \quad (2.33)$$

where the elements of the first row are irrational (due to $\ln(2)$), and all other matrix elements are rational. All adsorbate lattice points lie on the (21) lines of the substrate (dashed lines in Figure 2.12b). The order of coincidence is $(h, k) = (-2, 4)$ and $(h_s, k_s) = (2, 1)$. As before, this epitaxy matrix leads to an unusual surface unit cell (*cf.* Figure 2.12b, **a**, **b**), not fulfilling the rules derived above. The same adsorbate lattice points can be expressed by the surface unit cell given by **a'** and

\mathbf{b}' , resulting in the epitaxy matrix

$$C'_b = \begin{pmatrix} -\frac{1}{4} - \ln(2) & -\frac{3}{2} + 2 \ln(2) \\ -\frac{3}{4} + 2 \ln(2) & \frac{3}{2} - 4 \ln(2) \end{pmatrix}, \quad (2.34)$$

and the lattice parameters $a \approx 0.96$, $b \approx 2.01$, $\gamma \approx 98.18^\circ$ and $\varphi = -169.75^\circ$. Again, the determinant of C_b equals the determinant of C'_b .

Especially in the example shown in Figure 2.12b the lattice lines of coincidence might not be accessible at first glance. In this and similar cases it is convenient to investigate the problem in reciprocal instead of real space. First, a third unit cell vector \mathbf{c} is calculated such that it is perpendicular to \mathbf{a} and \mathbf{b} (*cf.* Equation 2.14). Then, the vectors \mathbf{a} and \mathbf{b} can be transformed to reciprocal space by Equation 2.5 and reciprocal lattice points of the substrate and adsorbate can be calculated according to Equation 2.6 while keeping the Miller index l zero. A plot of the resulting points allows easier determination of the lines of coincidence. Figure 2.13 shows the reciprocal-space representation of Figure 2.12b, where it can be seen that coinciding lattice points occur for the reciprocal substrate lattice vector $\mathbf{G}_{s,21}$, *i.e.* the real-space adsorbate lattice points lie on the (21) line of the substrate.

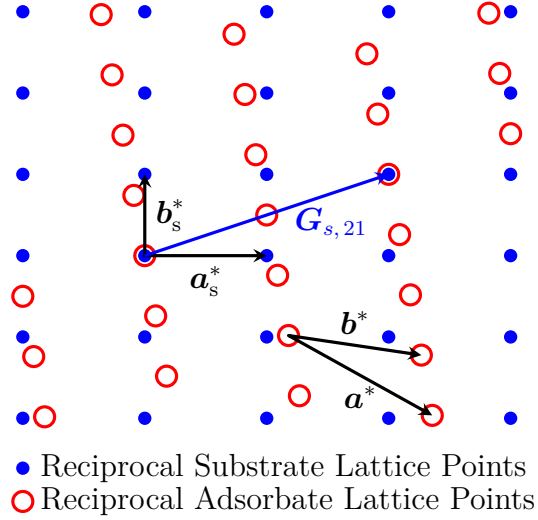


Figure 2.13 Reciprocal space representation (not to scale) of Figure 2.12b.

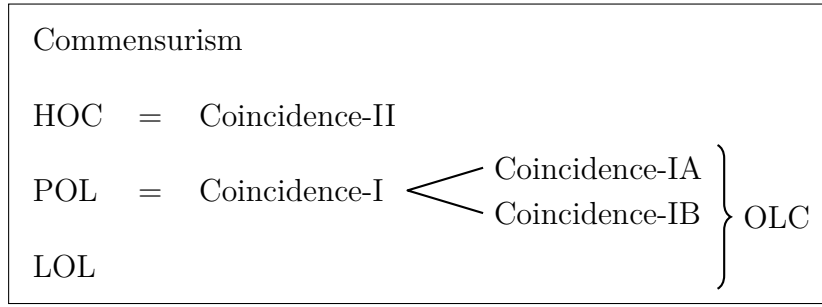


Figure 2.14 Different types of epitaxy.

Summary

Depending on the elements C_{ij} of the epitaxy matrix, epitaxy can be separated into different classes (*cf.* Figure 2.14). For commensurism, all C_{ij} have to be integers, while for HOC, all C_{ij} are rationals. In literature it was suggested to merge the epitaxy forms POL and LOL into OLC^[85], since their differentiation depends on the choice of the substrate lattice vectors. OLC can even be found when up to four elements C_{ij} of the epitaxy matrix are irrational, but additional conditions (may) need to be fulfilled.^[85] Although there are guidelines how to select the lattice vectors of the adsorbate layer, not all publications follow these, resulting in different epitaxy matrices for the same overlayer pattern but the same determinant.

Furthermore, experimental data always contains errors and scientists avoid to give insignificant digits by rounding numeric values. This might lead to incorrect conclusions about the type of epitaxy. For example, giving one matrix element as 3.1 does not necessarily mean it is the rational number $31/10$ but might just indicate that further digits could not be determined reliably.

2.5 X-Ray Diffraction

This section is based on Bennett^[37] and Weissmantel et al.^[38], unless noted.

2 Fundamentals

To investigate crystalline matter, diffraction experiments are employed. To observe diffraction maxima, the wavelength of the incoming beam has to be smaller than the order of the repeating unit, *i.e.* X-rays with wavelengths between 10^{-10} m and 10^{-12} m are used in crystallography, since atomic distances/netplane distances are in the range of 10^{-10} m = 1 Å.

In general, an incident X-ray beam illuminates the sample and the diffracted intensity is recorded with a detector. The incident beam is described by the wavevector \mathbf{k}_0 , the diffracted beam by \mathbf{k} . The length of \mathbf{k}_0 is $k_0 = 2\pi/\lambda$, and since diffraction is an elastic process, also $k = 2\pi/\lambda$. \mathbf{k}_0 and \mathbf{k} enclose the angles α_i and α_f respectively with the lattice planes and define the scattering vector \mathbf{q} (*cf.* Figure 2.15) via

$$\mathbf{q} = \mathbf{k} - \mathbf{k}_0, \quad (2.35)$$

The scattering vector \mathbf{q} has the unit of inverse length, typically Å⁻¹ or nm⁻¹.

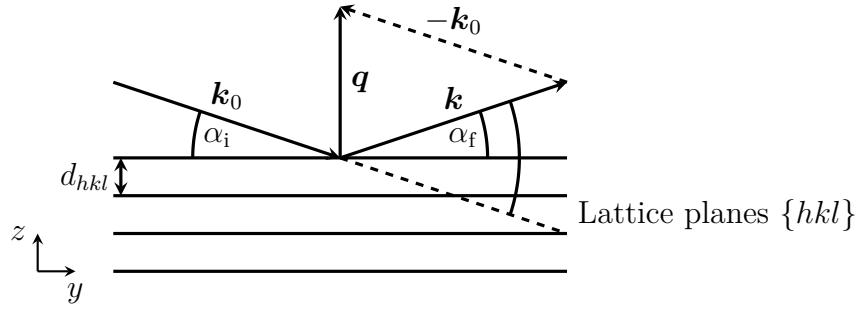


Figure 2.15 The wavevectors \mathbf{k}_0 and \mathbf{k} of the incident and diffracted beams and the scattering vector \mathbf{q} .

If $\alpha_i = \alpha_f$, the specular condition is fulfilled and the incident and exit angle are typically labelled θ . Then, the angle between the incident beam and the diffracted beam (*cf.* Figure 2.15) is 2θ .

In general, \mathbf{k}_0 , \mathbf{k} and \mathbf{q} are vectors in three-dimensional space. Depending on the experimental geometry and the scan performed, (components of) \mathbf{k}_0 and/or \mathbf{k} are varied, thus (components of) \mathbf{q} change(s). For example, in a specular scan ($\alpha_i = \alpha_f = \theta$) the angle θ is varied. This means that the x - and y -components of

the scattering vector are constantly zero, while the z -component is varied. Thus the direction of \mathbf{q} stays the same (perpendicular to the probed lattice plane) and only the length q changes.

Independent of the experimental geometry, a diffraction peak is observed when the Laue condition^[87] is fulfilled:

$$\mathbf{q} = \mathbf{G}_{hkl}. \quad (2.36)$$

This means that the scattering vector \mathbf{q} has to coincide with a reciprocal lattice vector \mathbf{G}_{hkl} . Since \mathbf{G}_{hkl} in reciprocal space is perpendicular to the corresponding (hkl) plane in real space, this also means that diffraction can only be observed when the scattering vector \mathbf{q} is perpendicular to the probed plane (hkl) . According to Equation 2.7, the netplane distance d_{hkl} of this plane can be calculated from the length q of the scattering vector by

$$d_{hkl} = \frac{2\pi}{q}. \quad (2.37)$$

Please note that the description of diffraction using the Laue condition is in reciprocal space. To represent the same in real space, two conditions are required. First of all, the Bragg equation^[88]

$$n\lambda = 2d \sin\left(\frac{2\theta}{2}\right), \quad (2.38)$$

which relates the netplane distance d , the scattering angle 2θ and the used wavelength λ , has to be fulfilled. n is an integer describing higher-order reflections of the same plane and is typically merged with d so that the Bragg equation becomes

$$\lambda = 2d_{hkl} \sin\left(\frac{2\theta}{2}\right). \quad (2.39)$$

Besides the Bragg equation the parallelism condition has to be fulfilled, which requires that the scattering vector \mathbf{q} is perpendicular to the probed plane, *i.e.* the incident and diffracted beam have to be symmetric with respect to this plane.

Combining Equation 2.37 and Equation 2.39 results in an important relationship which relates the experimentally defined quantity 2θ to the length of the scattering vector q :

$$q = \frac{4\pi}{\lambda} \sin\left(\frac{2\theta}{2}\right). \quad (2.40)$$

Please note that using this equation, diffraction patterns can be studied independent of the used wavelength, *i.e.* experimental peak positions can directly be compared after conversion to q , even when recorded with different wavelengths.

2.6 Grazing Incidence X-Ray Diffraction

The following section is based on Birkholz et al.^[33], unless mentioned differently.

GIXD is a frequently applied technique to obtain crystallographic information on a wide variety of samples. Due to its surface sensitivity, it is often used for thin films. In general, the wavevector of the incident beam \mathbf{k}_0 is kept fixed while several different outgoing wavevectors \mathbf{k} are probed by either moving a point detector in space or using two-dimensional detectors. Depending on the detector or pixel position, \mathbf{k} and thus \mathbf{q} vary and diffracted intensity is only observed if the Laue condition (Equation 2.36) is fulfilled.

Figure 2.16a schematically shows the GIXD experiment. The sample is illuminated with the primary beam described by the wavevector \mathbf{k}_0 which encloses the incident angle α_i with the sample surface. Two different diffracted beampaths are plotted, \mathbf{k}_1 and \mathbf{k}_2 , originating from two different families of crystal planes. Using Equation 2.35, the corresponding scattering vectors \mathbf{q}_1 and \mathbf{q}_2 can be calculated. \mathbf{q}_2 has no vanishing elements. However, since both, \mathbf{k}_0 and \mathbf{k}_1 , lie in the y - z -plane, \mathbf{q}_1 has an x -component being zero.

The result of a GIXD experiment are intensity values I as a function of q_x , q_y and q_z . These are usually visualized in so-called reciprocal space maps, where

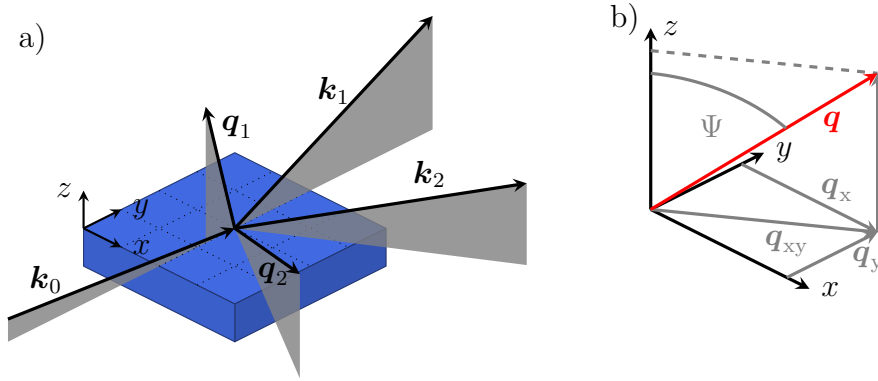


Figure 2.16 a) Geometry of a GIXD experiment, showing the incident wavevector \mathbf{k}_0 , two different outgoing wavevectors \mathbf{k}_1 and \mathbf{k}_2 and the corresponding scattering vectors \mathbf{q}_1 and \mathbf{q}_2 . Gray planes and dotted lines on the substrate surface are drawn as a guide to the eye. b) The scattering vector \mathbf{q} and its components in three-dimensional space.

the in-plane component $q_{xy} = \sqrt{q_x^2 + q_y^2}$ of the scattering vector (parallel to the sample surface, *cf.* Figure 2.16b) is plotted on the horizontal axis, the out-of-plane component q_z (perpendicular to the sample surface, *cf.* Figure 2.16b) on the vertical axis. Measured intensity at a combination of q_{xy}/q_z is color-coded, often scaled in square-root or logarithmic fashion to improve the visibility of low-intensity peaks. As a result of the geometry of the GIXD experiment, it is not possible to access the complete reciprocal space. For example, consider \mathbf{k}_1 and the corresponding scattering vector \mathbf{q}_1 in Figure 2.16. Although the x -component of \mathbf{q}_1 is zero in this case, $q_{xy} = \sqrt{q_x^2 + q_y^2}$ will still be larger than zero due to the non-zero y -component. Only for the specular condition, *i.e.* the incident angle and the exit angle are the same, q_{xy} will become zero. In the reciprocal space map, this leads to a missing wedge which cannot be accessed within a GIXD experiment (*cf.* Figure 2.17). Two semi-circles with radius $2\pi/\lambda$, where λ is the used wavelength, can be accessed (blue). The gray region, described by a semicircle with radius $4\pi/\lambda$ centered at the origin is only accessible within co-planar diffraction experiments, *i.e.* when incident and diffracted beam are located in the same plane.

For the GIXD experiment, the sample has to be precisely mounted and aligned with respect to the incident X-ray beam prior to any measurement (*cf.* section 4.1). This ensures that high-quality data are recorded and data evaluation can be performed

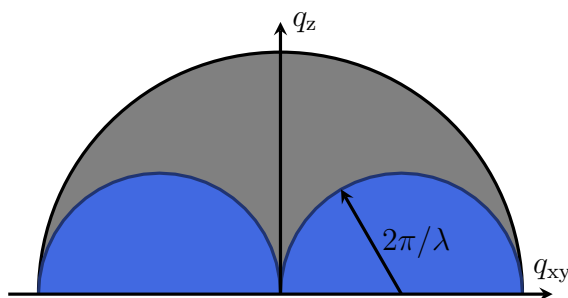


Figure 2.17 Accessible (blue) and inaccessible areas (gray) of reciprocal space in GIXD measurements.

with high accuracy.

Depending on the crystallite alignment with respect to the substrate surface (*cf.* section 2.3), the following two GIXD measurement techniques are typically applied.

2.6.1 Static Sample

In case of fiber-textured samples (*cf.* Figure 2.7a), the reciprocal lattice points are distributed along concentric circles in reciprocal space. A single GIXD measurement with a static sample cuts through reciprocal space, thus information of all concentric circles is obtained simultaneously (*cf.* Figure 2.18). Along each individual circle, the out-of-plane q_z and the in-plane component q_{xy} of the scattering vector are constant, only the contributions q_x and q_y to q_{xy} change. Thus, the ring translates to a single data point in the reciprocal space map. This data can then be used for phase analysis (*i.e.* determination which crystal structure is present on the sample), contact plane determination, *etc.*

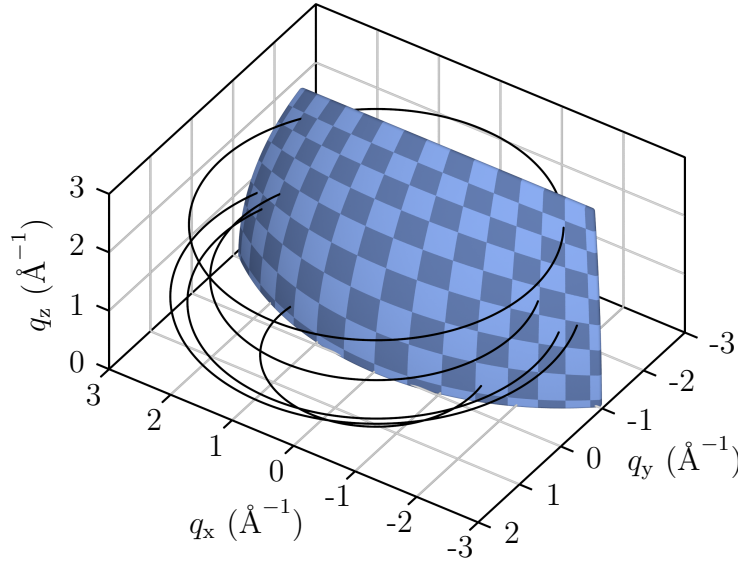


Figure 2.18 Reciprocal lattice points becoming concentric circles for fiber-textured samples (black) and a cut through the reciprocal space by a single static grazing incidence X-ray diffraction measurement (blue).

2.6.2 Rotating Sample

Samples with defined in- and out-of-plane alignment of the crystallites have distinct data points in reciprocal space. A single GIXD measurement with a static sample cuts through reciprocal space at a certain position and thus does not allow to access all diffraction information (*cf.* Figure 2.19). To overcome this problem, a sample rotation around the surface normal is necessary (rotating GIXD) to access large volumes of reciprocal space and to collect a wide range of the available diffraction information.^[89]

When integrating a full 360° rotation and plotting the obtained data in a reciprocal space map, the whole diffraction information of the sample is contained in this image, which can be used for data evaluation similar to the case of fiber-textured films. However, in this image the correlation between q_x and q_y has been lost since all combinations of q_x and q_y which give the same q_{xy} fall onto the same point in the reciprocal space map. To overcome this problem and to eventually obtain three-dimensional peak positions (q_x , q_y and q_z), several diffraction patterns,

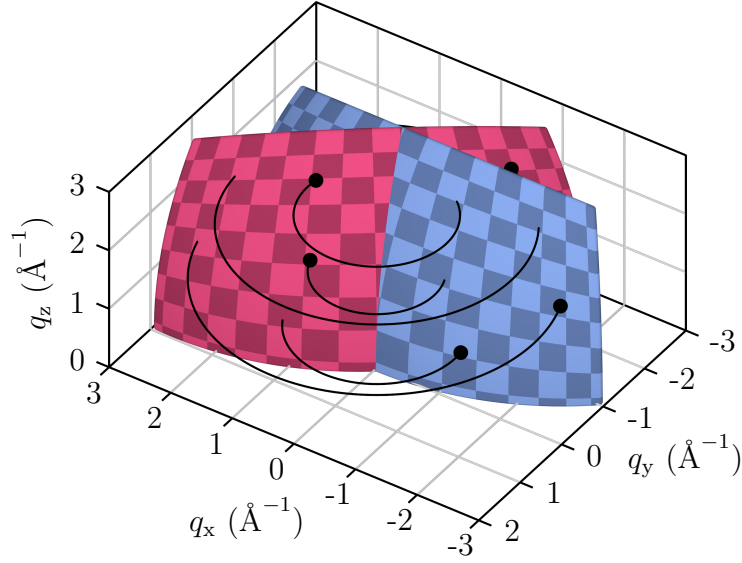


Figure 2.19 Two cuts through reciprocal space (blue, red) corresponding to different azimuthal sample rotation angles. Only reciprocal lattice points intersecting with the cuts can be accessed by grazing incidence X-ray diffraction measurements (black circles).

each covering a small part of the azimuthal sample rotation, have to be recorded which allows q_{xy} to be separated into its individual contributions q_x and q_y (*cf.* section 4.4). Furthermore, this data can be used to calculate PFs^[90], which allow the determination of epitaxial relationships between adsorbate and substrate and calculation of epitaxy matrices (*cf.* section 3.3). In a PF, the spatial distribution of poles (net-plane normals) is visualized. For this, a certain net-plane distance d corresponding to a specific q value (*cf.* Equation 2.37) is selected and the intensity measured for this q value during an azimuthal sample rotation is color-coded in a polar plot, where the radial part is the inclination Ψ of the scattering vector (*cf.* Figure 2.16b) and the azimuthal angle relates to the sample rotation.

Samples with statistical problems show only segments of the concentric circles observed for fiber-textured samples (*cf.* Figure 2.20). Thus, depending on the sample azimuth, not all information might be accessible within a static measurement. Therefore, an azimuthal rotation is also advantageous for this sample type (*cf.* section 4.3).

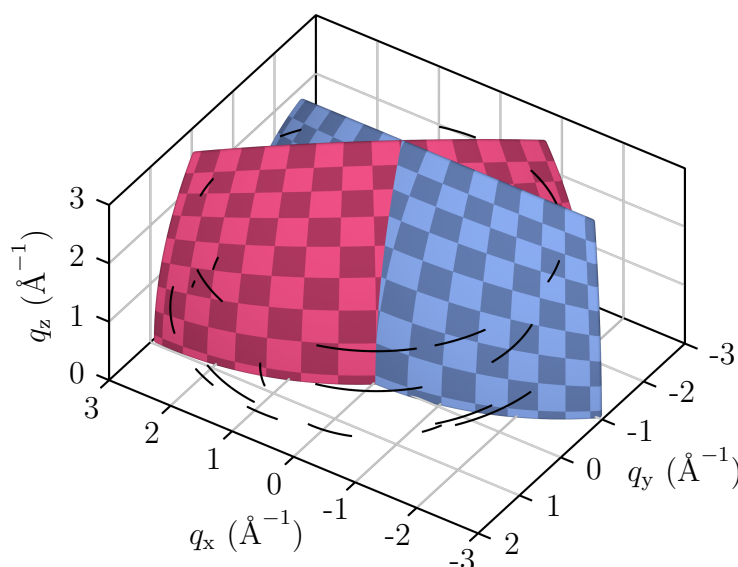


Figure 2.20 Two cuts through reciprocal space (blue, red) corresponding to different azimuthal sample rotation angles and segments of concentric circles in case of samples with statistical problems.

2.7 Indexing X-Ray Diffraction Data

Indexing is the process of assigning the corresponding hkl values to each measured peak and thus requires the determination of the lattice parameters a , b , c , α , β and γ (or their reciprocal space counter-parts). This process is well established for single-crystal and powder XRD. In the latter, only the length q of the scattering vector is experimentally determined, while single crystal diffraction uses the individual \mathbf{q} components q_x , q_y and q_z . In both cases, a large number of clearly defined and intense peaks is used, allowing the fitting of all experimental parameters and subsequent determination of the lattice parameters.

2.7.1 Indexing of Grazing Incidence X-Ray Diffraction Data

For GIXD data, typically only a small number of diffraction peaks is observed. This is due to the low scattering volume, the fact that films frequently grow with

2 Fundamentals

a defined contact plane and often suffer from statistical problems, which makes standard indexing algorithms unsuitable. To a large extent, statistical issues can be eliminated experimentally (*cf.* subsection 2.6.2), while due to the low number of peaks and the defined contact plane special indexing routines are required. Indexing algorithms for GIXD data have been developed and successfully applied to fiber-textured^[48,91] and epitaxially grown films^[36] (*cf.* section 4.4).

For fiber-textured films, peak positions in two dimensions, *i.e.* q_{xy} and q_z , are experimentally determined, which thus lies in-between the cases of powder (one dimensional data) and single-crystal diffraction (three dimensional data). For successful indexing, the lattice parameters a , b , c , α , β and γ and the contact plane, described by its Miller indices (hkl), have to be determined.

For epitaxially grown films, peak positions in three-dimensional reciprocal space can be determined, similar to single-crystal XRD. However, due to symmetries of the substrate and the possibility of several contact planes and different crystal structures coexisting on the same sample, standard data evaluation routines of single-crystal XRD are not applicable. Special indexing algorithms for GIXD data of epitaxially grown films not only allow the determination of the lattice parameters and the the contact plane but also rotation angles φ between the unit cell of the substrate and the adsorbate, *i.e.* the in-plane alignment, can be determined.

Independent of the sample's texture, information on the out-of-plane lattice spacing (typically obtained by a specular scan) allows a simplification of the indexing procedure of GIXD data. In case of fiber-textured samples, the number of unknowns is in a first step reduced to three real values (two lengths of the unit cell and the enclosed angle) and a set of two Miller indices which can be varied systematically. For example, one can reduce to the unknowns a , b , γ , h and k or a , c , β , h and l , *etc.* After solving this problem, the remaining unknown lattice parameters and the missing Miller index can be determined. For epitaxially grown films, the specular scan can be used as a criterion to reduce possible solutions. In a similar fashion, boundary conditions for the lattice parameters and the unit cell volume can be applied.

Please note that the determined lattice parameters are typically preliminary at first, since there is no unique choice of parameters, *i.e.* lattice points in three dimensions can be explained by different unit cells or the obtained solution is actually a supercell. By selection of the three shortest possible lattice vectors, one obtains the so-called Buerger cell^[92], which is not necessarily unique. A unambiguous unit cell, the reduced cell^[93,94], is found if the solution fulfils the criteria of Table 2.1.

Please note that a full crystal structure solution from GIXD data, *i.e.* obtaining the lattice parameters and the basis, is still very challenging. One possible and already successfully applied route is a combination of experimental and computational methods. After determination of lattice parameters from GIXD data, molecular dynamics (MD) simulations^[14,48,95], direct space methods treating the molecules as rigid bodies^[56,96] or crystal structure prediction (CSP) software^[97,98] can be used to find energetically favourable molecular arrangements inside the unit cell. In a subsequent step, promising candidates might be refined with more expensive density functional theory (DFT) calculations. Then, expected intensities can be calculated and compared to the experimentally determined values. Selecting the best match allows full crystal structure solution.

3 Methods

This section describes the rotating GIXD setup used for the experiments performed during this work, gives a short introduction of the software package GIDVis and shows a MATLAB-based evaluation script for PF measurements and subsequent determination of epitaxial relationships, epitaxy matrices and the creation of overlay plots, *i.e.* a visualization of the molecular arrangement of the adsorbate with respect to the substrate surface.

3.1 Rotating Grazing Incidence X-ray Diffraction

Compared to GIXD with a static sample, rotating GIXD poses special requirements on the experimental setup. These are met by the beamline XRD1 (Elettra synchrotron, Trieste, Italy) where the obtained data quality increased steadily during the course of this thesis, due to more experience in the operation and also an improved experimental setup.

3.1.1 Beamline XRD1 (Elettra)

Elettra is a storage ring of the 3rd generation and is located close to Trieste, Italy. All rotating GIXD experiments within this thesis were performed at Elettra's XRD1 beamline. XRD1 is using a multipole wiggler as radiation source and

3 Methods

a Si(111) double-crystal monochromator, allowing beam energies between 4 keV and 21 keV, corresponding to a wavelength of 3.10 Å to 0.59 Å.^[99] The sample position can be adapted using a Huber three-circle κ goniometer, allowing easy and reliable azimuthal sample rotation while keeping the incident angle α_i fixed. Diffracted intensity is collected with a large two-dimensional Pilatus 2M detector from DECTRIS (active area of 254 mm \times 289 mm^[100]), mounted on a rail parallel to the primary beam allowing different sample-detector distances (*sdd*) between 8 and 60 cm.

Additional details and improvements of the XRD1 setup for (rotating) GIXD measurements achieved in the context of this thesis are discussed below.

Goniometer

The goniometer is the central part of an XRD beamline and allows movement and orientation of the sample with respect to the primary X-ray beam. Figure 3.1a shows a schematic drawing of the important movements of the three-circle κ goniometer at XRD1. It is designed in such way that the rotation axes of χ , ω and Φ_{Sample} are intersecting at one point in space, the common center of rotation (COR) (\times symbol in Figure 3.1). The whole goniometer (together with the detector) is mounted on an experimental table, which allows small movements to make the primary beam pass through the COR. For rotating GIXD experiments, a reliable rotation of the sample around its surface normal is required (Φ_{Sample}). To make its rotation axis perpendicular to the sample surface and thus avoid a wobbling sample, the angles ξ_1 and ξ_2 are manually adapted. Please note that the rotation axes of ξ_1 and ξ_2 do not have to intersect with the COR, since no movements are performed around them during any measurement. Motorized translation stages x , y and z allow to bring the sample center into the COR. The motors ω and χ perform sample tilt perpendicular and parallel to the incoming X-ray beam respectively. Please note that typically $\chi = 0^\circ$, and thus ω equals the incident angle α_i . To easily perform rotating GIXD experiments, the Φ_{Sample} motor has to be mounted on-top of the

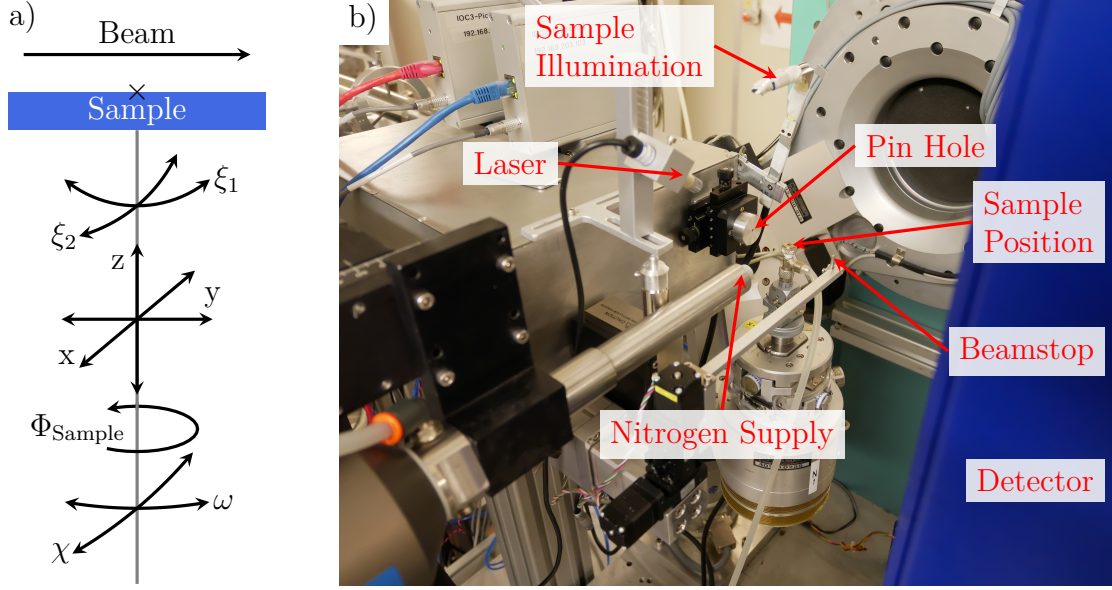


Figure 3.1 a) Sketch^[101] and b) photograph of the central goniometer part at the XRD1 beamline at Elettra synchrotron, Italy (Trieste).

ω and χ motors. Otherwise, the incident angle with respect to the sample would change during the azimuthal rotation requiring a time-consuming adaption of χ and ω as a function of Φ_{Sample} .

Please refer to section 4.1 for a more detailed description of the goniometer setup and the sample alignment procedure.

Detector and Center Pixel Position

The *sdd*, *i.e.* the distance between the sample center and the center pixel, is a parameter which can be easily varied to influence the range of reciprocal space covered during a measurement. Furthermore, the detector can – in a certain range – be translated in the plane perpendicular to the primary beam, resulting in changes of the center pixel position. This is especially important due to the blind areas typical for the Pilatus system: This kind of detector consists of several detection panels (8 vertical \times 3 horizontal ones in case of the 2M), which cannot be placed

3 Methods

directly adjacent to each other^[102,103]. This results in blind areas in-between the single panels where no signal can be recorded.

In order to obtain good diffraction images, the *sdd* and the center pixel position should be optimized with respect to the samples planned to be measured at the beginning of the beamtime. At XRD1, the Pilatus 2M detector can be moved approximately one panel upwards and roughly 30 % of a panel width to the side. Please note that the sideways movement is limited since the center of mass of the detector has to stay above the mounting. Otherwise, an unbalanced weight distribution and an unstable experimental table would be observed. With the large two-dimensional detector the diffraction signal can be recorded simultaneously for the left-hand and the right-hand side ($-q_{xy}$ and $+q_{xy}$ respectively). For the optimum detector and center pixel position, several points have to be considered:

1. Wavelength λ : For the experiments performed in the context of this thesis, typically $\lambda = 1.4 \text{ \AA}$ was chosen.
2. Sample-detector distance (*sdd*): The *sdd* together with the wavelength and the detector size basically determine the maximum accessible reciprocal space range. Depending on the investigated samples, different *sdd* values might be advantageous. For materials with large unit cells and high net-plane distances, *e.g.* metal-organic frameworks (MOFs), the diffraction pattern is expected at lower q values. Using a larger *sdd* allows recording these features with higher resolution and less influence of the primary beam (*e.g.* background due to air-scattering) but makes features at higher q values inaccessible. For the experiments performed during this thesis, *sdd* values of 150 mm or 200 mm were used.
3. Vertical center pixel position: Since features below the sample horizon (approximately below $q_z = 0 \text{ \AA}^{-1}$) are shadowed by the sample itself, it is preferential to have the direct beam position as close to the bottom of the detector as possible. Thus, the detector should be moved upwards to increase the measured range in q_z direction and reduce the shadowed area. At XRD1, this movement is limited to approximately 35 mm (about one panel height). Furthermore, the vertical center pixel position should always be slightly above

3.1 Rotating Grazing Incidence X-ray Diffraction

a panel gap, otherwise the gap might hide important in-plane features (close to $q_z = 0 \text{ \AA}^{-1}$). Additionally, it needs to be avoided that the primary beam hits a panel gap. In this case the beam could not be used for sample alignment anymore.

4. Horizontal center pixel position: Due to the detector gaps, centering the primary beam horizontally on the detector should be avoided, since this might lead to the same peak falling into the detector gap on the left- ($-q_{xy}$) and right-hand-side ($+q_{xy}$) of the detector. Data evaluation can then be performed for the side where more peaks are recorded or both sides to check the reliability of the measurement.

Please note that although the sdd can be varied between 8 and 60 cm, low values lead to increased difficulties for the experimenter. Together with the old sample mounting system (see below) a minimum sdd of 10 cm was used. Already at this distance, placing the sample on the stage is challenging due to space constraints.

To help finding the optimum detector and center pixel position already before the beamtime, GIDVis contains a setup simulation tool. Here, a predefined detector can be selected or a new one (including its gaps) defined and wavelength, sdd and center pixel position (among others) can be varied to study the accessible q range depending on the parameters. Figure 3.2 shows the result of such a simulation. It can be clearly seen that the Ag 200 peak would fall into a detector gap with the selected settings while the Ag 11 $\bar{1}$ peak would be collected (as long as an azimuthal sample rotation of sufficient range is performed during the measurement). On the $-q_{xy}$ side, the silver peaks are outside the observable range. The tool can also be used for detectors mounted on goniometer arms to optimize the goniometer angles and to allow subsequent stitching of the images.

Please note that for every detector position a calibration measurement of a sample with well-defined interplanar spacing, *e.g.* lanthanum hexaboride (LaB₆)^[104], silver behenate^[105], silicon^[106] or custom standars, should be performed. This allows the extraction of the conversion parameters (*e.g.* sdd , center pixel position, detector inclinations, *etc.*) with high accuracy^[34,107,108].

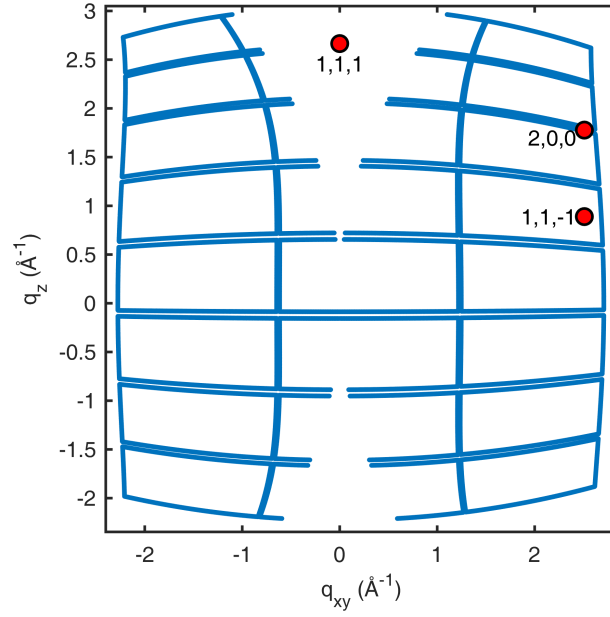


Figure 3.2 Simulated reciprocal space map using a Pilatus 2M detector, $\lambda = 1.4 \text{ \AA}$, $sdd = 200 \text{ mm}$ and a center pixel position of 656.01/1020. Red points indicate expected peak positions of silver in 111 orientation.

Sample Mounting

Several possibilities of sample mounting on the goniometer head have been used. For example, during experiments at the ID10 beamline at the European Synchrotron Radiation Facility (ESRF), Grenoble, France, samples were simply placed on the stage and not fixed further. This is sometimes sufficient, especially if the incident angles are small and no or only small further sample movements are performed (*e.g.* no azimuthal sample rotations were performed).

At the XRD1 beamline, samples were initially fixed to a magnetic sample holder. Since the investigated samples were not magnetic themselves, a small metal piece had to be glued onto their back side by double-sided sticky tape. Then, a sample was placed on the stage using tweezers. While approaching the stage, the metal piece was often lifted slightly from the sticky tape, resulting in very unreproducible sample placement. This resulted in several unwanted effects: a) The ellipses drawn during the laser alignment varied extensively in size, shape and center points,

3.1 Rotating Grazing Incidence X-ray Diffraction

making laser alignment a time-consuming process. b) When removing the sample and placing a new one, the reflected laser spot changed its position drastically, even when placing the same sample again. c) The connection between sample and stage was not strong enough, *i.e.* the sample moved slightly during measurements. This led to a wobbling sample, especially visible in integrations of 360° azimuthal sample rotations.

To improve the situation, a new sample holder was constructed. In short, it consists of a metal cylinder with a bottom part of correct dimensions to fit into a standard goniometer head. Along the axis of the cylinder a hole is drilled to a defined depth. Another hole is drilled radially to allow connection to a vacuum pump (*cf.* Figure 3.3a,b). The difference between the first and second version is the increased height above the horizontal drilling, which avoids signal from the small metal-pipe connection to the vacuum pump and also allows more space between the hose and the sample. The sample holder concept proved very successful; sample mounting time is heavily decreased and reproducibility increased. For example, when switching between different samples on substrates from the same batch, the center of the ellipse obtained during the laser alignment is often found at exactly the same spot and sometimes even no adaptations of the sample inclination angles ξ_1 and ξ_2 are necessary. It is expected that sample handling when using a very low *sdd* is improved as well. A vacuum sample holder based on the presented concept is now available at the XRD1 beamline for other users (*cf.* Figure 3.3c).

The only drawback of this approach in combination with the beamline XRD1 is the hose connection to the vacuum pump. To avoid tension on the hose and thus the goniometer head, care has to be taken to not wrap the hose around the κ goniometer arm. For this reason, the hose is not clamped to the vacuum holder and will slip from it in case too large tension is occurring, which might lead to the sample falling off. Furthermore, this sample holder concept cannot be easily applied to *in-situ* measurements, *e.g.* for variations of temperature using a heating stage.

3 Methods

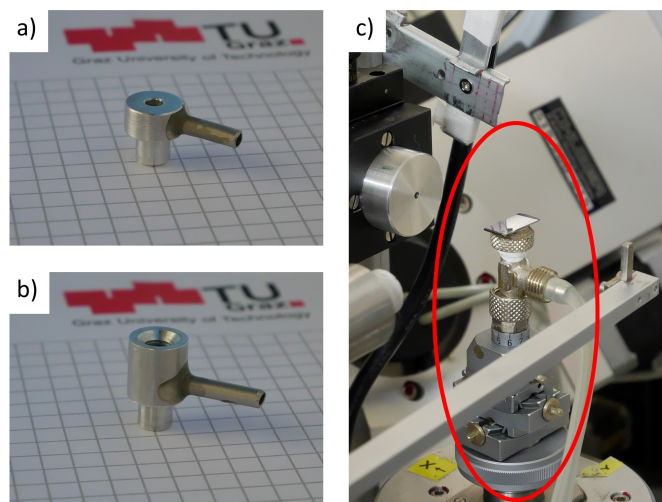


Figure 3.3 a,b) Version one and two of the constructed vacuum sample holder and c) the vacuum sample holder now available at the XRD1 beamline (red ellipse).

Sample Size

At XRD1, two different beam pin holes are available. One is short and of cylindrical shape (*cf.* Figure 3.1b), while the other is conical and reduces the distance the primary beam travels through air before reaching the sample, *i.e.* the exit opening is closer to the sample. In order to allow azimuthal sample rotations of large samples, the short cylindrical pin hole should be mounted. Samples of $2\text{ cm} \times 2\text{ cm}$ can be measured with the conical pin hole. Above these values it is advisable to change the pin hole to the cylindrical one.

Camera System

In the primary beam path a mirror is mounted so that a camera can be used to view along the beam, *i.e.* through the pin hole towards the sample. To make use of this camera, a strong light source is required after the sample, shining into the direction of the pin hole. This light source can be seen in Figure 3.1. In order to illuminate the sample from the back, the L-shaped frame with white light-emitting diodes

3.1 Rotating Grazing Incidence X-ray Diffraction

(LEDs) can be rotated downwards and then resides between sample and beamstop. By adjusting the sample height at an incident angle $\alpha_i = 0^\circ$ and observing the live camera image, a rough height alignment of the sample can be performed.

Beam Stop

A beam stop is used to avoid the direct X-ray beam reaching the detector, which would result in damage of the equipment. Since XRD1 is often used for single crystal X-ray diffraction, the original beamstop was of small circular shape, centered around the direct beam position. For a GIXD measurement, the exposure time was increased steadily so that the maximum intensity at any pixel did not exceed one million counts. For GIXD measurements of thin films on flat substrates, often the pixel reached by the specular reflected beam was limiting the exposure time. This is especially problematic since the reflected beam always hits the same pixel on the detector, even during an azimuthal sample rotation. If the high intensity would be related to a substrate peak, a small azimuthal rotation would break diffraction condition for the corresponding net plane and no intensity would be observed anymore. After discussion, the XRD1 beamline scientists could provide a higher beamstop (visible in *cf.* Figure 3.1), which also blocks the reflected beam before reaching the detector. To reduce inhomogeneous shadowing effects on the detector, the top part of the beam stop should be rounded. With the larger beam stop, higher exposure times could be reached and thus the signal-to-noise ratio was improved. The disadvantage is that without the reflected beam at the detector, the exact incident angle can not be calculated from its position anymore.

Beam Knife

One drawback of the XRD1 beamline is the relatively large beam size. For example, the beam dimensions are typically set to $200\text{ }\mu\text{m} \times 200\text{ }\mu\text{m}$ using a slit system. In comparison, the beam height at the ID10 beamline at ESRF can be limited to

3 Methods

below $15\text{ }\mu\text{m}$, while keeping the photon flux high. The big beam size results in large areas of the sample being illuminated, especially at low incident angles α_i , and thus broad diffraction features are observed. To reduce this problem, a so-called beam knife can be mounted. By bringing the beam knife close to the sample surface, the effectively illuminated area on the sample is reduced (*cf.* Figure 3.4a) since the back part of the sample is not illuminated at all and diffraction stemming from the front part is blocked by the beam knife itself. This means that only a small area below the beam knife contributes to the signal and narrower diffraction features are expected. Therefore, a test with a beam knife has been performed during one of the beamtimes (*cf.* Figure 3.4b). The beam knife was mounted on the 2Θ arm of the goniometer with $2\Theta = 90^\circ$ and could be moved towards the sample in a motorized way. As test case, a spin-coated film of lanthanum hexaboride (LaB_6)^[104] was measured at an incident angle $\alpha_i < 0.1^\circ$.

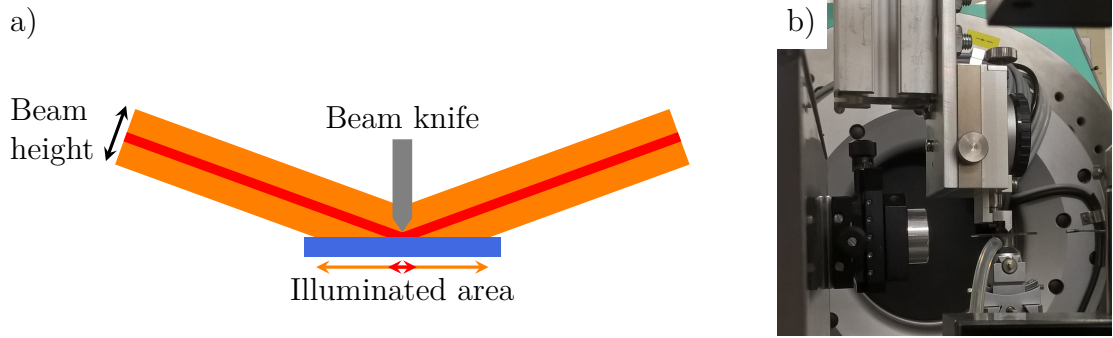


Figure 3.4 a) Reduction of the effectively illuminated area (orange and red arrows) using a beam knife (gray). b) Beam knife mounted at the XRD1 beamline.

The result for a measurement without and with beam knife is presented in Figure 3.5. In both cases, ring-like diffraction features are observed. However, the sample suffers from statistical problems resulting in distinct diffraction spots along the rings and no continuous diffraction pattern. Red lines represent the expected positions of Debye-Scherrer rings of LaB_6 , while black lines indicate the width of the inner-most ring. As can be seen in Figure 3.5a, the observed diffraction spots are equally distributed around the expected positions. Several effects on the resulting image are observed when the beam knife is brought closer to the sample surface (*cf.* Figure 3.5b): a) A clear shadow is seen in the image, *i.e.* the beam

3.1 Rotating Grazing Incidence X-ray Diffraction

knife itself is projected onto the detector. b) The background at low q -values is lowered. c) The ring width is reduced by approximately 50 % (as can be seen by the black rings), except for close to the in-plane direction ($q_z = 0 \text{ \AA}^{-1}$). This reduction, however, is asymmetric around the expected LaB_6 peak position; the outer part of the Debye-Scherrer rings vanish, while little to no effect is observed at the inner parts. This indicates that the beam knife was not aligned correctly with the center of rotation but slightly shifted along the direction parallel to the primary beam.

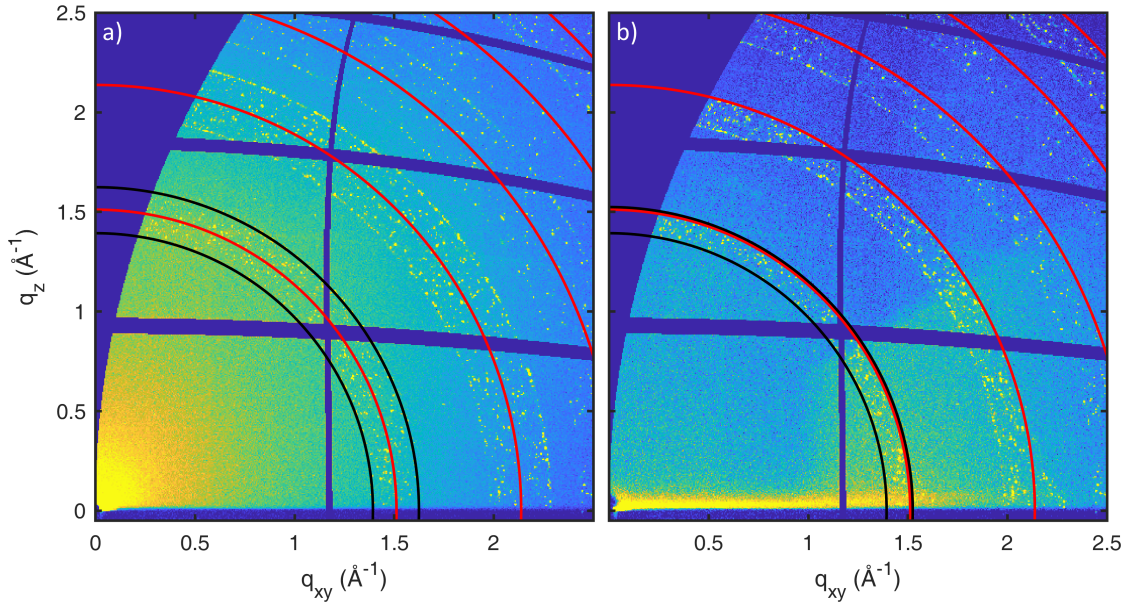


Figure 3.5 Influence of the beam knife on the diffraction pattern of LaB_6 : a) without beam knife, b) with beam knife. Red rings are expected Debye-Scherrer ring positions, black rings are drawn as a guide to the eye to estimate the width of the inner-most ring.

For a more precise positioning of the beamknife parallel to the incident beam, a translation stage was added to the mounting device. This allows a correct alignment of the beamknife to have a symmetric effect on the diffraction pattern. A measurement of a film of Ph-BTBT-C_{10} (approximate thickness 800 \AA) on $\text{Si}(001)$ with a 150 nm thermal oxide layer (data courtesy Andreas Hofer, Mike Ramsey and Roland Resel)^[109] with the adapted setup is shown in Figure 3.6. Little influence on the sharpness of the diffraction peaks is observed, which can be related to the relatively high incident angle of 1° . One clear difference is the shadowing in the image recorded with the beam knife at higher q_z values, where peaks can

3 Methods

be found up to $q_z = 2 \text{ \AA}^{-1}$, while in the image taken without beam knife clear peaks are observed up to $q_z = 2.5 \text{ \AA}^{-1}$. However, the beam knife slightly improves the visibility of the vertical rod around $q_{xy} = 0.8 \text{ \AA}^{-1}$ by partially suppressing contributions of the silicon oxide signal. Especially at q -values below $q = 1.5 \text{ \AA}^{-1}$, the beam knife clearly reduces the contribution of air scattering to the signal.

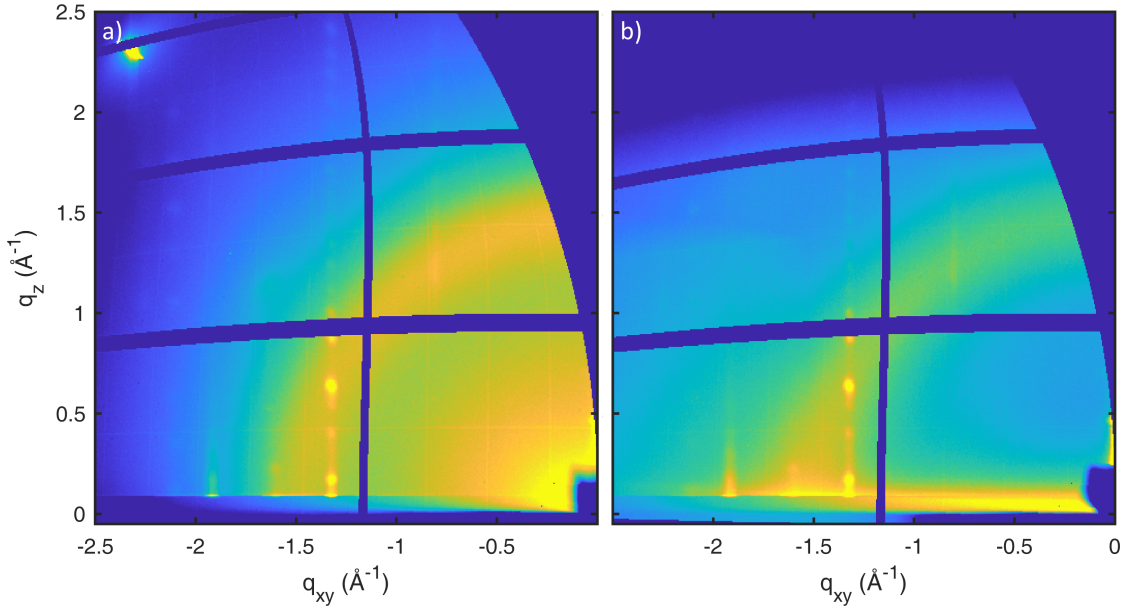


Figure 3.6 Influence of the beam knife on the diffraction pattern of Ph-BTBT-C₁₀ thin film: a) without beam knife, b) with beam knife. Please note that a) is an integrated image of a 60° rotation, while b) is a still image.

As can be seen from the examples, the beam knife can help to improve the data quality but also has disadvantages. Especially precisely mounting the knife to not influence the measured peak patterns in an asymmetric way and approaching the sample with the knife is a very time-consuming process. Furthermore, while regions of the reciprocal space map profit, others suffer due to shadowing effects. Thus, using the beam knife for several samples, especially if the films are not very thin, cannot be recommended. For thick films, where the advantage of amplified diffraction intensity at shallow incidence is not required, increased incident angles α_i can be used to reduce the size of the beam footprint instead. For measurements applying a beam knife, an optimized solution provided by the XRD1 beamline scientists would be preferable.

Extraction of z -Scans and Rocking Curves

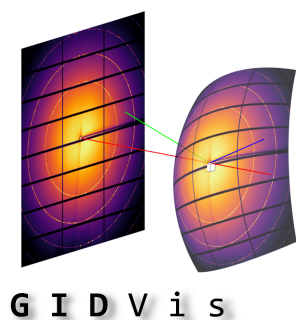
Unfortunately, no point detector is available at the XRD1 beamline to perform sample alignment and no region of interest can be determined for the detector. To record a z -scan or a rocking curve measurement, the data collection software available at XRD1 sets a new sample position (z or ω), performs the exposure by opening and closing the shutter and repeats this for a certain range of z or ω values and saves several images during the process. GIDVis was expanded to easily extract the one-dimensional intensity curves from such a series of images and to obtain the correct sample height z or incident angle α_i by *e.g.* fitting the sigmoid curve of the z -scan or the triangular shape of the rocking curve. Since GIDVis is installed at the data evaluation PC at XRD1, allowing fast access to the acquired data, this process is especially easy and thus sample alignment has become faster, especially in combination with the camera system for rough height alignment.

3.2 The Software Package GIDVis

Independent of the crystallite alignment with respect to the substrate surface and the chosen GIXD technique (static or rotating), several data processing and evaluation steps have to be performed after the measurement to extract reliable information. First, a calibration measurement has to be analyzed to obtain the necessary parameters (*e.g.* sdd , center pixel position, detector inclinations, *etc.*) for the conversion from real to reciprocal space. Then, the actual data has to be analysed, for example by extracting intensity profiles along different directions of reciprocal space, peak fitting, phase and texture analysis, *etc.* For experimental data obtained with the detector on a goniometer arm, stitching of the images should be available. For rotating GIXD data, special features are required. For example, it should be possible to project the individual images into a single image (*e.g.* by summing, averaging or by extracting highest intensities), quickly switch between the images, extract values and curves as a function of sample rotation, extract

3 Methods

PFs, *etc.* All the evaluation routines should be available independent of the data source, *i.e.* different beamlines, but also different file formats should be supported. Additionally, easy access to the metadata of a measurement (*e.g.* exposure time, goniometer angles, set and actual temperature, *etc.*) should be provided.



To cope with the described tasks, development of GIDVis was started by Christian Röthel (Institute of Pharmaceutical Sciences, Department of Pharmaceutical Technology, University of Graz and Institute of Solid State Physics, Graz University of Technology). Christian's PhD thesis^[110] contains a general introduction to diffraction from various types of samples and detailed information on GIXD data treatment and evaluation, PF calculations and software development. He developed a first version of the data conversion from pixel to reciprocal space, a small graphical user interface (GUI) for viewing diffraction images in pixel and reciprocal space, a separate GUI for setup calibration and a separate program including a GUI for PF calculations.

With the help of Stefan Pachmajer and valuable user-input from Andrew Jones (both Institute of Solid State Physics, Graz University of Technology), a more ordered and organized plan for the further development of GIDVis was developed. For easy extensibility, GIDVis is divided into separate independent modules which are started/opened from the main GIDVis window. Figure 3.7 gives an overview of the modules currently available.

GIDVis is already in use at several workgroups: Resel and Coclite groups (Graz University of Technology), Falcaro group (Graz University of Technology), Ameloot group (KU Leuven), Geerts group (Université Libre de Bruxelles) and is/was used by students from the University of Milano-Bicocca and the University of Manchester. Furthermore, GIDVis is installed at the XRD1 beamline at Elettra.

For more information relating to GIDVis, please refer to section 4.2, the GIDVis webpage^[111] and "GIDVis – Manual and Tutorials"^[112].

Toolbox Module <ul style="list-style-type: none"> • Set Parameters <ul style="list-style-type: none"> – Scaling – Space – Limits – Angles – Regridding – Intensity Corrections 	Load File Module <ul style="list-style-type: none"> • Select folder/file • Select conversion parameters • Features for multiple images <ul style="list-style-type: none"> – Summing – Merging – <i>etc.</i> 	Setup Simulation <p>Simulate accessible reciprocal space for given experimental parameters: detector, wavelength, incident angle, goniometer angles, center pixel position, <i>etc.</i></p>
Crystal Module <p>Phase and texture analysis</p>	Calibration Wizard <p>Analysis of calibrant measurements</p>	Peak Finder <p>Fitting of experimental peak positions</p>
Footprint Module <p>Visualization of the beam footprint</p>	Multiple Scans <p>Extract data from image series</p>	Beamline Setup <p>Adapt properties of experimental setup</p>
Annotation Module <p>Add annotations to the map</p>	Detector Module <p>Manage/change available detectors</p>	Project Module <p>Save and restore work progress</p>
Pole Figure Module <p>Calculate and export pole figures for specific q values from rotating GIXD data</p>	Other Modules <p>Line scans, powder plot, crosshair, add interactive rings (<i>e.g.</i> Debye-Scherrer rings), read intensity values, measure distances and angles, save image, export map data, export line data, <i>etc.</i></p>	

Figure 3.7 Overview and short description of modules currently available in the software package GIDVis.

3.3 Pole Figure Evaluation and Epitaxy Matrices

As already mentioned above, PFs are a useful tool for the evaluation of in-plane alignment of crystallites and determination of epitaxial relationships. Further, after this step one can also obtain the epitaxy matrix by calculating the surface unit cells of substrate and adsorbate and solving Equation 2.21.

To facilitate this evaluation process, the MATLAB script **CrystalOverlay** based on the implementations in **GIDVis_Crystal** has been developed (*cf.* Figure 3.8). All calculations and tasks related to crystal structures are contained in **GIDVis_Crystal** and its subfunctions, *e.g.* calculation of real- and reciprocal lattice vectors, peak positions, structure factors, plotting of the unit cell, directions, planes, *etc.* In **CrystalOverlay**, the user can define a directory containing PF data obtained from GIDVis^[34] (typically *mat* files) or stored in the *rwa* format. After that, several crystal structures (*e.g.* substrate and adsorbate) together with their contact plane and foldness can be added and expected peak positions, limited to a small range around the q value of the PF, are directly plotted onto the PF. For example, three crystal structures (magenta, red and blue) were added in Figure 3.8. The visibility of each crystal structure and its labels can be toggled independently. In Figure 3.8, the labels for the red crystal structure are switched on. The naming scheme is $h\ k\ l\ F$, where h , k and l are the indices of the peak and F gives the foldness. In the example, F are integers from one to six, *i.e.* there is a $360^\circ/6 = 60^\circ$ symmetry.

To match the peak positions in the azimuthal direction, buttons ($- \phi$, $+\phi$) allow independent rotation of the PF and of each crystal structure around the z -axis (the axis perpendicular to the contact plane) by a user-defined step (*Phi Step*). As can be seen in Figure 3.8, the peaks give good agreement between experiment and theory. Please note that there are no expected peaks of the magenta colored crystal structure since it does not have peaks around the q value where the PF was recorded. Clicking on one of the small colored buttons in front of each line opens the property window of the PF or the corresponding crystal.

3.3 Pole Figure Evaluation and Epitaxy Matrices

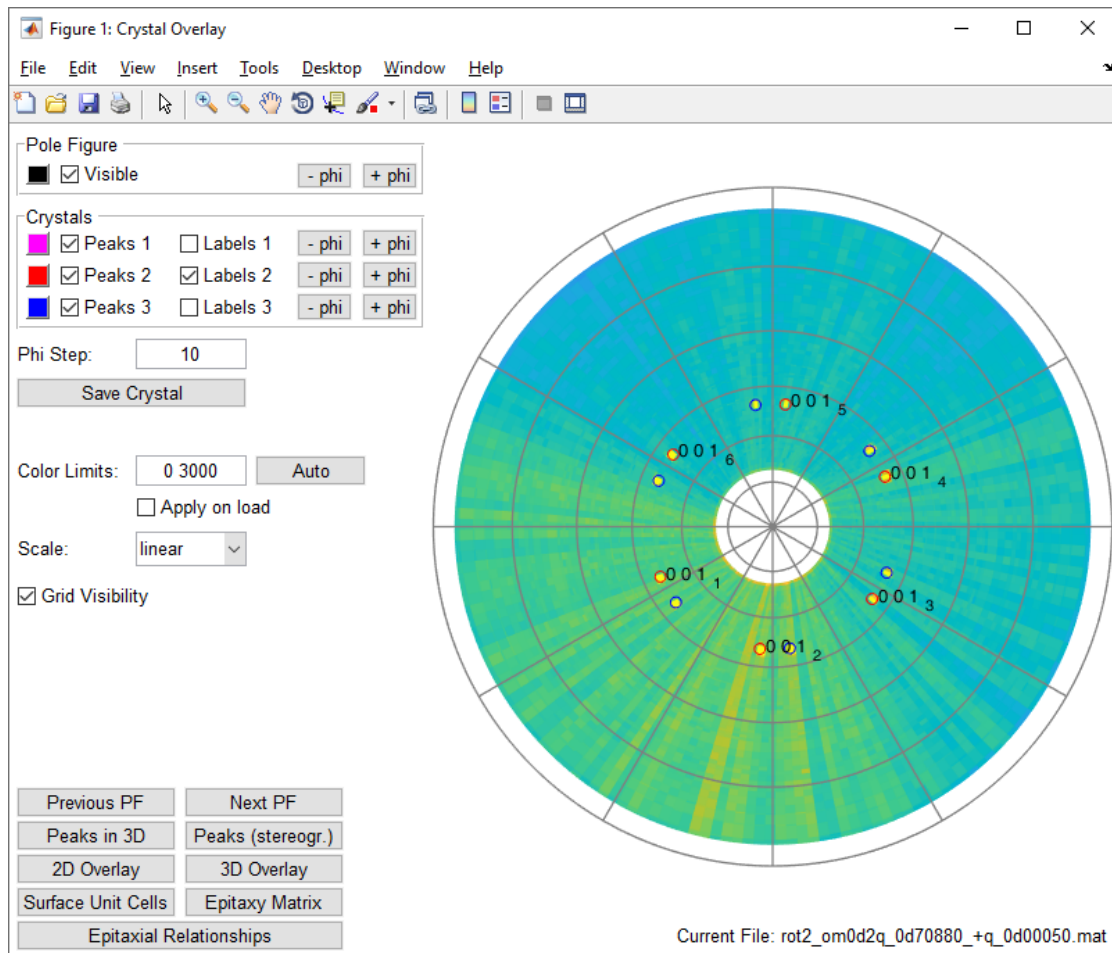


Figure 3.8 Screenshot of the graphical user interface of *CrystalOverlay*, a program to determine epitaxial relationships from PF measurements.

3 Methods

For the visualization of the PF data, the color limits can be adapted manually and the grid visibility can be toggled. Furthermore, the PF intensity can be plotted in linear, square-root or logarithmic scale. Buttons (*Previous PF*, *Next PF*) allow to quickly switch between to the previous or next PF to the previous or next one in the directory to check matching peak positions also for other q values. The expected peak positions of the loaded crystal structures can be plotted in three-dimensional space (q_x , q_y , q_z) or in a stereographic projection. Additionally, the surface unit cells and epitaxial relationships can be plotted (*Surface Unit Cells*, *Epitaxial Relationships*) and the epitaxy matrices (*Epitaxy Matrix*) can be calculated. Here, any of the imported crystals can be used as the substrate and the adsorbate crystal. Furthermore, a model of the molecular arrangement with respect to the substrate surface can be created (if the defined crystal structures contain information on the atom positions, *i.e.* are imported from a *res* file^[113–115]) in two- or three-dimensional style (*2D Overlay*, *3D Overlay*). These plots also include visualizations of the contact planes as well as three- and two-dimensional unit cells.

In general, **CrystalOverlay** is similar to the already existing PF evaluation software package *Stereopole*^[116]. However, **CrystalOverlay**

- can use PF data from GIDVis directly (*i.e.* without conversion to the *rwa* format by interpolation),
- handles foldness differently (*i.e.* defining a foldness applies it to all peaks),
- can limit plotting of expected peak positions based on the peaks' structure factors (requires that the crystal structure is imported from a *res* file),
- allows rotation angles around the z -axis which are smaller than 1° ,
- allows fast switching between different pole figures in a directory,
- can plot surface unit cells,
- can calculate epitaxy matrices,
- can plot the atomic arrangement of the adsorbate with respect to the substrate surface (requires that the crystal structure is imported from a *res* file),
- can plot the simulated peak position in three-dimensional reciprocal space and stereographic projection,

3.3 Pole Figure Evaluation and Epitaxy Matrices

- can display the intensity in linear, square-root and logarithmic scale.

Compared to *Stereopole* there are also shortcomings, *e.g.* **CrystalOverlay** cannot be run independently from MATLAB, requires changes in the source code (*e.g.* to add a crystal structure or to change the colormap), does not allow calculation of $\lambda/2$, $\lambda/3$, *etc.* peaks, ... Thus, **CrystalOverlay** is regarded a complement to *Stereopole*.

In the background of **CrystalOverlay**, several features of **GIDVis_Crystal** are used. By adding a crystal, the lattice vectors **a**, **b** and **c** are constructed according to Equation 2.1. Then, the crystal is rotated such that the plane (hkl) given by the orientation is parallel to the x - y -plane. For this, the $[hkl]^*$ direction is calculated and a rotation matrix is constructed^[117]. After its application on the lattice vectors the $[hkl]^*$ direction is parallel to the z -axis. Since $[hkl]^* \perp (hkl)$, this is equivalent to the plane (hkl) being parallel to the x - y -plane. To apply azimuthal rotations, the rotation matrix around the z -axis $R(\alpha)$ is applied on each lattice vector:

$$R(\alpha) = \begin{pmatrix} \cos \alpha & -\sin \alpha & 0 \\ \sin \alpha & \cos \alpha & 0 \\ 0 & 0 & 1 \end{pmatrix} \quad (3.1)$$

Application of any rotation matrix primarily changes the lattice vectors **a**, **b** and **c**. This, however, influences all other properties of the crystal constructed from the lattice vectors as well, *e.g.* directions, normal vectors, vertices of planes, peak positions via the reciprocal lattice vectors, *etc.* Furthermore, since atom positions inside the unit cell are given in fractional coordinates, their positions are also influenced by the applied rotations. Thus, the evaluation of the pole figure by finding the correct contact plane and azimuthal angles directly translates into the obtained epitaxial relationships, epitaxy matrices and overlayer plots.

CrystalOverlay is provided by the author upon request.

4 Results

4.1 Impact of Sample Misalignment on Grazing Incidence X-Ray Diffraction Patterns and the Resulting Unit Cell Determination

Impact of Sample Misalignment on Grazing Incidence X-ray Diffraction
Patterns and the Resulting Unit Cell Determination

Benedikt Schrode^{a*}, Josef Simbrunner^b, Sebastian Hofer^a, Luisa Barba^c, Roland Resel^a, Oliver Werzer^d

^a Institute of Solid State Physics, Graz University of Technology, Petersgasse 16, Graz 8010, Austria

^b Department of Neuroradiology, Vascular and Interventional Radiology, Medical University Graz, Auenbruggerplatz 9, Graz 8036, Austria

^c Institute of Crystallography, CNR, S.S. 14 Km 163.5 in Area Science Park, 34149 Basovizza, Trieste, Italy

^d Institute of Pharmaceutical Sciences, Department of Pharmaceutical Technology, University of Graz, Universitätsplatz 1, Graz 8010, Austria

4 Results

During several beamtimes performed in the course of this thesis, the importance of good sample alignment for any further data evaluation, *e.g.* calculation of lattice parameters, became evident. Thus, this publication studies the impact of sample misalignment, its influence on the calculated lattice parameters and gives advice for improved data acquisition. Sebastian Hofer and Benedikt Schrode carried out GIXD measurements, supported by Luisa Barba, who also provided expertise on sample alignment and setup realization. Benedikt Schrode evaluated the data and drew conclusions together with Roland Resel and Oliver Werzer. Josef Simbrunner contributed the code for the calculation of the lattice parameters. The manuscript was written by Benedikt Schrode, Oliver Werzer and Roland Resel. All authors were proof-reading the manuscript.

At the time of writing, the manuscript was submitted to *Review of Scientific Instruments* for consideration as full article. In the following, the revised version of this manuscript is printed.

Impact of Sample Misalignment on Grazing Incidence X-ray Diffraction Patterns and the Resulting Unit Cell Determination

Benedikt Schrode^{a*}, Josef Simbrunner^b, Sebastian Hofer^a, Luisa Barba^c, Roland Resel^a, Oliver Werzer^d

^a Institute of Solid State Physics, Graz University of Technology, Petersgasse 16, Graz 8010, Austria

^b Department of Neuroradiology, Vascular and Interventional Radiology, Medical University Graz, Auenbruggerplatz 9, Graz 8036, Austria

^c Institute of Crystallography, CNR, S.S. 14 Km 163.5 in Area Science Park, 34149 Basovizza, Trieste, Italy

^d Institute of Pharmaceutical Sciences, Department of Pharmaceutical Technology, University of Graz, Universitätsplatz 1, Graz 8010, Austria

Abstract

Grazing incidence X-ray diffraction is a frequently used tool for the crystallographic characterization of thin films in terms of polymorph analysis and determination of the crystallographic lattice parameters. To obtain high quality diffraction patterns the thin film sample has to be aligned carefully relative to the primary X-ray beam and relative to the X-ray detector. This work studies the effect of misalignment on the acquired diffraction pattern of a thin film sample. Typically, misalignment is observed as shifted peaks, which further translate to systematic errors in the estimation of the unit cell parameters. Depending on the type of misalignment and the performed measurement, some of the alignment errors can be reduced or even corrected; especially azimuthal sample rotations prove to be advantageous in these cases.

Introduction

The experimental method of grazing incidence X-ray diffraction (GIXD) is of fundamental importance for the structural characterization of thin films and surfaces. The surface sensitive

* Corresponding author: b.schrode@tugraz.at

method allows depth dependent analysis of thin films, where the thickness of the films can be reduced down to single molecular monolayers at substrate surfaces and to surfaces themselves¹⁻³. Crystallographic investigations of thin films employing GIXD are used to resolve crystallographic phase, texture, preferred orientation and epitaxial relationships⁴⁻⁸. Moreover, the solution of crystal structures from thin films became an important topic, since new polymorphs are frequently observed within thin films only (substrate-induced phases)⁹⁻¹¹. High quality diffraction measurements are required to get reliable input parameters for detailed crystallographic analysis^{12,13}.

GIXD measurements are commonly performed by means of a well-defined incidence angle of the incoming/primary beam, often provided by synchrotron sources¹⁴⁻¹⁶. This beam is then directed towards the sample, which scatters the beam, and depending on the sample, this will provide diffraction information at the detector side. For the collection of diffraction patterns of suitable quality, a precise alignment of the sample with respect to the incident beam is of fundamental importance¹⁷. It can be achieved by means of sample manipulation stages and/or simple goniometers. Eulerian cradles or κ -goniometers are two simple but very effective choices for sample alignment. Experimental demands might dictate that these standard geometries are exchanged by a combination of various translations and rotations which makes sample alignment more challenging.

Figure 1a shows a schematic sketch of a goniometer that can be used for GIXD measurements. Depending on the setups in use, several angles can be adjusted either in a motorized or manual way to orient the sample in space: The angles ξ_1 and ξ_2 are used to make the sample surface perpendicular to the rotation axis of ϕ_{sample} . The movements x and y allow lateral positioning of the sample, while z adapts the sample height. Furthermore, the angles of the incoming beam with respect to the sample surface, ω and χ , can be set. Please note that the angle ω corresponds to the incident angle α_i of the primary beam relative to the sample surface if $\chi = 0^\circ$, a setting frequently used (also in the following).

Depending on the sample's texture, two different measurement routines are usually applied in GIXD. In case of a two-dimensional powder, with the crystallites having a preferred out-of-plane orientation (one single crystallographic plane parallel to the substrate surface) but are randomly oriented in-plane, a static measurement (i.e. at fixed ϕ_{sample} angle) is sufficient to collect all available information¹⁸. In case the sample shows in-plane alignment, e.g. epitaxially grown films or if the two-dimensional powder suffers from statistic problems, the sample must be rotated around its surface normal (ϕ_{sample}) to access larger volumes of reciprocal space and collect all available diffraction information for sample investigation. During the sample rotation

a number of different diffraction patterns can be recorded. Here, each individual image accumulates information from a certain reciprocal space volume spanned by the detector area and the $\Delta\phi_{\text{Sample}}$ of the azimuthal rotation. Then this data allows various data analysis approaches. Data integrated over the full ϕ_{Sample} rotation is best used for texture and polymorph analysis. ϕ_{Sample} dependent data analysis via calculation of pole figures¹⁹ enables identification of local intensity variations or even determination of epitaxial relationships^{20–22}. For the determination of the crystallographic information, the scattering vector \mathbf{q} needs to be calculated. Figure 1b shows \mathbf{q} in the three-dimensional reciprocal space. It can be divided into an in-plane component $q_{xy} = \sqrt{q_x^2 + q_y^2}$ and the out-of-plane component q_z . The length q of the scattering vector is given by $q = (4\pi/\lambda) \sin \theta$, where θ is half the scattering angle and λ is the incident beam wavelength. The scattering vector \mathbf{q} encloses the angle Ψ with the z-axis.

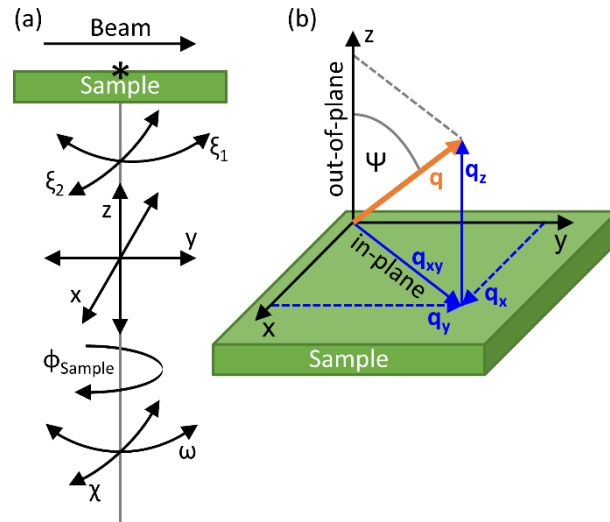


Figure 1: a) Schematic picture of the geometry for a grazing incidence X-ray diffraction goniometer showing angles and directions of possible sample movement relative to the sample surface. The * symbol marks the arcs' common center of rotation (COR). b) The scattering vector \mathbf{q} in three-dimensional reciprocal space consists of in-plane parts (q_x , q_y or $q_{xy} = \sqrt{q_x^2 + q_y^2}$) and an out-of-plane component q_z . The scattering vector and the z-axis (sample surface normal) enclose the angle Ψ .

Experimental Methods

To ensure high-quality data acquisition, the alignment of the sample should be carefully performed, e.g. by a procedure suggested in the Appendix. However, due to experimental limitations or errors, measurements often involve inaccuracies. In the following, sample

misalignment effects on the diffraction pattern are studied in detail. As a test case, a spin coated film of acetylsalicylic acid (ASS) on a 2 cm x 2 cm Si(001) wafer with a native oxide layer (Siebert Wafer, Germany) was prepared. Starting from a 22 mg/mL ASS solution in THF, 100 μ L were deposited and the substrate coated at a spin speed of 15 rpm for 60 seconds. The investigated sample does not show preferred in-plane alignment of the crystallites, thus it represents a rather good two-dimensional powder¹⁸. All GIXD experiments were performed at the XRD1 beamline at the Elettra Synchrotron Trieste, Italy, using a wavelength of 1.4000 Å and a stationary Dectris Pilatus 2M detector located 200 mm away from the center of the sample. The large detector allows simultaneous collection of the right-hand (+ q_{xy} , RHS) and left-hand side (- q_{xy} , LHS) of the diffraction pattern. Only one side would be sufficient for a GIXD diffraction study, since both sides should give identical information. The beam dimensions were set using a double-slit system limiting it to 200 μ m x 200 μ m. Setup calibration was performed by measuring polycrystalline lanthanum hexaboride²³ in a capillary and extraction of conversion parameters using the software GIDVis¹⁹. Conversion to reciprocal space and determination of peak positions were performed using scripts implemented in GIDVis. Due to the mosaicity of the sample, peak positions were determined in polar space by fitting a two-dimensional Gaussian functions with a background plane; followed by conversion of the obtained peak position to reciprocal space. Since only peak positions and not intensity were of interest for the evaluation, no intensity corrections in terms of Lorentz, polarization etc. were applied on the experimental data.

For all measurements, a defined sequence of alignment steps was performed to adjust the sample at the center of the goniometer as outlined in the appendix. In short, first, the rotation axis ϕ_{sample} was aligned perpendicular to the sample surface by adapting the angles ξ_1 and ξ_2 . Then, a z-scan and rocking curve measurements (i.e. ω -scans) were performed to determine the correct sample height and the incident angle α_i of the primary beam. At this point, errors in the alignment were intentionally introduced to study their influence on the detector image and the calculated results. For a more detailed description and general remarks on the sample alignment process, please refer to the Appendix.

Results

In this section, the influence of a sample height error, a wobbling sample and a lateral misalignment on the diffraction pattern (position of the diffraction peaks) and on the obtained lattice parameters is studied.

Impact of Common Alignment Errors on Diffraction Patterns

Height Error

The sample-detector distance (sdd) is measured from the center of rotation (COR) to the center pixel (the pixel the primary beam enters) at the detector. In case the sample is too high or too low, the sample will not be illuminated symmetrically around the COR but either more before or after. This changes the actual sdd to a larger or smaller value respectively compared to the real sdd , leading to a radial peak shift to higher/lower q values in the reciprocal space map. In short, this effect appears like zooming into or out from the diffraction pattern. To demonstrate this, the ASS sample was displaced in the z -direction and the peak positions from an integrated measurement over $\phi_{\text{sample}} = 360^\circ$ were extracted in terms of their q values. Figure 2 summarizes the changes of the length of the scattering vector for different incident angles, i.e. the difference of the q values for different peaks for the sample at the correct height z_0 and when offset by ± 0.05 mm (blue and red). Small incident angles α_i result in broadening of the diffraction peaks, as the beam footprint on the sample increases (cf. Fig S1), especially for large beam dimensions as used here. As Figure 2a demonstrates, this and eventual overspilling of the beam leads to a strong change in the peak positions on height error. Thus, when very low incident angles α_i are required, the sample height is crucial for recording correct diffraction patterns. At larger α_i the influence of the height error on the peak positions becomes less (cf. Figure 2b-e), but losing the advantage of the grazing geometry, i.e. losing the amplification of the diffraction signal stemming from the thin film as compared to the bulk signal, when the incident angle α_i is close to the critical angle of total external reflection.

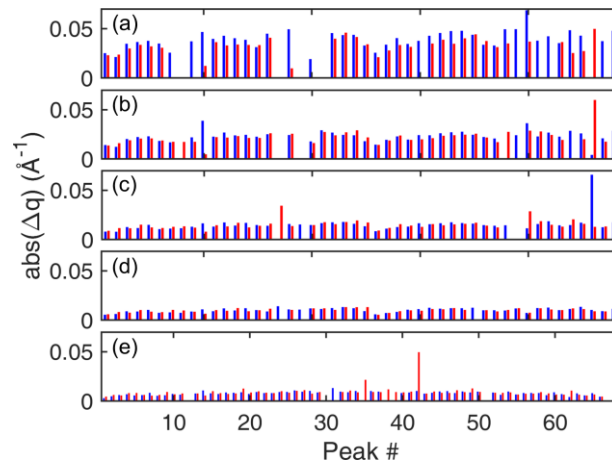


Figure 2: Changes of the length of the scattering vector q of several different peaks for the sample being 0.05 mm too low (blue) and the sample being 0.05 mm too high (red) for different incident angles α_i : (a) $\alpha_i = 0.6^\circ$, (b) $\alpha_i = 1.1^\circ$, (c) $\alpha_i = 1.7^\circ$, (d) $\alpha_i = 2.4^\circ$, (e) $\alpha_i = 3.0^\circ$.

Wobbling Sample

As mentioned above, rotating GIXD can be used to obtain all available diffraction information for samples showing poor statistics or preferred in-plane crystallite orientation. In case the rotation axis is not perfectly perpendicular to the sample surface, a wobbling sample is observed, which might be seen as varying incident and tilt angles depending on the ϕ_{Sample} rotation, and also a change in apparent height might take place.

In a measurement integrating a full 360° azimuthal sample rotation, a wobbling sample is easiest seen at strong peaks of a single crystal substrate. For example, when using a Si(001) substrate (i.e. the (001) plane is exactly parallel to the substrate surface), the Si(111), Si($\bar{1}\bar{1}1$), Si($1\bar{1}1$) and Si($\bar{1}\bar{1}\bar{1}$) peaks should fall exactly onto the same position on the detector during such a rotation. However, a wobbling sample leads to separated peaks, i.e. the corresponding scattering vectors have different inclinations Ψ (cf. Figure 1b). Depending on the misalignment angles and axes, two, three or four separated peaks can be observed. Furthermore, also the exact azimuthal position of the silicon peaks deviates from the 90° separated distribution on account of the additional inclinations. Depending on the q range covered by the measurement, similar considerations can be performed for the Si(220) peak.

Since the investigated sample in this work does not show preferred in-plane alignment of the crystallites the ASS peak positions can be monitored throughout the whole azimuthal sample rotation by taking individual images at different azimuths. This is different from the single crystal substrate which has peaks at only four clearly defined azimuthal positions (ϕ_{Sample}). To study the effect of wobbling in more detail, the sample was first set to the correct height z_0 and then the goniometer head was misaligned (cf. Figure 1, angles ξ_1 and ξ_2) to make the ϕ -axis slightly inclined with respect to the sample surface. Since this had to be done manually by screws, no numerical values for the inclination angles can be given. Figure 3a shows the inclination Ψ of the scattering vector as a function of the azimuthal sample rotation exemplarily for the ASS 212 peak and a nominal incident angle of 3° . 180 images each integrating over 2° were recorded. Since the large detector allows data collection for both sides of the reciprocal space map simultaneously ($+q_{xy}$ and $-q_{xy}$), two curves can be evaluated (RHS and LHS). It can easily be seen that Ψ varies sinusoidally and that RHS and LHS have an offset with respect to each other due to the scattering vector investigated being to the right and to the left of the primary beam, respectively. The length q of the scattering vector remains

constant (cf. Figure 3b). Going to lower nominal incident angles of 2° and 1° shows the same behavior (cf. Figures S2), with slightly larger deviations for lower incident angles due to broader diffraction features and thus less reliable peak fitting. Figures S3-S4 in the Supplementary Material present the same evaluation for the ASS 013 peak, where the same behavior, i.e. sinusoidal variation of Ψ but constant q , is observed.

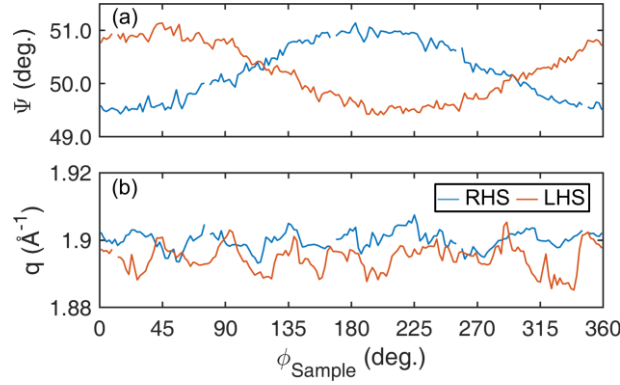


Figure 3: Influence of sample wobbling on the ASS 212 peak for the right-hand (RHS) and left-hand side of the detector (LHS): Inclination Ψ (a) and length q (b) of the scattering vector \mathbf{q} as a function of the azimuthal sample rotation angle ϕ_{Sample} using a nominal incident angle of 3° . Gaps in the lines are due to missing data points because of lack of convergence of the peak's fit.

Lateral Sample Misalignment

Shallow incident angles result in the beam illuminating a fair amount in the sample surface, often referred as beam footprint. This might even come to the point at which the footprint is larger than the sample, i.e. the beam is overspilling the substrate (cf. Figure S1). If the sample is displaced parallel to the primary beam, the beam footprint will cover different areas before and after the COR, and the diffraction signal will become asymmetric around the theoretical/true position of the diffraction spot. To study this influence, the sample was displaced on the sample stage parallel to the incoming beam (about 3 mm further away from the detector) and then aligned in terms of ξ_1 , ξ_2 and z . 60 images each integrating 6° of azimuthal sample rotation were recorded. Figure 4 shows the effect on the ASS 013 peak measured at an incident angle of 0.2° . In case the sample is placed too close to the detector, larger portions of the sample are illuminated between the COR and the detector, especially for low incident angles, leading to asymmetric peak broadening in radial direction towards lower q values (cf. Figure 4a). If the sample is rotated by 180° around its surface normal, the opposite situation occurs, i.e. the sample being too far from the detector. In this case, peaks broaden asymmetrically to higher q values (cf. Figure 4b). Integrating the diffraction pattern over the full 360° azimuthal sample rotation reduces the effect of the off-centered sample (cf. Figure

4c). Please note that the asymmetric peak shape in Figure 4c is a result of statistics, i.e. the crystallites do not show perfect fiber texture. Thus, depending on the sample azimuth, different contributions to the peak are observed, finally resulting in the asymmetric peak shape.

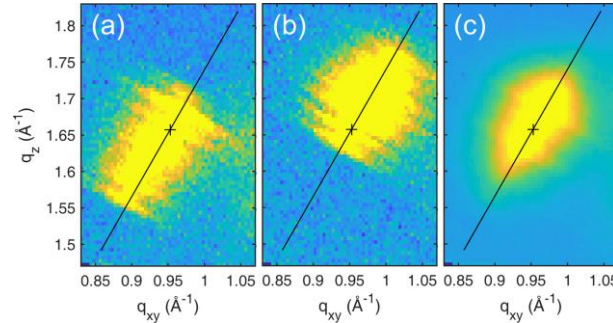


Figure 4: (a, b) The ASS 013 peak at an incident angle of 0.2° in the reciprocal space map with the sample positioned too close to and too far from the detector respectively. (c) The same peak but using integrated data from a 360° sample rotation. In all images the black + symbol shows the expected peak position, black lines give the radial direction as a guide to the eye.

Impact of Common Alignment Errors on Unit Cell Parameters

As described above, errors in the sample alignment cause the diffraction peaks to be at different actual positions compared to perfectly positioned samples. Here the question arises how big the impact on the evaluation of the unit cell parameters is when evaluating a number of different diffraction peaks simultaneously. For the ASS measurements presented above, up to 33 RHS and 32 LHS peak positions in reciprocal space were determined. Using this actual positional information, the unit cell parameters were determined (cf. Supplementary Material). To narrow the search space, the starting parameters were chosen to be the known unit cell of Aspirin²⁴ in a (002) orientation ($a = 11.446 \text{ \AA}$, $b = 6.596 \text{ \AA}$, $c = 11.388 \text{ \AA}$, $\beta = 95.55^\circ$). Although ASS is described with a monoclinic unit cell, the calculations in this work were not restricted to this crystal class so that other solutions were accessible.

Height Error

Figure 5 shows the unit cell parameters calculated for the correctly aligned sample (green) and for the sample offset by $\pm 0.05 \text{ mm}$ (blue, red). For the sample positioned too high, the peaks shift to higher q values, meaning reduced lattice spacing which in the calculation leads to smaller unit cell parameters a , b and c (Figure 5, blue). On the other hand, larger lattice constants are determined when the sample is positioned too low (Figure 5, red). The differences between the lattice parameters of the correctly aligned sample and of the misaligned one are reduced for measurements at larger incident angles. The values of the angles α , β and γ remain very similar to those of the monoclinic solution mentioned above.

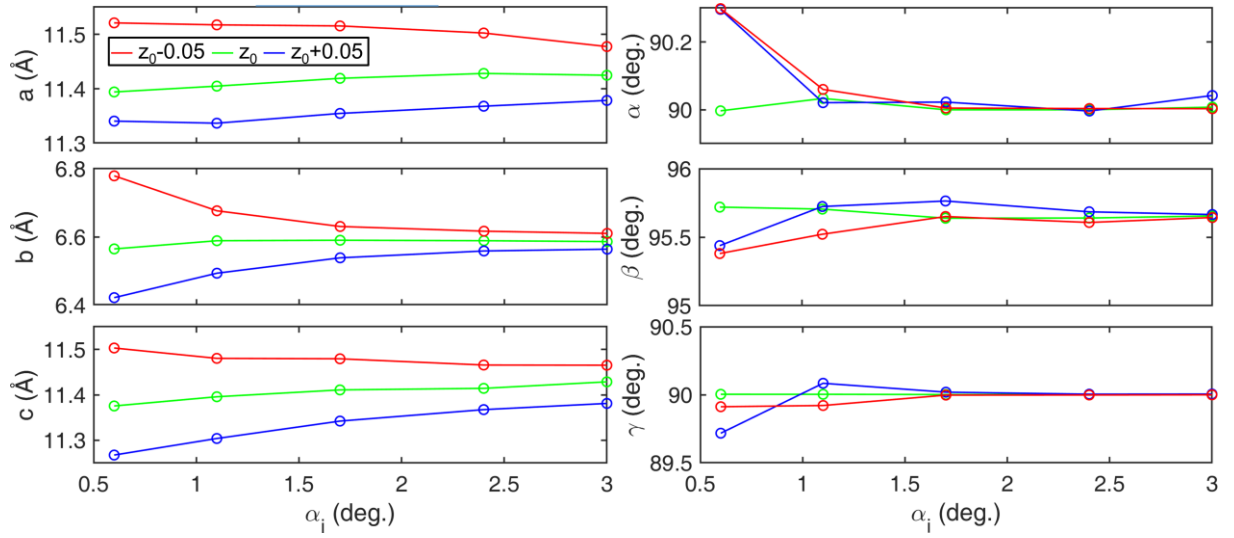


Figure 5: Influence of sample height misalignment on the lattice parameters as a function of the incident angle α_i .

Wobbling Sample

For each of the 180 images recorded during the full 360° sample rotation using a nominal incident angle of 3°, the peak positions and the unit cell parameters were determined. The resulting unit cell parameters are presented in Figure 6, for both the left-hand side of the detector (LHS) and the right-hand side (RHS). As for the peak positions, a sinusoidal behavior is observed, especially for the lattice parameters b and c . Depending on the sample azimuth, the lattice parameters are therefore either under- or overestimated. Using the data from the 360° integrated measurement, one obtains lattice parameters a , b , and c approximately at the mean value of the sinusoidally varying ones. While β and γ of the individual azimuth angles vary around the results for the integrated data, α is mostly found at higher values as compared to the data point from the integrated measurement (cf. Figure 6, dashed lines). Figures S5-S6 show the data obtained for nominal incident angles of 2° and 1°. As for the higher incident angle, sinusoidal behavior of the lattice parameters b and c can be observed, i.e. under- or overestimating the lattice parameters, while the angles α , β and γ show no clear trend.

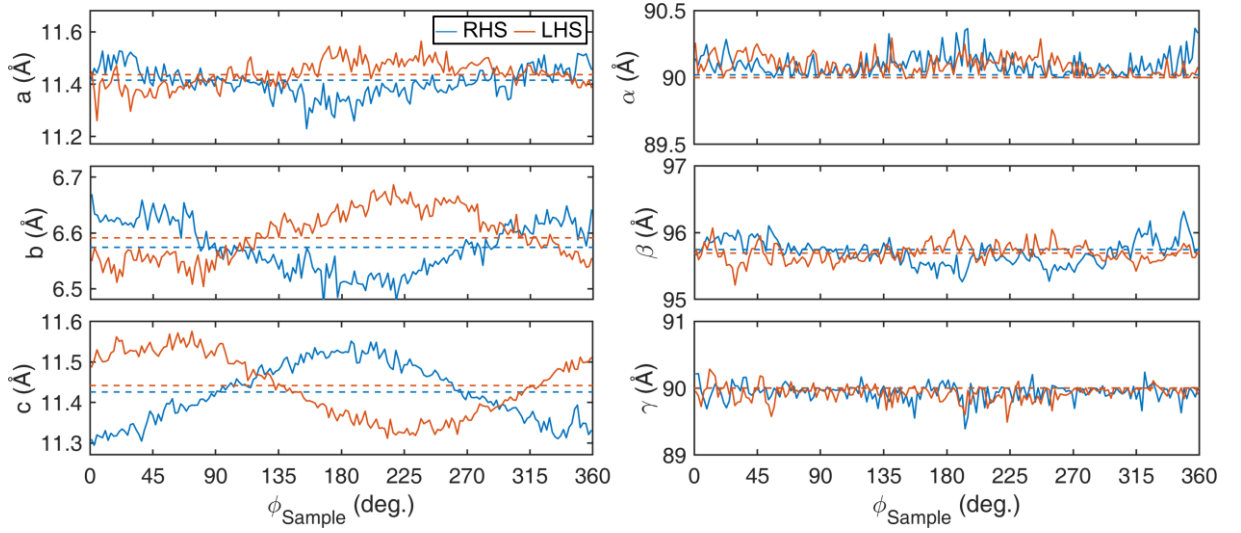


Figure 6: Influence of the wobbling sample on the lattice parameters as a function of the sample azimuth ϕ_{Sample} . Dashed lines indicate lattice parameters for integrated data of a 360° sample rotation. Data collected for a nominal incident angle of 3° .

Lateral Sample Misalignment

Figure 7 shows the unit cell parameters obtained for the sample being placed too close to and too far from the detector (blue and red line respectively) as a function of the incident angle α_i , calculated from the right-hand-side data. Additionally, the parameters obtained from the integration of the 360° sample rotation are given (green line). Here, no clear trend is found by variation of the incident angle α_i only. However, as for the height error, the influence on the lattice parameters reduces for higher α_i .

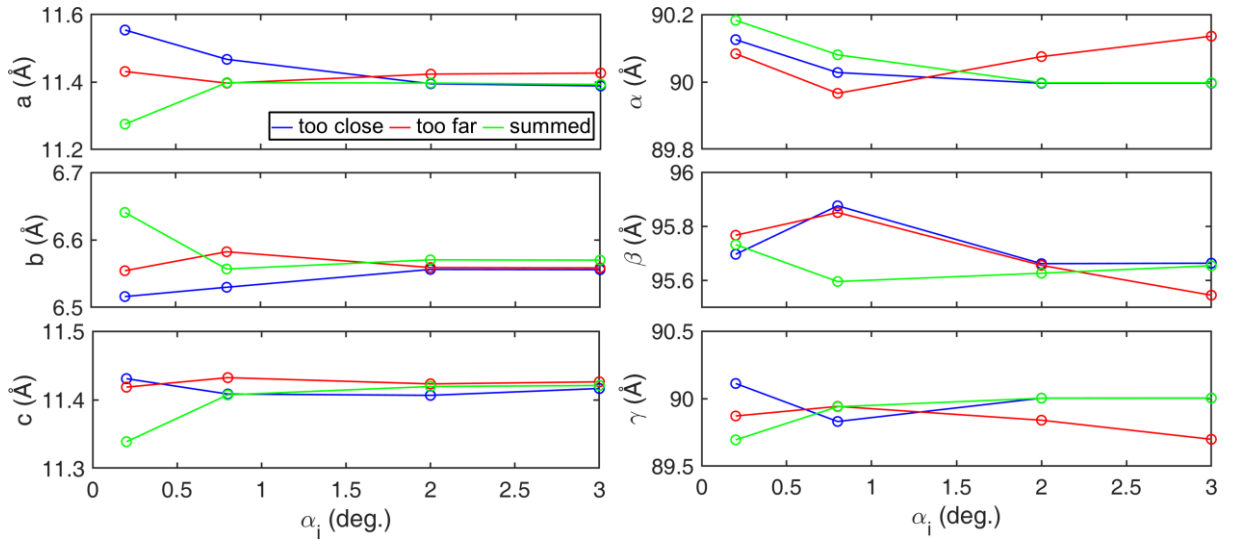


Figure 7: Influence of the sample being placed too close to and too far from the detector on the unit cell parameters calculated from the right-hand side of the detector as a function of

the incident angle α_i compared to the data from the 360° integrated (i.e. summed) measurement.

Discussion

This work shows the influence of sample misalignment on the experimental diffraction pattern and on the determination of the crystallographic unit cell. Although it is clear that much effort should be made to correctly align the sample in first place, some of the observed effects can be reduced and might even be corrected after the measurement depending on the performed measurement.

In case of a simple height misalignment, data conversion to reciprocal space can be performed using a different sample-detector distance and checking the position of well-defined substrate peaks which might be reminiscent to using an internal standard in powder diffraction experiments. This, however, requires a rotation of the sample around its surface normal to make sure that a substrate peak is collected by fulfilling the Laue conditions at certain azimuths. Since this procedure relies only on the substrate peak, it can be easily applied to fiber-textured films and films with preferred in-plane alignment of the crystallites. Please note that not all experimental setups allow reliable azimuthal sample rotations of suitable range.

In general, the angular displacement of a wobbling sample corresponds to a tilt of the reciprocal space. In case of both, a fiber-textured and also a sample with defined in-plane alignment of the crystallites, using the integrated data of the full 360° rotation averages out parts of the misalignment (cf. Figure 6) for the calculation of the unit cell. When going to smaller incident angles α_i , the angles of the misalignment are in the range of the incident angle, which might result in the sample surface not being illuminated correctly. Furthermore, the determination of exact peak positions becomes more challenging, since the peaks show larger broadening (cf. Figure S1), both making the errors on unit cell determination larger.

Also for a misalignment of the lateral position, using the integrated data reduces the effect. However, due to the typically square size of the substrates used and the applied incident angle, the illuminated area changes during the sample rotation, sometimes even leading to overspilling, and the effect cannot be completely eliminated. Another option to reduce the influence of this effect is to decrease the size of the beam footprint on the sample by using higher incident angles, smaller beam sizes or smaller samples.

To obtain errors for the determined unit cell parameters it is necessary to estimate the individual contributions of misalignment errors and their influence on the final result, a

process which in similar fashion is typically performed in single crystal or powder X-ray diffraction data analysis. There the advantage lies in the huge number of clearly defined and intense peaks available, which can be used to fit all experimental parameters and obtain errors for the crystal structure solution. In case of grazing incidence X-ray diffraction on thin films, due to low scattering volumes resulting in only a small number of diffraction peaks, this approach cannot be easily followed. In this case, it might be easier to perform a measurement integrating a full 360° azimuthal sample rotation to reduce the effects of misalignment.

Conclusion

In this work, the influence of sample misalignment on the obtained GIXD diffraction pattern is studied for static measurements and for rotating samples. Several possible errors are considered: a height error leads to a radial peak shift, which influences the unit cell determination as well, by either under- or overestimation of the lattice constants. A similar behavior is found for a wobbling of the sample (i.e. the sample rotation axis is not parallel to the normal of the sample surface); depending on the azimuthal sample angle, the calculated unit cell dimensions are too large or too small. A sample misalignment parallel to the incident beam results in radial peak shift but no clear trend in the calculated unit cell dimensions. All influences are reduced increasing the incidence angle α_i of the primary X-ray beam. Moreover, an integration over a full 360° azimuthal sample rotation reduces the effect of wobbling and of lateral sample misalignment on the lattice constant determination.

Supplementary Material

See Supplementary Material for images showing the influence of beam footprint on the diffraction peaks, algorithm for unit cell determination and results for the wobbling sample at the nominal incident angles of 2° and 1°.

Acknowledgements

This work was supported by the Austrian Science Fund (FWF), project P30222. The authors acknowledge Elettra Synchrotron Trieste for beamtime allocation at the beamline XRD1.

Appendix

Alignment Procedure

This chapter gives general information on the alignment procedure, starting with a short description of the goniometer in use and a detailed description of sample alignment procedure.

Goniometer

Although there is no unique way of performing sample alignment due to the vast amount of different setups available at home-lab machines or synchrotron sources, several steps have to be typically performed. To ease experimental efforts, the goniometer should be designed so that movements can be performed in such a way that at each sample position the exact angles with respect to the incoming and outgoing beam are known. This is done best by the rotation axes of the goniometer intersecting at one point in space, the common center of rotation (*COR*) for all relevant rotations.

In case of a rotating GIXD experiment, this means that the axes of the ω , the ϕ , and the χ rotation should intersect at one point, the *COR*. Consequently, the sample set into this point can be freely rotated so that at each time its angular position is known. Please note that it is not necessary that the axes of the ξ_1 and ξ_2 rotations are lying in the *COR* since during the measurement no rotations around these axes are performed. In general, the *COR* of the goniometer is found by various adjustment using a pin so that the center of rotation is very well determined prior any sample alignment. Further, the goniometer has then to be positioned so that the primary beam from the source passes through the *COR*.

For static GIXD experiments no sample rotations around ϕ_{Sample} are performed, i.e. ϕ_{Sample} is fixed. Furthermore, χ is typically 0° , which implies that the angle ω represents the incident angle α_i . An inclined Yoneda peaks (enhanced intensities for all scattering directions which enclose the critical angle of total external reflection with the sample surface) might indicate an offset in χ (or a rotation of the detector around the primary beam).

In some setups, especially when using for instance specific sample chambers, a common *COR* is absent. For this situation high quality measurements can be still obtained, but one needs to keep in mind that each angular sample position (i.e. ω , ϕ and χ) requires a new alignment with respect to the primary beam.

Calibration Measurement

For the conversion from real to reciprocal space several experimental parameters have to be known, e.g. position of the primary beam at the detector, the sample-detector distance, amongst others. For this, a standard measurement of a calibrant, e.g. polycrystalline lanthanum hexaboride (LaB_6)²³ or silver behenate²⁵, is typically performed. This allows precise determination of the required parameters^{19,26,27}. For this calibration one can use thin film samples or capillaries. The latter is more advantageous as much more scattering volume is at hand while keeping the beam footprint small, thus diffraction patterns of high quality and with low instrumental broadening can be easily collected.

Sample Mounting

Mounting of the sample on the goniometer head is crucial to make sure that the sample does not move during the measurements. Sticky tape and blu tack are often used but big variation in the sample position is observed after each exchange; sample tilt angles of up to 0.5° or more are observed. The most reproducible but still quick and non-sophisticated sample placement was achieved by constructing a vacuum system holding the sample in place. In short, the sample is put onto a flat plate with a hole connected to a vacuum pump. As the samples are typically small and low weight, the pump can be of small pumping power. Unfortunately, this system cannot be easily applied to in-situ measurements, e.g. temperature, and attention has to be paid with regard to the vacuum hose when performing continuous azimuthal sample rotations.

Sample Tilt

After the sample is fixed onto the goniometer, an alignment step has to be performed prior rotating GIXD measurements in order to ensure that the sample surface is perpendicular to the rotation axis ϕ_{Sample} . This guarantees that the sample is not wobbling during rotation. Using a two-dimensional detector wobbling might be observed by monitoring the position of a specular reflected beam or diffraction spots during rotation, as wobbling causes shifts of their positions. However, as these methods require prealignment of the sample (height and angles) and are limited in terms of resolution, another approach is commonly applied. Using a collimated light source (e.g. a laser beam) reflecting off the sample surface allows accurate alignment of the sample tilt. While the starting point of the beam is not crucial, the reflected beam is projected onto a screen far from the sample surface (cf. Figure 8a). Often distances of some meters are accessible making this method very precise. The position of the reflected spot is marked on a screen, followed by an azimuthal sample rotation (ϕ_{Sample}) of 90° . In the case of misalignment, the new reflected spot will not coincide with the first one, and is marked. Two

more spots are recorded for a sample rotation of 180° and 270° with respect to the initial position (cf. Figure 8b,c). Now, the two opposite points are connected with straight lines representing the axes of an ellipse (cf. Figure 8d). After this, the sample tilt angles ξ_1 and ξ_2 (cf. Figure 1) have to be adjusted in a way that the light is reflected to the intersection of the two lines. It should be noted that surface alignment can be achieved by using proper rotations of a standard single crystal alignment head, motorized motors or even a hexapod. The only requirement is that the rotations ξ_1 and ξ_2 are sitting on top of the ϕ_{Sample} -axis, as otherwise the rotation is adjusted onto an arbitrary axis in space rather than this particular one. To ensure high quality alignment, this procedure should be repeated and/or the distance between sample and screen should be maximized.

As this method requires a reflective surface, non-reflective or rough samples cannot be aligned, as the light beam is scattered off the surface. To overcome this issue, one can often use a bare substrate without the sample of interest. After performing the alignment on it, exchanging the sample on the vacuum holder is often sufficient or can be close enough to a good alignment to improve it further using diffraction spots of the sample or the substrate.

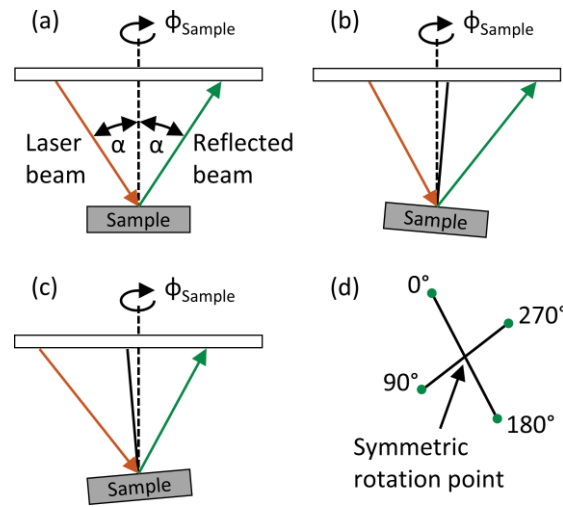


Figure 8: Principle of the Laser alignment used to make the azimuthal rotation axis perpendicular to the sample surface. a) A well aligned sample reflects the incoming light to the same spot, independent of ϕ_{Sample} , while a wobbling sample (b, c) leads to an elliptical trajectory of the reflected beam during a ϕ_{Sample} rotation of 360° (d).

Lateral Sample Position

To illuminate the sample symmetrically around the *COR*, the x- and y-positions of the goniometer (cf. Figure 1) need to be set. For a static measurement, aligning the sample position parallel to the beam is sufficient. When performing azimuthal rotations during the GIXD measurement, the direction perpendicular to the incoming beam becomes additionally

important. Therefore, the center of the sample has to be aligned with the center of the goniometer.

To do so, one can follow strategies either using the diffracted/reflected beam or the primary beam itself, both requiring translation capabilities of sufficient range on-top of the ϕ_{Sample} -axis. The sample is mounted and set at a defined position (i.e. height z and incident angle α_i) where one can identify reflection or diffraction at the detector. Then, the sample is continuously translated from one side to the other perpendicular to the primary beam. At some point the surface is illuminated by the beam, so that reflection/diffraction is observed. This signal will not change significantly until the beam leaves the sample surface, i.e. no more signal is obtained. Using the knowledge on the first/last position for each side when the signal was obtained, the middle of the translation can be found. For the other direction, one might do the same by using steeper incident angles moving the sample parallel to the beam, or one can rotate the sample by 90° in ϕ_{Sample} , so that the other translation direction is accessible.

Facilitating the primary beam (i.e. without beam stop and usually with reduced intensity by applying absorbers), one identifies the sample by its shadow on translation. Doing this in different directions will also enable the sample centering.

A third possibility is to use the same laser already applied during the correction of the sample tilt. By visual inspection of the laser spot on the sample during the azimuthal rotation a lateral sample displacement can be detected and corrected.

Sample Height

To move the sample to the correct height z_0 , a z -scan in the primary beam is best performed at a 0° incident angle without beam stop but absorbers applied, and collecting the intensity of the primary beam after the sample by either a point detector or reading out the intensity in a single/several pixels of a two-dimensional detector. Especially when using several pixels, care should be taken that during this process the reflected beam is not included in the region of interest, since this would have an impact on the obtained result. The measured intensity of the primary beam after the sample will go from a maximum value when the direct beam passes over the sample (cf. Figure 9 I), to zero when the beam is absorbed by the sample (cf. Figure 9 III). The curve obtained during the z -scan shows a sigmoid shape and the correct sample height is found at the inflection point (cf. Figure 9 II). In case no fitting is available, half the maximum value of the intensity or the minimum position of the derivative of the curve gives the correct height of the sample.

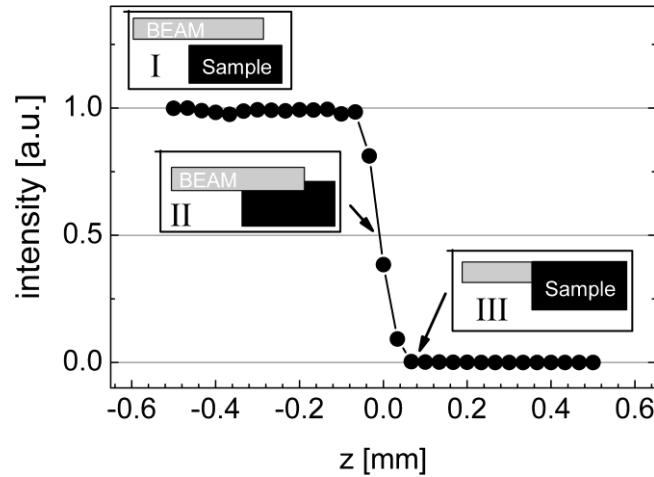


Figure 9: Typical intensity profile of the primary beam at the detector as a function of the sample height z where the primary beam I) passes above the sample, II) is partly and III) fully shadowed by the sample.

Having a well-aligned sample means that for large z -scan ranges the sample is shadowing the beam up to a certain point. After that one often finds high intensity again which is typically associated with the z value at which the beam passes between the sample and the sample stage.

Some beam stops are mounted in a way so that their reproducible removal and insertion is hardly achieved. In this case, the height scan can be performed using an inclined sample so that the reflected or diffracted signal can be used. Similar as for the lateral sample alignment, a signal will be observed when the beam illuminates the sample, no signal when the sample is too low or too high. From the starting and end point one can evaluate the proper height. However, this procedure requires that the sample is correctly aligned laterally as for such scan the height and translation along the beam are correlated. In case of lateral sample misalignment, this method results in a height error since the sample is aligned with respect to the center of the sample and not the *COR*.

Rocking Curves

These measurements allow to precisely determine the incident angle α_i of the primary beam. They are recorded by varying the incident angle and keeping 2θ fixed at 0° . In practice, this is again done by monitoring the intensity of the primary beam after the sample while varying the incident angle. As for the z -scan, only the primary beam, not the reflected beam, should be used for the evaluation. Having a parallel beam, the obtained curve shows a triangular shape where the center of the peak determines $\alpha_i = 0^\circ$. The parallel beam is shadowed by the sample

as it rotates around α_i cutting off the intensity at a certain angle; the size of the sample determines this cutoff with larger samples having the cutoff at smaller angles.

Besides the incident angle, two more important pieces of information are obtained from rocking curves. If the sample height is too low, the beam overshoots the sample, which can be identified by the maximum of the intensity being much larger than half the primary beam intensity. If the sample is located even lower than the beam height at $\alpha_i = 0^\circ$, the shape of the curve will be trapezoidal. In case the sample is too high the rocking curve remains triangular, but the intensity is reduced by a certain amount (cf. Figure 10a). On the other hand, the shape of the rocking curve provides a proof on the correct lateral sample position parallel to the beam direction. For a sample being symmetrically aligned around the *COR*, the shape is symmetric while an offset, even by 1 mm, results in a severe asymmetric shape (cf. Figure 10b) which then reflects in a later stage in asymmetric diffraction spots, especially at shallow incident angles.

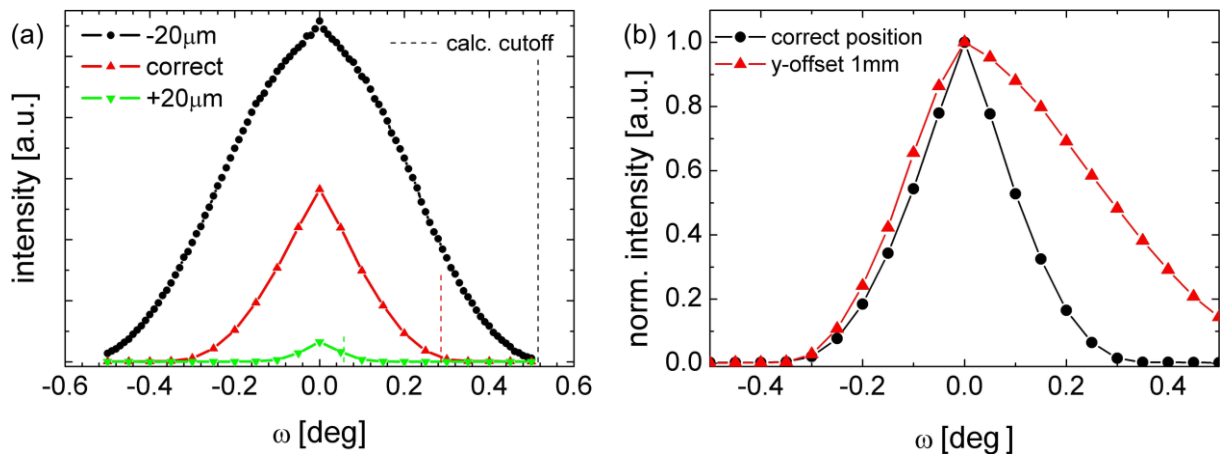


Figure 10: Intensity of the primary beam at the detector during rocking curve measurements (ω scans) for different sample heights (a) and for a sample misplaced 1 mm parallel to the beam compared to its correct position (b).[†]

Overall Considerations

Depending on the samples and the capabilities of the different experimental setups, one, several or all of the alignment steps can be performed. To achieve best results, one typically iteratively repeats some of the scans mentioned, e.g. a z-scan will not give the correct sample height if the incident angle α_i is not exactly zero.

[†] Data obtained on a Bruker D8 Discover in horizontal geometry with a Eulerian cradle, equipped with a sealed copper tube (wavelength 1.54 Å) on the primary, and a graphite monochromator and a scintillation detector on the secondary side.

References

- ¹ I.K. Robinson and D.J. Tweet, Reports on Progress in Physics **55**, 599 (1992).
- ² M. Birkholz, P.F. Fewster, and C. Genzel, *Thin Film Analysis by X-Ray Scattering* (Wiley-VCH, Weinheim, 2006).
- ³ W.C. Marra, P. Eisenberger, and A.Y. Cho, Journal of Applied Physics **50**, 6927 (1979).
- ⁴ Y. Nakayama, Y. Mizuno, T. Hosokai, T. Koganezawa, R. Tsuruta, A. Hinderhofer, A. Gerlach, K. Broch, V. Belova, H. Frank, M. Yamamoto, J. Niederhausen, H. Glowatzki, J.P. Rabe, N. Koch, H. Ishii, F. Schreiber, and N. Ueno, ACS Appl. Mater. Interfaces **8**, 13499 (2016).
- ⁵ T. Schmitz-Hübsch, T. Fritz, F. Sellam, R. Staub, and K. Leo, Phys. Rev. B **55**, 7972 (1997).
- ⁶ H. Yang, T.J. Shin, M.-M. Ling, K. Cho, C.Y. Ryu, and Z. Bao, J. Am. Chem. Soc. **127**, 11542 (2005).
- ⁷ S.C.B. Mannsfeld, A. Virkar, C. Reese, M.F. Toney, and Z. Bao, Adv. Mater. **21**, 2294 (2009).
- ⁸ S. Gaudet, K. De Keyser, S. Lambert-Milot, J. Jordan-Sweet, C. Detavernier, C. Lavoie, and P. Desjardins, Journal of Vacuum Science & Technology A: Vacuum, Surfaces, and Films **31**, 021505 (2013).
- ⁹ A.O.F. Jones, B. Chattopadhyay, Y.H. Geerts, and R. Resel, Advanced Functional Materials **26**, 2233 (2016).
- ¹⁰ H. Yoshida, K. Inaba, and N. Sato, Appl. Phys. Lett. **90**, 181930 (2007).
- ¹¹ G. Gbabode, N. Dumont, F. Quist, G. Schweicher, A. Moser, P. Viville, R. Lazzaroni, and Y.H. Geerts, Adv. Mater. **24**, 658 (2012).
- ¹² J. Simbrunner, C. Simbrunner, B. Schrode, C. Röthel, N. Bedoya-Martinez, I. Salzmänn, and R. Resel, Acta Crystallographica Section A Foundations and Advances **74**, 373 (2018).
- ¹³ S. Schiefer, M. Huth, A. Dobrinevski, and B. Nickel, J. Am. Chem. Soc. **129**, 10316 (2007).
- ¹⁴ H. Ogawa, H. Masunaga, S. Sasaki, S. Goto, T. Tanaka, T. Seike, S. Takahashi, K. Takeshita, N. Nariyama, H. Ohashi, T. Ohata, Y. Furukawa, T. Matsushita, Y. Ishizawa, N. Yagi, M. Takata, H. Kitamura, A. Takahara, K. Sakurai, K. Tashiro, T. Kanaya, Y. Amemiya, K. Horie, M. Takenaka, H. Jinnai, H. Okuda, I. Akiba, I. Takahashi, K. Yamamoto, M. Hikosaka, S. Sakurai, Y. Shinohara, Y. Sugihara, and A. Okada, Polym J **45**, 109 (2013).
- ¹⁵ Z. Jiang, X. Li, J. Strzalka, M. Sprung, T. Sun, A.R. Sandy, S. Narayanan, D.R. Lee, and J. Wang, J Synchrotron Rad **19**, 627 (2012).
- ¹⁶ A. Lausi, M. Polentarutti, S. Onesti, J.R. Plaisier, E. Busetto, G. Bais, L. Barba, A. Cassetta, G. Campi, D. Lamba, A. Pifferi, S.C. Mande, D.D. Sarma, S.M. Sharma, and G. Paolucci, Eur. Phys. J. Plus **130**, 43 (2015).
- ¹⁷ B.B. He, *Two-Dimensional X-Ray Diffraction* (John Wiley & Sons, Inc., Hoboken, NJ, USA, 2018).
- ¹⁸ A. Moser, O. Werzer, H.-G. Flesch, M. Koini, D.-M. Smilgies, D. Nabok, P. Puschnig, C. Ambrosch-Draxl, M. Schiek, H.-G. Rubahn, and R. Resel, Eur. Phys. J. Spec. Top. **167**, 59 (2009).
- ¹⁹ B. Schrode, S. Pachmajer, M. Dohr, C. Röthel, J. Domke, T. Fritz, R. Resel, and O. Werzer, J Appl Crystallogr **52**, 683 (2019).
- ²⁰ M. Hollerer, S. Pachmajer, D. Lüftner, B. Butej, E.-M. Reinisch, P. Puschnig, G. Koller, M.G. Ramsey, and M. Sterrer, Surface Science **678**, 149 (2018).
- ²¹ S. Pachmajer, O. Werzer, C. Mennucci, F. Buatier de Mongeot, and R. Resel, Journal of Crystal Growth **519**, 69 (2019).
- ²² H. Riegler, A. Rivalta, P. Christian, C. Röthel, T. Salzillo, E. Venuti, and O. Werzer, Thin Solid Films **683**, 67 (2019).
- ²³ D.R. Black, D. Windover, A. Henins, J. Filliben, and J.P. Cline, Advances in X-Ray Analysis **54**, 140 (2010).
- ²⁴ P.J. Wheatley, J. Chem. Soc. 6036 (1964).
- ²⁵ T.C. Huang, H. Toraya, T.N. Blanton, and Y. Wu, Journal of Applied Crystallography **26**, 180 (1993).

²⁶ D. Kriegner, E. Wintersberger, and J. Stangl, *Journal of Applied Crystallography* **46**, 1162 (2013).

²⁷ A.P. Hammersley, *Journal of Applied Crystallography* **49**, 646 (2016).

4.2 GIDVis: A Comprehensive Software Tool for Geometry-Independent Grazing-Incidence X-ray Diffraction Data Analysis and Pole-Figure Calculations



computer programs



ISSN 1600-5767

JOURNAL OF
APPLIED
CRYSTALLOGRAPHY

GIDVis: a comprehensive software tool for geometry-independent grazing-incidence X-ray diffraction data analysis and pole-figure calculations

**Benedikt Schrode,^{a,*} Stefan Pachmajer,^a Michael Dohr,^a Christian Röthel,^b Jari
Domke,^c Torsten Fritz,^c Roland Resel^a and Oliver Werzer^b**

Received 15 January 2019
Accepted 2 April 2019

Edited by A. Barty, DESY, Hamburg, Germany

^aInstitute of Solid State Physics, Graz University of Technology, Petersgasse 16, Graz 8010, Austria, ^bInstitute of
Pharmaceutical Sciences, Department of Pharmaceutical Technology, University of Graz, Universitätsplatz 1, Graz 8010,
Austria, and ^cInstitute of Solid State Physics, Friedrich Schiller University Jena, Helmholtzweg 5, Jena 07743, Germany.
*Correspondence e-mail: b.schrode@tugraz.at

This work is the result of a close collaboration between the groups of Oliver Werzer (Institute of Pharmaceutical Sciences, Department of Pharmaceutical Technology, University of Graz) and Roland Resel (Institute of Solid State Physics, Graz University of Technology) and describes the software package GIDVis, which can be used for data evaluation of (rotating) GIXD measurements. As an example, epitaxial relationships of the organic semiconductor P2O on Au(111) are determined. GIXD measurements were performed by Benedikt Schrode and Oliver Werzer. Data evaluation was performed by Benedikt Schrode, data interpretation by Benedikt Schrode together with Oliver Werzer and Roland Resel. Benedikt Schrode, Stefan Pachmajer and Christian Röthel are the main code contributors to GIDVis. Sample preparation was performed by Benedikt Schrode together with Jari Domke, supervised by Torsten Fritz. Michael Dohr advised on existing data evaluation software. The manuscript was prepared by Benedikt Schrode, Roland Resel and Oliver Werzer, with contributions on sample preparation by Jari Domke and Torsten Fritz. All authors were proof-reading the manuscript.

4 Results

The following article is reprinted from its original source with permission:

B. Schrode, S. Pachmajer, M. Dohr, C. Röthel, J. Domke, T. Fritz, R. Resel, and O. Werzer. *GIDVis: A Comprehensive Software Tool for Geometry-Independent Grazing-Incidence X-ray Diffraction Data Analysis and Pole-Figure Calculations*. *Journal of Applied Crystallography* 52.3 (June 2019), pages 683–689. ISSN: 1600-5767. DOI: 10.1107/S1600576719004485

The article is available at <https://doi.org/10.1107/S1600576719004485>.



***GIDVis*: a comprehensive software tool for geometry-independent grazing-incidence X-ray diffraction data analysis and pole-figure calculations**

Benedikt Schrode, Stefan Pachmajer, Michael Dohr, Christian Röthel, Jari Domke, Torsten Fritz, Roland Resel and Oliver Werzer

J. Appl. Cryst. (2019). **52**, 683–689



IUCr Journals

CRYSTALLOGRAPHY JOURNALS ONLINE

This open-access article is distributed under the terms of the Creative Commons Attribution Licence <http://creativecommons.org/licenses/by/4.0/legalcode>, which permits unrestricted use, distribution, and reproduction in any medium, provided the original authors and source are cited.





GIDVis: a comprehensive software tool for geometry-independent grazing-incidence X-ray diffraction data analysis and pole-figure calculations

Benedikt Schrode,^{a*} Stefan Pachmajer,^a Michael Dohr,^a Christian Röthel,^b Jari Domke,^c Torsten Fritz,^c Roland Resel^a and Oliver Werzer^b

Received 15 January 2019

Accepted 2 April 2019

Edited by A. Barty, DESY, Hamburg, Germany

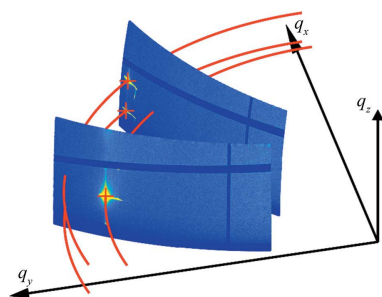
Keywords: grazing-incidence X-ray diffraction; thin films; pole figures; epitaxy; computer programs; *GIDVis*.

^aInstitute of Solid State Physics, Graz University of Technology, Petersgasse 16, Graz 8010, Austria, ^bInstitute of Pharmaceutical Sciences, Department of Pharmaceutical Technology, University of Graz, Universitätsplatz 1, Graz 8010, Austria, and ^cInstitute of Solid State Physics, Friedrich Schiller University Jena, Helmholtzweg 5, Jena 07743, Germany.
*Correspondence e-mail: b.schrode@tugraz.at

GIDVis is a software package based on MATLAB specialized for, but not limited to, the visualization and analysis of grazing-incidence thin-film X-ray diffraction data obtained during sample rotation around the surface normal. *GIDVis* allows the user to perform detector calibration, data stitching, intensity corrections, standard data evaluation (*e.g.* cuts and integrations along specific reciprocal-space directions), crystal phase analysis *etc.* To take full advantage of the measured data in the case of sample rotation, pole figures can easily be calculated from the experimental data for any value of the scattering angle covered. As an example, *GIDVis* is applied to phase analysis and the evaluation of the epitaxial alignment of pentacenequinone crystallites on a single-crystalline Au(111) surface.

1. Introduction

The experimental method of grazing-incidence X-ray diffraction (GIXD) has achieved huge success in the characterization of thin films and surfaces (Robinson & Tweet, 1992). The possibility of choosing an incidence angle for the primary beam close to the critical angle of total external reflection provides a number of advantages for thin-film characterization: the penetration depth into the sample system can be adjusted and the scattered intensity from the sample is enhanced considerably (Als-Nielsen & McMorrow, 2011). Several possibilities for the collection of GIXD data from films have to be considered, which are related to the texture of the crystallites within the sample (see Fig. 1). For fibre texture of crystallites or samples with random in-plane orientation of the crystallites (often found in organic thin films deposited on isotropic surfaces), GIXD studies are typically performed on static samples, *i.e.* without changing the azimuth of the sample. In these cases, the reciprocal information is distributed along rings [Fig. 1(a)]. One measurement at a single sample orientation, representing a cut through reciprocal space, is thus sufficient to gain access to the diffraction data for full sample analysis. However, there are several situations where the distribution of reciprocal-lattice points is not constant along rings in reciprocal space. Such cases are present in samples with large individual crystals hosted at surfaces, thus resulting in poor statistics [Fig. 1(b)], or epitaxially grown crystallites with a defined in-plane alignment (Haber *et al.*, 2005; Otto *et al.*, 2018) [Fig. 1(c)]. For both cases, the combination of a



OPEN ACCESS

GIXD experiment with rotation of the sample is required to collect all necessary information for phase and/or texture analysis (Röthel *et al.*, 2015, 2017). Moreover, sample rotation opens new possibilities for characterization methods that are inaccessible in a simple static experiment, like the determination of in-plane mosaicity.

There are various possibilities for rotating GIXD measurements, *i.e.* several different diffraction geometries are available (*e.g.* 2 + 2, z axis, κ geometry *etc.*; Moser, 2012; Kriegner *et al.*, 2013), allowing the measurement of diffraction data with respect to the sample surface. Irrespective of the experimental setup, the sample needs to be aligned with the incident X-ray beam. First, the sample requires precise spatial alignment (xy for the sample at the goniometer centre, and z for its height) as only this ensures that the centre of rotation is in the sample surface over the course of the experiments. Then the incident angle is set, typically in the range of the critical

angle α_c (the angle below which total external reflection occurs) up to few degrees. Higher incident angles allow for a reduction in the beam footprint on the sample surface, which is crucial in terms of in-plane smearing and q_z resolution when using two-dimensional detectors [$q = (4\pi/\lambda)\sin\theta$, where θ is half the scattering angle and λ is the wavelength of the incident radiation].

After the alignment process, the scattering information for the first azimuthal position is collected, followed by sample rotation around the surface normal and another image being taken [*cf.* Fig. 1(*d*)]. This is repeated until the entire upper hemisphere ($\Phi = 0\text{--}360^\circ$) is mapped. It should be noted that the incident angle has to be the same for each sample position. Considering the different geometries, this is achievable either by a complex and time-consuming adjustment of various moveable parts (goniometer and motor positions) at each point or by proper design of the sample movements, as for example offered by the κ or Eulerian geometry, which directly allow sample rotation around the surface normal. The data quality improves further if the intensity is collected continuously during azimuthal rotation as opposed to a stepped scan, so that information, even though smeared because of integration, is fully collected.

Diffracted intensities can be collected by various detectors. The current state of the art are solid-state area detectors which provide information on a large angular range together with fast data acquisition. The drawback here is that, owing to construction limitations, blind areas exist on the detector. These can be readily accepted for experiments with sufficient redundant data, but otherwise additional measurements need to be taken. Hereby the detector is moved by a certain amount by the goniometer or laterally, so that the blind areas point towards other areas of reciprocal space. From these additional measurements, (larger) images containing all of the diffraction information can be obtained.

To extract reliable information from the experimental data, several data processing and evaluation steps are required. There are a number of helpful software packages which assist in the visualization and analysis of (grazing-incidence) X-ray diffraction or small-angle X-ray scattering [(GI)SAXS] data (Benecke *et al.*, 2014; Breiby *et al.*, 2008; Hammersley, 2016; Jiang, 2015; Lazzari, 2002). There is also a specific solution for data extraction from three-dimensional reciprocal-space maps (Roobol *et al.*, 2015), *e.g.* collected by GIXD from rotating samples (Mocuta *et al.*, 2013).

Although software packages specializing in SAXS [*e.g.* *DPDAK* (Benecke *et al.*, 2014) and *GIXSGUI* (Jiang, 2015)] can typically be used for GIXD data visualization and reduction, analysis of diffraction data requires other features typically not available in SAXS software, *e.g.* calculation of expected peak positions and intensities from a known crystal structure, support for detectors mounted on goniometer arms, and subsequent data stitching or, in the case of textured samples, the extraction of pole figures.

Here we present the software *GIDVis*, which is a comprehensive tool for the data analysis of GIXD data of static or rotating samples, incorporating many aspects of other tools

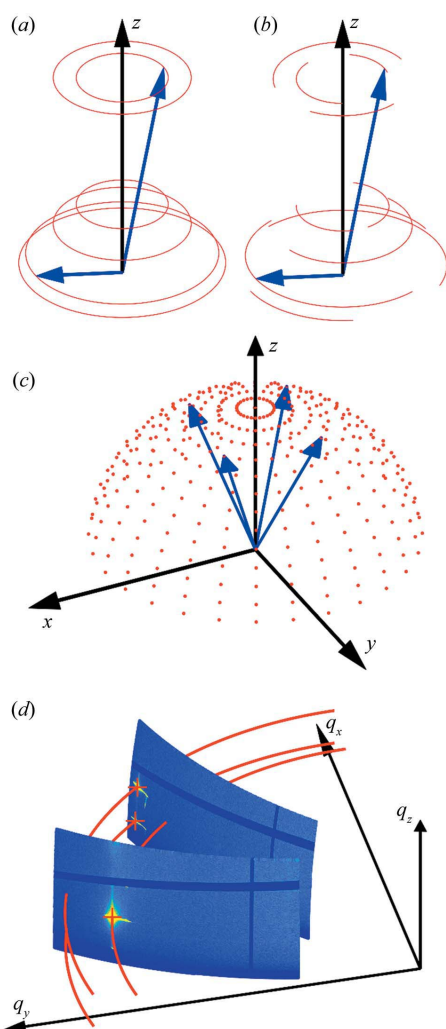


Figure 1

The distribution of reciprocal-lattice points (red) for samples with fibre-textured crystallites, (*a*) with the z axis as the rotation axis, (*b*) for samples with fibre texture combined with a partial in-plane texture, and (*c*) for azimuthally oriented crystallites. Blue arrows are selected reciprocal-lattice vectors. (*d*) Two cuts through reciprocal space by two GIXD measurements taken at different sample azimuths.

within one program, and adding additional and easy-to-use features for the evaluation of rotating GIXD data. The software is capable of dealing with all kinds of data, including linear and area-detector data from static detectors or detectors mounted on goniometer arms. It allows the user to perform all basic data handling like summation or stitching of data from different detector positions and contains a full set of tools to perform an evaluation of crystallographic properties.

2. Experimental procedure and data transformation

GIDVis uses various details from the experimental setup, including angles, distances, wavelength and the pixel size of the detector, to convert the diffraction data from the pixel space of the detector into reciprocal space. A summary of the required experimental parameters is provided in Fig. 2. The detector is described by *detlenx* times *detlenz* pixels of size *psx* and *psz*. Their positions are defined by the goniometer angles δ and γ and the sample-to-detector distance *sdd*. Any non-orthogonality of the detector relative to the primary beam for $\delta = \gamma = 0^\circ$ is described by the rotations *rx*, *ry* and *rz*. The sample position is set by the angular movements ω , χ and Φ . Additionally, the wavelength and the centre pixel position *cpz*/*cpz*, *i.e.* the pixel position of the direct beam, must be known. From these parameters one can directly calculate all necessary transformations so that finally the diffraction information is present in reciprocal-space coordinates. This has the advantage that measurements from other experimental stations or experimental setups are directly comparable without requiring knowledge about the specific setup. While such a procedure is directly accessible, inaccuracies in the angles or distances used have a large influence on the correctness and quality of the reciprocal data. Therefore, it is best practice to perform an additional detector calibration measurement beforehand.

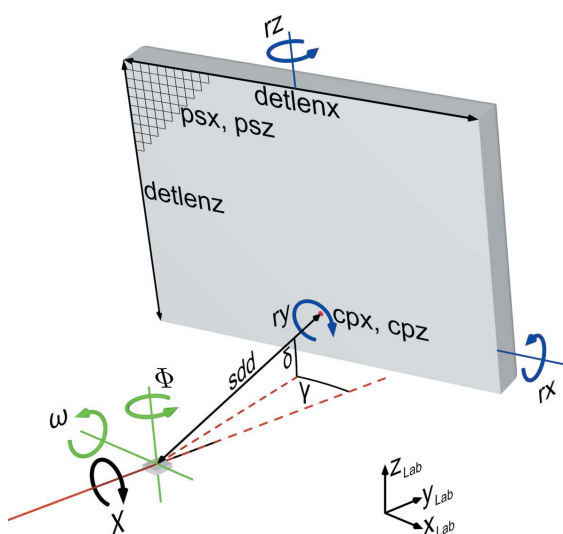


Figure 2
A typical measurement setup using an area detector mounted on a goniometer arm. The coordinate system describes the directions of the laboratory system. Rotations within the detector coordinate system are indicated in blue, rotations within the sample coordinate system in green, and rotations in the laboratory system in black.

Here, *GIDVis* provides the possibility of extracting the necessary parameters using standards like lanthanum hexaboride (LaB₆; Black *et al.*, 2010), silver behenate (Huang *et al.*, 1993), silicon standards (Black *et al.*, 2010) or custom calibrants. Based on these data, the transformation to reciprocal space is quite precise.

3. Pole-figure calculation

For some types of sample, the angle Φ is of no particular interest, so that information along q_x and q_y is merged into $q_{xy} = (q_x^2 + q_y^2)^{1/2}$, *i.e.* the component of the scattering vector parallel to the sample surface. This also means that information on the azimuth is lost. By including information from the angle Φ , reciprocal-space information in all directions, *i.e.* q_x , q_y and q_z , can be determined. Fig. 3 shows an example of the scattering vector \mathbf{q} in the sample coordinate system. The scattering vector can be separated into its in-plane component q_{xy} and the out-of-plane component q_z . The inclination of \mathbf{q} with respect to the z axis is described by the angle Ψ , ranging from 0 to 90° , and the angle Φ is defined as the angle between the in-plane component of the scattering vector q_{xy} and the x axis, going from 0 to 360° . So instead of using q_{xy} and q_z , the direction of the scattering vector is defined by the two angles Ψ and Φ (Alexander, 1979). Following the described definitions, they can be determined by

$$\tan \Psi = \frac{q_{xy}}{q_z} \quad \text{and} \quad \tan \Phi = \frac{q_y}{q_x}. \quad (1)$$

In a pole figure, the spatial distribution of the pole directions of certain net planes (defined by a distinct q value or a q range with a certain width) is plotted in a single polar plot with the radius being Ψ and the azimuthal part Φ (*cf.* Fig. 3, inset) and the measured intensity is colour coded. For practical reasons, a stereographic projection is chosen for visualization. In *GIDVis*, pole figures can be calculated from the experimental GIXD patterns and visualized directly. The data can also be converted for analysis with other software (Salzmann

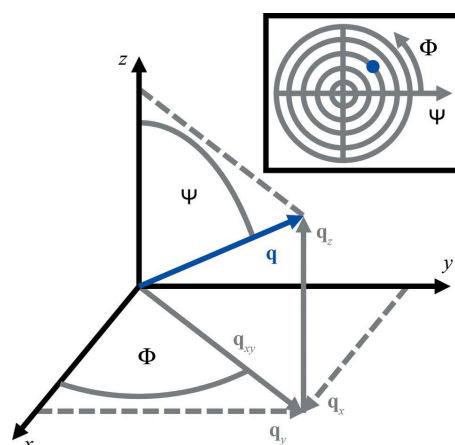


Figure 3
The angular relationships in the sample coordinate system used by the pole-figure calculation, and (inset) the approximate position of the plotted scattering vector \mathbf{q} in the pole figure.

& Resel, 2004) to determine the epitaxial relationship between the adsorbate and substrate and to obtain the orientation distribution function (ODF) (Alexander, 1979; Suwas & Ray, 2014).

4. Workflow

Fig. 4 shows a typical workflow employed in *GIDVis*. Starting from measurements of a polycrystalline powder calibrant with a well known interplanar spacing, the experimental parameters are extracted by comparison of the expected and actual measured peak positions [Fig. 4(a)]. The obtained calibration parameters are stored and can easily be applied to any other two-dimensional diffraction pattern recorded using the same setup to calculate the reciprocal-space or polar representation.

The detector gaps due to the construction restrictions of the detector leave some inaccessible areas which might cause problems. Having the possibility of recording diffraction images at different detector locations, using either a goniometer arm or a simple detector translation, the software is capable of using several data sets to generate a single merged data set without detector gaps and covering a larger volume of reciprocal space [Fig. 4(b)].

For a sample of poor statistics or high in-plane order, an experiment using a 360° azimuthal rotation is best. For some samples, it might be sufficient to collect all information

obtained during the rotation within a single image. However, if several images at distinct azimuths are recorded, *GIDVis* allows the user to combine the full diffraction information in one image afterwards by summing, averaging and extracting the maximum intensity of each pixel during the rotation. This provides a convenient way of reducing the data for an initial texture and polymorph phase analysis. Additionally, pole figures can easily be calculated, which takes full advantage of collecting data for the entire upper hemisphere [Fig. 4(c)].

Independently of the input data type – static, azimuthal sample rotations, different detector positions (including merged/stitched images) – several data evaluation routines, *e.g.* cuts and integrations along specific reciprocal-space directions, crystal phase analysis, intensity corrections, fitting of peak positions, transformation to powder-like patterns *etc.*, are available. Moreover, *GIDVis* can easily be used directly during measurements, *e.g.* to support sample alignment by extraction of height scans and rocking curves from two-dimensional intensity data, which can be directly evaluated further for the correct sample position, similar to what is done with a point detector. Because of the real-time data conversion to reciprocal space, *GIDVis* can also be used to monitor the measurement results, *e.g.* to make decisions on the optimum incident angle.

GIDVis is engineered using a very modular structure, allowing many different tasks to be carried out directly within a single program (automatic intensity extraction, structure data comparison or even a rudimentary structure viewer). For further demands, the modular structure means that *GIDVis* is highly adaptable and, more importantly, can be extended to even more specific needs. Interfaces to indexing routines using the diffraction pattern calculator (*DPC*; Hailey *et al.*, 2014) or *CRYSFIRE* (Shirley, 2006) might be easily generated, as well as comparisons with literature structure data (*e.g.* automatic structure searches). The model-fitting routines employing Gaussian fits implemented in *GIDVis* might be expanded using models suitable for SAXS and GISAXS (Hexemer & Müller-Buschbaum, 2015; Schwartzkopf & Roth, 2016). Other expansions could make corrections for multiple scattering effects in GIXD data available (Resel *et al.*, 2016) or handle dynamic diffraction effects in general to obtain more accurate peak intensity values and positions, as usually performed via the distorted-wave Born approximation (DWBA) (Dailliant & Alba, 2000; Lazzari, 2009).

5. Example: pentacenequinone on Au(111)

To demonstrate the advantage of using rotating GIXD and *GIDVis* we provide the example of measurements of epitaxially grown pentacenequinone (P2O) on an Au(111) single-crystalline surface. P2O (pentacenequinone, or pentacene-6,13-dione, $C_{22}H_{12}O_2$, CAS number 3029-32-1) is an organic semiconductor and is already known to exhibit several polymorphic phases (Simbrunner *et al.*, 2018; Salzmann *et al.*, 2011; Nam *et al.*, 2010; Dzyabchenko *et al.*, 1979).

Prior to deposition of the molecule, the substrate surface was cleaned by repeated cycles of Ar^+ sputtering with an

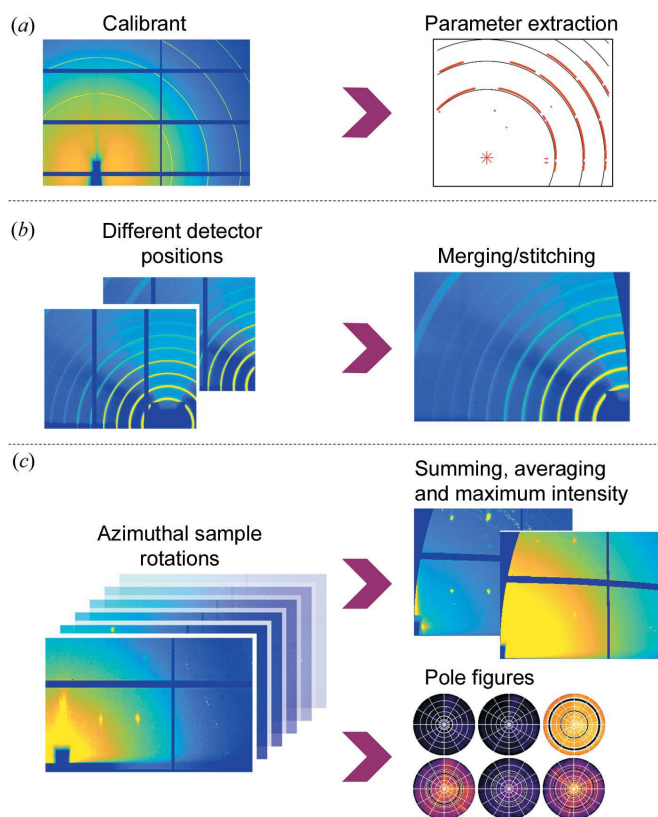


Figure 4

A schematic diagram of the data processing in *GIDVis*. (a) Starting from a standard measurement and calibration parameter extraction from it, the data (b) can be stitched/merged if necessary and (c) can be transformed to reciprocal space independently of the input and visualized in a variety of ways.

energy of 600 eV and thermal annealing at 773 K. The molecular film was then deposited from an effusion cell at a constant temperature of 463 K under ultra-high-vacuum conditions (base pressure 10^{-10} mbar = 10^{-8} Pa) directly onto the substrate held at room temperature. The film thickness was monitored *in situ* using optical differential reflectance spectroscopy (Forker & Fritz, 2009) and was calculated to be ten (not necessarily full and densely packed) layers.

After sample transfer to ambient conditions, the sample was investigated on the XRD1 beamline at the Elettra Synchrotron, Trieste, Italy, using a wavelength of 1.40 Å and a Pilatus 2M detector approximately 200 mm away from the sample. After setup calibration using an LaB₆ standard, sample alignment was performed using rocking curves, height scans and translation scans (x and y) to locate the midpoint of the substrate surface in the centre of rotation for all relevant movements required during rotating GIXD data collection. For all these scans, *GIDVis* was used for fast extraction of two-dimensional scans from sets of two-dimensional images and subsequent evaluation. For the rotating GIXD measurements the incident angle was set to 0.4° , which corresponds to around 80% of the critical angle of gold at this wavelength (Henke *et al.*, 1993). Using an exposure time of 10 s per image, 180 single images with a Φ step size (azimuthal rotation) of 2° were collected, so that information from a full 360° sample rotation was obtained. Diffraction data were recorded continuously, which means that even for very narrow peaks the intensity was still collected.

In the first step after the data collection, these data were transferred to reciprocal space. Inspection of individual images revealed that the single images do not look identical (data not shown). From this initial information it can be directly concluded that there is some in-plane texture, as expected for an epitaxially grown film.

In the next step, one can sum the intensities of all images pixel by pixel to construct an integrated image [Fig. 5(a)]. Such data then allow the identification of the contact plane, *i.e.* the crystallographic plane parallel to the substrate surface, and the polymorphic phase. A comparison of the measured peak positions with the expected positions from literature crystal structure solutions reveals the presence of the crystal phase reported by Dzyabchenko *et al.* (1979) with a (140) contact plane. *GIDVis* can directly plot the expected peak positions (centres of the rings) together with the squared absolute values of the structure factors (proportional to the areas of the rings) (*cf.* Fig. 5). Note that the measured intensity is corrected in terms of geometric factors, *i.e.* Lorentz and polarization factor, solid angle, pixel distance and detector efficiency corrections are applied. Using *GIDVis*, extracting the intensities by fitting a two-dimensional Gaussian function with a background plane is easily done and allows us to compare the measured intensity with the available structure solution using other representations [*cf.* Fig. 5(b)]. The intensities of most of the peaks are reproduced with good agreement, except for the $1\bar{1}1$, 111 , 011 and $1\bar{2}0$ peaks where no intensity could be extracted, *i.e.* the fit did not return a result. Note that the expected intensities of these peaks are very small.

To study the in-plane alignment of the crystallites in more detail, pole figures can easily be generated within *GIDVis*. Here, there are some advantages of the described approach compared with laboratory-based pole-figure investigations. The first is the greatly reduced measurement time, which is here about 30 min for a large range of q values compared with at least 15 h for a single q value using in-house texture goniometers. From 180 GIXD measurements of a 360° sample rotation, pole figures can be obtained for any value of the scattering angle covered in the images by extracting it from the present data set. This limitation is often reflected in the fact that reciprocal-space mapping, although a very powerful technique, is in fact rarely done in the home laboratory (Resel *et al.*, 2007), and usually epitaxy is tested for known phases only. The use of synchrotron radiation and the approach we implement makes the calculation of pole figures and their inspection for materials of unknown crystal structure reasonable and thus possible. Because of the geometry chosen in GIXD, even pole figures with very low q values can be calculated, which are often hard to access with classical texture goniometers owing to the strong background of the primary beam. Besides these advantages, elimination of the blind areas of the area detector would require three measurements with slightly different detector positions. Yet, as the information is often redundant because of higher-order reflections or scattering into another quadrant of a large detector, this is of minor importance for this kind of experiment. A real limitation of the GIXD geometry is its inherent insufficiency for

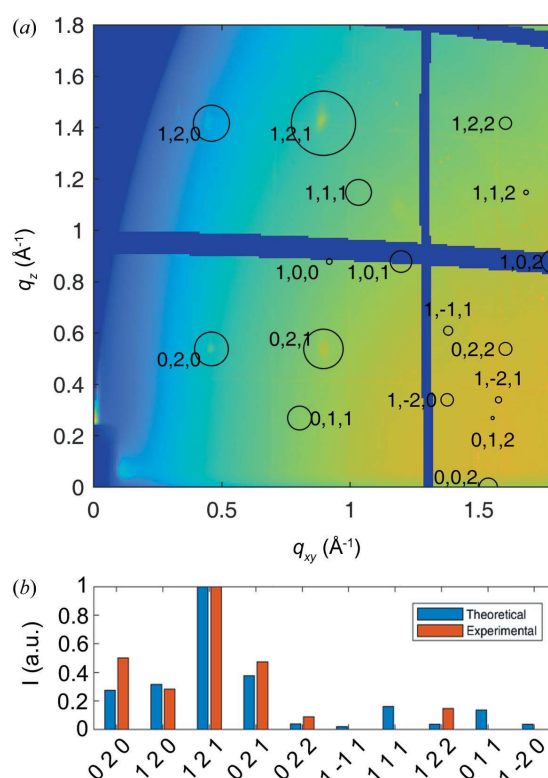


Figure 5
(a) The summation of intensity from all 360° azimuthal directions, and (b) a comparison of the expected and measured intensities.

measuring close to the specular direction (*i.e.* low q_x and q_y and thus q_{xy} values) due to the external reflection of the beam. Here, classical pole-figure geometries (*e.g.* Eulerian cradles) would be required, but at the expense of lacking the advantages of GIXD measurements.

Fig. 6 shows several pole figures calculated from the rotating GIXD experiment, allowing the determination of the in-plane orientation of the P2O crystallites with respect to the single-crystalline Au(111) substrate. For detailed analysis, the pole figures were exported from *GIDVis* as .rwa files and analysed using the standalone software *Stereopole* (Salzmann & Resel, 2004). Missing data points due to detector gaps are present as white concentric circles in Figs. 6(c)–6(f). For several of the

pole figures, six areas of high intensity (enhanced pole densities, EPD) are found [Figs. 6(a), 6(c) and 6(f)], while there is also one with only three [Fig. 6(g)]. The others show even more EPD within a single pole figure [Fig. 6(b), 6(d) and 6(e)]. Using the information gained from the integral measurements, we already know that the EPD can be explained by the P2O bulk crystal structure in a (140) orientation. Together with the sixfold gold surface symmetry, all of the observed peaks can be explained. Note that both the reciprocal-space map and the pole figures could also be explained with the crystallographic equivalent orientation ($\bar{1}40$).

A pole figure of the single-crystalline Au(111) substrate allows the determination of the symmetry directions of the gold surface [*cf.* Fig. 6(g)]. These crystallographic directions are indicated by arrows in an orientation image [Fig. 6(h)]. Using the same approach for the organic layers and comparing the results with those of gold shows that the main axis in plane, *i.e.* [001], is aligned along the gold $[\bar{1}10]$ axis. To summarize, the following relationships between the substrate and the organic layer are found: $(111)_{\text{Au}} \parallel \pm(140)_{\text{P2O}}$ and $(\bar{1}10)_{\text{Au}} \parallel (001)_{\text{P2O}}$.

6. Availability

GIDVis is based on MATLAB and released under the terms of the GNU General Public Licence, either version 3 of the licence or any later version. It can be obtained at <https://www.if.tugraz.at/amd/GIDVis/> free of charge. Two download options are provided. (i) For users without MATLAB, executable files for Windows and Linux are provided. To run, they require the MATLAB runtime, which can be downloaded from The Mathworks Inc. (<https://mathworks.com/products/compiler/matlab-runtime.html>) free of charge. (ii) The *GIDVis* source code is also provided in our online repository, allowing users to adapt the program to their needs (requires MATLAB).

Extended tutorials, additional help and the theoretical background of the algorithms implemented can be found in a separate documentation file that can also be downloaded from the web page mentioned above.

Acknowledgements

We acknowledge the Elettra Synchrotron Trieste for beam-time allocation and thank Luisa Barba and Nicola Demitri for assistance in using beamline XRD1. We acknowledge the European Synchrotron Radiation Facility for provision of synchrotron radiation facilities and we would like to thank Oleg Kononov and Andrey Chumakov for assistance in using beamline ID10.

Funding information

The following funding is acknowledged: Austrian Science Fund (project No. P30222); Bundesministerium für Bildung und Forschung (project No. 03VNE1052C).

References

Alexander, L. E. (1979). *X-ray Diffraction Methods in Polymer Science*. Huntington: Krieger.

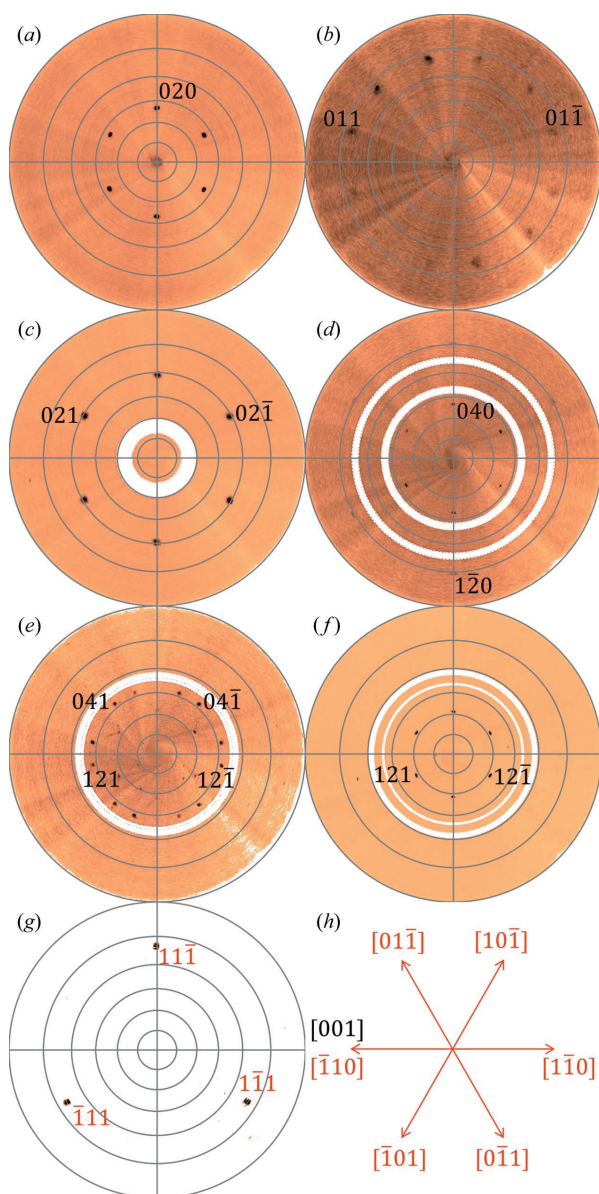


Figure 6
(a)–(g) A series of relevant pole figures at distinct q values, indexed with the bulk crystal structure of pentacenequinone in (140) orientation (black) and gold in (111) orientation (red). (h) The crystal directions in real space of the substrate (red) and the organic overlayer (black).

- Als-Nielsen, J. & McMorrow, D. (2011). *Elements of Modern X-ray Physics*. Hoboken: Wiley.
- Benecke, G., Wagermaier, W., Li, C., Schwartzkopf, M., Flucke, G., Hoerth, R., Zizak, I., Burghammer, M., Metwalli, E., Müller-Buschbaum, P., Trebbin, M., Förster, S., Paris, O., Roth, S. V. & Fratzl, P. (2014). *J. Appl. Cryst.* **47**, 1797–1803.
- Black, D. R., Windover, D., Henins, A., Filliben, J. & Cline, J. P. (2010). *Advances in X-ray Analysis*, Vol. 54, pp. 140–148. Heidelberg: Springer.
- Black, D. R., Windover, D., Henins, A., Gil, D., Filliben, J. & Cline, J. P. (2010). *Powder Diffr.* **25**, 187–190.
- Breiby, D. W., Bunk, O., Andreasen, J. W., Lemke, H. T. & Nielsen, M. M. (2008). *J. Appl. Cryst.* **41**, 262–271.
- Daillant, J. & Alba, M. (2000). *Rep. Prog. Phys.* **63**, 1725–1777.
- Dzyabchenko, A. V., Zavodnik, V. E. & Belsky, V. K. (1979). *Acta Cryst.* **B35**, 2250–2253.
- Forker, R. & Fritz, T. (2009). *Phys. Chem. Chem. Phys.* **11**, 2142–2155.
- Haber, T., Andreev, A., Thierry, A., Sitter, H., Oehzelt, M. & Resel, R. (2005). *J. Cryst. Growth*, **284**, 209–220.
- Hailey, A. K., Hiszpanski, A. M., Smilgies, D.-M. & Loo, Y.-L. (2014). *J. Appl. Cryst.* **47**, 2090–2099.
- Hammersley, A. P. (2016). *J. Appl. Cryst.* **49**, 646–652.
- Henke, B. L., Gullikson, E. M. & Davis, J. C. (1993). *At. Data Nucl. Data Tables*, **54**, 181–342.
- Hexemer, A. & Müller-Buschbaum, P. (2015). *IUCrJ*, **2**, 106–125.
- Huang, T. C., Toraya, H., Blanton, T. N. & Wu, Y. (1993). *J. Appl. Cryst.* **26**, 180–184.
- Jiang, Z. (2015). *J. Appl. Cryst.* **48**, 917–926.
- Kriegner, D., Wintersberger, E. & Stangl, J. (2013). *J. Appl. Cryst.* **46**, 1162–1170.
- Lazzari, R. (2002). *J. Appl. Cryst.* **35**, 406–421.
- Lazzari, R. (2009). *X-ray and Neutron Reflectivity*, Vol. 770, edited by J. Daillant & A. Gibaud, pp. 283–342. Berlin, Heidelberg: Springer.
- Mocuta, C., Richard, M.-I., Fouet, J., Stanescu, S., Barbier, A., Guichet, C., Thomas, O., Hustache, S., Zozulya, A. V. & Thiaudière, D. (2013). *J. Appl. Cryst.* **46**, 1842–1853.
- Moser, A. (2012). PhD thesis, Graz University of Technology, Austria.
- Nam, H.-J., Kim, Y.-J. & Jung, D.-Y. (2010). *Bull. Korean Chem. Soc.* **31**, 2413–2415.
- Otto, F., Huempfer, T., Schaal, M., Udhardt, C., Vorbrink, L., Schroeter, B., Forker, R. & Fritz, T. (2018). *J. Phys. Chem. C*, **122**, 8348–8355.
- Resel, R., Bainschab, M., Pichler, A., Dingemans, T., Simbrunner, C., Stangl, J. & Salzmänn, I. (2016). *J. Synchrotron Rad.* **23**, 729–734.
- Resel, R., Lengyel, O., Haber, T., Werzer, O., Hardeman, W., de Leeuw, D. M. & Wondergem, H. J. (2007). *J. Appl. Cryst.* **40**, 580–582.
- Robinson, I. K. & Tweet, D. J. (1992). *Rep. Prog. Phys.* **55**, 599–651.
- Roobol, S., Onderwaater, W., Drnec, J., Felici, R. & Frenken, J. (2015). *J. Appl. Cryst.* **48**, 1324–1329.
- Röthel, C., Radziown, M., Resel, R., Grois, A., Simbrunner, C. & Werzer, O. (2017). *CrystEngComm*, **19**, 2936–2945.
- Röthel, C., Radziown, M., Resel, R., Zimmer, A., Simbrunner, C. & Werzer, O. (2015). *Cryst. Growth Des.* **15**, 4563–4570.
- Salzmänn, I., Nabok, D., Oehzelt, M., Duhm, S., Moser, A., Heimel, G., Puschnig, P., Ambrosch-Draxl, C., Rabe, J. P. & Koch, N. (2011). *Cryst. Growth Des.* **11**, 600–606.
- Salzmänn, I. & Resel, R. (2004). *J. Appl. Cryst.* **37**, 1029–1033.
- Schwartzkopf, M. & Roth, S. (2016). *Nanomaterials*, **6**, 239.
- Shirley, R. (2006). *The CRYSFIRE System for Automatic Powder Indexing*, <http://www.ccp14.ac.uk/tutorial/crys/>
- Simbrunner, J., Simbrunner, C., Schrode, B., Röthel, C., Bedoya-Martinez, N., Salzmänn, I. & Resel, R. (2018). *Acta Cryst.* **A74**, 373–387.
- Suwas, S. & Ray, R. K. (2014). *Crystallographic Texture of Materials*. London: Springer.

4.3 Solvent Vapor Annealing of Amorphous Carbamazepine Films for Fast Polymorph Screening and Dissolution Alteration


This is an open access article published under a Creative Commons Attribution (CC-BY) License, which permits unrestricted use, distribution and reproduction in any medium, provided the author and source are cited.



Article

<http://pubs.acs.org/journal/acsodf>

Solvent Vapor Annealing of Amorphous Carbamazepine Films for Fast Polymorph Screening and Dissolution Alteration

Benedikt Schrode,^{†,‡} Brigitta Bodak,[†] Hans Riegler,[†] Andreas Zimmer,[†] Paul Christian,[‡] and Oliver Werzer^{*,†} 

[†]Institute of Pharmaceutical Sciences, NAWI Graz, Department of Pharmaceutical Technology, University Graz, Universitätsplatz 1, 8010 Graz, Austria

[‡]Institute for Solid State Physics, NAWI Graz, Graz University of Technology, Petersgasse 16, 8010 Graz, Austria

This work shows a second important application of rotating GIXD, the phase analysis of a thin film with statistical problems, where not all diffraction information would be accessible within a static measurement. It could be shown that starting from an amorphous sample of the pharmaceutically relevant molecule carbamazepine (CBZ), solvent vapor annealing at different conditions resulted in different crystallographic phases. Furthermore, the dissolution behavior as an estimate for the bioavailability was studied. Benedikt Schrode and Oliver Werzer performed GIXD measurements. Benedikt Schrode performed data conversion, analysed their crystallographic phase and drew conclusions together with Oliver Werzer and Paul Christian. Brigitta Bodak performed dissolution measurements and interpreted the results. Hans Riegler, together with Oliver Werzer, prepared samples and performed optical microscopy. Paul Christian shared his expertise in crystallographic phase identification. Andreas Zimmer advised on pharmaceutical aspects of the work. The manuscript was prepared by Benedikt Schrode, Brigitta Bodak and Oliver Werzer. All authors were proof-reading the manuscript.

4 Results

The following article is reprinted from its original source with permission:

B. Schrode, B. Bodak, H. Riegler, A. Zimmer, P. Christian, and O. Werzer. Solvent Vapor Annealing of Amorphous Carbamazepine Films for Fast Polymorph Screening and Dissolution Alteration. *ACS Omega* 2.9 (Sept. 2017), pages 5582–5590. ISSN: 2470-1343, 2470-1343. DOI: 10.1021/acsomega.7b00783

The article is available at <https://pubs.acs.org/doi/10.1021/acsomega.7b00783>. Further requests for permissions related to the material should be directed to the ACS.



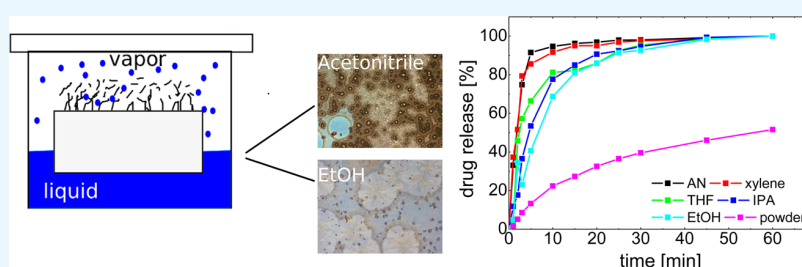
Solvent Vapor Annealing of Amorphous Carbamazepine Films for Fast Polymorph Screening and Dissolution Alteration

Benedikt Schrode,^{†,‡} Brigitta Bodak,[†] Hans Riegler,[†] Andreas Zimmer,[†] Paul Christian,[‡] and Oliver Werzer^{*,†,§}

[†]Institute of Pharmaceutical Sciences, NAWI Graz, Department of Pharmaceutical Technology, University Graz, Universitätsplatz 1, 8010 Graz, Austria

[‡]Institute for Solid State Physics, NAWI Graz, Graz University of Technology, Petersgasse 16, 8010 Graz, Austria

Supporting Information



ABSTRACT: Solubility enhancement and thus higher bioavailability are of great importance and a constant challenge in pharmaceutical research whereby polymorph screening and selection is one of the most important tasks. A very promising approach for polymorph screening is solvent vapor annealing where a sample is exposed to an atmosphere saturated with molecules of a specific chemical/solvent. In this work, amorphous carbamazepine thin films were prepared by spin coating, and the transformation into crystalline forms under exposure to solvent vapors was investigated. Employing grazing incidence X-ray diffraction, four distinct carbamazepine polymorphs, a solvate, and hydrates could be identified, while optical microscopy showed mainly spherulitic morphologies. *In vitro* dissolution experiments revealed different carbamazepine release from the various thin-film samples containing distinct polymorphic compositions: heat treatment of amorphous samples at 80 °C results in an immediate release; samples exposed to EtOH vapors show a drug release about 5 times slower than this immediate one; and all the others had intermediate release profiles. Noteworthy, even the sample of slowest release has a manifold faster release compared to a standard powder sample demonstrating the capabilities of thin-film preparation for faster drug release in general. Despite the small number of samples in this screening experiment, the results clearly show how solvent vapor annealing can assist in identifying potential polymorphs and allows for estimating their impact on properties like bioavailability.

INTRODUCTION

The search for polymorphic crystal forms is necessary to identify favorable properties for various fields.^{1–6} For active pharmaceutical ingredients (APIs), polymorphs should remain unchanged over the shelf-life time^{7,8} and be compatible with excipients and processes, and their production has to be very reproducible.⁹ As such, many screening experiments are applied to generate and discover new, potentially best suited and stable polymorphs.

Many different approaches exist which all aim at generating different processing pathways for finding new polymorphs. Bulk crystallization experiments employ seeding,¹⁰ different solvents,^{5,6,11} degree of saturation, and varying temperature, among others, to enable the production of new polymorphs which in other terms just represent the fact that the energy landscape is screened.¹² Even the usage of structure prediction methods is becoming more important as potential new polymorphs might be more easily accessible *in-silico* but with the prediction rate exhausting physical capabilities.^{2,12–14}

In recent years, optimization in thin-film technologies enables addition of new functionalities to surfaces which may assist in further stages or can even be used directly within application. As the simplest technique, the usage of the drop casting technique in terms of printing yields high quality deposition of inks for newspaper, organic electronic materials for solar cells,¹⁵ and transistors.¹⁶ Even personalized medication could become reality soon.^{17–21} Spin coating, dip coating, and vacuum deposition enable similar modifications to surfaces. Further, these deposition techniques are capable of adjusting the polymorphic form as well as the morphology; e.g., three different polymorphs of DH6T can be obtained by process parameter variation.²² Phenytoin can be processed so that at least nine different morphologies can be set without changing the polymorph,²³ and even new polymorphs were found by

Received: June 13, 2017

Accepted: August 24, 2017

Published: September 7, 2017

applying such thin-film techniques.^{24–26} The dissolution studies on the new phenytoin polymorph even showed to be of faster nature compared to the other form which again demonstrates the importance of polymorph screening in pharmaceutical research in general.

Very often, solution processing of drug molecules enables achieving homogeneous thin films at a solid substrate surface. Depending on the processing conditions the films might be crystalline or amorphous. Employing faster processing like present in spin coating, amorphous phases frequently remain after solvent removal as found in samples of acetometaphene,⁸ clotrimazole,^{27–29} or phenytoin.^{24,26,30} Having such an amorphous film, crystallization routes distinct from standard bulk solution processes can be tested. For instance, mechanical stressing using atomic force microscopy³⁰ might be employed for understanding crystallization in more detail. Another more common approach is temperature treatment:²⁶ higher temperatures favor molecular diffusion, facilitating nucleation, and finally resulting in crystallization. In a similar manner, solvent vapor annealing (SVA) is an excellent tool for changing the environmental parameters for crystal growth processes.^{24,28,31} Here, a sample is exposed to a solvent vapor of any chemical composition, similar to isothermal calorimetry experiments employing defined humidity levels and dynamic vapor sorption experiments. In the vapor phase solvent molecules interact with the molecules in the drug film which eventually facilitates specific crystallization into a defined polymorphic form (or morphology). Hereby the solvent–vapor interaction strength might be estimated using the Hansen-solubility parameters.²⁸ Using such a solvent vapor annealing treatment, the second polymorphic form of phenytoin was also accessible, while up to recently this polymorph was just accessible using drop casting under very defined conditions (temperature and solute concentration). SVA on clotrimazole thin films was unable to generate new polymorphs,²⁸ but strong changes in the morphology/crystal habit could be obtained. Having a chance to change only the habit (size and shape) provides the possibility to understand its role in the overall dissolution performance, i.e., how different facets or surface areas change the release from thin films.

In this work, it is demonstrated how the solvent vapor process can be utilized to deliver information on a potentially better sample state with faster dissolution properties. As the model substance here, carbamazepine (CBZ) is used. In general, carbamazepine is an anticonvulsant used to treat epileptic seizures and nerve pain such as trigeminal neuralgia. CBZ is a Biopharmaceutics Classification System Class II molecule, possessing low solubility and high permeability. The poor dissolution performance has most likely the biggest influence on the bioavailability, driving the search for ideal formulations providing enhanced properties and finally resulting in a higher bioavailability. Deriving a better understanding for handling this problem might remain one target in research as many (~40%) new chemical entities identified in screening are prone to fail due to their low water solubility. As one of the best ways to improve this situation, polymorph screening studies are advised. A simple change in the molecular arrangement (each polymorph is distinct) hereby might strongly change the lattice free energy reflected in a better solubility.

CBZ is a wonderful material to study such effects in more detail as it is prototypical for drug molecules with its hydrogen bonding potential. Especially, the formation of multiple readily

accessible polymorphic forms³² makes it an interesting candidate for fundamental research, like structure prediction,^{33,34} the screening process in general, or for this work. Fast processing of CBZ results in amorphous films of sufficient stability so that different film treatments can be tested, inducing deviating polymorphic forms and morphologies. Using grazing incidence X-ray diffraction^{35,36} and optical microscopy the impacts of the various treatments on the solid state properties are elucidated and discussed. Dissolution experiments assist in the identification of candidates for possible applications of potentially high bioavailability.

RESULTS

Layer Thickness Dependent Morphology. Spin coating carbamazepine solutions onto silicon wafers initially results in the formation of dry, homogeneous, and optically transparent layers which are amorphous. Upon storage at ambient conditions, such samples crystallize eventually. The initial CBZ concentration in solution has thereby a profound impact on the initial layer thickness. At the highest concentration employed in this study (16 mg/g), a film thickness of 157 nm was determined by X-ray reflectivity (data not shown). Halving the concentration value, so that a solution of 8 mg/g is used, the thickness reduces to 74 nm. Diluting the solution further the thickness reduces, whereby a minimum layer thickness of 3 nm was obtained at a concentration of 0.5 mg/g. The different thicknesses reflect the fact that the amount of CBZ for the crystallization process is different in each sample. In Figure 1,

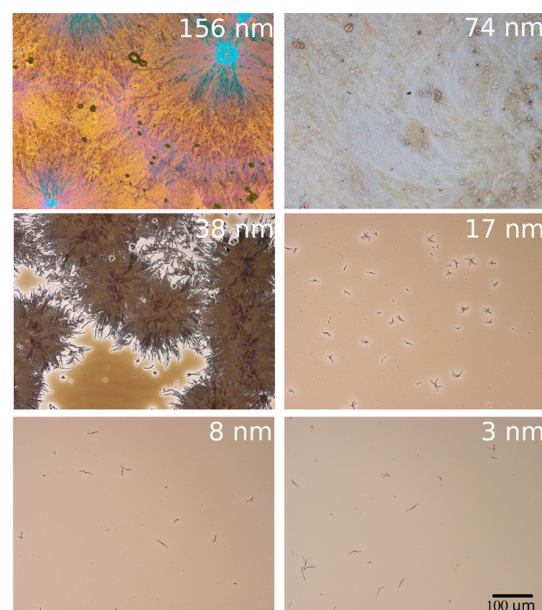


Figure 1. Optical micrographs of crystallized CBZ thin films as a function of the layer thickness obtained from different solute concentration after storage under ambient conditions.

optical micrographs of various samples 48 h after thin-film fabrication are depicted. For the lowest concentration, i.e., the thinnest film, few individual crystals randomly distributed at the silica surface are found. The needle-like shapes are about 100 μm long and are some micrometers wide. As the layer thickness increases to 8 nm, the spatial density of the needles increases, while leaving the size (almost) unaffected. In addition, a few smaller, dot-like structures appear, most likely of crystalline

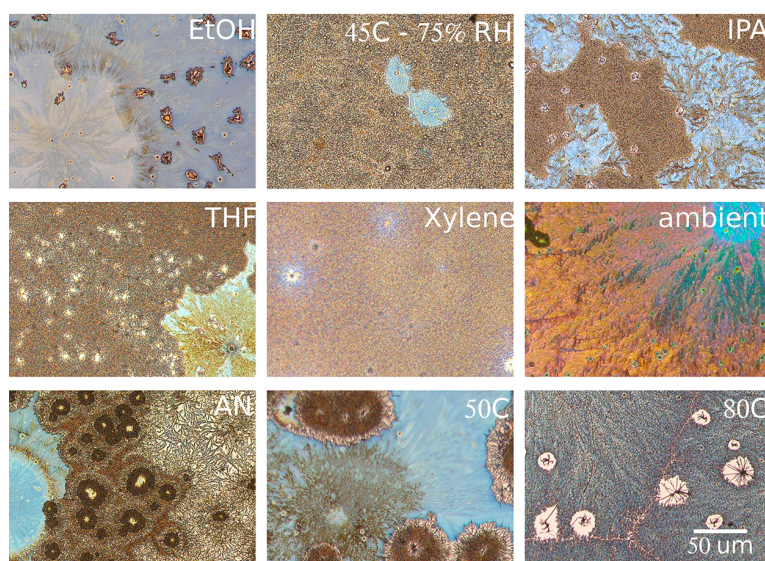


Figure 2. Various samples after heat treatment at different temperatures or being exposed to solvent vapor for 48 h. Sequence of images corresponds to their respective dissolution rate, ranging from lowest (top left) to highest (bottom right).

character. Reaching 17 nm, some interconnection with respect to each other exists, typical for the initial state of spherulitic growth. Here the crystals are accompanied by some vacant areas. While the film after deposition constitutes a homogeneous dense layer, nucleation and further crystal growth come at the expense of smaller crystallites, leaving these areas depleted. This is generally referred to as Ostwald ripening.³⁷ At 38 nm thickness, extended spherulitic structures with several hundreds of micrometer diameter emerge.

It takes an 8 mg/g CBZ–THF solution to achieve a thickness of 74 nm which can provide a crystalline layer covering the entire substrate surface. In this sample, the spherulitic character remains but shows significantly increased dimensions. Individual spherulite branches are absent as the individual branches pack densely. At 158 nm thickness, the most obvious difference is the change in color, which results from a change in the crystal thickness compared to the 74 nm sample. In the spherulite centers, the color is blueish, while in the other areas more orange/yellowish colors appear. Homogeneously spread, there are also some darker areas, which are likely the result of the dot-like structures noticed in thinner films being developed into more extended structures.

Solvent Vapor Annealing. For solvent vapor annealing and subsequent dissolution experiments, the thickest carbamazepine amorphous films were used (i.e., samples were prepared only from a 16 mg/g CBZ–THF solution). This way, a dense layer can (mostly) be maintained during solvent vapor treatment, and a larger carbamazepine fraction is available for diffraction and dissolution experiments. Depending on the treatment of the samples, drastic changes in the CBZ morphology occur. In Figure 2, optical micrographs of the various samples are summarized after their individual treatments. (For the sake of completeness the very same spots are also examined under crossed polarizers, and the data are provided in the Supporting Information section.) Hereby, the samples are ranked by their dissolution rate, starting from those of slowest release (EtOH vapor sample) to the highest, which is the sample only heat treated at 80 °C directly after sample preparation.

The different treatments of the samples results in the appearance of each sample being different, whereby similarities between individual samples exist. In all samples the crystalline CBZ coated the entire surface, and only in the sample just heat treated at 80 °C is the crystalline film disrupted; thus, some vacant areas exist. This sample shows clear spherulitic structures with distinct boundaries in between. In the disrupted area less densely packed spherulites exist. The xylene sample appears similarly homogeneous. A closer look under crossed polarizers weakly shows the presence of a Maltesian cross typical for spherulitic growth (see Supporting Information).

The sample treated at 45 °C and 75% RH as well as the samples exposed to IPA or THF vapor reveal two distinct types of spherulites, one appearing blueish in color and the other similar to the one observed in the xylene-treated sample and appears brownish. The sample exposed to EtOH vapor reveals the largest blueish spherulites of all samples investigated in this study, nearly covering the entire surface. Besides this, structures with an extension of even some micrometers are present. As these areas appear dark under crossed polarizers, they could be amorphous or consist of a crystal phase which is not birefringent. Similar structures also appear in most of the other samples but with their extension and frequency being smaller. The samples exposed to acetonitrile vapor or heat treated at 50 °C show brownish and blueish spherulites whereby the amount or frequency of these two structures seems to be vice versa.

Crystal Structure. In order to investigate the crystal structure/polymorphic form, grazing incidence X-ray diffraction (GIXD) measurements were performed. In such an experiment, the shallow incidence angle allows measuring diffraction from very thin films.^{35,36,38} An exemplary map is shown in Figure 3a for the sample after acetonitrile vapor annealing. Having an area detector, this allows identifying Debye–Scherrer type ring structures at different separations from the beam center (at around pixels $x = 764$, $y = 824$). In general, concentric rings in the pattern result from crystals behaving like a powder without preferred orientation (texture) whereby each ring corresponds to a defined net plane distance. (In GIXD measurements, the

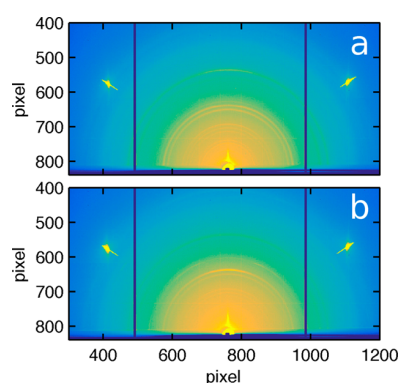


Figure 3. Grazing incidence X-ray diffraction maps of the carbamazepine film after solvent vapor annealing using acetonitrile (a) and another film treated at 50 °C (b). Both patterns share a common horizontal axis for clarity.

rings are disrupted in the lower half by the presence of the substrate so that only ring segments can be measured.) In all samples, the mostly powder-like character prevailed. Only in some samples a weak preferred orientation exist, which means that some crystal contact planes occur slightly more frequently along a certain direction than others. Figure 3b shows an example, which depicts the results of a sample heat treated at 50 °C. In the middle of the image, located at pixels $x = 764$ and $y = 640$, higher intensities are detected. In a GIXD image, this region corresponds to information from packing nearly parallel to the sample surface; i.e., the corresponding net plane is parallel to the substrate surface. The observed textures found for the individual samples are summarized in Table 1. The two

Table 1. Summary of the Samples, Their Polymorphic Forms, Identified Texture, and the Rate Parameter Determined from the Dissolution Profiles

sample	Form					texture	a (rate param. eq 1)
	I	II	III	IV	hydrate		
powder			X			none	0.02
EtOH				X	X	none	0.11
45 °C – 75% RH	X				X	002 (hyd)	0.13
IPA	X				X	none	0.14
THF		X				110 (II) solvate	0.21
xylene	X	X				none	0.42
ambient			X	X		510 (IV)	0.42
acetonitrile	X	X				none	0.44
50 °C	X					140 (I)	0.48
80 °C			X			none	1.86

sharp peaks in the pattern at pixels $x = 400$, $y = 580$ and $x = 1100$, $y = 580$, respectively, stem from the substrate; the silicon wafer is a 001 cut, making these peaks the 111 reflections diffracting into these very positions.

For the sake of polymorph identification, these 2-dimensional data are integrated to yield a representation of intensity as a function of the absolute scattering vector q (information on the scattering direction is lost, and only information on the d -spacing is extractable). Often this is referred to as a powder plot. These integrated diffraction curves are provided in Figure

4. Independent of the sample, all curves contain peaks showing that each preparation route induced crystallization in the films

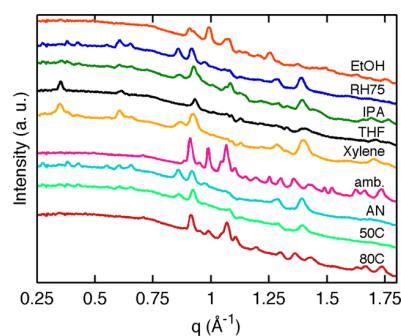


Figure 4. Powder plots extracted from the grazing incidence X-ray diffraction patterns. Data are shifted for clarity. Order of appearance compared to dissolution results and microscopy images.

which might already be expected from the microscopy images. At small scattering vectors the spectra contain a high diffraction background which reduces for larger scattering vectors. Such background behavior is due to air scattering from the primary beam, causing X-rays to bypass the beam stop. This behavior is identical for all samples and does not disturb the diffraction signal from the crystalline fraction of the samples, thus being of no further importance for the data analysis. On top of this background, distinct Bragg peaks are visible. From their position, the polymorphic form(s) of the respective sample is deduced by comparison with theoretical peak positions. The naming convention of the individual polymorphs here follows a previous report³² whereby the list of the individual unit-cell parameters is provided in the SI.

For example, using the example of the AN-treated sample of Figure 3a, the peak at $q = 0.35 \text{ Å}^{-1}$ (d spacing 17.95 Å) is explained by the 2–10 peak of CBZ form II. The peak at $q = 0.67 \text{ Å}^{-1}$ (d spacing 9.38 Å) results from the 0–12 reflection of the CBZ form I structure, whereas the peak at 0.62 Å^{-1} (d spacing 10.13 Å) is again explained by form II being the 300 reflection. This means this sample consists of two forms, i.e., forms I and II. In a similar fashion, the CBZ phases of the different samples are identified. The evaluations of all curves from Figure 4 are summarized in Table 1.

The results reveal that many of the samples consist of multiple polymorphs. Only heat treatment at higher temperature (50 and 80 °C) results in solely forms I–III being present. Form III is also found for the as-delivered powder, i.e., the polymorph which is provided by the supplier (see SI and Table 1). Further, the formation of solvates is noted on the exposure of EtOH or IPA or after storage at elevated humidity. Characteristic of carbamazepine form II are, in most cases, empty channels, in which, however, THF can be incorporated.^{39,40} In terms of lattice parameters, this structure is very similar to the standard form II, which is why they cannot be differentiated from the experimental data.

Dissolution. As an estimate for the bioavailability of CBZ from these different samples, dissolution studies were performed. For the sake of comparability, each sample was measured under identical conditions. Starting with the sample stored at 40 °C and high humidity of 75%, the release of CBZ over time increases as the time progresses (see blue curve in Figure 5a). After 10 min, nearly 75% of the material is released from the silica surface. Another 15 min is required, i.e., a total

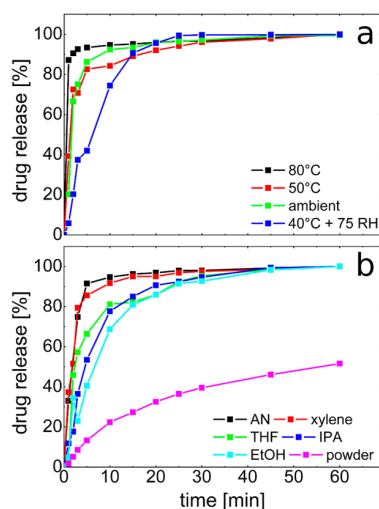


Figure 5. Carbamazepine release as a function of time for samples treated under the presence of only water (a) and under different organic solvent vapors (b). Both diagrams share a common abscissa.

time of 25 min, to dissolve all of the CBZ from the sample surface into the surrounding media. In comparison to that, storing the sample at ambient conditions or at an elevated temperature of 50 °C results in a quicker CBZ release so that already after 4 min about 75% of the entire drug amount is released. After this the ambient stored sample is slightly faster in its release, while the 50 °C one seems to have a reduced dissolution rate so that it takes around 30 min for the entire material to be dissolved. The sample heat treated at 80 °C releases most of the drug within 3 min, from which it can be assumed that this sample shows an immediate release.

Using different organic solvents for the vapor treatment, the dissolution profiles change. EtOH vapor-treated samples show rather slow drug release, taking about 10 min to release 70% and another 35 min (total 45 min) to achieve 100% release. By using IPA or THF for the SVA process the initial CBZ release can be increased, but for all of these samples the maximum is reached only after 30 min. It can be expected that 100% release is achieved slightly faster than for the EtOH sample, but the low amount of data points at this time frame does not allow clarification. Treating samples with xylene or AN results in very fast releases of nearly 90% in 5 min but still slower than the sample treated at 80 °C.

To gain numbers for comparison, a regression fit to the dissolution data was performed. A lot of different mathematical descriptions aim to provide some understanding of the dissolution behavior.⁴¹ As only one layer is at hand and also sink conditions are chosen, the situation is sufficiently described by a homogeneous model (often referred to as first-order release). The formula used for the evaluation is given by

$$C(t) = C_s(1 - e^{-at}) \quad (1)$$

whereby the concentration C as a function of time t is equal to the maximum concentration (C_s) minus an exponential decay over time with the exponent representing the fastness of drug release. For the evaluation of our samples, C_s is kept at 100% for all samples so that the only fitting parameter is a . The values for the various samples are tabulated in Table 1, ranging from 0.11 for the sample exposed to the EtOH vapor, representing a

slow dissolution, up to 1.86 for the sample heat treated at 80 °C which showed the fastest dissolution.

A dissolution experiment was also performed for the pristine CBZ powder as obtained from the supplier. Hereby, some of the powder was introduced into a vessel containing the same dissolution medium as used for the thin-film samples, and the increase in CBZ concentration over time was determined. Similar to the other samples, the amount of material released (dissolved) increased with progressing time. The drug release was about 5 times slower compared to the EtOH sample which was the sample with the slowest CBZ release from a thin-film surface after treatment. An X-ray diffraction experiment shows that the pristine powder sample obtained from the supplier was of pure form III (data provided in the SI).

DISCUSSION

CBZ possesses a rather complex phase behavior with a lot of different polymorphic forms resulting from sample preparation using varying experimental conditions. Within this study, the anhydrous forms I, II, III, and IV were found in different compositions. Indications of formation of form V were absent. Form V might be accessible from amorphous thin films of CBZ using different solvents, different temperatures, or combinations thereof or even a transformation from one of the other polymorphic phases. As the method used is very versatile, expanding these experiments is simple in order to explore additional forms.

Using experimental parameters that are easily accessible by tuning the temperature and the water content in the surrounding, our approach is directly adaptable for any manufacturing or drug formulation. In many areas, especially in pharmaceutical manufacturing, the usage of organic solvents should be limited or is even permitted. However, in an experiment, where harm to the environment or living organism can be prevented, such screening processes can be simply extended to more and/or even toxic solvents which might increase the chance of finding more (new) polymorphs or even leading to solvates. Following the procedures described in this work, only some of the amorphous films could be transferred into the crystalline state containing only a single polymorphic form. Likely, more optimization can provide monomorphic films. Recently it was demonstrated that SVA on crystalline samples can also induce changes of a crystalline polymorphic form, which might be associated with a solid–solid transition.³¹ A temperature treatment step can also help to reduce the amount of one species on account of the other(s) if this one is less stable. Combinations of different solvents within one exposure step might provide a sufficient environment to achieve more specific crystallization, but as such adjustments correspond more to process optimizations rather than a screening process this has not been of interest here.

Spin coating is very versatile in means of drug layer thickness, so that the carbamazepine amount can be adjusted easily. In this study, the focus was put on film thicknesses in which the crystalline CBZ starts covering the entire sample surface. As noticeable in Figure 1, thinner films still provide information on the CBZ crystallization, but in these cases, the solvent–API–substrate interactions are more complicated. Large areas of the substrate surface are exposed, which is often referred to as dewetting or depletion of the circumjacent area of a growing crystal, which can cause the appearance of different morphologies. In our spin-coated samples a maximum amount of CBZ of about 100 μg would be achievable. Above this

amount, crystallization is often initiated rapidly on account of being close to saturation concentration, leaving no time for the SVA process to be performed on amorphous CBZ. For most drugs this small amount is likely too low for therapy which might reduce the usage of spin coating in an upscale process. Employing other thin-film technologies like drop casting (dropping the solution onto a substrate followed by evaporation of the solvent), dip coating (withdrawal of a substrate from a solid solution under defined velocities), or a simple vacuum deposition process,^{24,30} the amount of CBZ on the surface might be strongly increased. As far as drop casting is concerned, much more material can be deposited, but the process velocity is limited which also limits amorphous layer formation. Dip coating, on the other hand, can be utilized to grow crystals of defined textures, which can tune the dissolution properties further. Recently also jet spraying of materials was demonstrated to achieve amorphous layers containing a large amount of drugs.^{42,43}

Drug dissolution is complex and according to the Noyes–Whitney⁴⁴ equation depends on the diffusion coefficient, boundary layer thickness, maximum solubility, and the drug concentration in the surrounding and the surface area. In fact, all our samples could be described by a first-order release, reflecting the fact that the underlying dissolution mechanism is, to the level of accuracy within our experiment, unaffected. Many experiments demonstrate that the polymorphic form impacts the dissolution behavior, as the different lattice and surface energies, among others, suggest that an altered interaction with the drug film takes place. In our experiments, the sample heat treated at 80 °C resulted in spherulitic structures homogeneously distributed over the entire surface, whereby only form III could be identified. The dissolution of this sample proceeded rapidly and was in fact the fastest of all samples investigated. Especially, the comparison with the as-obtained powder shows a 2 orders of magnitude faster release. The reason for this is the surface area being larger; a widespread thin film has a much bigger surface compared to some large powder particles even though it contains the same amount of material. Also, the microscopic roughness is very likely much larger compared to bulk grown crystals, and a lot of pores might exist in spin-coated samples which in addition enhance the surface area significantly. Having now a tool at hand that enables spreading drugs over large areas, this is another well-suited application for identifying potential limitations in the drug release on account of size reduction.

There are several treatments found which cause amorphous–crystalline transitions which then result in the drug release being very similar. This involves storing the sample at 50 °C or at ambient conditions and exposure to AN or xylene vapors. Surprisingly, the sample stored at ambient conditions has a completely different composition in terms of polymorphic form: forms III and IV are identified. In the other three samples, clearly form I exists, while also some form II is found in the AN and xylene sample. From the microscopy images, the samples appear different, at least in the amount of the individual structures being present. This would allow concluding that the change in the polymorphic form might change the dissolution properties, but this is counteracted by changes in the morphology. Likely, the deviation on the microscale in terms of surface area or even in the boundary layer formation can explain their similar dissolution profiles. Nevertheless, the experiment shows that four different routes are at hand that can provide samples of very comparable

dissolution performance, so that fabrication optimization is not limited to a specific route. Nevertheless, the dissolution performance is worse when compared to the sample heated to 80 °C. While their surfaces seem to be similarly coated, the morphology might differ at the microscopic scale. At 80 °C more energy for diffusion is at hand which often allows growing structures in directions independent of the substrate surface which can even lead to crystal growth perpendicular to the substrate surface rather than parallel to it. Such a behavior would then lead to the solid state of the 80 °C sample being more porous; i.e., it has a lower density which provides easier access for the dissolution medium, and thus faster dissolution is observable.

The sample exposed to THF vapor shows a somehow intermediate release rate with the rate constant a being around 0.2 which is smaller than the one previously discussed (~ 0.4 – 1.8). The X-ray investigation shows that this sample contains form II of CBZ, but also some of the crystals are solvates made from THF and CBZ. While this finding is very interesting in a screening process and for fundamental understanding, the usage of this very vapor might not be justified in any application as harm to the patient might occur.

There are several samples which contain hydrates besides anhydrous CBZ phases. In general, hydrate forms are expected to be less soluble in an aqueous dissolution media as they already contain water, and thus the free energy released when starting to interact with water is less for hydrates compared to anhydrate forms. This behavior is also clearly noticeable for samples investigated here, with samples containing hydrate forms having a values (from eq 1) of about half compared to those of the anhydrides. This is in agreement with previous findings of dissolution rate reduction of CBZ on the incorporation of H₂O into the crystal structure.⁴⁵

Grazing incident X-ray diffraction is an excellent tool as it provides information on very thin films in terms of polymorphic forms but also on the texture. Texture results in crystals contacting the substrate surface with preferred crystal planes. This might be due to the processing conditions or due to the interaction of the substrate with the drug, inducing specific molecular arrangements during crystallization. In this study, only some of the samples revealed preferred orientations; e.g., form I in the 50 °C treated sample reveals a preferable contact with the 140 plane. Most of the other CBZ forms show arbitrary contact with silica surfaces in accordance with other recent reports. Likely, using substrates of stronger surface–CBZ interaction might allow changing this behavior as in the case of CBZ on top of crystalline iminostilbene templates.⁴⁶ As a preferred crystal orientation results in specific facets being in contact with the dissolution medium, this might be used to reach a desired drug release profile.

CONCLUSION

Having only nine samples prepared, the screening using solvent vapor annealing experiments is very effective in the finding of polymorphs. Here we found four different anhydrous forms of the five CBZ forms known, hydrate formation, and even a solvate. The finding in this work suggests that by using SVA processes an understanding in the polymorphic landscape of a given material can be established quickly and with a very small set of samples. While the deconvolution of the crystal morphology, polymorphic form, and texture might remain difficult, especially for this complex set of samples containing

CBZ, possible routes for a much faster drug release can already be identified using information from this approach.

EXPERIMENTAL METHODS

Carbamazepine (CBZ) was purchased from AGFA Pharma and used without further treatment. Acetonitrile (AN), 96% ethanol (EtOH), isopropanol (IPA), tetrahydrofuran (THF), and xylene were purchased from different suppliers in spectroscopic grade and used as received. Solutions of carbamazepine were prepared in THF and stirred prior to usage. Polished silicon wafers with a native silicon oxide layer (silica) were purchased from Siegert Wafers (Germany) and cut into 2.5×2.5 cm² pieces. Prior to usage, the substrates were cleaned in acetone and ethanol and finally rinsed with Milli-Q water.

Sample preparation was performed in a two-step process. First, samples were spin coated onto a piece of silicon wafer (see Figure 6a). For this, a drop of approximately 100 μ L of

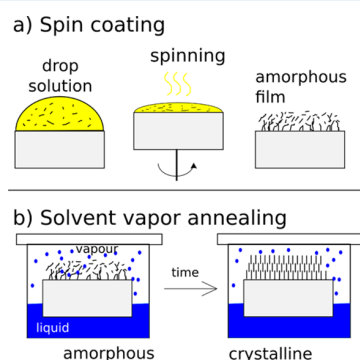


Figure 6. Scheme of sample preparation, depicting the preparation of amorphous carbamazepine films (a) and the subsequent solvent vapor annealing step (b) transferring the films to the crystalline state.

CBZ solution was placed onto the substrate followed by a continuous sample rotation around its surface normal at a rotation speed of 17 rps for 30 s. This results in the formation of a dry, homogeneous, and amorphous drug layer, as confirmed by X-ray diffraction experiments. Subsequently, selected samples were kept under ambient conditions and others at 50 or 80 °C for 48 h. Another set of samples was exposed to vapors of different chemical composition (see Figure 6b), typically referred to as solvent vapor annealing (SVA). In this, the amorphous samples are enclosed in a desiccator together with an excess amount of solvent. As the solvent vessel is not sealed against the sample, a saturated vapor develops within the desiccator which then interacts with the sample. For our purpose, all vapors are formed at ambient conditions (~ 1 atm, 22 °C) and either consist of AN, EtOH, IPA, THF, or xylene, respectively. Each sample was exposed to just one solvent vapor. After 48 h the respective sample was stored at ambient conditions until further experiments were performed.

Morphological investigations were performed on an Olympus BX51 microscope equipped with polarizers, and images were taken with a standard digital camera in reflection mode. Crystallographic information was obtained by X-ray diffraction under nearly grazing incidence conditions (GIXD), where also thin layers as used in this study provide sufficient diffraction signal to obtain structural information (using standard $\theta/2\theta$ scans, such samples provide only little or even

no diffracted intensities due to small diffraction volumes).³⁵ The measurements were performed at the XRD1 beamline⁴⁷ at the Elettra synchrotron, Trieste (Italy). Data were collected for a wavelength of 1.4 Å using a Pilatus-2 M detector from DECTRIS (Switzerland) by integrating for 2 min. Data acquisition took place while rotating the sample around the axes perpendicular to the film surface by 90° while maintaining constant grazing conditions to improve counting statistics. Due to the detector construction, detector gaps exist so that two images per sample needed to be recorded; the second image was taken at slightly elevated detector position. During data processing using the in-house developed software GIDVis, data from these images are merged and transferred from pixel space to reciprocal space using standard procedures.^{35,36} To identify the individual polymorphs, diffracted intensity data were integrated along constant q values ($\sim 1/d$ -spacing), yielding a graphical representation analogous to classic powder patterns. The data are compared to the calculated powder patterns of polymorphs with fully known crystal structures (Cambridge crystal structure database identifier: CBMZPN03, 11, 12, 14 and 16)³² using the software packages Mercury,⁴⁸ PowderCell,⁴⁹ and GIDVis.

In vitro dissolution testing was performed in 20 mL of Milli-Q water. As the amount of CBZ on each surface was low, standard dissolution apparatuses like an USP Apparatus 2 are improper. As only relative differences are of interest, a custom-made setup was used as introduced previously.^{25,26} For this, a sample was placed in a glass container filled with the dissolution media and gently shaken at 100 rpm at room temperature. An amount of 1 mL of the dissolution media was withdrawn at predetermined times for UV–vis absorption measurements using a NanoPhotometer from Implen GmbH, Germany, and fed back after measurement leaving the dissolution medium volume constant over the run of the experiment. The dissolved CBZ amount was determined at 211 nm using standard Quartz cuvettes. Each data point is an arithmetic mean of three identical samples/measurements. Error bars are omitted for sake of clarity.

ASSOCIATED CONTENT

Supporting Information

The Supporting Information is available free of charge on the ACS Publications website at DOI: 10.1021/acsomega.7b00783.

Optical microscopy taken at identical position but using crossed polarizers, X-ray diffraction powder pattern of as-purchased carbamazepine powder, and table of unit cell parameters of the different CBZ polymorphs (PDF)

AUTHOR INFORMATION

Corresponding Author

*E-mail: oliver.werzer@uni-graz.at.

ORCID

Oliver Werzer: 0000-0003-0732-4422

Notes

The authors declare no competing financial interest.

ACKNOWLEDGMENTS

B.B. wants to thank the Erasmus program “Erasmus+ Traineeship for recent graduates” for the provision of the resources to perform the experiments. The work was also funded by the Austrian Science Fund (FWF): [P25541–N19].

The authors want to thank the NAWI Graz for support. Elettra synchrotron is acknowledged for providing beamtime at the XRD1 beamline. The authors want to thank Luisa Barba and Nicola Demitri for excellent support.

REFERENCES

- (1) Jones, A. O. F.; Chattopadhyay, B.; Geerts, Y. H.; Resel, R. Substrate-Induced and Thin-Film Phases: Polymorphism of Organic Materials on Surfaces. *Adv. Funct. Mater.* **2016**, *26*, 2233.
- (2) Neumann, M. A.; de Streek, J. V.; Fabbiani, F. P. A.; Hidber, P.; Grassmann, O. Combined crystal structure prediction and high-pressure crystallization in rational pharmaceutical polymorph screening. *Nat. Commun.* **2015**, *6*, 7793.
- (3) Lang, P.; Kiss, V.; Ambrus, R.; Farkas, G.; Szabo-Revesz, P.; Aigner, Z.; Varkonyi, E. Polymorph screening of an active material. *J. Pharm. Biomed. Anal.* **2013**, *84*, 177.
- (4) Mensah, J.; Kim, K. J. Polymorph Screening Technology by Controlling Crystallization. *Chem. Eng. Trans.* **2013**, *32*, 2221.
- (5) Alleso, M.; Rantanen, J.; Aaltonen, J.; Cornett, C.; van den Berg, F. Solvent subset selection for polymorph screening. *J. Chemom.* **2008**, *22*, 621.
- (6) Alleso, M.; Van Den Berg, F.; Cornett, C.; Jorgensen, F. S.; Halling-Sorensen, B.; De Diego, H. L.; Hovgaard, L.; Aaltonen, J.; Rantanen, J. Solvent diversity in polymorph screening. *J. Pharm. Sci.* **2008**, *97*, 2145.
- (7) Baraldi, C.; Tinti, A.; Ottani, S.; Gamberini, M. C. Characterization of polymorphic ampicillin forms. *J. Pharm. Biomed. Anal.* **2014**, *100*, 329.
- (8) Ehmman, H. M.; Werzer, O. Surface Mediated Structures: Stabilization of Metastable Polymorphs on the Example of Paracetamol. *Cryst. Growth Des.* **2014**, *14*, 3680.
- (9) Wang, I. C.; Lee, M. J.; Seo, D. Y.; Lee, H. E.; Choi, Y.; Kim, W. S.; Kim, C. S.; Jeong, M. Y.; Choi, G. J. Polymorph transformation in paracetamol monitored by in-line NIR spectroscopy during a cooling crystallization process. *AAPS PharmSciTech* **2011**, *12*, 764.
- (10) Braga, D.; Grepioni, F.; Maini, L.; Polito, M.; Rubini, K.; Chierotti, M. R.; Gobetto, R. Hetero-seeding and solid mixture to obtain new crystalline forms. *Chem. - Eur. J.* **2009**, *15*, 1508.
- (11) Dichiarante, E.; Curzi, M.; Giaffreda, S. L.; Grepioni, F.; Maini, L.; Braga, D. Crystal forms of the hydrogen oxalate salt of o-desmethylvenlafaxine. *J. Pharm. Pharmacol.* **2015**, *67*, 823.
- (12) Braun, D. E.; McMahon, J. A.; Koztecki, L. H.; Price, S. L.; Reutzel-Edens, S. M. Contrasting Polymorphism of Related Small Molecule Drugs Correlated and Guided by the Computed Crystal Energy Landscape. *Cryst. Growth Des.* **2014**, *14*, 2056.
- (13) Braun, D. E.; Orlova, M.; Griesser, U. J. Creatine: Polymorphs Predicted and Found. *Cryst. Growth Des.* **2014**, *14*, 4895.
- (14) Braun, D. E.; Gelbrich, T.; Kahlenberg, V.; Griesser, U. J. Insights into Hydrate Formation and Stability of Morphinanes from a Combination of Experimental and Computational Approaches. *Mol. Pharmaceutics* **2014**, *11*, 3145.
- (15) Zhou, X. J.; Belcher, W.; Dastoor, P. Solar Paint: From Synthesis to Printing. *Polymers* **2014**, *6*, 2832.
- (16) Elkington, D.; Wasson, M.; Belcher, W.; Dastoor, P. C.; Zhou, X. Printable organic thin film transistors for glucose detection incorporating inkjet-printing of the enzyme recognition element. *Appl. Phys. Lett.* **2015**, *106*, 263301.
- (17) Planchette, C.; Pichler, H.; Wimmer-Teubenbacher, M.; Gruber, M.; Gruber-Woelfler, H.; Mohr, S.; Tetyczka, C.; Hsiao, W. K.; Paudel, A.; Roblegg, E.; Khinast, J. Printing medicines as orodispersible dosage forms: Effect of substrate on the printed micro-structure. *Int. J. Pharm.* **2016**, *509*, 518.
- (18) Rajada, D.; Genina, N.; Fors, D.; Wisaeus, E.; Peltonen, J.; Rantanen, J.; Sandler, N. Designing Printable Medicinal Products: Solvent System and Carrier-Substrate Screening. *Chem. Eng. Technol.* **2014**, *37*, 1291.
- (19) Kolakovic, R.; Viitala, T.; Ihalaenen, P.; Genina, N.; Peltonen, J.; Sandler, N. Printing technologies in fabrication of drug delivery systems. *Expert Opin. Drug Delivery* **2013**, *10*, 1711.
- (20) Urgan, I.; Chiu, L.; Pierce, A. Three-dimensional drug printing: A structured review. *J. Am. Pharm. Assoc.* **2013**, *53*, 136.
- (21) *Ink-Jet Printing of Pharmaceuticals*; Takala, M., Helkio, H., Sundholm, J., Genina, N., Kiviluoma, P., Widmaier, T., Sandler, N., Kuosmanen, P., Eds.; 2012.
- (22) Wedl, B.; Resel, R.; Leising, G.; Kunert, B.; Salzmann, I.; Oehzelt, M.; Koch, N.; Vollmer, A.; Duhm, S.; Werzer, O.; Gbabode, G.; Sferrazza, M.; Geerts, Y. Crystallisation kinetics in thin films of dihexyl-terthiophene: the appearance of polymorphic phases. *RSC Adv.* **2012**, *2*, 4404.
- (23) Ehmman, H. M. A.; Baumgartner, R.; Reischl, D.; Roblegg, E.; Zimmer, A.; Resel, R.; Werzer, O. One Polymorph and Various Morphologies of Phenytoin at a Silica Surface Due to Preparation Kinetics. *Cryst. Growth Des.* **2015**, *15*, 326.
- (24) Ehmman, H. M. A.; Baumgartner, R.; Kunert, B.; Zimmer, A.; Roblegg, E.; Werzer, O. Morphologies of Phenytoin Crystals at Silica Model Surfaces: Vapor Annealing versus Drop Casting. *J. Phys. Chem. C* **2014**, *118*, 12855.
- (25) Reischl, D.; Rothel, C.; Christian, P.; Roblegg, E.; Ehmman, H. M.; Salzmann, I.; Werzer, O. Surface-Induced Polymorphism as a Tool for Enhanced Dissolution: The Example of Phenytoin. *Cryst. Growth Des.* **2015**, *15*, 4687.
- (26) Rothel, C.; Ehmman, H. M. A.; Baumgartner, R.; Reischl, D.; Werzer, O. Alteration of texture and polymorph of phenytoin within thin films and its impact on dissolution. *CrystEngComm* **2016**, *18*, 588.
- (27) Ehmman, H. M.; Winter, S.; Griesser, T.; Keimel, R.; Schrank, S.; Zimmer, A.; Werzer, O. Dissolution testing of hardly soluble materials by surface sensitive techniques: clotrimazole from an insoluble matrix. *Pharm. Res.* **2014**, *31*, 2708.
- (28) Ehmman, H. M.; Zimmer, A.; Roblegg, E.; Werzer, O. Morphologies in solvent annealed clotrimazole thin films explained by Hansen-solubility parameters. *Cryst. Growth Des.* **2014**, *14*, 1386.
- (29) Christian, P.; Ehmman, H. M. A.; Coclite, A. M.; Werzer, O. Polymer Encapsulation of an Amorphous Pharmaceutical by initiated Chemical Vapor Deposition for Enhanced Stability. *ACS Appl. Mater. Interfaces* **2016**, *8*, 21177.
- (30) Ehmman, H. M. A.; Kellner, T.; Werzer, O. Non - contact - mode AFM induced versus spontaneous formed phenytoin crystals: the effect of layer thickness. *CrystEngComm* **2014**, *16*, 4950.
- (31) Jones, A. O.; Geerts, Y. H.; Karpinska, J.; Kennedy, A. R.; Resel, R.; Rothel, C.; Ruzie, C.; Werzer, O.; Sferrazza, M. Substrate-Induced Phase of a [1]Benzothieno[3,2-b]benzothiophene Derivative and Phase Evolution by Aging and Solvent Vapor Annealing. *ACS Appl. Mater. Interfaces* **2015**, *7*, 1868.
- (32) Grzesiak, A. L.; Lang, M. D.; Kim, K.; Matzger, A. J. Comparison of the four anhydrous polymorphs of carbamazepine and the crystal structure of form I. *J. Pharm. Sci.* **2003**, *92*, 2260.
- (33) Price, S. L. From crystal structure prediction to polymorph prediction: interpreting the crystal energy landscape. *Phys. Chem. Chem. Phys.* **2008**, *10*, 1996.
- (34) Karamertzanis, P. G.; Price, S. L. Energy minimization of crystal structures containing flexible molecules. *J. Chem. Theory Comput.* **2006**, *2*, 1184.
- (35) Birkholz, M. *Thin Film Analysis by X-ray Scattering*; Wiley-VCH: Weinheim, 2006.
- (36) Holý, V.; Pietsch, U.; Baumbach, T. High-resolution x-ray scattering from thin films and multilayers. *High-resolution X-ray scattering from thin films and multilayers* **1998**, 235.
- (37) Voorhees, P. W. The theory of Ostwald ripening. *J. Stat. Phys.* **1985**, *38*, 231.
- (38) Werzer, O.; Boucher, N.; de Silva, J. P.; Gbabode, G.; Geerts, Y. H.; Kononov, O.; Moser, A.; Novak, J.; Resel, R.; Sferrazza, M. Interface Induced Crystal Structures of Dioctyl-Terthiophene Thin Films. *Langmuir* **2012**, *28*, 8530.

- (39) Cruz Cabeza, A. J.; Day, G. M.; Motherwell, W. D.; Jones, W. Solvent inclusion in form II carbamazepine. *Chem. Commun. (Cambridge, U. K.)* **2007**, 1600.
- (40) Fabbiani, F. P. A.; Byrne, L. T.; McKinnon, J. J.; Spackman, M. A. Solvent inclusion in the structural voids of form II carbamazepine: single-crystal X-ray diffraction, NMR spectroscopy and Hirshfeld surface analysis. *CrystEngComm* **2007**, 9, 728.
- (41) Costa, P.; Manuel, J.; Lobo, S. Modeling and comparison of dissolution profiles. *Eur. J. Pharm. Sci.* **2001**, 13, 123.
- (42) Keloglu, N.; Verrier, B.; Sigaud-Roussel, D.; Trimaile, T.; Sohler, J. Jet-sprayed Hybrid Nanofibrillar Matrices with Controlled Deposition and Delivery of Nanoparticles. *Tissue Eng. Pt A* **2015**, 21, S341.
- (43) Peng, X.; Omasta, T.; Rigdon, W.; Mustain, W. E. Fabrication of High Performing PEMFC Catalyst-Coated Membranes with a Low Cost Air-Assisted Cylindrical Liquid Jets Spraying System. *J. Electrochem. Soc.* **2016**, 163, E407.
- (44) Gibson, M. *Pharmaceutical preformulation and formulation: a practical guide from candidate drug selection to commercial dosage form*; CRC Press, 2009.
- (45) Elqidra, R.; Unlu, N.; Capan, Y.; Sahin, G.; Dalkara, T.; Hincal, A. A. Effect of polymorphism on in vitro in vivo properties of carbamazepine conventional tablets. *J. Drug Delivery Sci. Technol.* **2004**, 14, 147.
- (46) Christian, P.; Rothel, C.; Tazreiter, M.; Zimmer, A.; Salzmann, I.; Resel, R.; Werzer, O. Crystallization of Carbamazepine in Proximity to Its Precursor Iminostilbene and a Silica Surface. *Cryst. Growth Des.* **2016**, 16, 2771.
- (47) Lausi, A.; Polentarutti, M.; Onesti, S.; Plaisier, J. R.; Busetto, E.; Bais, G.; Barba, L.; Cassetta, A.; Campi, G.; Lamba, D.; Pifferi, A.; Mande, S. C.; Sarma, D. D.; Sharma, S. M.; Paolucci, G. Status of the crystallography beamlines at Elettra. *Eur. Phys. J. Plus* **2015**, DOI: 10.1140/epjp/i2015-15043-3.
- (48) Macrae, C. F.; Bruno, I. J.; Chisholm, J. A.; Edgington, P. R.; McCabe, P.; Pidcock, E.; Rodriguez-Monge, L.; Taylor, R.; van de Streek, J.; Wood, P. A. Mercury CSD 2.0 - new features for the visualization and investigation of crystal structures. *J. Appl. Crystallogr.* **2008**, 41, 466.
- (49) Nolze, G.; Kraus, W. PowderCell 2.0 for Windows. *Powder Diff.* **1998**, 13, 256.

4.4 An Efficient Method for Indexing Grazing-Incidence X-ray Diffraction Data of Epitaxially Grown Thin Films



research papers



FOUNDATIONS
ADVANCES

ISSN 2053-2733

An efficient method for indexing grazing-incidence X-ray diffraction data of epitaxially grown thin films

Josef Simbrunner,^{a,*} Benedikt Schrode,^b Jari Domke,^c Torsten Fritz,^c Ingo
Salzmann^d and Roland Resel^b

Received 13 November 2019
Accepted 29 January 2020

Edited by P. R. Willmott, Swiss Light Source,
Switzerland

^aDepartment of Neuroradiology, Vascular and Interventional Radiology, Medical University Graz, Auenbruggerplatz 9, Graz, 8036, Austria, ^bInstitute of Solid State Physics, Graz University of Technology, Petersgasse 16, Graz, 8010, Austria, ^cInstitute of Solid State Physics, Friedrich Schiller University Jena, Helmholtzweg 5, Jena, 07743, Germany, and ^dDepartment of Physics, Department of Chemistry and Biochemistry, Centre for Research in Molecular Modeling (CERMM), Centre for NanoScience Research (CeNSR), Concordia University, 7141 Sherbrooke Street W., SP 265-20, Montreal, Québec H4B 1R6, Canada. *Correspondence e-mail: josef.simbrunner@medunigraz.at

This work shows the important application of rotating GIXD to an epitaxially grown film. The diffraction pattern is indexed using three-dimensional scattering vectors extracted from rotating GIXD data and the lattice parameters are determined. Josef Simbrunner developed the method for indexation and performed the calculations. Jari Domke, supervised by Torsten Fritz, prepared the sample. Benedikt Schrode suggested epitaxially grown thin films as a use-case of the algorithm, performed the GIXD measurements and evaluated the data in terms of three-dimensional peak positions. Ingo Salzmann advised on the manuscript. The manuscript was prepared by Josef Simbrunner, Benedikt Schrode and Roland Resel. All authors were proof-reading the manuscript.

The following article is reprinted from its original source with permission:

J. Simbrunner, B. Schrode, J. Domke, T. Fritz, I. Salzmann, and
R. Resel. An Efficient Method for Indexing Grazing-Incidence X-ray
Diffraction Data of Epitaxially Grown Thin Films. *Acta Crystallo-*

4.4 *An Efficient Method for Indexing Grazing-Incidence X-ray Diffraction Data of
Epitaxially Grown Thin Films*

graphica Section A Foundations and Advances 76.3 (May 2020). ISSN:
2053-2733. DOI: 10.1107/S2053273320001266

The article is available at [http://journals.iucr.org/a/issues/2020/03/00/wo5036/
index.html](http://journals.iucr.org/a/issues/2020/03/00/wo5036/index.html).



An efficient method for indexing grazing-incidence X-ray diffraction data of epitaxially grown thin films

Josef Simbrunner,^{a*} Benedikt Schrode,^b Jari Domke,^c Torsten Fritz,^c Ingo Salzmann^d and Roland Resel^b

^aDepartment of Neuroradiology, Vascular and Interventional Radiology, Medical University Graz, Auenbruggerplatz 9, Graz, 8036, Austria, ^bInstitute of Solid State Physics, Graz University of Technology, Petersgasse 16, Graz, 8010, Austria, ^cInstitute of Solid State Physics, Friedrich Schiller University Jena, Helmholtzweg 5, Jena, 07743, Germany, and ^dDepartment of Physics, Department of Chemistry and Biochemistry, Centre for Research in Molecular Modeling (CERMM), Centre for NanoScience Research (CeNSR), Concordia University, 7141 Sherbrooke Street W., SP 265-20, Montreal, Québec H4B 1R6, Canada. *Correspondence e-mail: josef.simbrunner@medunigraz.at

Received 13 November 2019

Accepted 29 January 2020

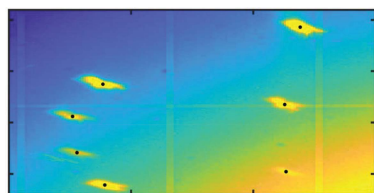
Edited by P. R. Willmott, Swiss Light Source, Switzerland

Keywords: epitaxy; indexing; mathematical crystallography.

Crystal structure identification of thin organic films entails a number of technical and methodological challenges. In particular, if molecular crystals are epitaxially grown on single-crystalline substrates a complex scenario of multiple preferred orientations of the adsorbate, several symmetry-related in-plane alignments and the occurrence of unknown polymorphs is frequently observed. In theory, the parameters of the reduced unit cell and its orientation can simply be obtained from the matrix of three linearly independent reciprocal-space vectors. However, if the sample exhibits unit cells in various orientations and/or with different lattice parameters, it is necessary to assign all experimentally obtained reflections to their associated individual origin. In the present work, an effective algorithm is described to accomplish this task in order to determine the unit-cell parameters of complex systems comprising different orientations and polymorphs. This method is applied to a polycrystalline thin film of the conjugated organic material 6,13-pentacenequinone (PQ) epitaxially grown on an Ag(111) surface. All reciprocal vectors can be allocated to unit cells of the same lattice constants but grown in various orientations [sixfold rotational symmetry for the contact planes (102) and ($\bar{1}0\bar{2}$)]. The as-determined unit cell is identical to that reported in a previous study determined for a fibre-textured PQ film. Preliminary results further indicate that the algorithm is especially effective in analysing epitaxially grown crystallites not only for various orientations, but also if different polymorphs are present in the film.

1. Introduction

Crystal structure identification of thin films entails a number of technical and methodological challenges: (i) low scattering volumes translate into only a small number of observable diffraction peaks and (ii) under the presence of a substrate the crystallites grow in a preferred orientation (texture) (Birkholz, 2006). The situation becomes even more complex in the case of thin films formed by conjugated organic molecules. Their typical growth in crystal systems of low symmetry (in most cases monoclinic and triclinic), their tendency to polymorphism and thus the presence of several phases make crystal structure determination a difficult task (Tolan, 1999). Additionally, unknown polymorphs of organic materials are frequently observed within thin films only and cannot be determined independently via traditional methods like single-crystal diffraction (Jones *et al.*, 2016). On isotropic substrates, the crystallization of molecular materials typically results in fibre-textured films comprising crystallites that share a common fibre axis perpendicular to the substrate surface but are azimuthally randomly oriented (Witte & Wöll, 2004). The



OPEN ACCESS

use of anisotropic substrates (like rubbed polymer surfaces or single-crystalline surfaces) or anisotropic preparation methods (like off-centre spin coating, dip coating or off-axis evaporation) can result in even more distinguished textures of the crystallites (Müller *et al.*, 1999; Brinkmann *et al.*, 2003; Qu *et al.*, 2016). In this context, particularly complicated cases include epitaxially grown molecular crystals on single-crystalline surfaces (Simbrunner *et al.*, 2011). There, multiple preferred orientations of the crystals relative to the substrate surface can occur together with several symmetry-related in-plane alignments of the crystallites. For example, for the epitaxial order of the conjugated organic molecule *para*-quaterphenyl on Au(111) surfaces two different preferred orientations have been found, which show 24 different in-plane alignments each (Müllegger *et al.*, 2003). For such films formed by epitaxially grown molecular crystals the identification and characterization of unknown polymorphs is a particularly challenging task (Dienel *et al.*, 2008).

Grazing-incidence X-ray diffraction (GIXD) is a well-established method for thin-film characterization (Schreiber, 2004). For non-fibre-textured films, in order to cover large volumes of the reciprocal space the sample has to be rotated around its surface normal during the GIXD experiment and at each rotation angle a reciprocal-space map has to be recorded (Fumagalli *et al.*, 2012; Schrodde *et al.*, 2019). Fig. 1(a) gives the geometry of a GIXD experiment illustrating such a sample rotation. The primary X-ray beam defining the wavevector \vec{k}_0 and the scattered X-ray beam characterized by the wavevector \vec{k} define the scattering vector \vec{q} as $\vec{q} = \vec{k}_0 - \vec{k}$. The three components of the scattering vector q_x , q_y and q_z can be calculated based on the geometries of primary and scattered X-ray beams by

$$q_x = \frac{2\pi}{\lambda} (\cos \alpha_i \cos \theta_i - \cos \alpha_f \cos \theta_f) \quad (1)$$

$$q_y = \frac{2\pi}{\lambda} (\cos \alpha_i \sin \theta_i + \cos \alpha_f \sin \theta_f) \quad (2)$$

$$q_z = \frac{2\pi}{\lambda} (\sin \alpha_i + \sin \alpha_f) \quad (3)$$

with α_i and α_f being the incident and exit angles of the primary and scattered beam (relative to the substrate surface), respectively, and θ_i , θ_f are the in-plane scattering angles. Note that the orthogonal directions of q_x , q_y and q_z are defined in the sample coordinate system. Fig. 1(b) illustrates (i) the path of reciprocal-lattice points during the sample rotation by φ_{sample} , and (ii) cuts through reciprocal space which correspond to reciprocal-space maps recorded at two defined φ_{sample} angles.

Crystal structure solutions require the indexing of the diffraction pattern, *i.e.* the assignment of Laue indices to the observed Bragg peaks. In the monochromatic approach of peak indexing as it is commonly employed for single-crystal diffraction patterns, all three components of the scattering vectors are recorded and, therefore, all three components of the reciprocal-lattice vectors can be determined. Three linearly independent reciprocal-lattice vectors are sufficient to span the reciprocal lattice. Any further experimentally determined reciprocal-lattice vector then must fit into this specific reciprocal lattice. Since complete three-dimensional vectors are used, even the indexing of configurations with multiple lattices can be successfully achieved (Jacobson, 1976; Higashi, 1990; Powell, 1999; Breiby *et al.*, 2008; Gildea *et al.*, 2014; Dejoie *et al.*, 2015). Plenty of indexing methods have already been described over the last decades. Typically, a set of positions of recorded reflections is converted into reciprocal-space vectors. These vectors are then analysed for periodicity to determine the basis vectors. Differences between reciprocal-space vectors are calculated and accumulated in a histogram (Kabsch, 1988, 2010), or a fast Fourier transform (FFT) is used to search for periodicities (Steller *et al.*, 1997; Campbell, 1998; Leslie, 2006; Otwinowski *et al.*, 2012; Sauter *et al.*, 2004). For example, the autoindexing method incorporated into the software *MOSFLM* (Leslie, 1992) employs FFT autoindexing routines written by the Rossmann group at Purdue University (Rossmann & van Beek, 1999) and relies on the calculation of many difference vectors between diffraction maxima in reciprocal space (Kabsch, 1993). The Fourier analysis is systematically performed for about 7300 separate, roughly equally spaced directions. For each direction, the distribution of the corresponding Fourier coefficients is searched to locate the largest local maximum, and refinement by a local search procedure increases the accuracy. From these directions, a linearly independent set of three basis vectors of a real-space unit cell is then chosen.

In the approach by Duisenberg, periodicities are sought by projecting all observed reciprocal-lattice vectors onto the normal to the plane given by three randomly selected points (Duisenberg, 1992). This method was developed for difficult

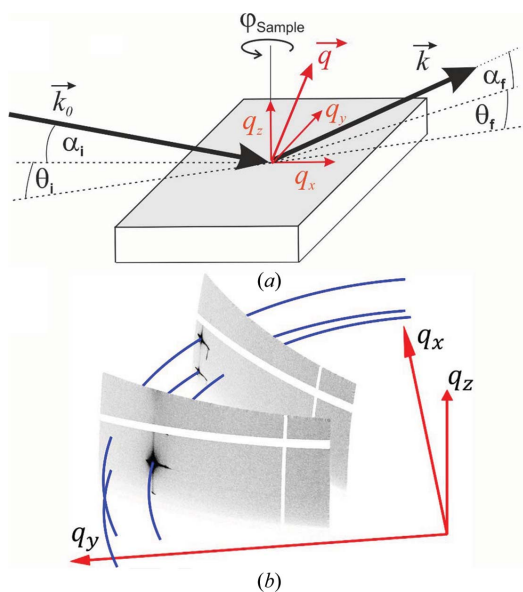


Figure 1
(a) Scattering geometry of a grazing-incidence X-ray diffraction experiment with a sample rotation around the angle φ_{sample} . (b) Trajectory of reciprocal-lattice points during the rotation of the sample around the angle φ_{sample} along concentric circles (blue lines) and two individual reciprocal-space maps at defined angles φ_{sample} .

cases such as twin lattices, fragmented crystals and unreliable data. For such cases, Morawiec has developed another algorithm in which systematic combinations of three reciprocal-lattice vectors each are formed to search for periodicities of the calculated unit-cell volumes (Morawiec, 2017).

In the case of GIXD, as usually performed on fibre-textured films, however, only two components (of the total three) of the reciprocal-lattice vectors – namely q_z and q_{xy} – are available for the indexing procedure. In previous work, we have presented an algorithm for indexing such diffraction patterns, where the additional presence of a specular diffraction peak is being explicitly taken into account (Simbrunner *et al.*, 2018, 2019). Furthermore, we have described an algorithm to find the reduced cell and derived mathematical expressions which can be applied when reciprocal-space vectors are obtained.

In the present work, we now aim to formulate this indexing method for GIXD patterns obtained for rotated samples of non-fibre-textured films, which then provides all three components of the scattering vector. Also, in this case, the combination of the diffraction peaks obtained from GIXD with the specular diffraction peak(s) simplifies the indexing procedure considerably, so that different phases, different preferred orientations and different crystal alignments can be identified. Finally, our algorithm is applied to a film of 6,13-pentacenequinone ($C_{22}H_{12}O_2$, CAS No. 3029-32-1) epitaxially grown on a single-crystalline Ag(111) surface readily providing the unit-cell parameters of the film from GIXD data.

2. Method

2.1. Fundamentals

For the following mathematical treatise a crystal-fixed Cartesian coordinate system is assumed, where the xy plane runs parallel to the substrate surface; a, b, c, α, β and γ are the parameters of the (direct) unit cell.

If the (001) lattice plane is parallel to the substrate surface, the reciprocal-lattice vector \mathbf{g} with its Laue indices h, k and l can be represented by the equation

$$\mathbf{g} = \begin{pmatrix} g_x \\ g_y \\ g_z \end{pmatrix} = \mathbf{A}_{001}^* \begin{pmatrix} h \\ k \\ l \end{pmatrix}. \quad (4)$$

The matrix \mathbf{A}_{001}^* is given as

$$\mathbf{A}_{001}^* = \begin{pmatrix} a^* \sin \beta^* \sin \gamma & 0 & 0 \\ -a^* \sin \beta^* \cos \gamma & b^* \sin \alpha^* & 0 \\ a^* \cos \beta^* & b^* \cos \alpha^* & c^* \end{pmatrix}, \quad (5)$$

where $a^* = 2\pi bc \sin \alpha / V$, $b^* = 2\pi ac \sin \beta / V$, $c^* = 2\pi ab \sin \gamma / V$, $\cos \alpha^* = (\cos \beta \cos \gamma - \cos \alpha) / (\sin \beta \sin \gamma)$ and $\cos \beta^* = (\cos \alpha \cos \gamma - \cos \beta) / (\sin \alpha \sin \gamma)$ are the reciprocal cell parameters and V is the unit-cell volume, which can be explicitly written as

$$V = abc(1 - \cos^2 \alpha - \cos^2 \beta - \cos^2 \gamma + 2 \cos \alpha \cos \beta \cos \gamma)^{1/2}. \quad (6)$$

When the Laue condition $\mathbf{q} = \mathbf{g}$ is fulfilled, diffraction can be observed. In real space, \mathbf{A}_{001} characterizes the matrix of lattice vectors $\mathbf{a}_0, \mathbf{b}_0$ and \mathbf{c}_0 , which is in the non-rotated system given by

$$\mathbf{A}_{001} = \begin{pmatrix} \mathbf{a}_0 \\ \mathbf{b}_0 \\ \mathbf{c}_0 \end{pmatrix} = \begin{pmatrix} a & 0 & 0 \\ b \cos \gamma & b \sin \gamma & 0 \\ c \cos \beta & -c \sin \beta \cos \alpha^* & c \sin \beta \sin \alpha^* \end{pmatrix}. \quad (7)$$

Equations (5) and (7) are connected via

$$\mathbf{A}_{001} = 2\pi \mathbf{A}_{001}^{*-1}. \quad (8)$$

The volume V of the unit cell can be calculated by $V = \det(\mathbf{A}_{001})$. If, however, the (001) plane is not parallel to the substrate surface, the reciprocal vector \mathbf{g} can be expressed as

$$\mathbf{g} = \mathbf{R}(\varphi) \mathbf{R}(\psi, \Phi) \mathbf{A}_{001}^* \begin{pmatrix} h \\ k \\ l \end{pmatrix}, \quad (9)$$

where $\mathbf{R}(\varphi) \mathbf{R}(\psi, \Phi)$ describes a general rotation. As explained previously (Simbrunner *et al.*, 2018), we prefer this notation. $\mathbf{R}(\varphi)$ performs a rotation in the xy plane counter-clockwise by an angle φ and is explicitly written as

$$\mathbf{R}(\varphi) = \begin{pmatrix} \cos \varphi & -\sin \varphi & 0 \\ \sin \varphi & \cos \varphi & 0 \\ 0 & 0 & 1 \end{pmatrix}. \quad (10)$$

The rotation matrix $\mathbf{R}(\psi, \Phi)$ is explicitly written as

$$\mathbf{R}(\psi, \Phi) = \begin{bmatrix} \cos^2 \psi + \cos \Phi \sin^2 \psi & \cos \psi \sin \psi (1 - \cos \Phi) & -\sin \psi \sin \Phi \\ \cos \psi \sin \psi (1 - \cos \Phi) & \sin^2 \psi + \cos \Phi \cos^2 \psi & \cos \psi \sin \Phi \\ \sin \psi \sin \Phi & -\cos \psi \sin \Phi & \cos \Phi \end{bmatrix}, \quad (11)$$

where ψ and Φ are the rotation angles. This rotation matrix was previously used for the mathematical formalism in GIXD experiments, where the composite component q_{xy} is measured and, therefore, rotation in the xy plane can be neglected. It has been shown that, if the specular diffraction scan q_{spec} of the sample provides useful information on the orientation, it is preferable to write the rotation parameters as follows:

$$\cos \psi = \frac{\frac{u}{a} \cos \gamma - \frac{v}{b}}{\left[\left(\frac{u}{a} \right)^2 + \left(\frac{v}{b} \right)^2 - 2 \frac{uv}{ab} \cos \gamma \right]^{1/2}}, \quad (12)$$

$$\sin \psi = \frac{\frac{u}{a} \sin \gamma}{\left[\left(\frac{u}{a} \right)^2 + \left(\frac{v}{b} \right)^2 - 2 \frac{uv}{ab} \cos \gamma \right]^{1/2}}, \quad (13)$$

Table 1

Unit-cell vectors for the parameters $a, b, c, \alpha, \beta, \gamma$, the Laue indices hkl and the Miller indices uvw and including the specular scan (g_{spec}) for the non-rotated (a) and the rotated (b) case.

$$g_{\text{spec}} = (u^2 a^{*2} + v^2 b^{*2} + w^2 c^{*2} + 2uv a^* b^* \cos \gamma^* + 2uw a^* c^* \cos \beta^* + 2vw b^* c^* \cos \alpha^*)^{1/2}.$$

(a) Non-rotated case ($u = v = 0$):

$$\mathbf{a} = a \begin{pmatrix} \cos \varphi \\ \sin \varphi \\ 0 \end{pmatrix}$$

$$\mathbf{b} = b \begin{bmatrix} \cos(\varphi + \gamma) \\ \sin(\varphi + \gamma) \\ 0 \end{bmatrix}$$

$$\mathbf{c} = c \begin{bmatrix} r_c \cos(\varphi + \Omega_c) \\ r_c \sin(\varphi + \Omega_c) \\ \frac{|w|}{c} \frac{2\pi}{g_{\text{spec}}} \end{bmatrix}$$

$$r_c = \left[1 - \left(\frac{w}{c} \frac{2\pi}{g_{\text{spec}}} \right)^2 \right]^{1/2}$$

$$\cos \Omega_c = \frac{1}{r_c} \cos \beta$$

(b) Rotated case:

$$\mathbf{a} = a \begin{bmatrix} r_a \cos(\varphi + \psi - \Omega_a) \\ r_a \sin(\varphi + \psi - \Omega_a) \\ \frac{u}{a} \frac{2\pi}{g_{\text{spec}}} \end{bmatrix}$$

$$r_a = \left[1 - \left(\frac{u}{a} \frac{2\pi}{g_{\text{spec}}} \right)^2 \right]^{1/2}$$

$$\cos \Omega_a = \frac{1}{r_a} \frac{\frac{u}{a} \cos \gamma - \frac{v}{b}}{\left[\left(\frac{u}{a} \right)^2 + \left(\frac{v}{b} \right)^2 - 2 \frac{u}{a} \frac{v}{b} \cos \gamma \right]^{1/2}}$$

$$\mathbf{b} = b \begin{bmatrix} r_b \cos(\varphi + \psi + \Omega_b) \\ r_b \sin(\varphi + \psi + \Omega_b) \\ \frac{v}{b} \frac{2\pi}{g_{\text{spec}}} \end{bmatrix}$$

$$r_b = \left[1 - \left(\frac{v}{b} \frac{2\pi}{g_{\text{spec}}} \right)^2 \right]^{1/2}$$

$$\cos \Omega_b = \frac{1}{r_b} \frac{\frac{u}{a} - \frac{v}{b} \cos \gamma}{\left[\left(\frac{u}{a} \right)^2 + \left(\frac{v}{b} \right)^2 - 2 \frac{u}{a} \frac{v}{b} \cos \gamma \right]^{1/2}}$$

$$\mathbf{c} = c \begin{bmatrix} r_c \cos(\varphi + \psi + \Omega_c) \\ r_c \sin(\varphi + \psi + \Omega_c) \\ \frac{w}{c} \frac{2\pi}{g_{\text{spec}}} \end{bmatrix}$$

$$r_c = \left[1 - \left(\frac{w}{c} \frac{2\pi}{g_{\text{spec}}} \right)^2 \right]^{1/2}$$

$$\cos \Omega_c = \frac{1}{r_c} \frac{\frac{u}{a} \cos \alpha - \frac{v}{b} \cos \beta}{\left[\left(\frac{u}{a} \right)^2 + \left(\frac{v}{b} \right)^2 - 2 \frac{u}{a} \frac{v}{b} \cos \gamma \right]^{1/2}}$$

$$\sin \psi = \frac{\frac{u}{a} \sin \gamma}{\left[\left(\frac{u}{a} \right)^2 + \left(\frac{v}{b} \right)^2 - 2 \frac{u}{a} \frac{v}{b} \cos \gamma \right]^{1/2}}$$

$$\cos \psi = \frac{\frac{u}{a} \cos \gamma - \frac{v}{b}}{\left[\left(\frac{u}{a} \right)^2 + \left(\frac{v}{b} \right)^2 - 2 \frac{u}{a} \frac{v}{b} \cos \gamma \right]^{1/2}}$$

$$\cos \Phi = (ua^* \cos \beta^* + vb^* \cos \alpha^* + wc^*)$$

$$\mathbf{A} = \mathbf{A}_{001} \mathbf{R}(\psi, \Phi)^T \mathbf{R}(\varphi)^T \quad (16)$$

$$\left/ \left[u^2 \left(\frac{2\pi}{a \sin \gamma} \right)^2 + v^2 \left(\frac{2\pi}{b \sin \gamma} \right)^2 - 2uv \frac{2\pi}{a \sin \gamma} \frac{2\pi}{b \sin \gamma} \cos \gamma + (ua^* \cos \beta^* + vb^* \cos \alpha^* + wc^*)^2 \right]^{1/2} \right., \quad (14)$$

equation (15) can be rewritten as

$$\mathbf{A} \mathbf{g} = \begin{pmatrix} \mathbf{a} \\ \mathbf{b} \\ \mathbf{c} \end{pmatrix} \mathbf{g} = 2\pi \begin{pmatrix} h \\ k \\ l \end{pmatrix}, \quad (17)$$

where u, v and w are the Miller indices of the contact plane (uvw) and thus the Laue indices of the specular scan. In the general case, u, v and w can be irrational numbers.

From equation (9), using equation (8), it follows that

$$\begin{pmatrix} h \\ k \\ l \end{pmatrix} = \mathbf{A}_{001}^*{}^{-1} \mathbf{R}(\psi, \Phi)^T \mathbf{R}(\varphi)^T \mathbf{g} = \frac{1}{2\pi} \mathbf{A}_{001} \mathbf{R}(\psi, \Phi)^T \mathbf{R}(\varphi)^T \mathbf{g}. \quad (15)$$

With

where \mathbf{a}, \mathbf{b} and \mathbf{c} are the rotated unit-cell vectors with the relations $|\mathbf{a}| = a, |\mathbf{b}| = b, |\mathbf{c}| = c, (\mathbf{a} \cdot \mathbf{b})/(|\mathbf{a}||\mathbf{b}|) = \cos \gamma, (\mathbf{a} \cdot \mathbf{c})/(|\mathbf{a}||\mathbf{c}|) = \cos \beta$ and $(\mathbf{b} \cdot \mathbf{c})/(|\mathbf{b}||\mathbf{c}|) = \cos \alpha$. The explicit forms of these vectors are given in Table 1. Note that the z components are only a function of the respective Miller index and the specular scan g_{spec} .

Thus, if three reciprocal vectors $\mathbf{g}_1, \mathbf{g}_2$ and \mathbf{g}_3 are given, the following relation holds:

$$\mathbf{G} \begin{pmatrix} \mathbf{a} \\ \mathbf{b} \\ \mathbf{c} \end{pmatrix}^T = \mathbf{G} \mathbf{A}^T = 2\pi \mathbf{H}^T, \quad (18)$$

where

$$\mathbf{G} = \begin{pmatrix} g_{x1} & g_{y1} & g_{z1} \\ g_{x2} & g_{y2} & g_{z2} \\ g_{x3} & g_{y3} & g_{z3} \end{pmatrix} \quad (19)$$

and (h_i, k_i, l_i) are the corresponding triples of Laue indices with

$$\mathbf{H} = \begin{pmatrix} h_1 & h_2 & h_3 \\ k_1 & k_2 & k_3 \\ l_1 & l_2 & l_3 \end{pmatrix}. \quad (20)$$

Equation (18) can be equivalently expressed as

$$\mathbf{A}^T = 2\pi\mathbf{G}^{-1}\mathbf{H}^T. \quad (21)$$

Furthermore, as $V = |\det(\mathbf{A})| = \det(\mathbf{A}_{001})$, the following relation for the determinants of \mathbf{G} and \mathbf{H} is valid:

$$|\det(\mathbf{G})| = (2\pi)^3 |\det(\mathbf{H})|/V \Leftrightarrow V = (2\pi)^3 |\det(\mathbf{H})|/|\det(\mathbf{G})|. \quad (22)$$

The unit-cell vectors must be solutions to all reciprocal vectors \mathbf{g}_i which can be written as

$$\mathbf{A}\mathbf{g}_i = 2\pi\mathbf{h}_i, \quad (23)$$

where

$$\mathbf{g}_i = \begin{pmatrix} g_{xi} \\ g_{yi} \\ g_{zi} \end{pmatrix} \quad \text{and} \quad \mathbf{h}_i = \begin{pmatrix} h_i \\ k_i \\ l_i \end{pmatrix}.$$

From equation (21) it can be deduced that $2\pi\mathbf{G}^{-1}\mathbf{m}$, the product of the inverse matrix of three reciprocal vectors with a vector \mathbf{m} , consisting of a triple of arbitrary integers (m_1, m_2, m_3) , leads to a vector of the reduced cell (Niggli, 1928) if \mathbf{m} matches $(h_1, h_2, h_3)^T$, $(k_1, k_2, k_3)^T$ or $(l_1, l_2, l_3)^T$. If a transformation matrix \mathbf{N} exists so that \mathbf{m} equals $\mathbf{N}(h_1, h_2, h_3)^T$, $\mathbf{N}(k_1, k_2, k_3)^T$ or $\mathbf{N}(l_1, l_2, l_3)^T$ a vector of a superlattice is obtained. According to equation (22) it is favourable to select three reciprocal vectors whose matrix results in a determinant which is as small as possible but unequal to zero. The Buerger cell (Buerger, 1957) and subsequently the reduced cell is obtained by choosing the three shortest vectors which are not coplanar and whose scalar products with all reciprocal vectors yield integers.

2.2. Indexing algorithm

We now suggest the following procedure for indexing an unknown crystalline system:

(i) Forming triplets of reciprocal vectors in all possible combinations, *i.e.* if n vectors are given these are

$$\binom{n}{3} = \frac{n(n-1)(n-2)}{6}$$

triplets $(\mathbf{g}_1, \mathbf{g}_2, \mathbf{g}_3)$, where $\mathbf{g}_1, \mathbf{g}_2$ and \mathbf{g}_3 are any three reciprocal vectors. According to equation (22), if the triplet corresponds to a unit cell, the determinant of its matrix is indirectly proportional to the volume of this unit cell, or if the matrix of the corresponding Laue indices has a determinant >1 , to some

integer fraction of it. As many reciprocal vectors belong to one unit cell, they accumulate to discernible clusters. Importantly, a vanishing determinant strongly indicates that the reciprocal-lattice vectors (and the corresponding Laue indices) are linearly dependent and belong to the same crystalline system. If several unit cells are contained in the sample, an overlap of smaller volumes with fractions of larger volumes occurs. A feasible strategy results in gathering the reciprocal vectors of the largest volume and repeating the procedure for the remaining reciprocal vectors.

If the crystallites are characterized by the same unit cell and differ only in their rotational arrangement in the xy plane, this algorithm can only be used if the unit-cell volume is *a priori* known. Otherwise, three reciprocal vectors are chosen from different subgroups with identical pairs of $q_{xy} = (q_x^2 + q_y^2)^{1/2}$ and q_z .

(ii) According to equation (19), the selected triplets of reciprocal vectors are combined into matrices. If they belong to the same system, their inverse matrices multiplied with the vectors of the corresponding Laue indices will result in the vectors of the unit cell [*cf.* equation (21)]. This can be achieved by multiplying the inverse matrices \mathbf{G}^{-1} with vectors $2\pi(m_1, m_2, m_3)^T$, where the m_i are systematically varied integers in a reasonable range (*e.g.* between -3 and 3). Then, lattice vectors of the unit cell and of its superlattices are obtained (Simbrunner *et al.*, 2018). The three shortest vectors which are not coplanar are chosen to obtain the Buerger cell. The as-obtained matrices contain the vectors \mathbf{a} , \mathbf{b} and \mathbf{c} of the reduced unit cells which may have various orientations. If the reciprocal-space vectors are correctly combined, *i.e.* if they belong to the same system, the scalar product criteria (Niggli, 1928) are intrinsically fulfilled; otherwise they are useful to eliminate falsely combined vector triplets. The associated integers are the corresponding triples of Laue indices [see equation (18)]. If a contact plane exists and the specular scan q_{spec} can be measured, the triplets whose z components are (almost) integer multiples of $2\pi/q_{\text{spec}}$ can be assigned as possible solutions.

(iii) The tentative unit-cell matrices are multiplied with all reciprocal vectors. If the scalar products yield integers [*i.e.* the corresponding Laue indices according to equation (23)], the matrices and reciprocal vectors belong to the same system. Due to experimental imperfections, errors must be considered. For a system of reciprocal vectors, the unit cell with the smallest deviations from perfect integers will be chosen.

(iv) From the unit-cell matrix, the cell parameters and rotation parameters can be obtained. From equation (17) it follows that the sides of the unit cell are the magnitudes and its angles are the scalar products of the matrix vectors. The Niggli criteria for reduced cells demand that $\mathbf{a}^2 \leq \mathbf{b}^2 \leq \mathbf{c}^2$ and that the angles are either acute (type I) or obtuse (type II) (Niggli, 1928). Therefore, the vectors have to be designated

$$\mathbf{a} = \begin{pmatrix} a_x \\ a_y \\ a_z \end{pmatrix}, \mathbf{b} = \begin{pmatrix} b_x \\ b_y \\ b_z \end{pmatrix}, \mathbf{c} = \begin{pmatrix} c_x \\ c_y \\ c_z \end{pmatrix}$$

accordingly. Furthermore, the angles must be adopted. By multiplying one vector with -1 two angles change to their complementary ones, *e.g.* for $\mathbf{a} \rightarrow -\mathbf{a}$ we obtain $\beta \rightarrow \pi - \beta$ and $\gamma \rightarrow \pi - \gamma$. The rotation angles φ , ψ and ϕ can be obtained by using the equations provided in Appendix A.

(v) According to equation (21) the unit-cell vectors can be calculated from every linearly independent triple of reciprocal-lattice vectors of the same system. This redundancy can be used to determine mean values and standard deviations of the unit-cell parameters. Alternatively, the matrix of the unit-cell vectors may be optimized in real space (see Appendix B) and in reciprocal space (see Appendix C). In a last step, the lattice parameters may be optimized with respect to the lengths q_{xyz} and the components q_z of the reciprocal-space vectors, which are independent of the rotation angle φ . This can be accomplished analytically (see Appendix D).

3. Example: 6,13-pentacenequinone (PQ) on Ag(111)

We now apply the above methodology to an epitaxially grown film of the conjugated organic molecule 6,13-pentacenequinone (PQ, $\text{C}_{22}\text{H}_{12}\text{O}_2$, CAS No. 3029-32-1) on an Ag(111) surface. PQ was purchased from Sigma Aldrich (purity 99%) and purified via vacuum sublimation before usage. Substrate preparation and film preparation were conducted in an ultra high vacuum (UHV) chamber with a base pressure of 1×10^{-8} Pa. Before thin-film deposition, the substrate surface was cleaned by repeated cycles of Ar^+ sputtering at an energy of 700 eV and angles of $\pm 45^\circ$ to the sample normal, followed by thermal annealing at 770 K for 30 min. Surface quality was confirmed by low-energy electron diffraction (LEED). PQ was deposited by thermal evaporation from a quartz crucible at a constant temperature of 480 K for 60 min with the deposition time controlled by a shutter, resulting in an approximate film thickness of 10 nm. During deposition, the substrate was kept at room temperature and the chamber pressure increased to 4×10^{-7} Pa. A top layer of aluminium tris-(8-hydroxyquinoline) (Alq_3 , $\text{C}_{27}\text{H}_{18}\text{AlN}_3\text{O}_3$, CAS No. 2085-33-8), known to grow amorphously, was deposited from a quartz crucible at a constant temperature of 550 K for 55 min to keep the PQ crystals free from environmental influences and to reduce beam damage during the X-ray diffraction experiments. Alq_3 was obtained from Sigma Aldrich at sublimed grade with a purity of 99.995% trace metal basis and was used without further purification.

The sample was first investigated by specular X-ray diffraction using in-house equipment and then by GIXD using synchrotron radiation. Specular X-ray diffraction was performed on a PANalytical Empyrean system using a sealed copper tube together with an X-ray mirror for monochromatization and a PIXcel3D detector operating in scanning line mode (255 channels). Measured data were converted to reciprocal space using $q_z = (4\pi/\lambda) \sin \theta$, with θ being half of the scattering angle 2θ and $\lambda = 1.5406$ Å. GIXD measurements were performed at the XRD1 beamline at the Elettra Synchrotron, Trieste (Italy), using a wavelength of 1.4000 Å. Diffracted intensity was recorded with a stationary Pilatus 2M

detector (Dectris) with a sample-to-detector distance of about 200 mm. The primary X-ray beam was slightly offset from the centre of the detector to allow for simultaneously recording both the right- and the left-hand side of the reciprocal-space map, but to avoid missing peaks due to detector gaps typical for the Pilatus system. The calibration of the setup (to obtain exact values for sample-detector distance, position of the primary beam on the detector, detector inclinations *etc.*) was performed by measuring polycrystalline lanthanum hexaboride (LaB_6) (Black *et al.*, 2010) in a capillary. The incident angle α_i for the thin-film measurement was set to 0.7° to reduce the footprint of the beam on the sample and, thus, enable data evaluation with higher accuracy. The sample was rotated around its surface normal [*cf.* Fig. 1(b), φ_{sample}] during the GIXD measurement recording 180 images, with therefore each exposure integrating 2° in φ_{sample} of the azimuthal rotation. Note that the angle φ_{sample} is the experimentally used

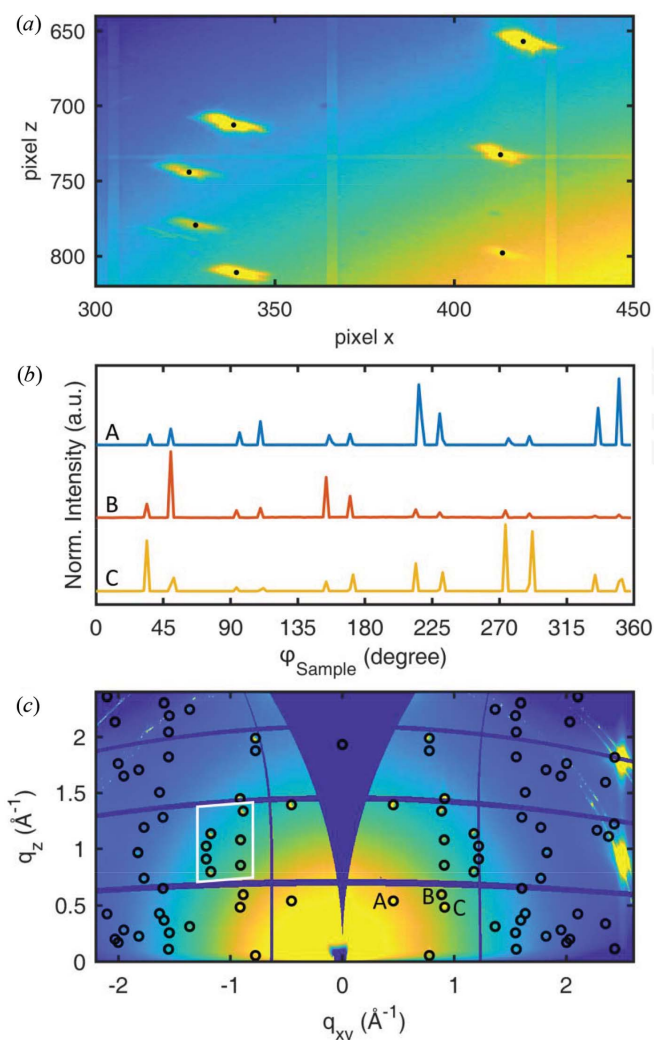


Figure 2
(a) Section of the integrated pixel image with black markers indicating the peak positions obtained from the fitting process. (b) Intensities of peaks A, B and C of (c) as a function of the sample rotation angle φ_{sample} . (c) Integrated reciprocal-space map overlaid with the calculated peak positions of the determined crystal structure. The white box indicates the approximate section visualized in (a).

sample azimuth, while the angle φ is used to describe a rotation of the unit cell in the xy plane in the counterclockwise direction [cf. equations (9)–(10)].

To determine the peak positions from the diffraction images, the following process was performed: in a first step, all diffraction images recorded during the 360° sample rotation were summed up pixel by pixel resulting in a single image showing the overall integrated diffraction information. The peak positions were then fitted using a two-dimensional Gaussian function with a background plane, giving the pixel position of each peak [cf. Fig. 2(a)].

To determine the peak positions as a function of the sample rotation, the intensity at the obtained peak positions was monitored throughout the 180 separate data files which translates into a curve representing intensity versus φ_{sample} . Three curves are given in Fig. 2(b), where due to both the symmetry of the crystal structure and that of the substrate, several peaks are then observed for a given set of Miller indices. Most peaks show a full width at half-maximum (as a measure of in-plane mosaicity) of about 2° . Their positions were determined by fitting the corresponding part of the curve with a one-dimensional Gaussian function with linear background. In the next step, a small area around the peak position of the summed image was fitted with a two-dimensional Gaussian function in the specific data file corresponding to the rounded φ_{sample} value where the peak maximum was observed. These pixel positions together with the corresponding (unrounded) φ_{sample} values were used to convert the data into reciprocal space using source code provided by the software package *GIDVis* (Schrode *et al.*, 2019). No refraction corrections were included during the conversion. As mentioned above, the diffraction pattern was recorded simultaneously at the right-hand side (RHS) as well as at the left-hand side (LHS) of the detector. Therefore, the above-described data evaluation can be applied separately to the data from the RHS and the LHS, since each detector side (apart from the detector gaps) contains the same information for the data analysis, resulting in individual solutions for RHS and LHS data. Large

differences between peak positions obtained from the LHS and RHS would indicate a sample misalignment, but were not observed here.

The specular X-ray diffraction pattern shows dominant features of the Ag(111) substrate and a clear diffraction peak which is assigned to PQ crystals (compare Fig. 3). According to our notation the position of this peak is $q_{\text{spec}} = q_z = 1.942 \text{ \AA}^{-1}$. The GIXD experiments gave 227 and 279 reciprocal-lattice vectors with the three components q_x , q_y and q_z on the RHS and LHS, respectively. The different number is due to some peaks falling into the detector gaps at one detector side only. The reciprocal-lattice vectors could be split into 31 groups with up to 12 related pairs of $q_{xy} = (q_x^2 + q_y^2)^{1/2}$ and q_z . Therefore, it could be concluded that there are 12 different in-plane alignments of the crystallites which are oriented with the same contact plane (uvw or $-u-v-w$). Three reciprocal vectors from different groups were then systematically combined, and the matrix was formed according to equation (16). Note that the determinant of the matrix is indirectly proportional to the volume of the unit cell [see equation (22)], and a determinant of zero expresses that linearly dependent lattice vectors have been chosen. In a next step the inverse matrix was multiplied with vectors of systematically varied integers, and the three shortest lattice vectors were chosen (Buerger cell) for a guess of a unit cell. If the z components of these tentative lattice vectors were integer multiples of $2\pi/q_{\text{spec}}$ and the Niggli criteria were fulfilled, they were assigned as possible solutions. The obtained integers could be assigned as the Miller indices $uvw = (102)$ or $(\bar{1}02)$ of the contact plane which finally gives the preferred orientation of the PQ crystals relative to the substrate surface. In a next step the tentative lattice matrix was multiplied with all reciprocal vectors of the other groups. If the lattice matrix was indeed a solution, triples of Laue indices could be assigned to the associated reciprocal vectors, according to equation (23). In a further step, the matrix of the unit-cell vectors was optimized (see Appendices B and C). On request, the used code can be provided. Fig. 4(a) shows the result of the indexing procedure for a single type of epitaxially aligned crystallites with the contact plane $uvw = (102)$ for the RHS data; the assigned peaks are marked with blue circles.

For each solution the lattice vectors **a**, **b** and **c** were used to determine the respective lattice constants, the contact plane [$uvw = (102)$ or $(\bar{1}02)$] and the rotation angle φ (see Appendix A). As φ can be independently calculated from each of the three lattice vectors, the accuracy can be checked. In our case, the mean error was about 0.15%. Rotation angles between the different solutions were obtained in steps of $\Delta\varphi = 60.00^\circ$ ($\pm 0.26^\circ$) for the (102) contact plane and $\Delta\varphi = 60.00^\circ$ ($\pm 0.94^\circ$) for the $(\bar{1}02)$ contact plane. This clearly reflects the symmetry of the Ag(111) surface. By repeating the procedure, all reciprocal vectors could be allocated to unit cells with the same lattice constants but various orientations.

In the case of Fig. 4(b) two types of epitaxially aligned crystallites are indexed with contact planes (102) and $(\bar{1}02)$, denoted by blue and red circles, respectively. Fig. 4(c) gives indexing of all diffraction peaks by the two contact planes

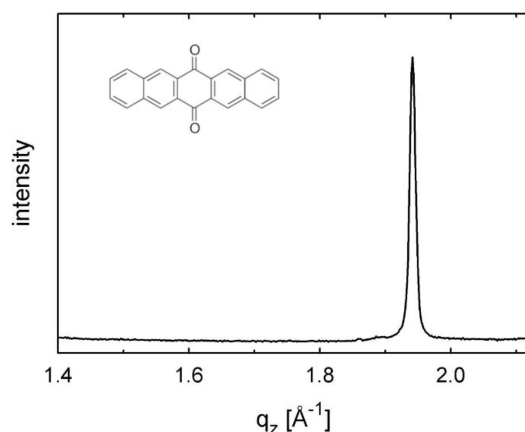


Figure 3
Specular X-ray diffraction of epitaxially grown pentacenequinone crystals on an Ag(111) surface deposited with a nominal thickness of 10 nm. The chemical structure of the molecules is given in the inset.

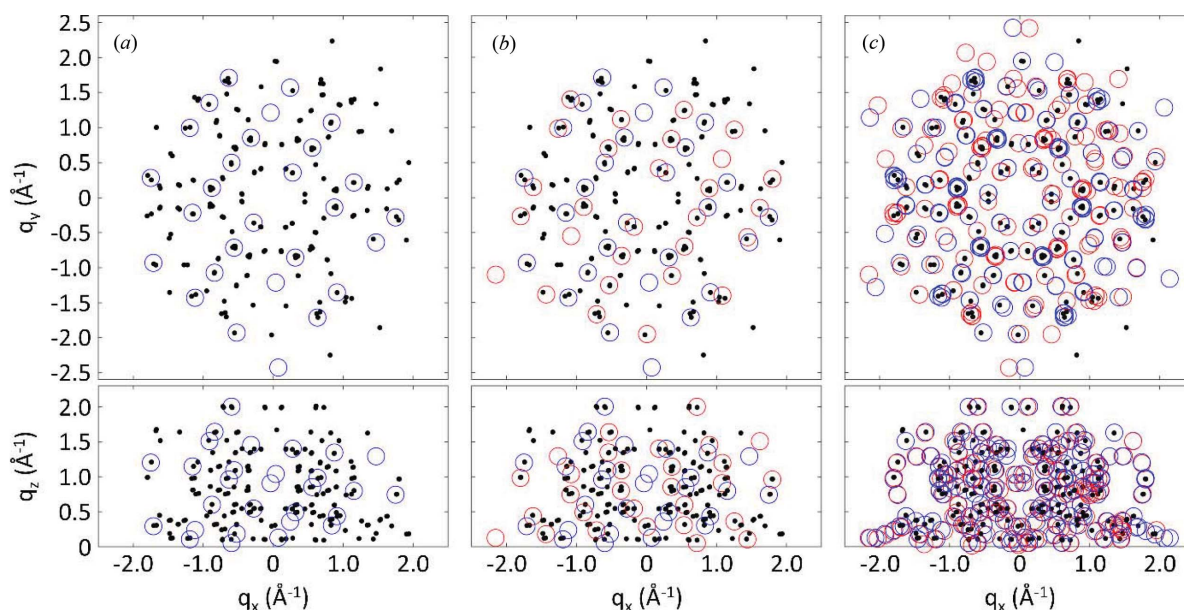


Figure 4

Positions of X-ray diffraction peaks (black) of pentacenequinone crystals grown on an Ag(111) surface obtained from rotating GIXD experiments. Top: q_y/q_x positions of the diffraction peaks; bottom: q_z/q_x positions. (a) Indexing (blue circles) of a single type of epitaxially oriented crystals grown with the (102) plane parallel to the substrate surface; (b) a second type of crystals grown with the (102) contact plane is indexed (red circles); (c) indexing of all 12 types of epitaxially oriented crystals.

(102) and $(\bar{1}0\bar{2})$, each showing six different types of in-plane alignment of the crystallites. We found the following epitaxial relationships: $(111)_{\text{Ag}} \parallel \pm (102)_{\text{PQ}}$; the b axis $[010]$ of PQ in (102) orientation is rotated by -7° (i.e. clockwise) with respect to the $\langle 01\bar{1} \rangle_{\text{Ag}}$ directions and the b axis $[010]$ of PQ in $(\bar{1}0\bar{2})$ orientation is rotated by $+7^\circ$ (i.e. counterclockwise) with respect to the $\langle 01\bar{1} \rangle_{\text{Ag}}$ directions. An evaluation of the data from the LHS and RHS of the detector was then performed. As expected, no significant differences in the unit-cell vectors (including contact planes, epitaxial relationships and lattice constants) were found. The lattice constants were determined by averaging over all 24 sets of lattice constants. We then obtained $a = 5.059 \pm 0.012$, $b = 8.097 \pm 0.026$, $c = 8.916 \pm 0.032$ Å, $\alpha = 91.64 \pm 0.24^\circ$, $\beta = 92.95 \pm 0.56^\circ$, $\gamma = 94.17 \pm 0.23^\circ$, $V = 363.5$ Å³.

In a last step, we optimized the lattice parameters with respect to the vector lengths q_{xyz} and the components q_z (see Appendix D) and obtained the following values: $a = 5.063$, $b = 8.091$, $c = 8.916$ Å, $\alpha = 91.61^\circ$, $\beta = 92.92^\circ$, $\gamma = 94.13^\circ$, $V = 363.6$ Å³. These parameters differ only slightly from the values given above and the error function $E_{xyz,z}$ decreases only minimally from 0.0113 to 0.0112 Å⁻¹.

The expected peak positions of this solution are plotted together with the two-dimensional reciprocal-space map in Fig. 2(c). A three-dimensional representation of the experimental data and the expected peak positions is given in Fig. 4. In both, a good agreement is observed. The lattice constants we obtain by following this protocol are in excellent agreement with the crystal structure of PQ reported for thin films grown on a highly oriented pyrolytic graphite (HOPG) surface (Simbrunner *et al.*, 2018). Furthermore, comparison of experimental with expected peak intensities shows good

agreement. Therefore, the known crystal structure solution can be used to develop a model of the arrangement of PQ molecules with respect to the Ag(111) surface. Fig. 5(a) shows the situation of the $(\bar{1}0\bar{2})$ contact plane and a b -axis rotation angle of $+7^\circ$ with respect to the high-symmetry direction of the silver surface. Nearly completely flat-lying molecules are found which are rotated with respect to the high-symmetry silver directions. Adjacent molecules are slightly slipped to

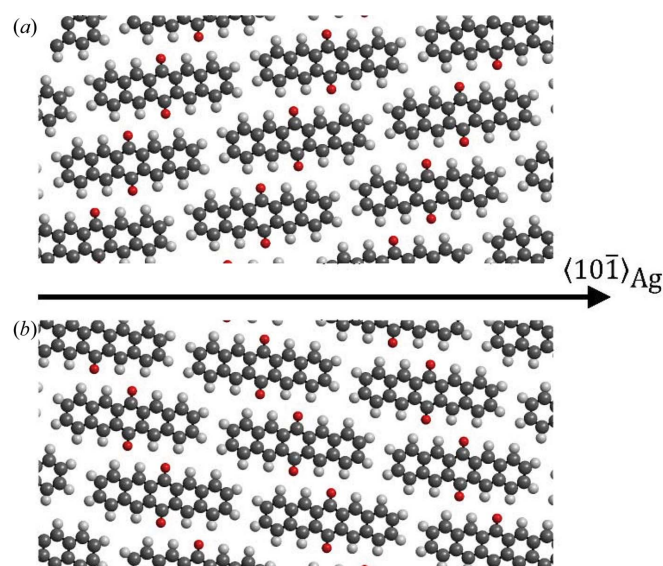


Figure 5

Two different epitaxial alignments of pentacenequinone crystals on the Ag(111) surface, (a) with the (102) plane and (b) with the (102) plane parallel to the surface. The b axis is rotated by $\pm 7^\circ$ with respect to the high-symmetry direction on the Ag(111) surface.

form short contacts between neighbouring oxygen and hydrogen atoms, which highlights the role of hydrogen bonding in the formation of the PQ crystal structure. In turn, for the (102) contact plane a b -axis rotation angle of -7° with respect to the silver high-symmetry direction [*cf.* Fig. 5(*b*)] is found, *i.e.* a rotation of the molecules in the opposite direction.

4. Discussion

We regard our algorithm for the analysis of X-ray diffraction patterns of thin films via rotating the sample to determine reciprocal-lattice vectors advantageous for the following reasons: (i) the lattice vectors of the involved unit cells and their orientation can be determined simultaneously. The method is suitable for implementation of (semi)automatic processing. (ii) Only a few reciprocal vectors are required. Theoretically, only three vectors are sufficient to determine the parameters and orientation of the unit cell if the determinant of the matrix of the corresponding Laue indices is ± 1 . (iii) Indexing is possible even if crystals with different crystallographic unit cells and orientations are present. Depending on measurement accuracy and available boundary conditions, about six to eight related reciprocal vectors may be sufficient for a correct assignment to the corresponding unit cell. The knowledge of a contact plane as determined by available specular diffraction data can be of considerable help for selecting the proper unit-cell vectors. (iv) No previous knowledge of the structure is necessary, and the intensities of the various reflections are not required. For symmetry considerations, however, the diffraction intensities must be included.

We note that our method of combination of three reciprocal-lattice vectors has been suggested before (Duisenberg, 1992; Morawiec, 2017). In both cases this approach is used for solving difficult cases in single-crystal diffractometry such as twin lattices, fragmented crystals and unreliable data. Duisenberg takes the end points of three observed reflection vectors to build the normal to the plane formed by any three of these points. Then all observed points are projected onto this normal. This helps in eliminating spurious vectors which do not belong to the direct cell. Morawiec combines three reciprocal-lattice vectors to calculate the corresponding unit-cell volumes and searches for periodicities to select the vectors that support the definite parallelepiped. This procedure is related to the algorithm we suggest for selecting the proper reciprocal-lattice vectors. In our case, however, the direct unit cell is determined first, and then further reciprocal-lattice vectors are selected.

Immediately switching into real space for finding the unit-cell vectors is advantageous as several possible criteria and boundary conditions may exist for reducing possible solutions: (i) unit-cell volume and parameters, (ii) scalar product criteria (Niggli conditions) and (iii) including information from the specular scan if a contact plane is experimentally determined. To reduce the errors due to experimental imperfections, the lattice vectors of one unit cell are fitted before calculating the

cell parameters and orientation angles. This is accomplished by analytically minimizing error functions, which can be defined both for reciprocal and real space.

Finally, our methodology allows the direct analytical determination of the orientation parameters, *i.e.* the angles ϕ , ψ (or the Miller indices u , v , w of the contact plane) and φ of the rotation matrices. These angles refer to the chosen reference system.

If a very large number of reciprocal vectors are obtained, alternative algorithms may be advantageous. The existing autoindexing method incorporated in *MOSFLM* (Leslie, 1992) – FFT autoindexing routines written by the Rossmann group at Purdue University (Rossmann & van Beek, 1999) – relies on the calculation of many difference vectors between diffraction maxima in reciprocal space (Kabsch, 1993). Preliminary results, however, show that our method is especially effective in analysing epitaxially grown crystallites not only with various orientations but also with various polymorphs.

5. Conclusion

In this work, we present an algorithm for indexing GIXD diffraction patterns obtained with monochromatic radiation, where three-dimensional reciprocal-lattice vectors are determined as is done in single-crystal diffraction experiments. Our method is particularly advantageous if the number of reflections is relatively small or the sample is inhomogeneous and consists of various crystal lattices or orientations, as is commonly found for thin films grown on single-crystalline substrates. For easy access to epitaxial relationships the lattice constants of the involved unit cells and the parameters of the orientation matrix can be determined simultaneously.

APPENDIX A

Determining the rotation angles ψ , ϕ and φ

The rotation parameters ψ and ϕ and the parameters Ω_a , Ω_b and Ω_c can be preferably obtained by using the following equations, which can easily be derived from the expressions in Table 1 and equation (14):

$$\cos \psi = \frac{a_z \cos \gamma - b_z \frac{a}{b}}{\left[a_z^2 + b_z^2 \left(\frac{a}{b} \right)^2 - 2a_z b_z \frac{a}{b} \cos \gamma \right]^{1/2}} \quad (24)$$

$$\begin{aligned} \cos \Phi = & (a_z a^* \cos \beta^* + b_z b^* \cos \alpha^* + c_z c^*) \\ & \left/ \left[a_z^2 \left(\frac{2\pi}{a \sin \gamma} \right)^2 + b_z^2 \left(\frac{2\pi}{b \sin \gamma} \right)^2 - 2a_z b_z \frac{2\pi}{a \sin \gamma} \frac{2\pi}{b \sin \gamma} \cos \gamma \right. \right. \\ & \left. \left. + (a_z a^* \cos \beta^* + b_z b^* \cos \alpha^* + c_z c^*)^2 \right]^{1/2} \right. \end{aligned} \quad (25)$$

$$\cos \Omega_a = \frac{a}{(a^2 - a_z^2)^{1/2}} \frac{a_z \cos \gamma - b_z \frac{a}{b}}{\left[a_z^2 + b_z^2 \left(\frac{a}{b} \right)^2 - 2a_z b_z \frac{a}{b} \cos \gamma \right]^{1/2}} \quad (26)$$

$$\cos \Omega_b = \frac{b}{(b^2 - b_z^2)^{1/2}} \frac{a_z - b_z \frac{a}{b} \cos \gamma}{\left[a_z^2 + b_z^2 \left(\frac{a}{b} \right)^2 - 2a_z b_z \frac{a}{b} \cos \gamma \right]^{1/2}} \quad (27)$$

$$\cos \Omega_c = \frac{c}{(c^2 - c_z^2)^{1/2}} \frac{a_z \cos \alpha - b_z \frac{a}{b} \cos \beta}{\left[a_z^2 + b_z^2 \left(\frac{a}{b} \right)^2 - 2a_z b_z \frac{a}{b} \cos \gamma \right]^{1/2}}. \quad (28)$$

Note that two special cases must be considered:

(i) If $a_z < 0$ (i.e. $u < 0$) then $\psi \rightarrow 2\pi - \psi$ [as ψ is in the interval $[\pi, 2\pi]$, see equation (13)].

(ii) If $a_z = 0$ and $b_z = 0$ (i.e. $u = v = 0$) then $\psi = 0$, $\Phi = 0$, $\Omega_a = 0$, $\Omega_b = \gamma$ and $\cos \Omega_c = \cos(\beta)/r_c$.

If the ratios $a_z/b_z = u/v$, $a_z/c_z = u/w$ and $b_z/c_z = v/w$ are rational numbers, one can conclude that a contact plane (with the Miller indices uvw) exists. If the specular diffraction peak is known, the indices can be directly calculated from $u = (a_z/a)(g_{\text{spec}}/2\pi)$, $v = (b_z/b)(g_{\text{spec}}/2\pi)$ and $w = (c_z/c)(g_{\text{spec}}/2\pi)$.

From Table 1 the following expressions for the phase φ can be deduced:

$$\frac{a_x}{(a^2 - a_z^2)^{1/2}} = \frac{a_x}{(a_x^2 + a_y^2)^{1/2}} = \cos(\varphi + \psi - \Omega_a) \quad (29)$$

$$\frac{a_y}{(a^2 - a_z^2)^{1/2}} = \frac{a_y}{(a_x^2 + a_y^2)^{1/2}} = \sin(\varphi + \psi - \Omega_a). \quad (30)$$

As φ covers the range between 0 and 2π , equations (29) and (30) must be considered. This can be expressed in the following way:

$$\varphi = \begin{cases} \tan^{-1} \frac{a_y}{a_x} - \psi + \Omega_a, & a_x > 0 \\ \tan^{-1} \frac{a_y}{a_x} - \psi + \Omega_a + \pi, & a_x < 0 \end{cases}. \quad (31)$$

Analogously, the following relations are valid:

$$\varphi = \begin{cases} \tan^{-1} \frac{b_y}{b_x} - \psi - \Omega_b, & b_x > 0 \\ \tan^{-1} \frac{b_y}{b_x} - \psi - \Omega_b + \pi, & b_x < 0 \end{cases} \quad (32)$$

$$\varphi = \begin{cases} \tan^{-1} \frac{c_y}{c_x} - \psi - \Omega_c, & c_x > 0 \\ \tan^{-1} \frac{c_y}{c_x} - \psi - \Omega_c + \pi, & c_x < 0 \end{cases}. \quad (33)$$

As φ can be independently calculated from the lattice vectors **a**, **b** and **c**, the accuracy of the result can be checked and a mean value of φ can be determined.

APPENDIX B

Optimizing the matrix of the unit-cell vectors in real space

From equation (23) the error regarding the unit-cell vector **a** with respect to N associated reciprocal-lattice vectors **g_i** and the corresponding Laue indices h_i can be expressed as

$$E_{a,N}(a_x, a_y, a_z) = \left[\frac{1}{N} \sum_{i=1}^N (a_x g_{x,i} + a_y g_{y,i} + a_z g_{z,i} - h_i)^2 \right]^{1/2}. \quad (34)$$

$E_{a,N}$ becomes minimal if

$$\frac{\delta E_{a,N}}{\delta a_x} = \frac{\delta E_{a,N}}{\delta a_y} = \frac{\delta E_{a,N}}{\delta a_z} = 0$$

is fulfilled. From this condition the following relations can be derived:

$$\begin{pmatrix} a_x \\ a_y \\ a_z \end{pmatrix} = 2\pi \mathbf{Q}^{-1} \begin{pmatrix} \sum_{i=1}^N g_{x,i} h_i \\ \sum_{i=1}^N g_{y,i} h_i \\ \sum_{i=1}^N g_{z,i} h_i \end{pmatrix}, \quad (35)$$

where

$$\mathbf{Q} = \begin{pmatrix} \sum_{i=1}^N g_{x,i}^2 & \sum_{i=1}^N g_{x,i} g_{y,i} & \sum_{i=1}^N g_{x,i} g_{z,i} \\ \sum_{i=1}^N g_{x,i} g_{y,i} & \sum_{i=1}^N g_{y,i}^2 & \sum_{i=1}^N g_{y,i} g_{z,i} \\ \sum_{i=1}^N g_{x,i} g_{z,i} & \sum_{i=1}^N g_{y,i} g_{z,i} & \sum_{i=1}^N g_{z,i}^2 \end{pmatrix}. \quad (36)$$

Analogously, the error functions for the cell vectors **b** and **c** with respect to the measured reciprocal-lattice vectors **g_i** and the corresponding Laue indices k_i and l_i , respectively, can be expressed as

$$E_{b,N}(b_x, b_y, b_z) = \left[\frac{1}{N} \sum_{i=1}^N (b_x g_{x,i} + b_y g_{y,i} + b_z g_{z,i} - k_i)^2 \right]^{1/2}, \quad (37)$$

$$E_{c,N}(c_x, c_y, c_z) = \left[\frac{1}{N} \sum_{i=1}^N (c_x g_{x,i} + c_y g_{y,i} + c_z g_{z,i} - l_i)^2 \right]^{1/2}. \quad (38)$$

Then, $E_{b,N}$ and $E_{c,N}$ become minimal for

$$\begin{pmatrix} b_x \\ b_y \\ b_z \end{pmatrix} = 2\pi \mathbf{Q}^{-1} \begin{pmatrix} \sum_{i=1}^N g_{x,i} k_i \\ \sum_{i=1}^N g_{y,i} k_i \\ \sum_{i=1}^N g_{z,i} k_i \end{pmatrix}, \quad (39)$$

$$\begin{pmatrix} c_x \\ c_y \\ c_z \end{pmatrix} = 2\pi \mathbf{Q}^{-1} \begin{pmatrix} \sum_{i=1}^N g_{x,i} l_i \\ \sum_{i=1}^N g_{y,i} l_i \\ \sum_{i=1}^N g_{z,i} l_i \end{pmatrix}. \quad (40)$$

APPENDIX C

Optimizing the matrix of the unit-cell vectors in reciprocal space

In analogy to equations (4) and (9) the reciprocal-lattice vectors **g_i** can be written as

$$\mathbf{g}_i = \begin{pmatrix} a_x^* \\ a_y^* \\ a_z^* \end{pmatrix} h_i + \begin{pmatrix} b_x^* \\ b_y^* \\ b_z^* \end{pmatrix} k_i + \begin{pmatrix} c_x^* \\ c_y^* \\ c_z^* \end{pmatrix} l_i \quad (41)$$

where $a_x^*, a_y^*, a_z^*, b_x^*, b_y^*, b_z^*, c_x^*, c_y^*, c_z^*$ are the components of the reciprocal-space vectors, and h_i, k_i, l_i are the corresponding Laue indices. Then, for N reciprocal-space vectors the error function $E_{x,N}$ can be expressed as

$$E_{x,N}(a_x^*, b_x^*, c_x^*) = \left[\frac{1}{N} \sum_{i=1}^N (a_x^* h_i + b_x^* k_i + c_x^* l_i - q_{x,i})^2 \right]^{1/2} \quad (42)$$

E_x becomes minimal if

$$\frac{\delta E_{x,N}}{\delta a_x^*} = \frac{\delta E_{x,N}}{\delta b_x^*} = \frac{\delta E_{x,N}}{\delta c_x^*} = 0$$

is fulfilled. From this condition the following relations can be derived:

$$\begin{pmatrix} a_x^* \\ b_x^* \\ c_x^* \end{pmatrix} = \mathbf{Q}^{*-1} \begin{pmatrix} \sum_{i=1}^N g_{x,i} h_i \\ \sum_{i=1}^N g_{x,i} k_i \\ \sum_{i=1}^N g_{x,i} l_i \end{pmatrix}, \quad (43)$$

where

$$\mathbf{Q}^* = \begin{pmatrix} \sum_{i=1}^N h_i^2 & \sum_{i=1}^N h_i k_i & \sum_{i=1}^N h_i l_i \\ \sum_{i=1}^N h_i k_i & \sum_{i=1}^N k_i^2 & \sum_{i=1}^N k_i l_i \\ \sum_{i=1}^N h_i l_i & \sum_{i=1}^N k_i l_i & \sum_{i=1}^N l_i^2 \end{pmatrix}. \quad (44)$$

Analogously, the error functions for the cell vectors \mathbf{b} and \mathbf{c} with respect to the measured reciprocal-lattice vectors \mathbf{g}_i and the corresponding Laue indices h_i, k_i and l_i can be expressed as

$$E_{y,N}(a_y^*, b_y^*, c_y^*) = \left[\frac{1}{N} \sum_{i=1}^N (a_y^* h_i + b_y^* k_i + c_y^* l_i - g_{y,i})^2 \right]^{1/2}, \quad (45)$$

$$E_{z,N}(a_z^*, b_z^*, c_z^*) = \left[\frac{1}{N} \sum_{i=1}^N (a_z^* h_i + b_z^* k_i + c_z^* l_i - g_{z,i})^2 \right]^{1/2}. \quad (46)$$

Then, $E_{y,N}$ and $E_{z,N}$ become minimal for

$$\begin{pmatrix} a_y^* \\ b_y^* \\ c_y^* \end{pmatrix} = \mathbf{Q}^{*-1} \begin{pmatrix} \sum_{i=1}^N g_{y,i} h_i \\ \sum_{i=1}^N g_{y,i} k_i \\ \sum_{i=1}^N g_{y,i} l_i \end{pmatrix}, \quad (47)$$

$$\begin{pmatrix} a_z^* \\ b_z^* \\ c_z^* \end{pmatrix} = \mathbf{Q}^{*-1} \begin{pmatrix} \sum_{i=1}^N g_{z,i} h_i \\ \sum_{i=1}^N g_{z,i} k_i \\ \sum_{i=1}^N g_{z,i} l_i \end{pmatrix}. \quad (48)$$

The components of the unit cell in real space can be calculated from the following expression:

$$\mathbf{A} = \begin{pmatrix} a_x & a_y & a_z \\ b_x & b_y & b_z \\ c_x & c_y & c_z \end{pmatrix} = 2\pi \mathbf{A}^{*-1} = 2\pi \begin{pmatrix} a_x^* & b_x^* & c_x^* \\ a_y^* & b_y^* & c_y^* \\ a_z^* & b_z^* & c_z^* \end{pmatrix}^{-1}. \quad (49)$$

APPENDIX D

Analytical optimization of the unit-cell parameters with respect to q_{xyz} and q_z

If the Laue indices are determined and the unit-cell parameters are calculated by evaluating the reciprocal vectors as described above, in a last step they may be optimized with respect to the measured vector length q_{xyz} and the component q_z , which are phase-invariant. This can be accomplished analytically by considering small errors and first-order correction. It is convenient to use the reciprocal cell parameters and minimize the quadratic error function $E_{xyz,z}$:

$$\begin{aligned} E_{xyz,z}^n(a^*, b^*, c^*, \alpha^*, \beta^*, \gamma^*) \\ = \left\{ [E_{xyz}^n(a^*, b^*, c^*, \alpha^*, \beta^*, \gamma^*)]^2 \right. \\ \left. + [E_z^n(a^*, b^*, c^*, \alpha^*, \beta^*, \gamma^*)]^2 \right\}^{1/2}, \end{aligned} \quad (50)$$

where

$$\begin{aligned} E_{xyz}^n = \left[\frac{1}{n} \sum_{i=1}^n \left(g_{xyz,i} + \frac{\delta g_{xyz,i}}{\delta a^*} \varepsilon_{a^*} + \frac{\delta g_{xyz,i}}{\delta b^*} \varepsilon_{b^*} + \frac{\delta g_{xyz,i}}{\delta c^*} \varepsilon_{c^*} \right. \right. \\ \left. \left. + \frac{\delta g_{xyz,i}}{\delta \alpha^*} \varepsilon_{\alpha^*} + \frac{\delta g_{xyz,i}}{\delta \beta^*} \varepsilon_{\beta^*} + \frac{\delta g_{xyz,i}}{\delta \gamma^*} \varepsilon_{\gamma^*} - q_{xyz,i} \right)^2 \right]^{1/2}, \end{aligned} \quad (51)$$

$$\begin{aligned} E_z^n = \left[\frac{1}{n} \sum_{i=1}^n \left(g_{z,i} + \frac{\delta g_{z,i}}{\delta a^*} \varepsilon_{a^*} + \frac{\delta g_{z,i}}{\delta b^*} \varepsilon_{b^*} + \frac{\delta g_{z,i}}{\delta c^*} \varepsilon_{c^*} \right. \right. \\ \left. \left. + \frac{\delta g_{z,i}}{\delta \alpha^*} \varepsilon_{\alpha^*} + \frac{\delta g_{z,i}}{\delta \beta^*} \varepsilon_{\beta^*} + \frac{\delta g_{z,i}}{\delta \gamma^*} \varepsilon_{\gamma^*} - q_{z,i} \right)^2 \right]^{1/2}. \end{aligned} \quad (52)$$

($q_{xyz,i}, q_{z,i}$) are the measured and ($g_{xyz,i}, g_{z,i}$) are the calculated peak positions of the i th reflection, n is the number of reflections and $\varepsilon_{a^*}, \varepsilon_{b^*}, \varepsilon_{c^*}, \varepsilon_{\alpha^*}, \varepsilon_{\beta^*}, \varepsilon_{\gamma^*}$ are the correction terms. $E_{xyz,z}^n$ becomes minimal if

$$\frac{\delta E_{xyz,z}^n}{\delta a^*} = \frac{\delta E_{xyz,z}^n}{\delta b^*} = \frac{\delta E_{xyz,z}^n}{\delta c^*} = \frac{\delta E_{xyz,z}^n}{\delta \alpha^*} = \frac{\delta E_{xyz,z}^n}{\delta \beta^*} = \frac{\delta E_{xyz,z}^n}{\delta \gamma^*} = 0$$

is fulfilled. From this condition the following relation can be derived:

$$\sum_{i=1}^n \begin{pmatrix} \mathbf{f}_{a^*,i}^2 & \mathbf{f}_{a^*,i}\mathbf{f}_{b^*,i} & \mathbf{f}_{a^*,i}\mathbf{f}_{c^*,i} & \mathbf{f}_{a^*,i}\mathbf{f}_{\alpha^*,i} & \mathbf{f}_{a^*,i}\mathbf{f}_{\beta^*,i} & \mathbf{f}_{a^*,i}\mathbf{f}_{\gamma^*,i} \\ \mathbf{f}_{a^*,i}\mathbf{f}_{b^*,i} & \mathbf{f}_{b^*,i}^2 & \mathbf{f}_{b^*,i}\mathbf{f}_{c^*,i} & \mathbf{f}_{b^*,i}\mathbf{f}_{\alpha^*,i} & \mathbf{f}_{b^*,i}\mathbf{f}_{\beta^*,i} & \mathbf{f}_{b^*,i}\mathbf{f}_{\gamma^*,i} \\ \mathbf{f}_{a^*,i}\mathbf{f}_{c^*,i} & \mathbf{f}_{b^*,i}\mathbf{f}_{c^*,i} & \mathbf{f}_{c^*,i}^2 & \mathbf{f}_{c^*,i}\mathbf{f}_{\alpha^*,i} & \mathbf{f}_{c^*,i}\mathbf{f}_{\beta^*,i} & \mathbf{f}_{c^*,i}\mathbf{f}_{\gamma^*,i} \\ \mathbf{f}_{a^*,i}\mathbf{f}_{\alpha^*,i} & \mathbf{f}_{b^*,i}\mathbf{f}_{\alpha^*,i} & \mathbf{f}_{c^*,i}\mathbf{f}_{\alpha^*,i} & \mathbf{f}_{\alpha^*,i}^2 & \mathbf{f}_{\alpha^*,i}\mathbf{f}_{\beta^*,i} & \mathbf{f}_{\alpha^*,i}\mathbf{f}_{\gamma^*,i} \\ \mathbf{f}_{a^*,i}\mathbf{f}_{\beta^*,i} & \mathbf{f}_{b^*,i}\mathbf{f}_{\beta^*,i} & \mathbf{f}_{c^*,i}\mathbf{f}_{\beta^*,i} & \mathbf{f}_{\alpha^*,i}\mathbf{f}_{\beta^*,i} & \mathbf{f}_{\beta^*,i}^2 & \mathbf{f}_{\beta^*,i}\mathbf{f}_{\gamma^*,i} \\ \mathbf{f}_{a^*,i}\mathbf{f}_{\gamma^*,i} & \mathbf{f}_{b^*,i}\mathbf{f}_{\gamma^*,i} & \mathbf{f}_{c^*,i}\mathbf{f}_{\gamma^*,i} & \mathbf{f}_{\alpha^*,i}\mathbf{f}_{\gamma^*,i} & \mathbf{f}_{\beta^*,i}\mathbf{f}_{\gamma^*,i} & \mathbf{f}_{\gamma^*,i}^2 \end{pmatrix} \times \begin{pmatrix} \varepsilon_a^* \\ \varepsilon_b^* \\ \varepsilon_c^* \\ \varepsilon_{\alpha^*}^* \\ \varepsilon_{\beta^*}^* \\ \varepsilon_{\gamma^*}^* \end{pmatrix} = \sum_{i=1}^n \begin{pmatrix} \mathbf{f}_{a^*,i} \\ \mathbf{f}_{b^*,i} \\ \mathbf{f}_{c^*,i} \\ \mathbf{f}_{\alpha^*,i} \\ \mathbf{f}_{\beta^*,i} \\ \mathbf{f}_{\gamma^*,i} \end{pmatrix} \begin{pmatrix} q_{xyz,i} - g_{xyz,i} \\ q_{z,i} - g_{z,i} \end{pmatrix}, \quad (53)$$

where the matrix contains the inner products of the vectors

$$\begin{aligned} \mathbf{f}_{a^*,i} &= \left(\frac{\delta g_{xyz,i}}{\delta a^*}, \frac{\delta g_{z,i}}{\delta a^*} \right), \mathbf{f}_{b^*,i} = \left(\frac{\delta g_{xyz,i}}{\delta b^*}, \frac{\delta g_{z,i}}{\delta b^*} \right), \\ \mathbf{f}_{c^*,i} &= \left(\frac{\delta g_{xyz,i}}{\delta c^*}, \frac{\delta g_{z,i}}{\delta c^*} \right), \mathbf{f}_{\alpha^*,i} = \left(\frac{\delta g_{xyz,i}}{\delta \alpha^*}, \frac{\delta g_{z,i}}{\delta \alpha^*} \right), \\ \mathbf{f}_{\beta^*,i} &= \left(\frac{\delta g_{xyz,i}}{\delta \beta^*}, \frac{\delta g_{z,i}}{\delta \beta^*} \right) \text{ and } \mathbf{f}_{\gamma^*,i} = \left(\frac{\delta g_{xyz,i}}{\delta \gamma^*}, \frac{\delta g_{z,i}}{\delta \gamma^*} \right). \end{aligned}$$

Furthermore, for the length $g_{xyz,i}$, the out-of-plane component $g_{z,i}$ of the i th reciprocal vector and the specular scan g_{spec} the following expressions are valid:

$$g_{xyz,i}^2 = h_i^2 a^{*2} + k_i^2 b^{*2} + l_i^2 c^{*2} + 2h_i k_i a^* b^* \cos \gamma^* + 2h_i l_i a^* c^* \cos \beta^* + 2k_i l_i b^* c^* \cos \alpha^*, \quad (54)$$

$$g_{z,i} = [h_i u a^{*2} + k_i v b^{*2} + l_i w c^{*2} + (h_i v + k_i u) a^* b^* \cos \gamma^* + (h_i w + l_i u) a^* c^* \cos \beta^* + (k_i w + l_i v) b^* c^* \cos \alpha^*] / g_{\text{spec}}, \quad (55)$$

$$g_{\text{spec}} = (u^2 a^{*2} + v^2 b^{*2} + w^2 c^{*2} + 2u v a^* b^* \cos \gamma^* + 2u w a^* c^* \cos \beta^* + 2v w b^* c^* \cos \alpha^*)^{1/2}. \quad (56)$$

From equation (54) the following derivatives of $g_{xyz,i}$ can be obtained:

$$\frac{\delta g_{xyz,i}}{\delta a^*} = \frac{h_i^2 a^* + h_i k_i b^* \cos \gamma^* + h_i l_i c^* \cos \beta^*}{g_{xyz,i}}, \quad (57)$$

$$\frac{\delta g_{xyz,i}}{\delta b^*} = \frac{k_i^2 b^* + h_i k_i a^* \cos \gamma^* + k_i l_i c^* \cos \alpha^*}{g_{xyz,i}}, \quad (58)$$

$$\frac{\delta g_{xyz,i}}{\delta c^*} = \frac{l_i^2 c^* + h_i l_i a^* \cos \beta^* + k_i l_i b^* \cos \alpha^*}{g_{xyz,i}}, \quad (59)$$

$$\frac{\delta g_{xyz,i}}{\delta \alpha^*} = -\frac{k_i l_i b^* c^* \sin \alpha^*}{g_{xyz,i}}, \quad (60)$$

$$\frac{\delta g_{xyz,i}}{\delta \beta^*} = -\frac{h_i l_i a^* c^* \sin \beta^*}{g_{xyz,i}}, \quad (61)$$

$$\frac{\delta g_{xyz,i}}{\delta \gamma^*} = -\frac{h_i k_i a^* b^* \sin \gamma^*}{g_{xyz,i}}. \quad (62)$$

From equation (55), using equation (56), the following derivatives of $g_{z,i}$ result:

$$\begin{aligned} \frac{\delta g_{z,i}}{\delta a^*} &= \frac{a^*}{g_{\text{spec}}} \left(2h_i u - u^2 \frac{g_{z,i}}{g_{\text{spec}}} \right) \\ &+ \frac{b^* \cos \gamma^*}{g_{\text{spec}}} \left(h_i v + k_i u - u v \frac{g_{z,i}}{g_{\text{spec}}} \right) \\ &+ \frac{c^* \cos \beta^*}{g_{\text{spec}}} \left(h_i w + l_i u - u w \frac{g_{z,i}}{g_{\text{spec}}} \right), \end{aligned} \quad (63)$$

$$\begin{aligned} \frac{\delta g_{z,i}}{\delta b^*} &= \frac{b^*}{g_{\text{spec}}} \left(2k_i v - v^2 \frac{g_{z,i}}{g_{\text{spec}}} \right) \\ &+ \frac{a^* \cos \gamma^*}{g_{\text{spec}}} \left(h_i v + k_i u - u v \frac{g_{z,i}}{g_{\text{spec}}} \right) \\ &+ \frac{c^* \cos \alpha^*}{g_{\text{spec}}} \left(k_i w + l_i v - v w \frac{g_{z,i}}{g_{\text{spec}}} \right), \end{aligned} \quad (64)$$

$$\begin{aligned} \frac{\delta g_{z,i}}{\delta c^*} &= \frac{c^*}{g_{\text{spec}}} \left(2l_i w - w^2 \frac{g_{z,i}}{g_{\text{spec}}} \right) \\ &+ \frac{a^* \cos \beta^*}{g_{\text{spec}}} \left(h_i w + l_i u - u w \frac{g_{z,i}}{g_{\text{spec}}} \right) \\ &+ \frac{b^* \cos \alpha^*}{g_{\text{spec}}} \left(k_i w + l_i v - v w \frac{g_{z,i}}{g_{\text{spec}}} \right), \end{aligned} \quad (65)$$

$$\frac{\delta g_{z,i}}{\delta \alpha^*} = -\frac{b^* c^* \sin \alpha^*}{g_{\text{spec}}} \left(k_i w + l_i v - v w \frac{g_{z,i}}{g_{\text{spec}}} \right), \quad (66)$$

$$\frac{\delta g_{z,i}}{\delta \beta^*} = -\frac{a^* c^* \sin \beta^*}{g_{\text{spec}}} \left(h_i w + l_i u - u w \frac{g_{z,i}}{g_{\text{spec}}} \right), \quad (67)$$

$$\frac{\delta g_{z,i}}{\delta \gamma^*} = -\frac{a^* b^* \sin \gamma^*}{g_{\text{spec}}} \left(h_i v + k_i u - u v \frac{g_{z,i}}{g_{\text{spec}}} \right). \quad (68)$$

From equation (52) the correction terms can be determined and added to the corresponding reciprocal cell parameters to obtain the new values. For larger errors it is advantageous to repeat this procedure. The cell parameters in real space are finally obtained by using their relations with the reciprocal-lattice parameters [*c.f.* equation (5)].

Acknowledgements

The authors acknowledge the Elettra Synchrotron Trieste for allocation of beamtime and thank Luisa Barba for assistance in using beamline XRD1.

Funding information

Financial support was given by the Austrian Science Foundation FWF (grant No. P30222). IS acknowledges the support of the Natural Sciences and Engineering Research Council of Canada (NSERC) (funding reference number RGPIN-2018-05092), the Fonds de recherche du Québec – Nature et technologies (FRQNT) (funding reference 2020-NC-271447) and Concordia University. The Jena group acknowledges funding from the German BMBF, grant No. 03VNE1052C.

References

- Birkholz, M. (2006). *Thin Film Analysis by X-ray Scattering*. Weinheim: Wiley-VCH.
- Black, D. R., Windover, D., Henins, A., Filliben, J. & Cline, J. P. (2010). *Adv. X-ray Anal.* **54**, 140–148.
- Breiby, D. W., Bunk, O., Andreassen, J. W., Lemke, H. T. & Nielsen, M. M. (2008). *J. Appl. Cryst.* **41**, 262–271.
- Brinkmann, M., Graff, S., Straupé, C., Wittmann, J. C., Chaumont, C., Nuesch, F., Aziz, A., Schaer, M. & Zuppiroli, L. (2003). *J. Phys. Chem. B*, **107**, 10531–10539.
- Buerger, M. J. (1957). *Z. Kristallogr.* **109**, 42–60.
- Campbell, J. W. (1998). *J. Appl. Cryst.* **31**, 407–413.
- Dejoie, C., Smeets, S., Baerlocher, C., Tamura, N., Pattison, P., Abela, R. & McCusker, L. B. (2015). *IUCrJ*, **2**, 361–370.
- Dienel, T., Loppacher, C., Mannsfeld, S. C. B., Forker, R. & Fritz, T. (2008). *Adv. Mater.* **20**, 959–963.
- Duisenberg, A. J. M. (1992). *J. Appl. Cryst.* **25**, 92–96.
- Fumagalli, E., Campione, M., Raimondo, L., Sassella, A., Moret, M., Barba, L. & Arrighetti, G. (2012). *J. Synchrotron Rad.* **19**, 682–687.
- Gildea, R. J., Waterman, D. G., Parkhurst, J. M., Axford, D., Sutton, G., Stuart, D. I., Sauter, N. K., Evans, G. & Winter, G. (2014). *Acta Cryst.* **D70**, 2652–2666.
- Higashi, T. (1990). *J. Appl. Cryst.* **23**, 253–257.
- Jacobson, R. A. (1976). *J. Appl. Cryst.* **9**, 115–118.
- Jones, A. O. F., Chattopadhyay, B., Geerts, Y. H. & Resel, R. (2016). *Adv. Funct. Mater.* **26**, 2233–2255.
- Kabsch, W. (1988). *J. Appl. Cryst.* **21**, 916–924.
- Kabsch, W. (1993). *J. Appl. Cryst.* **26**, 795–800.
- Kabsch, W. (2010). *Acta Cryst.* **D66**, 125–132.
- Leslie, A. G. W. (1992). *Joint CCP4 and ESF-EACBM Newsletter on Protein Crystallography*, Number 26. Daresbury Laboratory, Warrington, Cheshire, UK.
- Leslie, A. G. W. (2006). *Acta Cryst.* **D62**, 48–57.
- Morawiec, A. (2017). *J. Appl. Cryst.* **50**, 647–650.
- Müllegger, S., Salzmann, I., Resel, R. & Winkler, A. (2003). *Appl. Phys. Lett.* **83**, 4536–4538.
- Müller, B., Cai, C. Z., Kundig, A., Tao, Y., Bosch, M., Jager, M., Bosshard, C. & Gunter, P. (1999). *Appl. Phys. Lett.* **74**, 3110–3112.
- Niggli, P. (1928). *Handbuch der Experimentalphysik*, Vol. 7, Part 1. Leipzig: Akademische Verlagsgesellschaft.
- Otwinowski, Z., Minor, W., Borek, D. & Cymborowski, M. (2012). *International Tables for Crystallography*, Vol. F, ch. 11.4, pp. 282–295. Chichester: John Wiley.
- Powell, H. R. (1999). *Acta Cryst.* **D55**, 1690–1695.
- Qu, G., Kwok, J. J. & Diao, Y. (2016). *Acc. Chem. Res.* **49**, 2756–2764.
- Rossmann, M. G. & van Beek, C. G. (1999). *Acta Cryst.* **D55**, 1631–1640.
- Sauter, N. K., Grosse-Kunstleve, R. W. & Adams, P. D. (2004). *J. Appl. Cryst.* **37**, 399–409.
- Schreiber, F. (2004). *Phys. Status Solidi A*, **201**, 1037–1054.
- Schrode, B., Pachmajer, S., Dohr, M., Röthel, C., Domke, J., Fritz, T., Resel, R. & Werzer, O. (2019). *J. Appl. Cryst.* **52**, 683–689.
- Simbrunner, C., Nabok, D., Hernandez-Sosa, G., Oehzelt, M., Djuric, T., Resel, R., Romaner, L., Puschnig, P., Ambrosch-Draxl, C., Salzmann, I., Schwabegger, G., Watzinger, I. & Sitter, H. (2011). *J. Am. Chem. Soc.* **133**, 3056–3062.
- Simbrunner, J., Hofer, S., Schrode, B., Garmshausen, Y., Hecht, S., Resel, R. & Salzmann, I. (2019). *J. Appl. Cryst.* **52**, 428–439.
- Simbrunner, J., Simbrunner, C., Schrode, B., Röthel, C., Bedoya-Martinez, N., Salzmann, I. & Resel, R. (2018). *Acta Cryst.* **A74**, 373–387.
- Steller, I., Bolotovskiy, R. & Rossmann, M. G. (1997). *J. Appl. Cryst.* **30**, 1036–1040.
- Tolan, M. (1999). *X-ray Scattering from Soft-Matter Thin Films. Springer Tracts in Modern Physics*, Vol. 148. Berlin, Heidelberg: Springer Verlag.
- Witte, G. & Wöll, C. (2004). *J. Mater. Res.* **19**, 1889–1916.

4.5 Other Publications Employing Rotating Grazing Incidence X-ray Diffraction

Further publications employing rotating GIXD with the author of this thesis being co-author are listed below. Depending on the publication, his contributions range from the rotating GIXD measurements to data evaluation and interpretation, figure preparation and manuscript writing/proof reading.

D. E. Braun, A. Rivalta, A. Giunchi, N. Bedoya-Martinez, B. Schrode, E. Venuti, R. G. Della Valle, and O. Werzer. Surface Induced Phenytoin Polymorph. 1. Full Structure Solution by Combining Grazing Incidence X-Ray Diffraction and Crystal Structure Prediction. *Crystal Growth & Design* (Oct. 2019). ISSN: 1528-7483, 1528-7505. DOI: 10.1021/acs.cgd.9b00857

A. Giunchi, A. Rivalta, N. Bedoya-Martínez, B. Schrode, D. E. Braun, O. Werzer, E. Venuti, and R. G. Della Valle. Surface Induced Phenytoin Polymorph. 2. Structure Validation by Comparing Experimental and Density Functional Theory Raman Spectra. *Crystal Growth & Design* (Sept. 2019). ISSN: 1528-7483. DOI: 10.1021/acs.cgd.9b00863

V. Vandalon, A. Sharma, A. Perrotta, B. Schrode, M. A. Verheijen, and A. A. Bol. Polarized Raman Spectroscopy to Elucidate the Texture of Synthesized MoS₂. *Nanoscale* (2019), 10.1039.C9NR08750H. ISSN: 2040-3364, 2040-3372. DOI: 10.1039/C9NR08750H

A. Rivalta, A. Giunchi, L. Pandolfi, T. Salzillo, S. d'Agostino, O. Werzer, B. Schrode, N. Demitri, M. Mas-Torrent, A. Brillante, R. Della Valle, and E. Venuti. Crystal Alignment of Surface Stabilized Polymorph in Thioindigo Films. *Dyes and Pigments* 172 (Jan. 2020), page 107847. ISSN: 01437208. DOI: 10.1016/j.dyepig.2019.107847

4.6 Other Publications Employing Static Grazing Incidence X-ray Diffraction

Publications employing static GIXD with the author of this thesis being co-author are listed below. Depending on the publication, his contributions range from the static GIXD measurements to data evaluation and interpretation, figure creation and manuscript writing/proof reading.

J. Simbrunner, C. Simbrunner, B. Schrode, C. Röthel, N. Bedoya-Martinez, I. Salzmann, and R. Resel. Indexing of Grazing-Incidence X-Ray Diffraction Patterns: The Case of Fibre-Textured Thin Films. *Acta Crystallographica Section A Foundations and Advances* 74.4 (July 2018), pages 373–387. ISSN: 2053-2733. DOI: 10.1107/S2053273318006629

A. Petritz, M. Krammer, E. Sauter, M. Gärtner, G. Nascimbeni, B. Schrode, A. Fian, H. Gold, A. Cojocar, E. Karner-Petritz, R. Resel, A. Terfort, E. Zojer, M. Zharnikov, K. Zojer, and B. Stadlober. Embedded Dipole Self-Assembled Monolayers for Contact Resistance Tuning in p-Type and n-Type Organic Thin Film Transistors and Flexible Electronic Circuits. *Advanced Functional Materials* 28.45 (Nov. 2018), page 1804462. ISSN: 1616301X. DOI: 10.1002/adfm.201804462

M. Rooney, F. Carulli, S. Luzzati, R. Resel, B. Schrode, R. Ruffo, M. Sassi, and L. Beverina. Diketopyrrolopyrrole Latent Pigment-Based Bilayer Solar Cells. *Organic Photonics and Photovoltaics* 6.1 (Dec. 2018), pages 8–16. ISSN: 2299-3177. DOI: 10.1515/oph-2018-0002

J. Simbrunner, S. Hofer, B. Schrode, Y. Garmshausen, S. Hecht, R. Resel, and I. Salzmann. Indexing Grazing-Incidence X-Ray Diffraction Patterns of Thin Films: Lattices of Higher Symmetry. *Journal of Applied Crystallography* 52.2 (Apr. 2019), pages 428–439. DOI: 10.1107/s1600576719003029

T. Stassin, S. Rodríguez-Hemida, B. Schrode, A. J. Cruz, F. Carraro, D. Kravchenko,

4.6 Other Publications Employing Static Grazing Incidence X-ray Diffraction

V. Creemers, I. Stassen, T. Hauffman, D. E. De Vos, P. Falcaro, R. Resel, and R. Ameloot. Vapour-Phase Deposition of Oriented Copper Dicarboxylate Metal-Organic Framework Thin Films. *Chemical Communications* (2019), 10.1039.C9CC05161A. ISSN: 1359-7345, 1364-548X. DOI: 10.1039/C9CC05161A

A. O. F. Jones, R. Resel, B. Schrode, E. Machado Charry, C. Röthel, B. Kunert, I. Salzmann, E. Kontturi, D. Reishofer, and S. Spirk. Structural Order in Cellulose Thin Films Prepared from a Trimethylsilyl Precursor. *Biomacromolecules* (Nov. 2019), acs.biomac.9b01377. ISSN: 1525-7797, 1526-4602. DOI: 10.1021/acs.biomac.9b01377

5 Conclusion

This thesis presented the method of rotating GIXD. This technique is especially suited for crystalline thin-film samples with out-of-plane and an additional in-plane alignment of the crystallites. This is due to the surface sensitivity achieved by limited penetration depths and the possibility of a sample rotation around its surface normal. Rotation allows mapping of large volumes of reciprocal space to gain access to a wide range of the available diffraction information. Rotating GIXD can be applied independent of the reason for the in-plane alignment, *e.g.* very defined epitaxial growth due to the interplay of the adsorbate molecules with the substrate, samples with statistical problems due to a low number of large crystallites or in-plane alignment introduced by sample preparation.

To allow users to employ rotating GIXD several aspects of the experimental setup were discussed in detail (with an emphasis on the XRD1 beamline at the Elettra synchrotron, Trieste, Italy). For example, the detector position plays an important role during measurements, since it defines which part of reciprocal space is accessible. The detailed discussion of further related topics such as sample mounting, common procedures applied in sample alignment, the influence of misalignment on the diffraction patterns and its impact on the lattice constant determination will avoid repetition of errors previously made and will ensure maintaining the current high quality of diffraction data obtained at the XRD1 beamline.

For the evaluation of the rotating GIXD data, the software package GIDVis was presented. GIDVis can be used during several steps of the experiment: In the alignment procedure, it can be conveniently used to extract z -scans and rocking

5 Conclusion

curves from two-dimensional detector images. Then, a calibration measurement can be analysed which subsequently allows the conversion of experimental data to reciprocal space. Several data evaluation features can be used, *e.g.* extracting intensity profiles along different directions of reciprocal space, texture and crystal phase analysis, intensity corrections, *etc.* Furthermore, GIDVis can be used to extract PFs from the available diffraction data. From them, the in-plane-alignment of the crystallites can be determined, independent of the source of the alignment. A MATLAB script was presented for this evaluation step. During this thesis, GIDVis was applied to differentiate the polymorphs of the pharmaceutical molecule carbamazepine, where thin films show statistical problems and thus were measured with rotating GIXD. Additionally, the identification of the crystal structure, out-of-plane and in-plane alignment of crystallites of a thin film of the organic semiconductor P2O epitaxially grown on a single-crystalline metal substrate from rotating GIXD data and PFs was presented.

In case the film crystallizes in an unknown crystal structure, indexing has to be performed, *i.e.* assigning the corresponding hkl indices to the observed diffraction peaks. This requires knowledge of the lattice parameters and the contact plane. Therefore, an algorithm was presented which uses the three-dimensional peak positions from rotating GIXD for the evaluation. Additionally, information about the out-of-plane spacing (*i.e.* perpendicular to the substrate surface) can be used to reduce the number of possible solutions. Although this information cannot be accessed via GIXD measurements, it is typically obtained by simple specular scans. The presented approach was applied to a thin film of the organic semiconducting molecule P2O grown on a single-crystalline metal surface and confirms the already known lattice parameters. Additionally, the algorithm allowed the determination of the in-plane alignment of the crystallites with high accuracy.

Bibliography

- [1] E. Bauer. Phänomenologische Theorie der Kristallabscheidung an Oberflächen. I. *Zeitschrift für Kristallographie – Crystalline Materials* 110.1-6 (Jan. 1958). ISSN: 2196-7105, 2194-4946. DOI: 10.1524/zkri.1958.110.16.372.
- [2] K. Oura, editor. *Surface Science: An Introduction*. Advanced Texts in Physics. Berlin; New York: Springer, 2003. ISBN: 978-3-540-00545-2.
- [3] H. Lüth. *Solid Surfaces, Interfaces and Thin Films*. Graduate Texts in Physics. Berlin, Heidelberg: Springer Berlin Heidelberg, 2010. ISBN: 978-3-642-13591-0 978-3-642-13592-7. DOI: 10.1007/978-3-642-13592-7.
- [4] A. Lopez-Otero. Hot Wall Epitaxy. *Thin Solid Films* 49.1 (Feb. 1978), pages 3–57. ISSN: 00406090. DOI: 10.1016/0040-6090(78)90309-7.
- [5] B. Wedl, R. Resel, G. Leising, B. Kunert, I. Salzmann, M. Oehzelt, N. Koch, A. Vollmer, S. Duhm, O. Werzer, G. Gbabode, M. Sferrazza, and Y. Geerts. Crystallisation Kinetics in Thin Films of Dihexyl-Terthiophene: The Appearance of Polymorphic Phases. *RSC Advances* 2.10 (2012), page 4404. ISSN: 2046-2069. DOI: 10.1039/c2ra20272g.
- [6] B. M. Ocko, A. Braslau, P. S. Pershan, J. Als-Nielsen, and M. Deutsch. Quantized Layer Growth at Liquid-Crystal Surfaces. *Physical Review Letters* 57.1 (July 1986), pages 94–97. ISSN: 0031-9007. DOI: 10.1103/PhysRevLett.57.94.

- [7] M. Dohr, H. M. A. Ehmman, A. O. F. Jones, I. Salzmman, Q. Shen, C. Teichert, C. Ruzié, G. Schweicher, Y. H. Geerts, R. Resel, M. Sferrazza, and O. Werzer. Reversibility of Temperature Driven Discrete Layer-by-Layer Formation of Dioctyl-Benzothieno-Benzothiophene Films. *Soft Matter* 13.12 (2017), pages 2322–2329. ISSN: 1744-683X, 1744-6848. DOI: 10.1039/C6SM02541B.
- [8] R. L. Schwoebel and E. J. Shipsey. Step Motion on Crystal Surfaces. *Journal of Applied Physics* 37.10 (Sept. 1966), pages 3682–3686. ISSN: 0021-8979, 1089-7550. DOI: 10.1063/1.1707904.
- [9] Z. Zhang. Atomistic Processes in the Early Stages of Thin-Film Growth. *Science* 276.5311 (Apr. 1997), pages 377–383. ISSN: 00368075, 10959203. DOI: 10.1126/science.276.5311.377.
- [10] A. Abdellah, D. Baierl, B. Fabel, P. Lugli, and G. Scarpa. “Exploring Spray Technology for the Fabrication of Organic Devices Based on Poly(3-Hexylthiophene)”. *2009 9th IEEE Conference on Nanotechnology (IEEE-NANO)*. July 2009, pages 831–934. ISBN: 1944-9399.
- [11] J. Smith, R. Hamilton, Y. Qi, A. Kahn, D. D. C. Bradley, M. Heeney, I. McCulloch, and T. D. Anthopoulos. The Influence of Film Morphology in High-Mobility Small-Molecule:Polymer Blend Organic Transistors. *Advanced Functional Materials* 20.14 (June 2010), pages 2330–2337. ISSN: 1616301X, 16163028. DOI: 10.1002/adfm.201000427.
- [12] A. A. Virkar, S. Mannsfeld, Z. Bao, and N. Stingelin. Organic Semiconductor Growth and Morphology Considerations for Organic Thin-Film Transistors. *Advanced Materials* 22.34 (Sept. 2010), pages 3857–3875. ISSN: 09359648. DOI: 10.1002/adma.200903193.
- [13] Y. Diao, L. Shaw, Z. Bao, and S. C. B. Mannsfeld. Morphology Control Strategies for Solution-Processed Organic Semiconductor Thin Films. *Energy Environ. Sci.* 7.7 (2014), pages 2145–2159. ISSN: 1754-5692, 1754-5706. DOI: 10.1039/C4EE00688G.

- [14] M. Truger, O. M. Roscioni, C. Röthel, D. Kriegner, C. Simbrunner, R. Ahmed, E. D. Głowacki, J. Simbrunner, I. Salzmann, A. M. Coclite, A. O. F. Jones, and R. Resel. Surface-Induced Phase of Tyrian Purple (6,6'-Dibromoindigo): Thin Film Formation and Stability. *Crystal Growth & Design* 16.7 (July 2016), pages 3647–3655. ISSN: 1528-7483, 1528-7505. DOI: 10.1021/acs.cgd.6b00104.
- [15] H. Marchetto, U. Groh, T. Schmidt, R. Fink, H.-J. Freund, and E. Umbach. Influence of Substrate Morphology on Organic Layer Growth: PTCDA on Ag(111). *Chemical Physics* 325.1 (June 2006), pages 178–184. ISSN: 03010104. DOI: 10.1016/j.chemphys.2006.01.006.
- [16] G. Hlawacek and C. Teichert. Nucleation and Growth of Thin Films of Rod-like Conjugated Molecules. *Journal of Physics: Condensed Matter* 25.14 (Apr. 2013), page 143202. ISSN: 0953-8984, 1361-648X. DOI: 10.1088/0953-8984/25/14/143202.
- [17] H. Spreitzer, B. Kaufmann, C. Ruzié, C. Röthel, T. Arnold, Y. H. Geerts, C. Teichert, R. Resel, and A. O. F. Jones. Alkyl Chain Assisted Thin Film Growth of 2,7-Dioctyloxy-Benzothienobenzothiophene. *Journal of Materials Chemistry C* 7.27 (2019), pages 8477–8484. ISSN: 2050-7526, 2050-7534. DOI: 10.1039/C9TC01979K.
- [18] H. Jiang, X. Yang, Z. Cui, Y. Liu, H. Li, W. Hu, Y. Liu, and D. Zhu. Phase Dependence of Single Crystalline Transistors of Tetrathiafulvalene. *Applied Physics Letters* 91.12 (Sept. 2007), page 123505. ISSN: 0003-6951, 1077-3118. DOI: 10.1063/1.2784970.
- [19] O. D. Jurchescu, D. A. Mourey, S. Subramanian, S. R. Parkin, B. M. Vogel, J. E. Anthony, T. N. Jackson, and D. J. Gundlach. Effects of Polymorphism on Charge Transport in Organic Semiconductors. *Physical Review B* 80.8 (Aug. 2009), page 085201. ISSN: 1098-0121, 1550-235X. DOI: 10.1103/PhysRevB.80.085201.
- [20] S. Riera-Galindo, A. Tamayo, and M. Mas-Torrent. Role of Polymorphism and Thin-Film Morphology in Organic Semiconductors Processed by Solution

- Shearing. *ACS Omega* 3.2 (Feb. 2018), pages 2329–2339. ISSN: 2470-1343, 2470-1343. DOI: 10.1021/acsomega.8b00043.
- [21] C. Winkler, A. Jeindl, F. Mayer, O. T. Hofmann, R. Tonner, and E. Zojer. Understanding the Correlation between Electronic Coupling and Energetic Stability of Molecular Crystal Polymorphs: The Instructive Case of Quinacridone. *Chemistry of Materials* 31.17 (Sept. 2019), pages 7054–7069. ISSN: 0897-4756, 1520-5002. DOI: 10.1021/acs.chemmater.9b01807.
- [22] J.-F. Liu and W. A. Ducker. Surface-Induced Phase Behavior of Alkyltrimethylammonium Bromide Surfactants Adsorbed to Mica, Silica, and Graphite. *The Journal of Physical Chemistry B* 103.40 (Oct. 1999), pages 8558–8567. ISSN: 1520-6106, 1520-5207. DOI: 10.1021/jp991685w.
- [23] S. Schiefer, M. Huth, A. Dobrinevski, and B. Nickel. Determination of the Crystal Structure of Substrate-Induced Pentacene Polymorphs in Fiber Structured Thin Films. *Journal of the American Chemical Society* 129.34 (Aug. 2007), pages 10316–10317. ISSN: 0002-7863, 1520-5126. DOI: 10.1021/ja0730516.
- [24] G. Gbabode, N. Dumont, F. Quist, G. Schweicher, A. Moser, P. Viville, R. Lazzaroni, and Y. H. Geerts. Substrate-Induced Crystal Plastic Phase of a Discotic Liquid Crystal. *Advanced Materials* 24.5 (Feb. 2012), pages 658–662. ISSN: 09359648. DOI: 10.1002/adma.201103739.
- [25] A. O. F. Jones, B. Chattopadhyay, Y. H. Geerts, and R. Resel. Substrate-Induced and Thin-Film Phases: Polymorphism of Organic Materials on Surfaces. *Advanced Functional Materials* 26.14 (Apr. 2016), pages 2233–2255. ISSN: 1616301X. DOI: 10.1002/adfm.201503169.
- [26] U. F. Kocks, C. N. Tomé, and H.-R. Wenk, editors. *Texture and Anisotropy: Preferred Orientations in Polycrystals and Their Effect on Materials Properties*. OCLC: 247162037. Cambridge: Cambridge Univ. Press, 1998. ISBN: 978-0-521-46516-8.
- [27] S. Galindo, A. Tamayo, F. Leonardi, and M. Mas-Torrent. Control of Polymorphism and Morphology in Solution Sheared Organic Field-Effect Transis-

- tors. *Advanced Functional Materials* 27.25 (July 2017), page 1700526. ISSN: 1616301X. DOI: 10.1002/adfm.201700526.
- [28] E. Hadjittofis, M. A. Isbell, V. Karde, S. Varghese, C. Ghoroi, and J. Y. Y. Heng. Influences of Crystal Anisotropy in Pharmaceutical Process Development. *Pharmaceutical Research* 35.5 (May 2018), page 100. ISSN: 0724-8741, 1573-904X. DOI: 10.1007/s11095-018-2374-9.
- [29] D. Stifter and H. Sitter. Hot Wall Epitaxy of C₆₀ Thin Films on Mica. *Applied Physics Letters* 66.6 (Feb. 1995), pages 679–681. ISSN: 0003-6951, 1077-3118. DOI: 10.1063/1.114097.
- [30] A. O. F. Jones, Y. H. Geerts, J. Karpinska, A. R. Kennedy, R. Resel, C. Röthel, C. Ruzié, O. Werzer, and M. Sferrazza. Substrate-Induced Phase of a [1]Benzothieno[3,2-*b*]Benzothiophene Derivative and Phase Evolution by Aging and Solvent Vapor Annealing. *ACS Applied Materials & Interfaces* 7.3 (Jan. 2015), pages 1868–1873. ISSN: 1944-8244, 1944-8252. DOI: 10.1021/am5075908.
- [31] D. Reischl, C. Röthel, P. Christian, E. Roblegg, H. M. A. Ehmann, I. Salzmann, and O. Werzer. Surface-Induced Polymorphism as a Tool for Enhanced Dissolution: The Example of Phenytoin. *Crystal Growth & Design* 15.9 (Sept. 2015), pages 4687–4693. ISSN: 1528-7483, 1528-7505. DOI: 10.1021/acs.cgd.5b01002.
- [32] I. K. Robinson and D. J. Tweet. Surface X-Ray Diffraction. *Reports on Progress in Physics* 55.5 (May 1992), pages 599–651. ISSN: 0034-4885, 1361-6633. DOI: 10.1088/0034-4885/55/5/002.
- [33] M. Birkholz, P. F. Fewster, and C. Genzel. *Thin Film Analysis by X-Ray Scattering*. Weinheim: Wiley-VCH, 2006. ISBN: 978-3-527-31052-4.
- [34] B. Schrode, S. Pachmajer, M. Dohr, C. Röthel, J. Domke, T. Fritz, R. Resel, and O. Werzer. *GIDVis*: A Comprehensive Software Tool for Geometry-Independent Grazing-Incidence X-ray Diffraction Data Analysis and Pole-Figure Calculations. *Journal of Applied Crystallography* 52.3 (June 2019), pages 683–689. ISSN: 1600-5767. DOI: 10.1107/S1600576719004485.

- [35] B. Schrode, B. Bodak, H. Riegler, A. Zimmer, P. Christian, and O. Werzer. Solvent Vapor Annealing of Amorphous Carbamazepine Films for Fast Polymorph Screening and Dissolution Alteration. *ACS Omega* 2.9 (Sept. 2017), pages 5582–5590. ISSN: 2470-1343, 2470-1343. DOI: 10.1021/acsomega.7b00783.
- [36] J. Simbrunner, B. Schrode, J. Domke, T. Fritz, I. Salzmann, and R. Resel. An Efficient Method for Indexing Grazing-Incidence X-ray Diffraction Data of Epitaxially Grown Thin Films. *Acta Crystallographica Section A Foundations and Advances* 76.3 (May 2020). ISSN: 2053-2733. DOI: 10.1107/S2053273320001266.
- [37] D. W. Bennett. *Understanding Single-Crystal X-Ray Crystallography*. Weinheim: Wiley-VCH, 2010. ISBN: 978-3-527-32677-8 978-3-527-32794-2.
- [38] C. Weissmantel, C. Hamann, and H. Burghardt. *Grundlagen der Festkörperphysik*. 4., bearbeitete Auflage. OCLC: 75607926. Heidelberg, Leipzig: Johann Ambrosius Barth, 1995. ISBN: 978-3-335-00421-9.
- [39] T. Hahn, editor. *International Tables for Crystallography. Volume A: Space-Group Symmetry*. 5th edition, reprinted with corrections. OCLC: 255316244. Dordrecht: Springer, 2005. ISBN: 978-0-7923-6590-7.
- [40] C. S. Weiss. Über eine verbesserte Methode für die Bezeichnung der verschiedenen Flächen eines Kristallisationssystemes. *Abhandlungen der Königlichen Preussischen Akademie der Wissenschaften zu Berlin* (1817), pages 286–336.
- [41] W. H. Miller. *A Treatise on Crystallography*. 1839.
- [42] R. Resel and B. Schrode. Guide for the Exercise X-Ray Scattering (Jan. 2018).
- [43] E. A. Wood. Vocabulary of Surface Crystallography. *Journal of Applied Physics* 35.4 (Apr. 1964), pages 1306–1312. ISSN: 0021-8979, 1089-7550. DOI: 10.1063/1.1713610.

- [44] F. Jona, J. A. Strozier, and W. S. Yang. Low-Energy Electron Diffraction for Surface Structure Analysis. *Reports on Progress in Physics* 45.5 (May 1982), pages 527–585. ISSN: 0034-4885, 1361-6633. DOI: 10.1088/0034-4885/45/5/002.
- [45] H. E. Farnsworth. Penetration of Low Speed Diffracted Electrons. *Physical Review* 49.8 (Apr. 1936), pages 605–609. DOI: 10.1103/PhysRev.49.605.
- [46] E. Prince, editor. *International Tables for Crystallography. Volume C: Mathematical, Physical and Chemical Tables*. 3rd edition. OCLC: 249097712. Dordrecht, Boston, London: Kluwer Academic Publishers, 2004. ISBN: 978-1-4020-1900-5.
- [47] R. W. G. Wyckoff. *Crystal Structures*. Second. Volume 1. Interscience Publishers, 1963.
- [48] J. Simbrunner, C. Simbrunner, B. Schrode, C. Röthel, N. Bedoya-Martinez, I. Salzmann, and R. Resel. Indexing of Grazing-Incidence X-Ray Diffraction Patterns: The Case of Fibre-Textured Thin Films. *Acta Crystallographica Section A Foundations and Advances* 74.4 (July 2018), pages 373–387. ISSN: 2053-2733. DOI: 10.1107/S2053273318006629.
- [49] D. M. Mattox. *Handbook of Physical Vapor Deposition (PVD) Processing*. 2. ed. OCLC: 845532687. Amsterdam: Elsevier, 2010. ISBN: 978-0-8155-2037-5.
- [50] D. M. Dobkin and M. K. Zuraw. *Principles of Chemical Vapor Deposition*. OCLC: 851366869. Dordrecht: Springer Netherlands, 2003. ISBN: 978-94-017-0369-7.
- [51] S. R. Forrest. Ultrathin Organic Films Grown by Organic Molecular Beam Deposition and Related Techniques. *Chemical Reviews* 97.6 (Oct. 1997), pages 1793–1896. ISSN: 0009-2665, 1520-6890. DOI: 10.1021/cr941014o.
- [52] T. F. Kuech and T. Nishinaga, editors. *Handbook of Crystal Growth. Vol. 3 Pt. A: Thin Films and Epitaxy Basic Techniques*. 2. ed. OCLC: 931850001. Amsterdam: Elsevier, 2015. ISBN: 978-0-444-63339-2 978-0-444-63304-0.
- [53] F. Schreiber. Organic Molecular Beam Deposition: Growth Studies beyond the First Monolayer. *physica status solidi (a)* 201.6 (May 2004), pages 1037–1054. ISSN: 0031-8965, 1521-396X. DOI: 10.1002/pssa.200404334.

Bibliography

- [54] C. Reese, M. Roberts, M.-m. Ling, and Z. Bao. Organic Thin Film Transistors. *Materials Today* 7.9 (Sept. 2004), pages 20–27. ISSN: 13697021. DOI: 10.1016/S1369-7021(04)00398-0.
- [55] C. J. Heffelfinger and R. L. Burton. X-Ray Determination of the Crystallite Orientation Distributions of Polyethylene Terephthalate Films. *Journal of Polymer Science* 47.149 (Nov. 1960), pages 289–306. ISSN: 00223832, 15426238. DOI: 10.1002/pol.1960.1204714926.
- [56] A. Pichler, R. Resel, A. Neuhold, T. Dingemans, G. Schwabegger, C. Simbrunner, M. Moret, and I. Salzmann. Crystal Structure Determination of Organic Thin-Films: The Example of 2,2':6',2''-Ternaphthalene. *Zeitschrift für Kristallographie – Crystalline Materials* 229.5 (Jan. 2014). ISSN: 2196-7105, 2194-4946. DOI: 10.1515/zkri-2013-1704.
- [57] F. Otto, T. Huempfer, M. Schaal, C. Udhardt, L. Vorbrink, B. Schroeter, R. Forker, and T. Fritz. Ordered Growth and Electronic Properties of 1,2:8,9-Dibenzopentacene (*Trans*-DBPen) on Ag(111). *The Journal of Physical Chemistry C* 122.15 (Apr. 2018), pages 8348–8355. ISSN: 1932-7447, 1932-7455. DOI: 10.1021/acs.jpcc.8b00095.
- [58] K. Glöckler, C. Seidel, A. Soukopp, M. Sokolowski, E. Umbach, M. Böhringer, R. Berndt, and W.-D. Schneider. Highly Ordered Structures and Submolecular Scanning Tunnelling Microscopy Contrast of PTCDA and DM-PBDCI Monolayers on Ag(111) and Ag(110). *Surface Science* 405.1 (May 1998), pages 1–20. ISSN: 00396028. DOI: 10.1016/S0039-6028(97)00888-1.
- [59] C. Röthel, M. Radziown, R. Resel, A. Grois, C. Simbrunner, and O. Werzer. Crystal Alignment of Caffeine Deposited onto Single Crystal Surfaces via Hot-Wall Epitaxy. *CrystEngComm* 19.21 (2017), pages 2936–2945. ISSN: 1466-8033. DOI: 10.1039/C7CE00515F.
- [60] G. Koller, R. Blyth, S. Sardar, F. Netzer, and M. Ramsey. Growth of Ordered Bithiophene Layers on the p(2×1)O Reconstructed Cu(110) Surface. *Surface Science* 536.1-3 (June 2003), pages 155–165. ISSN: 00396028. DOI: 10.1016/S0039-6028(03)00592-2.

- [61] R. Resel, M. Koini, J. Novak, S. Berkebile, G. Koller, and M. Ramsey. Epitaxial Order Driven by Surface Corrugation: Quinquephenyl Crystals on a Cu(110)-(2×1)O Surface. *Crystals* 9.7 (July 2019), page 373. ISSN: 2073-4352. DOI: 10.3390/cryst9070373.
- [62] S. Pachmajer, O. Werzer, C. Mennucci, F. Buatier de Mongeot, and R. Resel. Biaxial Growth of Pentacene on Rippled Silica Surfaces Studied by Rotating Grazing Incidence X-Ray Diffraction. *Journal of Crystal Growth* 519 (Aug. 2019), pages 69–76. ISSN: 00220248. DOI: 10.1016/j.jcrysgro.2019.05.013.
- [63] M. Era, T. Tsutsui, and S. Saito. Polarized Electroluminescence from Oriented *P*-sexiphenyl Vacuum-deposited Film. *Applied Physics Letters* 67.17 (Oct. 1995), pages 2436–2438. ISSN: 0003-6951, 1077-3118. DOI: 10.1063/1.114599.
- [64] A. Rivalta, A. Giunchi, L. Pandolfi, T. Salzillo, S. d’Agostino, O. Werzer, B. Schrode, N. Demitri, M. Mas-Torrent, A. Brillante, R. Della Valle, and E. Venuti. Crystal Alignment of Surface Stabilized Polymorph in Thioindigo Films. *Dyes and Pigments* 172 (Jan. 2020), page 107847. ISSN: 01437208. DOI: 10.1016/j.dyepig.2019.107847.
- [65] L. E. Alexander. *X-Ray Diffraction Methods in Polymer Science*. Huntington, N.Y: Krieger, 1979. ISBN: 978-0-88275-801-5.
- [66] L. Royer. Recherches expérimentales sur l’épitanie ou orientation mutuelle des cristaux d’espèces différentes. *Bulletin de la Société française de Minéralogie* 51 (1928), pages 7–159.
- [67] M. Gebhardt and A. Neuhaus. *Epitanie-Daten anorganischer und organischer Kristalle*. Edited by K.-H. Hellwege, A. M. Hellwege, and K.-H. Hellwege. Volume Gruppe III, Band 8. Landolt-Börnstein – Zahlenwerte und Funktionen aus Naturwissenschaften und Technik. Berlin, Heidelberg, New York: Springer, 1972.
- [68] A. Hoshino, S. Isoda, H. Kurata, and T. Kobayashi. Scanning Tunneling Microscope Contrast of Perylene-3,4,9,10-tetracarboxylic-dianhydride on Graphite and Its Application to the Study of Epitanie. *Journal of Applied*

Bibliography

- Physics* 76.7 (Oct. 1994), pages 4113–4120. ISSN: 0021-8979, 1089-7550. DOI: 10.1063/1.357361.
- [69] D. E. Hooks, T. Fritz, and M. D. Ward. Epitaxy and Molecular Organization on Solid Substrates. *Advanced Materials* 13.4 (Feb. 2001), pages 227–241. ISSN: 0935-9648. DOI: 10.1002/1521-4095(200102)13:4<227::AID-ADMA227>3.0.CO;2-P.
- [70] A. Hoshino, S. Isoda, H. Kurata, T. Kobayashi, and Y. Yamashita. Prediction of the Epitaxial Orientation of Ultrathin Organic Films on Graphite. *Japanese Journal of Applied Physics* 34 (1995), pages 3858–3863.
- [71] T. Schmitz-Hübsch, T. Fritz, F. Sellam, R. Staub, and K. Leo. Epitaxial Growth of 3,4,9,10-Perylene-Tetracarboxylic-Dianhydride on Au(111): A STM and RHEED Study. *Physical Review B* 55.12 (Mar. 1997), pages 7972–7976. ISSN: 0163-1829, 1095-3795. DOI: 10.1103/PhysRevB.55.7972.
- [72] R. Resel, T. Haber, O. Lengyel, H. Sitter, F. Balzer, and H.-G. Rubahn. Origins for Epitaxial Order of Sexiphenyl Crystals on Muscovite(001). *Surface and Interface Analysis* 41.9 (Sept. 2009), pages 764–770. ISSN: 01422421, 10969918. DOI: 10.1002/sia.3095.
- [73] A. C. Hillier and M. D. Ward. Epitaxial Interactions between Molecular Overlayers and Ordered Substrates. *Physical Review B* 54.19 (Nov. 1996), pages 14037–14051. ISSN: 0163-1829, 1095-3795. DOI: 10.1103/PhysRevB.54.14037.
- [74] S. C. B. Mannsfeld and T. Fritz. Understanding Organic–Inorganic Heteroepitaxial Growth of Molecules on Crystalline Substrates: Experiment and Theory. *Physical Review B* 71.23 (June 2005), page 235405. ISSN: 1098-0121, 1550-235X. DOI: 10.1103/PhysRevB.71.235405.
- [75] S. C. B. Mannsfeld and T. Fritz. Advanced Modelling of Epitaxial Ordering of Organic Layers on Crystalline Surfaces. *Modern Physics Letters B* 20.11 (May 2006), pages 585–605. ISSN: 0217-9849, 1793-6640. DOI: 10.1142/S0217984906011189.

- [76] G. Copie, Y. Makoudi, C. Krzeminski, F. Chérioux, F. Palmino, S. Lamare, B. Grandidier, and F. Cleri. Atomic Scale Modeling of Two-Dimensional Molecular Self-Assembly on a Passivated Si Surface. *The Journal of Physical Chemistry C* 118.24 (June 2014), pages 12817–12825. ISSN: 1932-7447, 1932-7455. DOI: 10.1021/jp501955v.
- [77] T. J. Roussel, E. Barrena, C. Ocal, and J. Faraudo. Predicting Supramolecular Self-Assembly on Reconstructed Metal Surfaces. *Nanoscale* 6.14 (2014), pages 7991–8001. ISSN: 2040-3364, 2040-3372. DOI: 10.1039/C4NR01987C.
- [78] M. Scherbela, L. Hörmann, A. Jeindl, V. Obersteiner, and O. T. Hofmann. Charting the Energy Landscape of Metal/Organic Interfaces via Machine Learning. *Physical Review Materials* 2.4 (Apr. 2018), page 043803. ISSN: 2475-9953. DOI: 10.1103/PhysRevMaterials.2.043803.
- [79] L. Hörmann, A. Jeindl, A. T. Egger, M. Scherbela, and O. T. Hofmann. SAMPLE: Surface Structure Search Enabled by Coarse Graining and Statistical Learning. *Computer Physics Communications* 244 (Nov. 2019), pages 143–155. ISSN: 00104655. DOI: 10.1016/j.cpc.2019.06.010.
- [80] G. Ertl. Untersuchung von Oberflächenreaktionen mittels Beugung langsamer Elektronen (LEED). *Surface Science* 6.2 (Feb. 1967), pages 208–232. ISSN: 00396028. DOI: 10.1016/0039-6028(67)90005-2.
- [81] R. F. Howe, R. N. Lamb, K. Wandelt, and H. K. V. Lotsch, editors. *Surface Science: Principles and Applications*. Volume 73. Springer Proceedings in Physics. Berlin, Heidelberg: Springer Berlin Heidelberg, 1993. ISBN: 978-3-642-84935-0 978-3-642-84933-6. DOI: 10.1007/978-3-642-84933-6.
- [82] R. E. Schlier and H. E. Farnsworth. Structure and Adsorption Characteristics of Clean Surfaces of Germanium and Silicon. *The Journal of Chemical Physics* 30.4 (Apr. 1959), pages 917–926. ISSN: 0021-9606, 1089-7690. DOI: 10.1063/1.1730126.
- [83] G. Binnig, H. Rohrer, C. Gerber, and E. Weibel. 7×7 Reconstruction on Si(111) Resolved in Real Space. *Physical Review Letters* 50.2 (Jan. 1983), pages 120–123. ISSN: 0031-9007. DOI: 10.1103/PhysRevLett.50.120.

Bibliography

- [84] R. L. Park and H. H. Madden. Annealing Changes on the (100) Surface of Palladium and Their Effect on CO Adsorption. *Surface Science* 11.2 (July 1968), pages 188–202. ISSN: 00396028. DOI: 10.1016/0039-6028(68)90066-6.
- [85] R. Forker, M. Meissner, and T. Fritz. Classification of Epitaxy in Reciprocal and Real Space: Rigid versus Flexible Lattices. *Soft Matter* 13.9 (2017), pages 1748–1758. ISSN: 1744-683X, 1744-6848. DOI: 10.1039/C6SM02688E.
- [86] S. C. B. Mannsfeld, K. Leo, and T. Fritz. Line-on-Line Coincidence: A New Type of Epitaxy Found in Organic-Organic Heterolayers. *Physical Review Letters* 94.5 (Feb. 2005), page 056104. ISSN: 0031-9007, 1079-7114. DOI: 10.1103/PhysRevLett.94.056104.
- [87] M. von Laue. Röntgenstrahlinterferenzen. *Physikalische Zeitschrift* 14.22/23 (1913), pages 1075–1079.
- [88] W. H. Bragg and W. L. Bragg. The Reflection of X-Rays by Crystals. *Proceedings of the Royal Society A: Mathematical, Physical and Engineering Sciences* 88.605 (July 1913), pages 428–438. ISSN: 1364-5021, 1471-2946. DOI: 10.1098/rspa.1913.0040.
- [89] S. Gaudet, K. De Keyser, S. Lambert-Milot, J. Jordan-Sweet, C. Detavernier, C. Lavoie, and P. Desjardins. Three Dimensional Reciprocal Space Measurement by X-Ray Diffraction Using Linear and Area Detectors: Applications to Texture and Defects Determination in Oriented Thin Films and Nanoprecipitates. *Journal of Vacuum Science & Technology A: Vacuum, Surfaces, and Films* 31.2 (Mar. 2013), page 021505. ISSN: 0734-2101, 1520-8559. DOI: 10.1116/1.4789984.
- [90] C. Mocuta, M.-I. Richard, J. Fouet, S. Stanescu, A. Barbier, C. Guichet, O. Thomas, S. Hustache, A. V. Zozulya, and D. Thiaudière. Fast Pole Figure Acquisition Using Area Detectors at the DiffAbs Beamline – Synchrotron SOLEIL. *Journal of Applied Crystallography* 46.6 (Dec. 2013), pages 1842–1853. ISSN: 0021-8898. DOI: 10.1107/S0021889813027453.
- [91] J. Simbrunner, S. Hofer, B. Schrode, Y. Garmshausen, S. Hecht, R. Resel, and I. Salzmann. Indexing Grazing-Incidence X-Ray Diffraction Patterns of

- Thin Films: Lattices of Higher Symmetry. *Journal of Applied Crystallography* 52.2 (Apr. 2019), pages 428–439. DOI: 10.1107/s1600576719003029.
- [92] M. J. Buerger. Reduced Cells. *Zeitschrift für Kristallographie – Crystalline Materials* 109.1-6 (Jan. 1957). ISSN: 2196-7105, 2194-4946. DOI: 10.1524/zkri.1957.109.16.42.
- [93] P. Niggli. “Krystallographische und strukturtheoretische Grundbegriffe”. *Handbuch der Experimentalphysik*. Edited by W. Wien and F. Harms. Volume 7. Leipzig: Akademische Verlagsgesellschaft, 1928.
- [94] A. Santoro and A. D. Mighell. Determination of Reduced Cells. *Acta Crystallographica Section A* 26.1 (Jan. 1970), pages 124–127. ISSN: 0567-7394. DOI: 10.1107/S0567739470000177.
- [95] A. O. F. Jones, C. Röthel, R. Lassnig, O. N. Bedoya-Martínez, P. Christian, I. Salzmann, B. Kunert, A. Winkler, and R. Resel. Solution of an Elusive Pigment Crystal Structure from a Thin Film: A Combined X-Ray Diffraction and Computational Study. *CrystEngComm* 19.14 (2017), pages 1902–1911. ISSN: 1466-8033. DOI: 10.1039/C7CE00227K.
- [96] P. Ferrer, I. da Silva, and I. Puente-Orench. Solid Acetone Structure Dependence on Pressure: A New Fibre Textured Thin Film Crystallographic Structure Studied by Grazing-Incidence X-Ray Diffraction. *CrystEngComm* 18.42 (2016), pages 8220–8228. ISSN: 1466-8033. DOI: 10.1039/C6CE01333C.
- [97] D. E. Braun, A. Rivalta, A. Giunchi, N. Bedoya-Martínez, B. Schrode, E. Venuti, R. G. Della Valle, and O. Werzer. Surface Induced Phenytoin Polymorph. 1. Full Structure Solution by Combining Grazing Incidence X-Ray Diffraction and Crystal Structure Prediction. *Crystal Growth & Design* (Oct. 2019). ISSN: 1528-7483, 1528-7505. DOI: 10.1021/acs.cgd.9b00857.
- [98] A. Giunchi, A. Rivalta, N. Bedoya-Martínez, B. Schrode, D. E. Braun, O. Werzer, E. Venuti, and R. G. Della Valle. Surface Induced Phenytoin Polymorph. 2. Structure Validation by Comparing Experimental and Density Functional Theory Raman Spectra. *Crystal Growth & Design* (Sept. 2019). ISSN: 1528-7483. DOI: 10.1021/acs.cgd.9b00863.

- [99] A. Lausi, M. Polentarutti, S. Onesti, J. R. Plaisier, E. Busetto, G. Bais, L. Barba, A. Cassetta, G. Campi, D. Lamba, A. Pifferi, S. C. Mande, D. D. Sarma, S. M. Sharma, and G. Paolucci. Status of the Crystallography Beamlines at Elettra. *The European Physical Journal Plus* 130.3 (Mar. 2015), page 43. ISSN: 2190-5444. DOI: 10.1140/epjp/i2015-15043-3.
- [100] P. Kraft. PILATUS 2M: A Detector for Small Angle X-Ray Scattering. PhD thesis. ETH Zurich, 2010. DOI: 10.3929/ethz-a-006023165.
- [101] B. Schrode, J. Simbrunner, S. Hofer, L. Barba, R. Resel, and O. Werzer. Impact of Sample Misalignment on Grazing Incidence X-Ray Diffraction Patterns and the Resulting Unit Cell Determination. *Review of Scientific Instruments (submitted)* (2019).
- [102] P. Kraft, A. Bergamaschi, C. Broennimann, R. Dinapoli, E. F. Eikenberry, B. Henrich, I. Johnson, A. Mozzanica, C. M. Schlepütz, P. R. Willmott, and B. Schmitt. Performance of Single-Photon-Counting PILATUS Detector Modules. *Journal of Synchrotron Radiation* 16.3 (May 2009), pages 368–375. ISSN: 0909-0495. DOI: 10.1107/S0909049509009911.
- [103] P. Kraft, A. Bergamaschi, C. Bronnimann, R. Dinapoli, E. F. Eikenberry, H. Graafsma, B. Henrich, I. Johnson, M. Kobas, A. Mozzanica, C. M. Schlepütz, and B. Schmitt. Characterization and Calibration of PILATUS Detectors. *IEEE Transactions on Nuclear Science* 56.3 (June 2009), pages 758–764. ISSN: 0018-9499. DOI: 10.1109/TNS.2008.2009448.
- [104] D. R. Black, D. Windover, A. Henins, J. Filliben, and J. P. Cline. STANDARD REFERENCE MATERIAL 660B FOR X-RAY METROLOGY. *Advances in X-ray Analysis* 54 (Aug. 2010), pages 140–148.
- [105] T. C. Huang, H. Toraya, T. N. Blanton, and Y. Wu. X-Ray Powder Diffraction Analysis of Silver Behenate, a Possible Low-Angle Diffraction Standard. *Journal of Applied Crystallography* 26.2 (Apr. 1993), pages 180–184. ISSN: 00218898. DOI: 10.1107/S0021889892009762.
- [106] D. R. Black, D. Windover, A. Henins, D. Gil, J. Filliben, and J. P. Cline. Certification of NIST Standard Reference Material 640d. *Powder Diffraction*

- 25.02 (June 2010), pages 187–190. ISSN: 0885-7156, 1945-7413. DOI: 10.1154/1.3409482.
- [107] D. Kriegner, E. Wintersberger, and J. Stangl. Xrayutilities: A Versatile Tool for Reciprocal Space Conversion of Scattering Data Recorded with Linear and Area Detectors. *Journal of Applied Crystallography* 46.4 (Aug. 2013), pages 1162–1170. ISSN: 0021-8898, 1600-5767. DOI: 10.1107/S0021889813017214.
 - [108] A. P. Hammersley. *FIT2D*: A Multi-Purpose Data Reduction, Analysis and Visualization Program. *Journal of Applied Crystallography* 49.2 (Apr. 2016), pages 646–652. ISSN: 1600-5767. DOI: 10.1107/S1600576716000455.
 - [109] A. Hofer. Physical Vapor Deposition and Characterisation of Decyl-Phenyl-Benzothieno-Benzothiophene Thin Films. Masters Thesis. 2019.
 - [110] C. Röthel. X-Ray Diffraction of Organic Thin Films: Crystalline Texture in Uniplanar Systems. PhD thesis. Graz University of Technology, Oct. 2017.
 - [111] B. Schrode, C. Röthel, S. Pachmajer, R. Resel, and O. Werzer. GIDVis – A Modular MATLAB Program to Analyze Grazing Incidence Diffraction Images. <https://www.if.tugraz.at/amd/GIDVis/>. Feb. 2019.
 - [112] B. Schrode. GIDVis – Guide and Tutorials.
 - [113] G. M. Sheldrick. A Short History of *SHELX*. *Acta Crystallographica Section A Foundations of Crystallography* 64.1 (Jan. 2008), pages 112–122. ISSN: 0108-7673. DOI: 10.1107/S0108767307043930.
 - [114] G. M. Sheldrick. Crystal Structure Refinement with *SHELXL*. *Acta Crystallographica Section C Structural Chemistry* 71.1 (Jan. 2015), pages 3–8. ISSN: 2053-2296. DOI: 10.1107/S2053229614024218.
 - [115] G. M. Sheldrick. Alphabetical List of SHELXL Instructions. http://shelx.uni-goettingen.de/shelxl_html.php. Mar. 2018.
 - [116] I. Salzmann and R. Resel. *STEREOPOLE*: Software for the Analysis of X-Ray Diffraction Pole Figures with IDL. *Journal of Applied Crystallography* 37.6 (Dec. 2004), pages 1029–1033. ISSN: 0021-8898. DOI: 10.1107/S002188980402165X.

Bibliography

- [117] T. Möller and J. F. Hughes. Efficiently Building a Matrix to Rotate One Vector to Another. *Journal of Graphics Tools* 4.4 (Jan. 1999), pages 1–4. ISSN: 1086-7651. DOI: 10.1080/10867651.1999.10487509.


Acronyms

BAMS	Bar-Assisted Meniscus Shearing
CBZ	Carbamazepine
COR	Center of Rotation
CSP	Crystal Structure Prediction
CVD	Chemical Vapor Deposition
DFT	Density Functional Theory
ESRF	European Synchrotron Radiation Facility
GIXD	Grazing Incidence X-ray Diffraction
GUI	Graphical User Interface
HOC	Higher-Order Commensurism
HOPG	Highly Oriented Pyrolytic Graphite
HWE	Hot-Wall Epitaxy
LED	Light-Emitting Diode
LEED	Low-Energy Electron Diffraction
LOL	Line-on-Line
MBE	Molecular-Beam Epitaxy
MD	Molecular Dynamics

Acronyms

MOF	Metal-Organic Framework
OLC	On-Line Coincidence
OMBE	Organic Molecular-Beam Epitaxy
P2O	6,13-Pentacenequinone
PF	Pole Figure
POL	Point-on-Line
PVD	Physical Vapour Deposition
<i>sdd</i>	Sample-Detector Distance
SIP	Substrate-Induced Phase
XRD	X-ray Diffraction

Personal Information

Date of birth	December, 1990
Place of birth	Coburg, Germany
Address	Graz, Austria
 iD	https://orcid.org/0000-0003-2013-9272

Education

since 01/2017	Doctoral School Physik – Graz University of Technology
09/2013–05/2016	Master's Degree Programme Technical Physics – Graz University of Technology, Austria
09/2014–09/2015	Master's Thesis at the Institute of Solid State Physics – Graz University of Technology, Austria: <i>Crystal Structure Phase Analysis of C₈O–BTBT–OC₈ Films by Raman and Infrared Spectroscopy</i> . Supervisor: Ao.Univ.-Prof. Dipl.-Ing. Dr.techn. Roland Resel
10/2009–09/2013	Bachelor's Degree Programme Technical Physics – Graz University of Technology, Austria. Bachelor's thesis at the Institute of Theoretical and Computational Physics: <i>Wellenpakete im eindimensionalen Kristallgitter</i> . Supervisor: Ao.Univ.-Prof. Dipl.-Ing. Dr.techn. tit.Univ.-Prof. Heinrich Sormann
06/2009–07/2009	BG Sport RG Saalfelden, Austria

Professional Experience

since 08/2017	Doctoral Research Assistant – Institute of Solid State Physics, Graz University of Technology, Austria
01/2017–06/2017	Scientific Project Assistant – Institute of Pharmaceutical Sciences, Department of Pharmaceutical Technology, University of Graz
10/2018–02/2019	Teaching Assistant <i>Laboratory Course Biobased Materials</i> for students of the Master’s Degree Programme Advanced Materials Science (NAWI Graz)
10/2017–09/2018	Teaching Assistant <i>Fortgeschrittenenpraktikum Technische Physik 1 & 2</i> for Students of the Bachelor’s Degree Programme Physics (NAWI Graz)
06/2016–12/2016	Project Assistant – Institute of Solid State Physics, Graz University of Technology, Austria

Technical Skills and Research Experience

- Extensive theoretical knowledge in X-ray diffraction
- Highly experienced in MATLAB programming (*e.g.* development of data analysis software)
- Advanced knowledge of C#, VB.net (Windows Forms, UWP) and version-control systems (bitbucket)
- Highly experienced in X-ray diffraction experiments performed at synchrotron facilities, especially on thin films
- Extensive experience in X-ray diffraction and reflectivity experiments using lab-based equipment and associated data evaluation
- Proficient in data analysis of grazing incidence X-ray diffraction experiments using in-house developed software packages
- Organization of and several research stays at the synchrotrons Elettra (Trieste, Italy) and ESRF (Grenoble, France)

- Experience in training colleagues on performing and evaluating results of different X-ray diffraction methods

Publications

- B. Schrode, J. Simbrunner, S. Hofer, L. Barba, R. Resel, and O. Werzer. Impact of Sample Misalignment on Grazing Incidence X-Ray Diffraction Patterns and the Resulting Unit Cell Determination. *Review of Scientific Instruments (submitted)* (2019)
- J. Simbrunner, B. Schrode, J. Domke, T. Fritz, I. Salzmann, and R. Resel. An Efficient Method for Indexing Grazing-Incidence X-ray Diffraction Data of Epitaxially Grown Thin Films. *Acta Crystallographica Section A Foundations and Advances* 76.3 (May 2020). ISSN: 2053-2733. DOI: 10.1107/S2053273320001266
- A. Rivalta, A. Giunchi, L. Pandolfi, T. Salzillo, S. d’Agostino, O. Werzer, B. Schrode, N. Demitri, M. Mas-Torrent, A. Brillante, R. Della Valle, and E. Venuti. Crystal Alignment of Surface Stabilized Polymorph in Thioindigo Films. *Dyes and Pigments* 172 (Jan. 2020), page 107847. ISSN: 01437208. DOI: 10.1016/j.dyepig.2019.107847
- A. O. F. Jones, R. Resel, B. Schrode, E. Machado Charry, C. Röthel, B. Kunert, I. Salzmann, E. Kontturi, D. Reishofer, and S. Spirk. Structural Order in Cellulose Thin Films Prepared from a Trimethylsilyl Precursor. *Biomacromolecules* (Nov. 2019), acs.biomac.9b01377. ISSN: 1525-7797, 1526-4602. DOI: 10.1021/acs.biomac.9b01377
- D. E. Braun, A. Rivalta, A. Giunchi, N. Bedoya-Martinez, B. Schrode, E. Venuti, R. G. Della Valle, and O. Werzer. Surface Induced Phenytoin Polymorph. 1. Full Structure Solution by Combining Grazing Incidence X-Ray Diffraction and Crystal Structure Prediction. *Crystal Growth & Design* (Oct. 2019). ISSN: 1528-7483, 1528-7505. DOI: 10.1021/acs.cgd.9b00857
- A. Giunchi, A. Rivalta, N. Bedoya-Martínez, B. Schrode, D. E. Braun, O. Werzer, E. Venuti, and R. G. Della Valle. Surface Induced Phenytoin Polymorph. 2. Structure Validation by Comparing Experimental and Density

- Functional Theory Raman Spectra. *Crystal Growth & Design* (Sept. 2019). ISSN: 1528-7483. DOI: 10.1021/acs.cgd.9b00863
- B. Schrode, S. Pachmajer, M. Dohr, C. Röthel, J. Domke, T. Fritz, R. Resel, and O. Werzer. *GIDVis: A Comprehensive Software Tool for Geometry-Independent Grazing-Incidence X-ray Diffraction Data Analysis and Pole-Figure Calculations*. *Journal of Applied Crystallography* 52.3 (June 2019), pages 683–689. ISSN: 1600-5767. DOI: 10.1107/S1600576719004485
 - J. Simbrunner, S. Hofer, B. Schrode, Y. Garmshausen, S. Hecht, R. Resel, and I. Salzmann. Indexing Grazing-Incidence X-Ray Diffraction Patterns of Thin Films: Lattices of Higher Symmetry. *Journal of Applied Crystallography* 52.2 (Apr. 2019), pages 428–439. DOI: 10.1107/s1600576719003029
 - V. Vandalon, A. Sharma, A. Perrotta, B. Schrode, M. A. Verheijen, and A. A. Bol. Polarized Raman Spectroscopy to Elucidate the Texture of Synthesized MoS₂. *Nanoscale* (2019), 10.1039.C9NR08750H. ISSN: 2040-3364, 2040-3372. DOI: 10.1039/C9NR08750H
 - T. Stassin, S. Rodríguez-Hemida, B. Schrode, A. J. Cruz, F. Carraro, D. Kravchenko, V. Creemers, I. Stassen, T. Hauffman, D. E. De Vos, P. Falcato, R. Resel, and R. Ameloot. Vapour-Phase Deposition of Oriented Copper Dicarboxylate Metal-Organic Framework Thin Films. *Chemical Communications* (2019), 10.1039.C9CC05161A. ISSN: 1359-7345, 1364-548X. DOI: 10.1039/C9CC05161A
 - M. Skałoń, M. Hebda, B. Schrode, R. Resel, J. Kazior, and C. Sommitsch. In Situ Formation of TiB₂ in Fe-B System with Titanium Addition and Its Influence on Phase Composition, Sintering Process and Mechanical Properties. *Materials* 12.24 (2019). ISSN: 1996-1944. DOI: 10.3390/ma12244188
 - M. Rooney, F. Carulli, S. Luzzati, R. Resel, B. Schrode, R. Ruffo, M. Sassi, and L. Beverina. Diketopyrrolopyrrole Latent Pigment-Based Bilayer Solar Cells. *Organic Photonics and Photovoltaics* 6.1 (Dec. 2018), pages 8–16. ISSN: 2299-3177. DOI: 10.1515/opph-2018-0002
 - A. Petritz, M. Krammer, E. Sauter, M. Gärtner, G. Nascimbeni, B. Schrode, A. Fian, H. Gold, A. Cojocar, E. Karner-Petritz, R. Resel, A. Terfort, E. Zojer, M. Zharnikov, K. Zojer, and B. Stadlober. Embedded Dipole Self-Assembled Monolayers for Contact Resistance Tuning in p-Type and n-Type

Organic Thin Film Transistors and Flexible Electronic Circuits. *Advanced Functional Materials* 28.45 (Nov. 2018), page 1804462. ISSN: 1616301X. DOI: 10.1002/adfm.201804462

- J. Simbrunner, C. Simbrunner, B. Schrode, C. Röthel, N. Bedoya-Martinez, I. Salzmann, and R. Resel. Indexing of Grazing-Incidence X-Ray Diffraction Patterns: The Case of Fibre-Textured Thin Films. *Acta Crystallographica Section A Foundations and Advances* 74.4 (July 2018), pages 373–387. ISSN: 2053-2733. DOI: 10.1107/S2053273318006629
- B. Schrode, A. O. F. Jones, R. Resel, N. Bedoya, R. Schennach, Y. H. Geerts, C. Ruzié, M. Sferrazza, A. Brillante, T. Salzillo, and E. Venuti. Substrate-Induced Phase of a Benzothiophene Derivative Detected by Mid-Infrared and Lattice Phonon Raman Spectroscopy. *ChemPhysChem* (Mar. 2018). ISSN: 14394235. DOI: 10.1002/cphc.201701378
- B. Schrode, B. Bodak, H. Riegler, A. Zimmer, P. Christian, and O. Werzer. Solvent Vapor Annealing of Amorphous Carbamazepine Films for Fast Polymorph Screening and Dissolution Alteration. *ACS Omega* 2.9 (Sept. 2017), pages 5582–5590. ISSN: 2470-1343, 2470-1343. DOI: 10.1021/acsomega.7b00783
- N. Bedoya-Martínez, B. Schrode, A. O. F. Jones, T. Salzillo, C. Ruzié, N. Demitri, Y. H. Geerts, E. Venuti, R. G. Della Valle, E. Zojer, and R. Resel. DFT-Assisted Polymorph Identification from Lattice Raman Fingerprinting. *The Journal of Physical Chemistry Letters* 8.15 (Aug. 2017), pages 3690–3695. ISSN: 1948-7185. DOI: 10.1021/acs.jpcllett.7b01634

Talks

- R. Resel, B. Schrode, S. Hofer, L. Legenstein, M. Kräuter, C. Winkler, T. Burger, A. M. Coclite, S. Borisov, P. Falcaro, and R. Ameloot. Phase Analysis of Metal Organic Frameworks: Examples from the Network Porous Materials@Work. Porous Materials@Work – 2nd Scientific Meeting, Reinischkogel, Austria, Feb. 2020
- B. Schrode, S. Pachmajer, C. Röthel, S. Hofer, J. Domke, T. Fritz, R. Resel,

- and O. Werzer. Mapping of Large Volumes of Reciprocal Space by Rotating Grazing-Incidence X-Ray Diffraction. EMRS Fall Meeting, Warsaw, Poland, Sept. 2019
- B. Schrode. The Software Package GIDVis. Presentation in the Hofmann Group, Institute of Solid State Physics, Graz University of Technology, Austria, Aug. 2019
 - B. Schrode. From Grazing Incidence Diffraction to Pole Figures and Epitaxy. Doctoral School Seminar, Graz University of Technology, Austria, May 2019
 - B. Schrode. Epitaxial Growth of Pentacene Derivatives. Presentation in Organic Materials and Structural Research, Graz University of Technology, Austria, Oct. 2018
 - M. Kaltenegger, B. Schrode, and O. Werzer. Finding New Drug Polymorphs within Thin Films. 68th Annual Meeting of the Austrain Physical Society, Graz, Austria, Sept. 2018
 - B. Schrode, S. Hofer, and R. Resel. X-Ray Methods @ If. Porous Materials@Work, 1st Scientific Meeting, Reinischkogel, Austria, Sept. 2018
 - B. Schrode. Epitaxial Growth of Pentacene Derivatives. Presentation in Organic Materials and Structural Research and the Hofmann Group, Graz University of Technology, Austria, May 2018, June 2018
 - B. Schrode. Polymorph Selection of a BTBT Derivative by Optical Spectroscopy. Workshop on Substrate induced Crystallisation, Graz, Austria, Apr. 2018
 - B. Schrode. Methoden der Röntgenbeugung zur Untersuchung (epitaktischer) Dünn-Filme. Presentation at the Fritz Group, Institute of Solid State Physics, Friedrich Schiller University Jena, Germany, Feb. 2018
 - B. Schrode. Investigations of Solution Processed Caffeine on Glass and Muscovite Mica. Presentation in Organic Materials and Structural Research, Graz University of Technology, Austria, Oct. 2017
 - B. Schrode. Infrared and Raman Investigations on the Surface Induced Phase of the Molecule Dioctyloxy-Benzothieno-Benzothiophene. Workshop on Surface induced crystallographic structures, Brussels, Belgium, May 2015

Posters

- B. Schrode, S. Hofer, R. Ricco, F. Carraro, P. Falcaro, M. Takahashi, K. Ikagaki, and R. Resel. Alignment Study of Epitaxially Grown Cu(BDC)-MOFs via X-Ray Pole Figure Technique. Poster. Porous Materials@Work Summer School, Graz, Austria, Sept. 2019
- J. Simbrunner, S. Hofer, B. Schrode, I. Salzmänn, and R. Resel. Indexing Grazing Incidence X-Ray Diffraction Patterns of Thin Films. Poster. 32nd European Crystallographic Meeting, Vienna, Austria, Aug. 2019
- B. Schrode, S. Pachmajer, M. Dohr, C. Röthel, J. Domke, R. Resel, and O. Werzer. The Software GIDVis and Its Application to the Evaluation of Rotating Grazing Incidence X-Ray Diffraction Experiments. Poster. MRS Spring Meeting 2019, Phoenix, AZ, USA, Apr. 2019
- B. Schrode, S. Pachmajer, M. Dohr, C. Röthel, J. Domke, T. Fritz, R. Resel, and O. Werzer. The Software Package GIDVis and Its Application to Rotating Grazing Incidence X-Ray Diffraction Data. Poster. NESY Winterschool, Altaussee, Austria, Mar. 2019
- J. Simbrunner, S. Hofer, B. Schrode, R. Resel, and I. Salzmänn. Indexing Grazing Incidence X-Ray Diffraction Patterns of Thin Films: Lattices of Higher Symmetry. Poster. NESY Winterschool, Altaussee, Austria, Mar. 2019
- B. Schrode, M. Grünwald, F. Sojka, J. Domke, T. Fritz, O. T. Hofmann, and R. Resel. Epitaxial Order of Pentacenequinone Films on Graphene and Au(111). Poster. 68th Annual Meeting of the Austrian Physical Society, Graz, Austria, Sept. 2018
- J. Simbrunner, B. Schrode, C. Röthel, N. Bedoya-Martínez, I. Salzmänn, and R. Resel. Crystal Structure Solution from Thin Films: Indexation of Grazing Incidence X-Ray Diffraction Patterns. Poster. XTOP 2018, Bari, Italy, Sept. 2018
- B. Schrode, M. Grünwald, F. Sojka, J. Domke, T. Fritz, O. T. Hofmann, and R. Resel. Epitaxial Film Growth of Pentacenequinone on Graphene and Au(111). Poster. Graz, July 2018
- B. Schrode, A. O. F. Jones, R. Resel, N. Bedoya-Martínez, E. Zojer, R.

- Schennach, Y. H. Geerts, M. Sferrazza, A. Brillante, T. Salzillo, and E. Venuti. The Substrate-Induced Phase of C₈O-BTBT-OC₈ Detected by Mid-Infrared and Lattice Phonon Raman Spectroscopy. Poster. Conference on Progress in Organic Optoelectronics, Valencia, Spain, Dec. 2017
- B. Schrode, A. O. F. Jones, R. Resel, R. Schennach, A. Brillante, T. Salzillo, and E. Venuti. The Substrate-Induced Phase of C₈O-BTBT-OC₈ Detected by Mid-Infrared and Lattice Phonon Raman Spectroscopy. Poster. 9th Workshop on Substrate-Mediated Polymorphism in Organic Thin Films, Graz, Austria, Sept. 2017
 - A. O. F. Jones, B. Schrode, M. Sferrazza, and R. Resel. Polymorphic Phases of an Organic Semiconductor: A Combined Raman and Grazing Incidence X-Ray Diffraction Study. Poster. 29th European Crystallographic Meeting, Rovinj, Croatia, Aug. 2015

Grants

- Research funding scheme “International Communication” of the “Österreichische Forschungsgemeinschaft” (ÖFG) for the *2019 MRS Spring Meeting* (Apr. 2019)
- KUWI of “Graz University of Technology” for a research stay at the University of Bologna (Dec. 2014)